Transforming Doppler tomography to unravel the accretion dynamics in cataclysmic variables

Enrico Juan Kotze

10 March 2017

Thesis Presented for the Degree of
DOCTOR OF PHILOSOPHY
in the Department of Astronomy
UNIVERSITY OF CAPE TOWN

Supervisors: Drs Vanessa A. McBride and Stephen B. Potter

When we are born, we cry that we are come to this great stage of fools.

– William Shakespeare, *King Lear*, Act 4, Scene 6

Abstract

Name: **Enrico Juan Kotze**
Title: **Transforming Doppler tomography to unravel the accretion dynamics in cataclysmic variables**
Date: **10 March 2017**

Doppler tomography has revolutionised the interpretation of phase-resolved spectra of interacting binaries. The standard technique extracts emission and kinematic information contained in such spectra and projects it onto a two-dimensional velocity coordinate frame.

This thesis describes my investigation of constructing Doppler tomograms in 'inside-out' coordinates by reversing the velocity axis. The aim was to determine if the emission distribution in the inside-out tomogram is more intuitive to interpret than the standard tomogram, and if it reveals indiscernible or enhances less discernible details. The inside-out tomogram is constructed by projecting the spectra onto the inside-out coordinate frame with zero velocity transposed to the outer circumference and the maximum velocities to the centre of the tomogram. In addition, this thesis describes a new flux modulation mapping technique applied to the standard and inside-out Doppler tomography of magnetic cataclysmic variables. I developed this technique with the aim to obtain more information from their observed spectra and present it in a useful format. It extracts the flux modulation from consecutive half-phase tomograms and constructs maps of the amplitude and phasing characteristics of the modulation in these systems.

My investigation, involving the spectra of non-magnetic and magnetic cataclysmic variables, shows that the inside-out projection redistributes the relative contrast levels in and amongst the emission components. The inside-out projection exposes low-velocity emission details which are overly compacted and enhances high-velocity emission details which are overly tenuous in the standard projection. In addition, the flux modulation mapping technique gives a significant improvement in reproducing the input spectra adding more confidence in the interpretation of the modulation maps.

Notable results were obtained for the polars where the blob-like low-velocity emission in their standard tomograms is more exposed in their inside-out tomograms, making it easier to distinguish between the ballistic and magnetic accretion flows that are evident in their trailed spectra. Also, for all the polars investigated the high-velocity magnetic accretion flows not seen in their standard tomograms are revealed in their inside-out tomograms. This extra information is extremely valuable to form a more complete picture of the emission components, broadening our knowledge of the accretion dynamics in these systems.

Preface

The fool doth think he is wise, but the wise man knows himself to be a fool.

– William Shakespeare, *As You Like It*, Act V, Scene 1

Cataclysmic variables are quintessential stellar objects for the study of mass transfer, accretion flows and accretion discs. These systems are semi-detached, interacting binary systems in which a white dwarf star accretes material that is being transferred from a low-mass red dwarf star. Depending on the strength of the magnetic field of the primary and the system dimensions the transferred ionised gas may or may not form an accretion disc around the primary before it is finally accreted. I provide a short overview of cataclysmic variables in Chapter 1.

Doppler tomography is a technique aimed at rendering information locked-up in the phase-resolved spectra of an interacting binary, such as a cataclysmic variable, into a two-dimensional image of its emission components in velocity coordinates. It has been invaluable in the quest to expand the understanding of the accretion structures in cataclysmic variables. I give an overview of the standard technique of Doppler tomography in Chapter 2.

I describe a new 'inside-out' projection technique that can be used in Doppler tomography in Chapter 3. I developed this technique with the objective to determine if the emission distribution in the inside-out tomogram is more intuitive to interpret than the standard tomogram, and if it reveals indiscernible or enhances less discernible details. The inside-out projection reverses the velocity axis and constructs tomograms by directly projecting the spectra onto the inside-out coordinate frame with zero velocity transposed to the outer circumference and the maximum velocities to the centre of the tomogram.

I present the results of applying the inside-out projection to the spectra of various non-magnetic and magnetic cataclysmic variables in Chapter 4. The results show that the inside-out projection redistributes the relative contrast levels in and amongst the emission components: it exposes low-velocity emission details which are overly compacted and enhances high-velocity emission details which are overly tenuous in the standard projection.

I describe a new flux modulation mapping technique applied to the standard and inside-out Doppler tomography of magnetic cataclysmic variables (mCVs) in Chapter 5. I developed this technique with the objective to extract more information from the observed spectra and present it in a useful format. The flux modulation is extracted from consecutive half-phase tomograms and presented in maps of the amplitude and phasing characteristics of the

modulation. The results neatly confirm the expected phased modulation of the emission components in the mCVs investigated and show a significant improvement in reproducing the input spectra, adding more confidence in the interpretation of the modulation maps.

I present new observations of the polar CTCV J1928−5001 in Chapter 6. These observations included high-speed photometry obtained with the South African Astronomical Observatory (SAAO) 1.9 m telescope and long-slit spectroscopy obtained with the Southern African Large Telescope (SALT). The chapter focusses mainly on applying standard and inside-out Doppler tomography, and flux modulation mapping, to the new phase-resolved spectra.

I summarise the results of my investigation of inside-out Doppler tomography and flux modulation mapping in Chapter 7. I conclude the chapter with an overview of some future work that will build on the work done for this thesis. The photometric and spectroscopic results obtained for CTCV J1928−5001 (described in Chapter 6), as well as the polarimetric results and the investigation into the apparent lack of any orbital period variations, are in preparation to be submitted to an appropriate peer-reviewed journal. Also, preliminary standard and inside-out Doppler tomography results obtained from spectra generated from full three-dimensional magnetohydrodynamic simulations are showing enormous promise to establish a better understanding of the accretion flows in polars. This preliminary investigation will be refined and the simulations will be exploited further in a future work.

During the course of my postgraduate studies I was able to get considerable observing experience with most of the facilities at the SAAO's site in Sutherland. Over the last four years I observed for a total of seventeen weeks:

- five weeks on the 1.0 m telescope,
- eleven weeks on the 1.9 m telescope and
- one week on the 1.4 m telescope of the InfraRed Survey Facility (IRSF).

These observations involved photometry, polarimetry and spectroscopy with the following instruments:

- SAAO CCD Camera (STE4),
- Sutherland High Speed Optical Cameras (SHOC),
- HIgh speed Photo-Polarimeter (HIPPO),
- Simultaneous-3color InfraRed Imager for Unbiased Survey (SIRIUS) and
- Spectrograph Upgrade – Newly Improved Cassegrain (SpUpNIC).

At the end of December 2015 I was afforded the opportunity to be the SALT operator for two nights – a remarkable and awe-inspiring experience.

I was also involved in several publications during the course of my postgraduate studies. These do not only include the publication of the major results from this work, but also several conference proceedings and co-authored articles.

List of refereed first author articles:

- "Exploring inside-out Doppler tomography: non-magnetic cataclysmic variables"
  Kotze E. J., Potter S. B., McBride V. A., 2015, A&A, 579, A77
- "Exploring inside-out Doppler tomography: magnetic cataclysmic variables"
  Kotze E. J., Potter S. B., McBride V. A., 2016, A&A, 595, A47
- "Unravelling the accretion flows in the polar CTCV J1928–5001"
  Kotze E. J., Potter S. B., McBride V. A., 2017, in preparation

List of conference proceedings:

- "New Observations of Accretion Phenomena in Magnetic Cataclysmic Variables"
  Buckley D. A. H., Potter S. B., Kotze E., Kotze M., Breytenbach H., 2014, EPJWC, 64, 07005
- "New Insights from Inside-Out Doppler Tomography"
  Kotze E. J., Potter S. B., 2015, AcPPP, 2, 170
- "Multi-tomography of polars from SALT spectroscopy"
  Potter S., Kotze E., McBride V., 2015, salt.conf, 51
- "Observational aspects of magnetic accretion: Doppler tomography"
  Potter S. B., Kotze E. J., McBride V. A., 2015, PoS, in press

List of co-authored articles:

- "SALT spectral observations of a new, bright, southern CV: MASTER OT J142023.5–485540"
  Gulbis A. A. S., Kotze M. M., Kotze E. J., Worters H. L., Buckley D. A. H., O'Donoghue D., Shara M., 2013, ATel, 5207
  Contribution: Data analysis
- "New binaries among UV-selected, hot subdwarf stars and population properties"
  Kawka A., Vennes S., O'Toole S., Németh P., Burton D., Kotze E., Buckley D. A. H., 2015, MNRAS, 450, 3514
  Contribution: Observations
- "Seven temperate terrestrial planets around the nearby ultracool dwarf star TRAPPIST-1"
  Gillon M., et al., 2017, Natur, 542, 456
  Contribution: Observations

Astra inclinant, sed non obligant...

Enrico Kotze
Cape Town
March 2017

Acknowledgements

My soul is in the sky.

– William Shakespeare, *A Midsummer Night's Dream*, Act V, Scene 1

I thank Stephen Potter for his unwavering enthusiasm in our endeavour to 'turn Doppler tomography inside-out'. Thank you, Steve! It was a privilege to have you as my guide on the sometimes bumpy and slippery road of postgraduate research. Thank you for sponsoring me to present our humble results at *The Golden Age of Cataclysmic Variables and Related Objects – II workshop 2013* and *HIRES 2014: Astronomy at high angular resolution – a cross-disciplinary approach workshop*. Also, thank you for promoting our results at *The Golden Age of Cataclysmic Variables and Related Objects – III workshop 2015* and the *SALT Science Conference 2015*.

I thank Vanessa McBride and Patrick Woudt for their contributions as my supervisors at the University of Cape Town. Thank you, Vanessa, for your diligence in all things administrative, your ready smile and moral support. Patrick, thank you for agreeing to take care of the final administrative tasks regarding my thesis.

I am grateful to Keith Horne for his encouragement and helpful comments when I showed him some of my first inside-out tomograms. I thank Axel Schwope for sharing the seminal HU Aqr data set – the first time I saw Axel's tomogram of HU Aqr I was in awe. I also thank Danny Steeghs and Coel Hellier for providing the IP Peg and PQ Gem data sets, respectively. I am extremely grateful to Henk Spruit for his elegant and efficient code which I could easily refactor to incorporate the inside-out projection. I thank Dmitry Bisikalo for providing the solutions of the MHD simulations and Pavel Kaygorodov for providing the code for generating the synthetic spectra from the simulations.

I thank all the people at the South African Astronomical Observatory – in Cape Town and Sutherland – for their friendship and support. Allow me to thank at least some of you by name: Thank you, Ellen, Jackie and Jennifer, for ensuring the much needed morning coffee is strong and always on time. Also, thank you, Ayanda, Sithembele, Mitchell and Livingstone, for making the Observatory site in Cape Town an oasis. Thank you, Antie Martha, Sina, Gertruida, Sylvia, Bettie, Sherelene and Thandi for providing the gastronomical delights to augment the astronomical delights I experienced on all my observing runs and other visits to Sutherland. Also, thank you to the technicians and other support staff – John,

Hilton, Carlson, Sinethemba and Mavela. All you beautiful people are indeed the heart and backbone of the Observatory.

Funding for all postgraduate education and research was directly or indirectly provided by the South African National Research Foundation and the Department of Science and Technology. All postgraduate coursework was completed as part of the National Astrophysics and Space Science Program, hosted at the University of Cape Town.

I dedicate this thesis to Fred Marang – a mentor and dear friend. Thank you, Fred, for sharing copiously from your almost 40 years of observing experience, life wisdom and easy laughter. You are a true gentle soul.

I am forever grateful to Marissa – my soul mate and partner in crime. Your love, honesty, integrity and humility are a bottomless well of inspiration. Thank you, Marissa, for walking by my side – and sometimes carrying me – on this awesome journey called life.

Enrico Kotze
Cape Town
March 2017

Plagiarism Declaration

I, Enrico J. Kotze, hereby declare that the work on which this thesis is based is my original work (except where acknowledgements indicate otherwise) and that neither the whole work nor any part of it has been, is being, or is to be submitted for another degree in this or any other university. I authorise the University to reproduce for the purpose of research either the whole or any portion of the contents in any manner whatsoever.

Signature:

Date: 10 March 2017

Contents

List of Figures

List of Tables

Chapter 1

Introduction

Now, now, you stars, that move in your right spheres,
Where be your pow'rs?

– William Shakespeare, *King John*, Act V, Scene 7

Even though most stars appear as point sources in the night sky it is believed that at least half of all stars are in fact binary or multiple systems in orbit around a common centre of mass (Carroll & Ostlie 2007). Binary stars present themselves in many guises with a wide range in observed spectral types and values for system parameters such as the mass ratio and separation distance of the component stars. In most binary stars the separation between the component stars is sufficiently large to produce only a gentle gravitational bond between them. These systems follow mostly independent evolutionary paths. On the other hand, in a close binary system the gravitational bond between the component stars can be strong enough to deform the outer layers of one or both stars. This dynamical interaction can have a severe impact on how the stars evolve.

This chapter is in reference to and represents a humble interpretation of especially Warner (2003) and Hellier (2001), as well as relevant articles, with specific references included where necessary. Section 1.1 is an introduction to the geometry and broad classification of close binary star systems. The close binary systems of importance for this thesis are the semi-detached systems known as cataclysmic variables. Section 1.2 provides a short overview of cataclysmic variables, quintessential stellar systems for the study of mass transfer, accretion flows and accretion discs on observable time scales. Where applicable I extend the overview to *magnetic* cataclysmic variables with specific elaboration of the peculiarities brought about by the magnetism of the primary. Section 1.3 gives short overviews of the indirect imaging techniques* eclipse mapping, Roche tomography, Stokes imaging and accretion stream mapping. These techniques have added greatly to our understanding of cataclysmic variables and other interacting binary systems. Overall this chapter lays the scene for the scientific enquiry into the accretion dynamics in cataclysmic variables.

*The whole Chapter 2 is devoted to the technique of Doppler tomography.

1.1 Close binary star systems

In order to understand the gravitational and centrifugal dynamics in a close binary system it is necessary to evaluate the effective potential of the forces for the entire system. This presents a very complicated analysis if, for example, time-dependent potentials due to an elliptical orbit and surface distortions in the component stars caused by their axial rotation and tidal interaction are taken into account. The analysis is simplified by the *centrally-condensed* Roche model introduced by Kopal (1959).

1.1.1 Roche model

The Roche model assumes that the system's orbit has been circularised. This is a fair assumption because the tidal interactions in close binary star systems like CVs often bring about this condition (Hut 1981). It also assumes that the masses of the component stars can be treated as point masses at their centres. Again this is a fair assumption for close binary systems like CVs. The primary stars in CVs are highly condensed white dwarfs for which the distortion from spherical symmetry due to tidal and rotational forces is negligible. Even though the secondary stars in CVs are distorted they are very similar to single main sequence stars which are mostly centrally condensed.

Consider a close binary system which consists of a primary star with mass M_1 and a secondary star with mass M_2, separated by a distance a. Their common centre of mass is at the origin of a co-rotating cartesian coordinate frame. The stars are located on the x-axis at distances r_1 and r_2, respectively, from the origin such that $r_1 + r_2 = a$. The xy-plane represents the orbital plane of the system. The effective potential Φ acting on a gas particle, located at a distance r from the origin, is given by

$$\Phi(\boldsymbol{r}) = -\frac{GM_1}{|\boldsymbol{r}-\boldsymbol{r}_1|} - \frac{GM_2}{|\boldsymbol{r}-\boldsymbol{r}_2|} - \frac{1}{2}(\boldsymbol{\omega}\times\boldsymbol{r})^2, \tag{1.1}$$

where $\boldsymbol{\omega}$ is the angular frequency of the system about its centre of mass. The first and second terms constitute the gravitational potential due to the gravitational influence of the primary and secondary, respectively. The third term is the centrifugal inertial (pseudo-) potential, based upon the assumption that the centrifugal potential energy is zero if r is zero. Equation 1.1 is called the *Roche potential* in honour of the nineteenth-century French mathematician Édouard Roche ($1820-1883$). The points in the system that have the same Roche potential Φ constitute a surface of equal gravitational potential, that is, an equipotential surface. These equipotential surfaces are symmetric to reflection across the xz-plane, that is to say, about a line through the centres of the stars.

In order to visualise the Roche potential, consider the top panel of Figure 1.1 which shows a surface representing the Roche potential in the orbital plane of a system with a mass ratio* $q = M_2/M_1 = 0.2$. The more massive M_1 creates the larger potential well. The 'centrifugal'

*This definition of the mass ratio q, that is, the ratio of the mass of the less massive star to that of the more massive star, is used throughout this thesis.

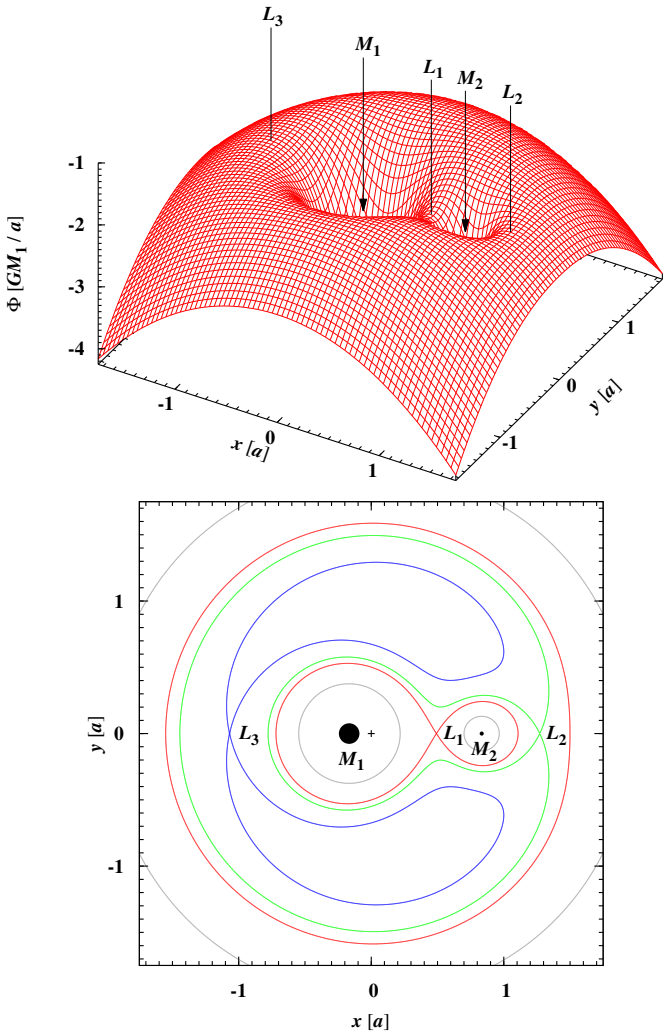

Figure 1.1. Roche model of a close binary system. The system consists of a primary star with mass M_1 and a secondary star with mass M_2; mass ratio $q = 0.2$. The top panel shows a surface plot that represents the Roche potential Φ in the orbital plane of a close binary system. The three Lagrangian points on the line that connects the two stars are L_1, L_2 and L_3. These saddle points are labelled accordingly. The bottom panel shows a contour plot of four Roche equipotentials from the surface shown in the top panel. These contours are colour-coded grey, red, green and blue in order of increasing Φ = constant. The red, green and blue contours include the Lagrangian points L_1, L_2 and L_3, respectively. The centre of mass of the system is indicated with a plus (+).

term in the Roche potential causes the downward curvature near the edges of the surface (if a test particle attempts to co-rotate with the stars at these distances it experiences a net outward force). The three saddle points labelled L_1, L_2 and L_3 are Lagrangian points. At these points the gravitational forces on a test particle due to the masses of the stars are balanced by the centrifugal inertial force, that is to say, the gradient of the effective potential is zero.

A number of equipotential contours are shown in the bottom panel of Figure 1.1. These contours are intersections between the equipotential surfaces and the orbital plane. The equipotential surfaces close to the centres of mass of the stars are nearly spherical and centred (inner grey contours). Further away the equipotential surfaces are distorted by the gravitational influence of the stars. The mass ratio q drives the shape of the equipotentials while the orbital separation a determines the overall scale of the Roche model. The Roche potential has a critical value at the inner Lagrangian point (L_1) where the apices of the equipotential surfaces around the stars touch in a 'pinch'-shape (red contour). The two teardrop-shaped surfaces defined by this equipotential are called the Roche lobes of the stars.

1.1.2 Roche lobe overflow

The Roche lobes define the gravitational sphere of influence of each star. For example, within the Roche lobe of the primary a gas particle feels a stronger attraction from the primary than from the secondary. The inner Lagrangian point (L_1) is a saddle between the potential wells corresponding to the primary and secondary, that is to say, a gas particle at L_1 belongs equally to both stars. This implies that L_1, at the meeting point of the Roche lobes of the primary and secondary, constitutes a convenient 'gate' through which mass can transfer between the stars. For example, if the primary evolves into a giant and it expands to overfill its Roche lobe then gas in its tenuous outer layers can be 'pushed' through L_1 by atmospheric pressure into the Roche lobe of the secondary. The transfer of mass through the inner Lagrangian point from one star to another is called *Roche lobe overflow* (RLOF). Figure 1.2 shows the shape, plotted along the x-axis of the surface representing the Roche potential in the orbital plane (see left panel of Figure 1.1). Because L_1 is lower than L_3, this means that if star M_2 fills its Roche lobe, matter will pass through L_1 into the potential well of M_1.

The Roche model provides a convenient basis for a broad classification of close binary star systems. When both of the component stars remain well within their Roche lobes the system is called a *detached* binary.* Mass transfer is unlikely in a detached system except if one star has a very strong stellar wind and the other star captures gas particles from this wind. The system is called a *semi-detached* binary if one of the stars fills or overfills its Roche lobe, while the other remains well within its lobe. Mass transfer in a semi-detached system takes place via RLOF. When both of the stars fill or overfill their Roche lobes the system is called a *contact* binary. The filled Roche lobes form a common envelope (CE) of gas around both the stars, but mass transfer may continue as long as the masses of the stars are unequal (Kuiper 1941). However, if the CE reaches L_2 or L_3 (i.e., the other two Lagrangian points that lie along the line through the centres of the stars) then gas can be pushed through them into the space that surrounds the system. This can possibly lead to the formation of a circumbinary disc.

*All wide binary star systems are also detached binaries.

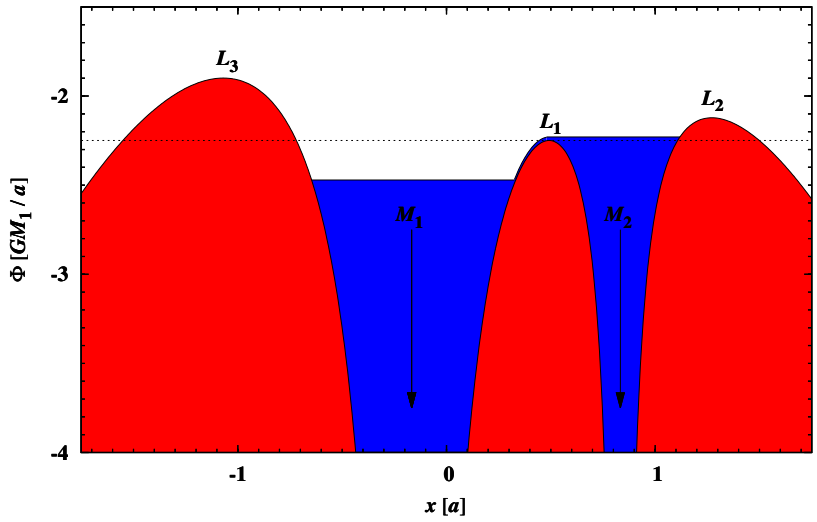

Figure 1.2. Roche lobe overflow in a close binary system. The dashed line is the value of Φ at the inner Lagrangian point (L_1). If the total energy per unit mass of a particle exceeds this value of Φ, it can flow 'over' L_1 between the two stars.

1.2 Cataclysmic variables

Cataclysmic variables (CVs) are semi-detached, interacting binary systems in which a white dwarf primary star accretes material that is being transferred from a low-mass red dwarf secondary star. The primary (the accretor) is the degenerate remnant of a low to intermediate mass ($0.8M_{\odot} < M < 8M_{\odot}$) main sequence star in its final stage of evolution. In general, the secondary (the donor) adheres to empirically derived properties of late type main sequence stars (Patterson 1984; Warner 1995). If the primary is non- or weakly magnetic the transferred material spirals inwards, forming an accretion disc around the primary before it is accreted onto the primary's surface near its equator. On the other hand, if the primary is strongly magnetic the transferred material, consisting mostly of ionised hydrogen, is threaded along the field lines before it is accreted onto the primary's surface near its magnetic poles. See, for example, Warner (2003) and Hellier (2001) for comprehensive, general reviews of all CVs.

Cataclysmic variables are essential objects for studying accretion mechanisms on observable time scales. In addition, they form an integral part of binary evolution studies and the effects of mass transfer and accretion on the evolutionary process. As the name 'cataclysmic variable' suggests, the mass transfer and accretion in these systems can lead to an extreme change in their observable brightness when they experience nova outbursts every few days to months or years (see classifications below). They also exhibit more 'benign' variability such as flickering and quasi-periodic oscillations originating in the accretion flow every few seconds to minutes. The broad classification of CVs are based on the observed outbursts

that characterise each class (Warner 2003).

Classical novae: Systems with only one observed nova outburst are called classical novae (CNe). These outbursts have amplitudes up to 20 magnitudes and are adequately modelled as thermonuclear runaways of the hydrogen-rich material that accretes onto the surface of the white dwarf primary. During the outburst a substantial shell of material is ejected at high velocities into the circumbinary space.

Recurrent novae: CNe that are observed to have more than one nova outburst are called recurrent novae (RNe).

Dwarf novae: Dwarf novae (DNe) are characterised by regular outbursts with amplitudes between two and five magnitudes which occur every $\sim$ ten days to tens of years. These outbursts are associated with the sudden release of gravitational energy due to the sporadic accretion onto the primary caused by a thermal instability in the accretion disc (Osaki 1974). DNe are split into three subcategories, namely Z Cam, SU UMa and U Gem stars. Z Cam stars undergo periods of rapid outburst activity, but also extended periods of standstills at ~ 0.7 magnitudes below maximum amplitude. SU UMa stars also have unusually long and bright superoutbursts with amplitudes ~ 0.7 magnitudes higher and lasting about five times longer than their regular dwarf nova outbursts. U Gem stars form an inhomogeneous subcategory that includes all DNe not classified as Z Cam or SU UMa stars. DN outbursts have been observed for some CNe.

Nova-like variables: All the CVs without an observed nova or dwarf nova outburst are called nova-like variables (NLs). This inhomogeneous group include pre- and post novae, as well as systems with an inadequate observational baseline. In general, magnetic CVs (see Section 1.2.2) are classified as NLs unless they have been identified as CNe or another class.

1.2.1 Origin

Most CVs begin as a detached binary star system in which the component stars are main sequence stars with different masses. The initial orbital period $P_{\rm orb}$ is of the order of a few months to a few years. The more massive primary star (mass M_1) evolves faster to become a red giant or supergiant star, depending on its initial mass. As it expands into a giant star it fills its Roche lobe and starts to transfer mass to the less massive secondary (mass M_2). The angular momentum of the transferred mass increases as the mass moves further away from the centre of mass of the system. The orbital separation a decreases slightly in order to conserve the total angular momentum in the system. As the orbital separation a decreases, the Roche lobe of the primary shrinks. However, a giant star with a convective envelope tends to expand in response to mass loss. The primary therefore overfills its Roche lobe even more and mass transfer to the secondary increases. This feedback produces a runaway mass transfer to the secondary. The Roche lobe of the secondary cannot adjust fast enough to contain all the material transferred into it. The transferred material spills

over into larger equipotential surfaces and eventually forms a CE around both stars (e.g., Iben & Livio 1993).

While in the CE the system loses orbital energy at an increased rate due to the drag force on the stars from frictional interactions with the material in the CE. The orbital separation a decreases drastically as the cores of the stars spiral inwards towards the centre of the envelope. The spiralling components inevitably produce differential rotation in the largely convective CE, creating a powerful magnetic dynamo (Regős & Tout 1995). The resulting magnetic fields can accelerate the spiralling-in process and help create a propeller action inside the CE which ejects the CE into interstellar space as a planetary nebula. A close, detached binary star system is exposed in the centre of the planetary nebula. However, the secondary main sequence star now orbits a primary hot subdwarf star.

After the CE phase the subdwarf core contracts as it evolves to become a fully degenerate white dwarf. The magnetic field of the white dwarf becomes frozen in, leading to a range of field strengths depending on the strength of the magnetic field generated by the dynamo in the CE phase (Regős & Tout 1995). The system continues to lose orbital energy due to magnetic braking (Huang 1966) and gravitational radiation (Paczyński 1967). This decreases the orbital separation a further to the point where the secondary fills its Roche lobe and mass transfer via RLOF is induced. The now semi-detached system is then considered to be a CV. Figure 1.3 shows a schematic of the evolutionary process described above. See, for example, Ritter (2012) for a review of pre-CV evolution.

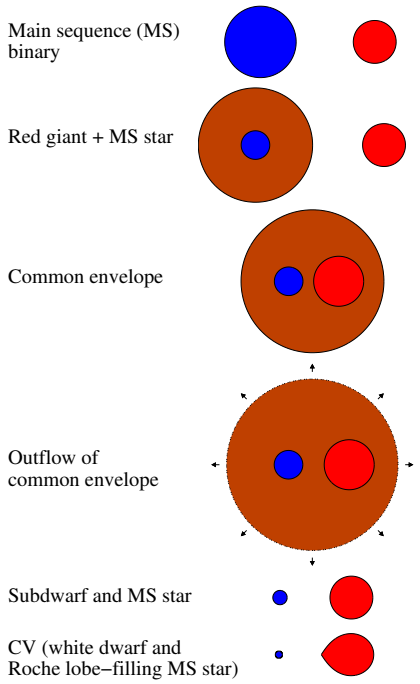

Figure 1.3. A schematic of the origin of a CV. The original primary (blue) with mass M_1 stays the more massive component of the binary throughout the evolution. Adapted from Seward & Charles (2010) – Figure 10.10.

1.2.2 Mass transfer and accretion

CVs are quintessential stellar objects for the study of mass transfer, accretion flows and accretion discs. In CVs the secondary fills its Roche lobe, allowing mass to be transferred via RLOF into the Roche lobe of the primary. The stream of transferred gas, which is orbiting the binary's centre of mass at a speed in excess of $100\,\mathrm{km\,s^{-1}}$, enters the Roche lobe of the primary at a thermal sound speed $\sim 10\,\mathrm{km\,s^{-1}}$. Therefore, even though it is now gravitationally under the influence of the primary, the gas does not fall directly onto it, but it flows in a free fall trajectory towards the primary, being partially ionised by particle collisions in the gas stream.

Depending on the strength of the magnetic field of the primary and the system dimensions this ionised ballistic gas stream may or may not form an accretion disc around the primary before it is finally accreted. In non- or weakly-magnetic CVs the primary's magnetic field is not strong enough to have a dynamic influence on the ballistic stream and an accretion disc will form around the primary. On the other hand, in magnetic CVs (mCVs) the primary's magnetic field is strong enough, given the system dimensions, to totally or partially disrupt the formation of an accretion disc and the transferred gas is ultimately accreted in a magnetically confined accretion flow.

1.2.2.1 Disc accretion

The turbulence caused by the ballistic stream colliding with itself and the resulting dissipation of energy allows the gas to settle in a circular orbit in the orbital plane with a radius that facilitates the conservation of angular momentum in the transferred gas. This circularisation radius is not exactly the same for every particle and therefore the gas forms a ring that has a level of radial dimensionality. Particles at different radii in the ring orbit at different speeds which leads to friction and turbulence. This generates heat which drains energy from the ring's gravitational potential energy causing some of the gas to move closer to, and some further away from the primary in order to conserve the overall angular momentum in the ring. Over time the ring is flattened into a thin disc around the primary from where the gas eventually accretes onto the surface of the primary. However, before it accretes the gas passes through the disc boundary layer, a transition zone between the disc and the surface of the primary where all, or at least a significant factor, of the kinetic energy of the gas is converted to heat. As much as $\sim 50\%$ of the total luminosity of the system can be ascribed to emission from the hot boundary layer (e.g., Hellier 2001). The kinetic energy of the ballistic stream flowing from the secondary is converted into heat where it collides with the edge of the disc, creating a region of extreme luminosity called the bright spot. The structure of this region is an open problem and it has been suggested that it is more a 'line' than a 'spot' caused by the impact wave between the stream and disc (e.g., Kononov et al. 2012). Emission from the bright spot can account for up to $\sim 30\%$ of the total luminosity of the system (e.g., Hellier 2001). Figure 1.4 shows a schematic illustration of the basic inferred structure of a CV with an accretion disc and Figure 1.5 shows zoomed

views of the boundary layer.

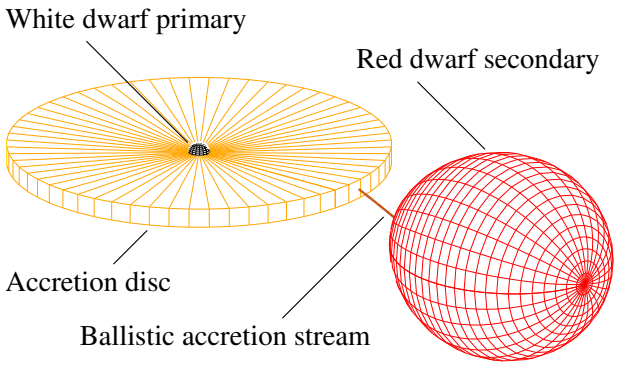

Figure 1.4. A schematic illustration of a CV with an accretion disc.

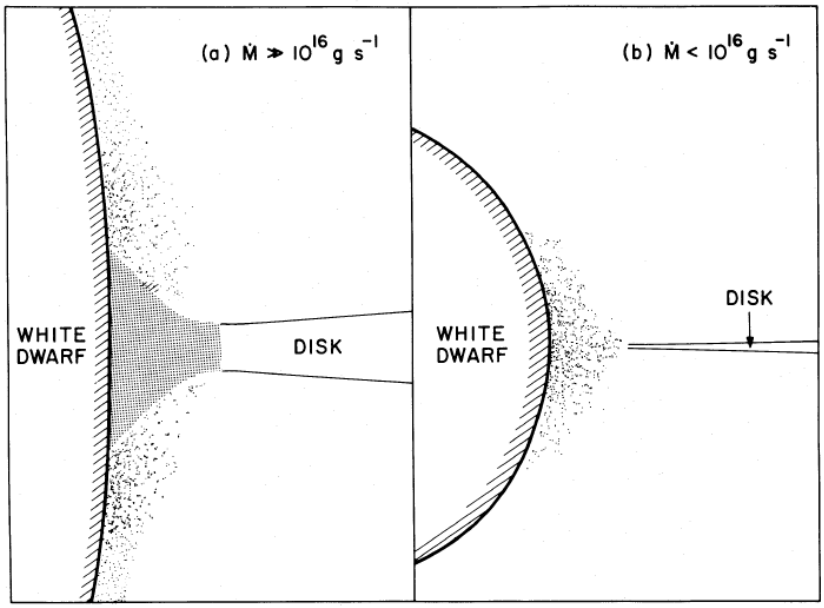

Figure 1.5. A schematic illustration of the accretion disc boundary layer. The left panel shows the region at a high accretion rate (i.e., in outburst). The increased gas flow is optically thick, producing soft X-rays. It is surrounded by hotter, optically thin regions. The right panel shows the region at a lower accretion rate (i.e., in quiescence). The gas being accreted is optically thin and hot ($T \sim 10^8$ K), producing mostly hard X-rays. Described by and taken from Patterson & Raymond (1985) – Figure 8.

1.2.2.2 Magnetic accretion

The mCVs comprise about $20 - 25\%$ of all known CVs (Ritter & Kolb 2003) and are split into two classes, namely polars and intermediate polars (IPs).

Polars: In polars, so named by Krzemiński & Serkowski (1977) on the grounds of the high circular polarisation detected in these systems, the magnetic field of the primary, given the system dimensions, is so strong that the trajectory of the gas stream is prevented from passing around the primary to form an accretion disc. In other words, the primary's magnetosphere (i.e., the extent of its magnetic field where the magnetic pressure exceeds the ram and gas pressure of the gas) stretches beyond the circularisation radius, preventing the gas stream from orbiting freely and forming an accretion disc. Instead the gas stream is threaded along the magnetic field lines in accretion columns (curtain) onto small accretion regions close to one or both of the magnetic poles of the primary (see below for an extended description). The orientation of the primary can be such that only one accretion region is continuously observable, creating a 'one-pole' system, but it is also possible that the second accretion region is periodically or continuously observable, creating a 'two-pole' system. Some systems display the presence of one or two accretion regions at different times of observation and the one-pole and two-pole configurations have been taken to be indicative of a lower and higher rate of accretion, respectively. A minimalistic schematic illustration of a polar with a two-pole accretion configuration is presented in Figure 1.6. See, for example, Cropper (1990) for a specific review of polars.

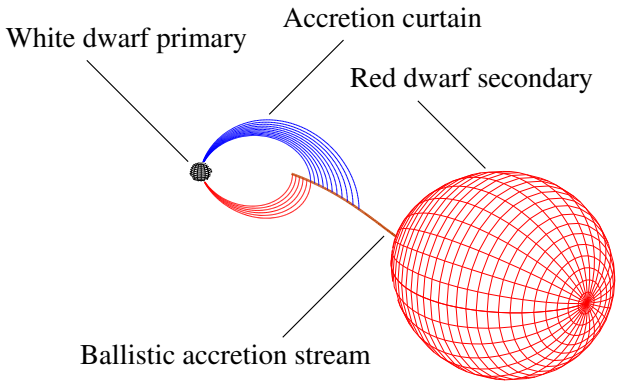

Figure 1.6. A schematic illustration of a mCV with ballistic and magnetic accretion flows only. The upper and lower magnetic accretion curtains are shown in blue and red, respectively.

The magnetic field strengths for polars, determined by Zeeman and cyclotron spectroscopy, are in the range $7 - 240\,\mathrm{MG}$ (Ferrario et al. 2015, and references therein). The magnetic moment of the primary in polars is sufficiently high to ensure that the primary rotates synchronously, that is to say, the rotation of the primary is phase-locked in the orbit of the system. However, as mass is accreted it is expected that the angular velocity of the primary will increase, but it appears that the rotational synchronism of the primary is preserved as the magnetic field lines of the primary are able to connect with the secondary, thereby introducing a magnetic braking torque opposing the accretion torque. Only four known systems have a confirmed degree of asynchronism: BY Cam (e.g., Silber et al. 1992), V1432 Aql (e.g., Patterson et al. 1995), V1500 Cyg (e.g., Stockman et al. 1988), and CD

Ind (e.g., Schwope et al. 1997a).

Intermediate polars: In most IPs the magnetic field of the primary, given the system dimensions, is not strong enough to prevent the trajectory of the gas stream from passing around the primary to form an accretion disc. In other words, the primary's magnetosphere is smaller than the circularisation radius, allowing the gas stream to orbit freely and form an accretion disc. However, where the inner edge of the disc encounters the magnetosphere the disc is prevented from extending further inwards, creating a truncated accretion disc. The gas at the boundary between the inner disc and the primary's magnetosphere is threaded along the magnetic field lines in accretion columns (curtain) onto small accretion regions close to one or both of the magnetic poles of the primary (see below for an extended description). Figure 1.7 shows a schematic illustration of the basic inferred structure of an IP with a truncated accretion disc and two magnetic accretion curtains. See, for example, Patterson (1994) for a specific review of IPs.

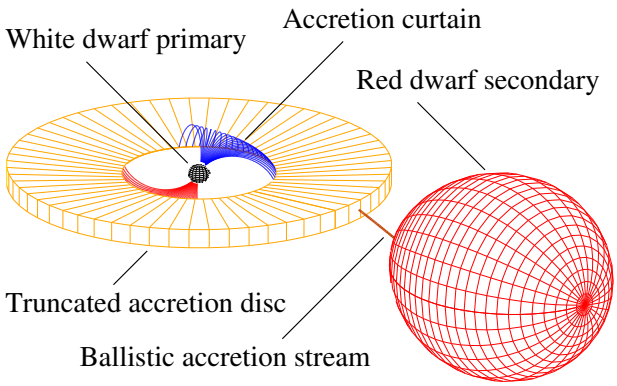

Figure 1.7. A schematic illustration of a mCV with a truncated accretion disc and magnetic accretion curtains. The upper and lower magnetic accretion curtains are shown in blue and red, respectively.

For IPs the inferred field strengths, from observed circular polarisation, are in the range $4 - 32\,\mathrm{MG}$ (Ferrario et al. 2015, and references therein). The magnetic moment of the primary in IPs is not sufficiently high to ensure that the primary rotates synchronously, that is to say, the rotation of the primary is not phase-locked in the orbit of the system.

Accretion column: As the gas in the accretion column falls towards the primary it reaches supersonic velocity and becomes highly ionised, releasing more and more electrons. Close to the surface of the primary the density in the gas starts to increase and it is forced to slow down to subsonic velocity, creating an accretion shock where the gas is heated to temperatures of tens of kilo electron volts. The free electrons in the gas are spiralling around the strong magnetic field lines producing highly polarised cyclotron radiation at near infrared, optical and ultraviolet wavelengths. The deceleration of the gas produces bremsstrahlung in the form of hard X-rays, emitted from the region between the shock and the surface of the primary as the gas cools down in the post-shock flow. The polarisation and

the hard X-ray emission happen close to the surface of the primary and both are modulated at the spin period of the primary. Most of the hard X-rays are absorbed by the surface of the primary and re-emitted as soft X-rays and (or) ultraviolet radiation, but some of it may contribute to the ionisation of the accretion flow. Figure 1.8 shows a zoomed view of an accretion column.

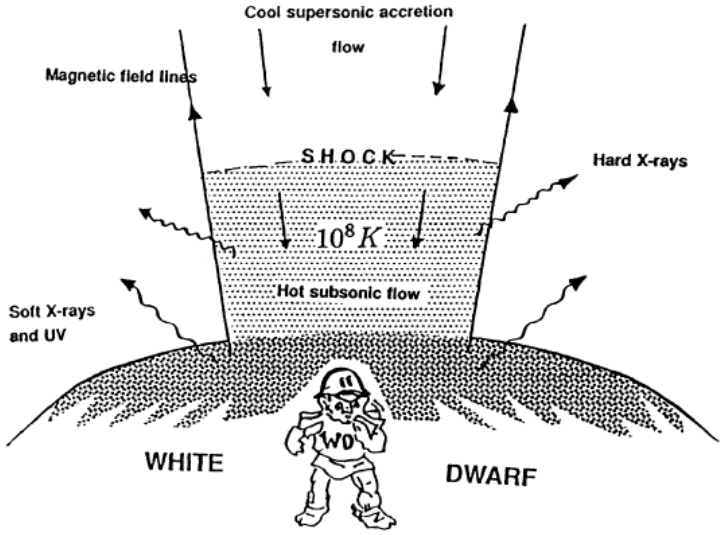

Figure 1.8. A schematic illustration of an accretion column. See text for more details. Taken from Patterson (1994) – Figure 1.

1.2.3 Orbital period distribution

Kraft (1962) introduced "a spectroscopic test for binary motion" which showed that five systems of the U Gem subcategory of CV are short period binaries with orbital periods less than 9 hours (hr). This formed the basis for the hypothesis that all CVs are short period spectroscopic binaries, that is, close binary systems not resolved optically (not yet), but that are inferred from a periodic shift in their observed spectral lines. The data collected for hundreds of CVs over the last five decades support this hypothesis.

The Ritter & Kolb (2003) V7.23 (July 2015) catalogue with references therein, contains data for 1321 CVs of various subclasses (excluding AM CVn stars). The orbital periods for 1312 systems are listed, ranging from $\sim$ 26 minutes (min) to $\sim$ 6 days (d), with only 40 systems having orbital periods greater than 12 hr. See Figure 1.9 for the distribution of orbital periods less than 13 hr for all non-magnetic CVs (non-mCVs) and mCVs. The orbital period distributions of the non-mCVs and mCVs are very similar. The main features are the long-period cut-off at $P_{\rm orb} \sim 12$ hr, the drop in the number of systems with $2\,{\rm hr} \lesssim P_{\rm orb} \lesssim 3\,{\rm hr}$, the so-called period gap $P_{\rm gap}$, and the short-period cut-off, which coincides with the predicted period minimum $P_{\rm min}$ at $P_{\rm orb} \sim 80$ min (see Section 1.2.4 for the discussion of probable causes). Early theoretical estimates placed the period minimum at $P_{\rm min} =$

81 ± 6 min (Paczynski 1981), while later estimates placed it as low as $\sim$ 70 min (Kolb & Baraffe 1999) and $\sim$ 65 min (Howell et al. 2001). More recently, Knigge et al. (2011) calculated the period minimum as $P_{\rm min} = 81.8 \pm 0.9$ min which is in good agreement with the observed period minimum of $P_{\rm min} = 82.4 \pm 0.7$ min obtained by Gänsicke et al. (2009) from a Sloan Digital Sky Survey sample of CVs. Knigge (2006) calculated the period gap to be 2.15 ± 0.03 hr $< P_{\rm gap} < 3.18 \pm 0.04$ hr while Knigge et al. (2011) places the upper limit of the period gap at 3.24 ± 0.05 hr.

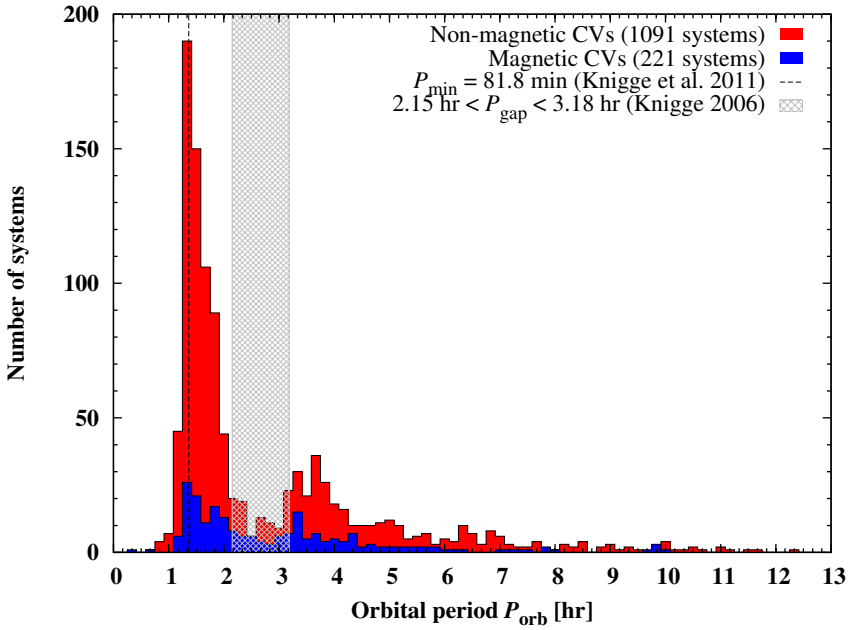

Figure 1.9. Distribution of orbital periods of CVs ($P_{\rm orb} < 13$ hr). The two subsets of non-mCVs and mCVs are shown in red and blue, respectively. The period minimum $P_{\rm min} = 81.8$ min (dashed line) from Knigge et al. (2011) and the period gap 2.15 hr $< P_{\rm gap} <$ 3.18 hr (grey mesh) from Knigge (2006) are also shown. Data from the Ritter & Kolb (2003) catalogue.

1.2.4 Secular evolution

The secular evolution of CVs, in general, is inextricably tied to a sustained, long-lived mass transfer (or the interruption thereof) from the lower-mass secondary onto the white dwarf primary. Sustained mass transfer alters the mass ratio q, as well as the angular momentum distribution in the system. The redistribution of angular momentum changes the binary separation a and orbital period $P_{\rm orb}$ as the secondary moves to a wider orbit to conserve the total orbital angular momentum. These changing system parameters, that is to say, the mass ratio q, the binary separation a and the orbital period $P_{\rm orb}$, have a direct impact on the Roche geometry. Because continued mass transfer depends on the secondary filling its Roche lobe the question arises whether these changes cause the secondary's Roche lobe to

shrink or expand.

Frank et al. (2002) showed that, if all the mass lost by the secondary is accreted by the primary, the secondary's Roche lobe shrinks in response to mass loss if the mass ratio $q > \frac{5}{6}$. If the secondary's envelope does not shrink at the same rate then the RLOF will become a runaway process on a thermal (or dynamical) time scale if the envelope is radiative (or convective). On the other hand, the secondary's Roche lobe expands in response to mass loss if the mass ratio $q < \frac{5}{6}$. If the secondary's envelope does not stay in contact with its Roche lobe the RLOF will be short-lived. Continued stable mass transfer is possible only if the secondary expands due to it evolving off the main sequence or if the Roche geometry of the system changes to keep the secondary's envelope in contact with its Roche lobe. The evolutionary expansion of the secondary is unlikely because typically the main sequence lifetime of the low-mass secondary in a CV is longer than the Hubble time. The evolutionary change in the Roche geometry of the system to ensure stable mass transfer is linked to processes that induce angular momentum loss (AML) in the system.

The two most probable processes causing AML in CVs are magnetic braking induced by stellar winds (e.g., Eggleton 1976; Verbunt & Zwaan 1981; Spruit & Ritter 1983; Rappaport et al. 1983) and gravitational radiation (e.g., Faulkner 1971, 1976; Paczyński & Sienkiewicz 1981; Rappaport et al. 1982). According to this standard evolutionary model of CVs magnetic braking is the main driver of AML if the system's orbital period $P_{\rm orb}$ is above the period gap (see Section 1.2.3), while gravitational radiation is the sole driver of AML if the system's orbital period $P_{\rm orb}$ is below the period gap. The presence of a circumbinary disc as an additional driver of AML has also been proposed (Spruit & Taam 2001).

It is reasonable to expect that in a CV the secondary is tidally locked with the orbital motion of the system (Hut 1981). This implies a rapid rotation period for the secondary given the short orbital periods observed in the majority of CVs (see Section 1.2.3). Add to the rapid rotation a radiative core and convective envelope, which the secondary most likely has being a late type main sequence star, then it is reasonable to expect a dynamo producing a strong magnetic field (e.g., Tout & Pringle 1992). The solar wind of ionised particles produced by the Sun is well studied and it is expected that late type main sequence stars produce similar ionised stellar winds. In the presence of the strong inferred magnetic field the expected outflow of charged particles from the secondary is captured by the field lines, and forced to co-rotate with the magnetic field and the secondary. The particles captured on *open* field lines are accelerated as they flow outwards along the lines, carrying angular momentum away from the centre of rotation. This exerts a braking torque which tends to slow down the rotation of the secondary, similar to the way a fast spinning ice skater slows down by gradually extending his or her arms. However, because the secondary is tidally locked to the orbital motion of the system the angular momentum is drained from the orbit leading thereto that the binary separation a and hence the orbital period $P_{\rm orb}$ decrease. When the system reaches an orbital period $P_{\rm orb} \sim 3\,{\rm hr}$ the secondary becomes fully convective and the magnetic dynamo is disrupted. Magnetic braking switches off and the secondary's envelope shrinks, losing contact with its Roche lobe. Mass transfer stops

and the now detached system becomes less visible. This hypothesis of disrupted magnetic braking is used to explain the presence of the period gap (Spruit & Ritter 1983; Rappaport et al. 1983).

The magnetic braking model, however, is complicated by the presence of a strong external magnetic field. Wickramasinghe & Wu (1994) suggested that the relatively high fraction of polars in the period gap ($\sim$ 24% versus $\sim$ 9% for DNe; from Ritter & Kolb 2003) can be attributed to reduced magnetic braking after these systems become synchronised. In support of this suggestion Li & Wickramasinghe (1998), for example, showed that for polars with $30 - 500$ MG the magnetic braking rate can be at least an order of magnitude smaller than for non-mCVs (assuming the white dwarf magnetic field inclination $< 45°$). However, in IPs with field strengths of $3 - 30$ MG, normal magnetic braking may be expected (Zhang et al. 2009).

According to Einstein's theory of general relativity the presence of a massive object results in the curvature of space-time, with more massive objects producing a larger curvature. Massive moving objects can have a 'ripple'-effect in space-time, called gravitational waves. Gravitational radiation in a binary system has been inferred from the observed orbital decay of the neutron star-neutron star binary PSR B1913+16 (Hulse & Taylor 1975). In a binary system the energy needed to generate the waves, that is, the gravitational radiation, is extracted from the orbital motion of the components, causing them slowly to lose angular momentum and spiral inwards. It is believed that gravitational radiation is the driver in decreasing the orbit when a CV enters the period gap after the secondary has detached from its Roche lobe and mass transfer has stopped. Gravitational radiation causes the orbit to decrease, which shrinks the Roche lobe of the secondary allowing it to fill again and resume mass transfer below the period gap when the system reaches an orbital period $P_{\rm orb} \sim 2$ hr.

Below the period gap stable mass transfer continues as long as the secondary retains its main sequence characteristics. However, at the point where its mass has been reduced to $\sim 0.1\,M_{\odot}$ it loses the ability to burn hydrogen. It leaves the main sequence and becomes degenerate. This happens when the orbital period of the system has evolved to reach the period minimum. The degenerate secondary then starts to expand in response to mass loss and the orbit will increase to compensate, leading to a longer orbital period. Systems that have evolved beyond the period minimum towards longer orbital periods are called period bouncers. For a general review of the evolution of CVs see, for example, Knigge (2011).

1.2.5 Spectral characteristics

It is potentially possible to extract information relating to an astronomical object's composition, temperature, motion, density and magnetic field from the emission or absorption lines in its spectrum. The information extracted from their spectroscopic observations forms the base of our current knowledge of CVs. The spectrum of a CV may include observable contributions from various components in the system such as the white dwarf primary, the red dwarf secondary, an accretion disc or magnetically confined curtain (column) and a bright spot (where the ballistic accretion stream collides with the edge of the disc or the accretion

column impacts the primary). Most of these components peak in different parts of the spectrum due to them having different temperatures. Here I focus mainly on the features seen in the optical spectra of CVs. In general, the optical spectra of CVs show emission lines of H, He I, He II and Ca II on a blue continuum (Warner 1976). In quiescence the hydrogen Balmer lines have mostly a flat decrement, that is to say, the ratios of the line strengths are close to unity (Williams 1983). Figure 1.10 shows example spectra of various types of CVs.

Primary: Typically the primary in a CV has an effective temperature in the range $10000-40000\,\mathrm{K}$ (e.g., Sion 1991; Townsley & Gänsicke 2009; Knigge et al. 2011). This places its peak flux in the ultraviolet part of the spectrum. In CVs with dominant emission from the primary the optical spectrum, however, is characterised by Balmer absorption lines.

Secondary: The broad spectral types of the secondaries in CVs range from M for shorter orbital periods ($P_{\mathrm{orb}} \lesssim 5\,\mathrm{h}$) to K and even G for longer orbital periods (e.g., Patterson 1984; Warner 1995; Beuermann et al. 1998; Knigge 2006). This implies an effective temperature roughly in the range $1000-6000\,\mathrm{K}$. The typical spectrum of the secondary in a shorter period CV shows broad absorption bands of molecular TiO and lines of Na I in the near infrared.

Accretion disc: An accretion disc in a CV has a complex temperature distribution compared to the stellar components. The disc's outer edge can be relatively cool, but it becomes hotter towards the inner edge due to the release of gravitational energy. The cooler low-density outer disc ($\lesssim 7000\,\mathrm{K}$), assumed to be optically thin, generally is believed to be the origin of the Balmer emission lines seen in the spectra of CVs (e.g., Williams 1980; Tylenda 1981; Williams 1991). The disc chromosphere, that is, an optically thin ionised emission layer above the disc surface illuminated by the primary, is also believed to be a source of optical line emission (Schwarzenberg-Czerny 1981). In high-inclination systems with the disc observed nearly edge-on, the emission lines generally have a double-peaked profile, as expected from a rotating ring of gas (Smak 1969; Huang 1972). The typical observed disc spectrum is influenced also by the outburst state of the system which changes the optical thickness of the disc. For example, the primarily broad Balmer *emission* lines seen at quiescence for low-inclination systems changes to *absorption* lines at outburst (e.g., SS Cyg; Kiplinger 1979; Clarke et al. 1984). The broadening of the emission lines produced in the disc are mainly due to the Doppler shifts induced by the disc's orbital motion around the system's centre of mass.

Bright spots: There may exist various hot (bright) spots in a CV such as the impact region between the ballistic stream and the disc, the accretion region on the primary and even the irradiated side of the secondary. These bright spots contribute mainly to the formation of emission lines. For example, the bright spot of the stream-disc impact presents as a narrow emission line component which moves back and forth in a characteristic 'S-wave' pattern through the broad emission line component of the disc over the course of an orbit.

The optical spectra of mCVs without accretion discs (i.e., polars) show multiple narrow

and broad emission line components associated with the ballistic stream, the magnetically confined curtain (column) and the irradiated side of the secondary. The Balmer series is prominent, but it mostly has an inverted decrement with Hγ or Hδ the strongest. Also prominent is He II λ4686, typically of comparable strength to Hβ. The Bowen fluorescence complex at $4640-50$ Å, that is, the doubly ionised carbon (C III) and nitrogen (N III) blend, is often observed and is indicative of the high excitation of the emission line region (Mukai 1988).

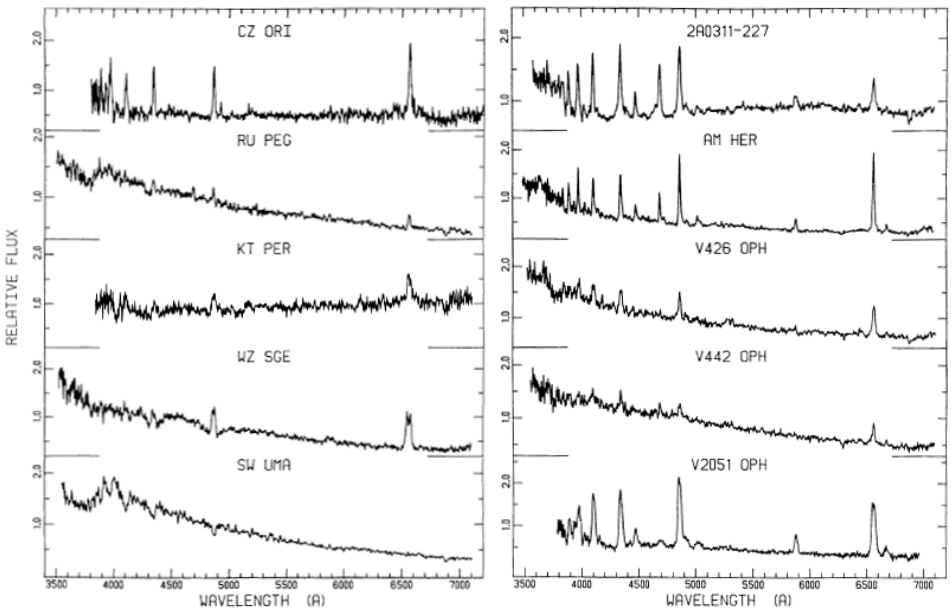

Figure 1.10. Example spectra of CVs. Notable features are the Balmer absorption in the spectrum of the dwarf nova SW UMa, the double-peaked profile of the Hα emission line in the spectrum of the high-inclination dwarf nova WZ Sge, the presence of He II λ4686 in the spectra of the polars AM Her and EF Eri (2A0311−227), as well as the inverted Balmer decrement in the spectrum of EF Eri. Taken from Williams (1983) – Figures 10 and 13.

1.3 Indirect imaging techniques

CVs and mCVs are found at typical distances of hundreds of parsecs (e.g., Patterson 2011; Pretorius et al. 2013) and have sizes of the order of a few solar radii. This means they subtend only a few micro-arcseconds on the sky as observed from the Earth and it is not possible to resolve their components with any of the current direct imaging techniques, including interferometry. Resolving any of the emission components in a CV or mCV is therefore presently possible only with indirect imaging techniques. In this section I give short overviews of a number of such techniques, namely eclipse mapping, Roche tomography, Stokes imaging and accretion stream mapping. This is not an exhaustive list of indirect imaging techniques, but all of these has had a major impact on the study of CV and mCVs.

The short overviews also serve as a prelude to the overview of the technique of Doppler tomography presented in Chapter 2 and which is at the core of this thesis.

1.3.1 Eclipse mapping

Horne (1985) introduced eclipse mapping, a technique that constructs a two-dimensional map of the spatial surface brightness distribution of the accretion disc of an *eclipsing* disc-accreting CV. This is achieved by exploiting information contained in the eclipse profile in the photometric light curve of such a system. Eclipse mapping is a well established and mature technique that has had an enormous impact on the study of disc accretion dynamics. See Baptista (2001) and Baptista (2016) for comprehensive reviews of the technique and its applications.

Method: In general, the orbital light curve of a high-inclination eclipsing CV is characterised by a prominent eclipse. With a given geometry for the system, uniquely defined by its mass ratio q and inclination angle i, it is possible to calculate the eclipse profile in the light curve. However, the profile is determined mostly by the surface brightness distribution of the accretion disc and therefore different brightness distributions will produce different profiles. The aim of eclipse mapping is to find the brightness distribution that reproduces an observed eclipse profile. The spatial surface brightness distribution of the accretion disc is represented in an eclipse map, that is, a grid of discrete brightness elements. Each element is considered to be a free parameter. Starting with a predefined default brightness distribution in the eclipse map the technique iteratively adjusts the map until the calculated light curve fits the observed light curve with a chosen precision. The uncertainty caused by constructing two-dimensional maps from one-dimensional data is dealt with by employing the maximum entropy method (see Section 2.1.4) to choose the map that is most consistent with the observed data (Horne 1985). Figure 1.11 shows example eclipse maps of the dwarf nova EX Dra on the rise to the maximum of the 1995 November outburst and in quiescence.

Extensions: Notable extensions to the standard eclipse mapping technique are

- spectrally resolved eclipse mapping (Rutten et al. 1994), which uses time-resolved spectroscopic observations to construct spectra from isolated regions of the accretion disc;
- three-dimensional eclipse mapping (Rutten 1998), which allows for the modelling of a three-dimensional accretion disc; and
- physical parameter eclipse mapping (Vrielmann et al. 1999), which uses multi-colour photometric observations to resolve spatially physical parameters such as surface density and temperature.

1.3.2 Roche tomography

Rutten & Dhillon (1994) introduced Roche tomography, a technique that uses information contained in the phase-resolved spectra of a CV to construct a two-dimensional map of

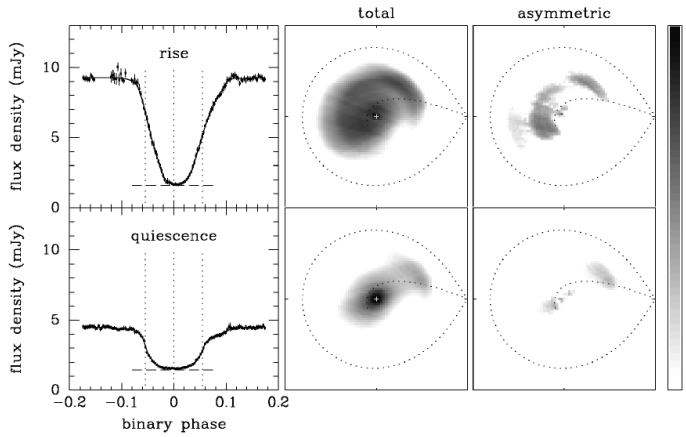

Figure 1.11. Example eclipse maps of the dwarf nova EX Dra. The left panels show the rise to maximum and in quiescence light curves. The middle and right panels show the corresponding total and asymmetric (after subtracting the symmetric part) eclipse maps. The maps are in a logarithmic grey scale with brighter regions being darker. Taken from Baptista & Catalán (2000) – Figure 1.

the spatial surface brightness distribution of the Roche-lobe filling secondary. The technique uses the shape of the secondary's Roche lobe to model the brightness variations and Doppler shifts in the spectra over an orbital phase. Roche tomography has been used to constrain the inclination angle i and mass ratio q of CVs (e.g., Rutten & Dhillon 1994; Watson et al. 2003) and to detect surface inhomogeneities such as star spots on their secondaries (e.g., Watson et al. 2006, 2007; Dunford et al. 2012). Recently, Hill et al. (2014) were able to detect differential rotation in the secondary of AE Aqr with the help of Roche tomography. See Dhillon & Watson (2001), Watson & Dhillon (2001) and Morin et al. (2016) for comprehensive reviews of the technique.

Method: A grid of quadrilateral surface elements of approximately equal size is used to model the critical Roche surface of the secondary. The intrinsic profile of the spectral line, incorporating the effects of instrumental resolution, limb darkening and obscuration, is assigned to each surface element. Phase-dependent Doppler shifts are added based on the radial velocity of each surface element at specific phase intervals. The total line profile at specific phases is calculated through the summation of the contributions from all the surface elements. The calculated line profiles can then be compared with the observed line profiles before they are assigned back to the grid of surface elements to produce a map of the surface brightness distribution of the secondary. The strength of the profile in each surface element of the map is adjusted iteratively until the calculated line profiles fit the observed line profiles with a chosen precision. However, different brightness distributions can yield calculated line profiles that are consistent with the observed line profiles. The maximum entropy method (see Section 2.1.4) is used to obtain the map, that is, the Roche tomogram, that is most consistent with the input data. Figure 1.12 shows example Roche tomograms of the polar HU Aqr.

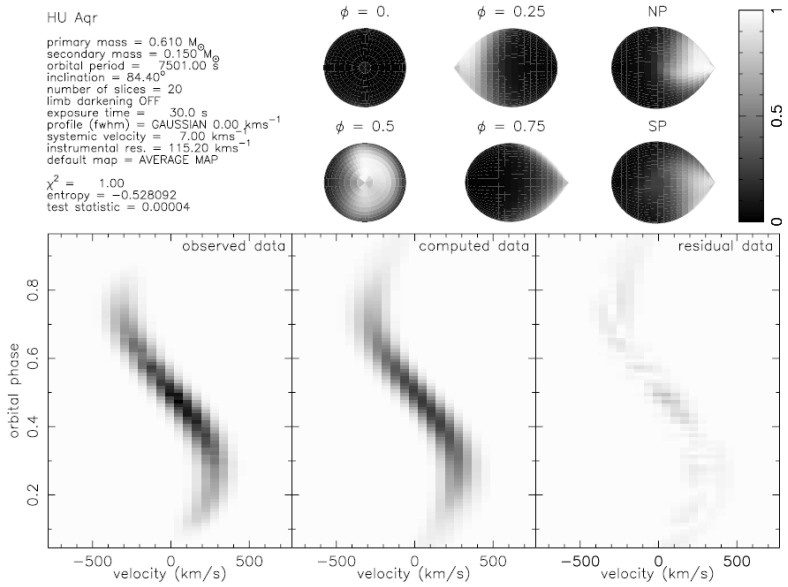

Figure 1.12. Example Roche tomograms of the polar HU Aqr. The tomograms are in a grey scale with regions of enhanced emission being lighter. The grey scale is reversed in the trailed spectra with the enhanced emission being darker. Taken from Watson et al. (2003) – Figure 11.

1.3.3 Stokes imaging

Potter et al. (1998) introduced Stokes imaging, a technique that reconstruct the shape, size and location of the region(s) on the surface of the white dwarf primary in an mCV that produces cyclotron emission. The technique utilises the observed polarisation light curves of such a system and has its origin in earlier polarisation modelling techniques (e.g., Bailey et al. 1985; Ramsay et al. 1996; Potter et al. 1997). The technique is uniquely suited to constrain the 'one-pole' or 'two-pole' accretion configuration in polars. See Potter et al. (2001), Potter et al. (2004) and Potter (2016) for comprehensive reviews of the technique.

Method: Polarimetric observations of mCVs, especially polars, are characterised by variations in the detected polarisation over the orbit of the system. The structure of these observed variations depends on the shape, size and location of the regions on the surface of the white dwarf that emits cyclotron emission. The cyclotron emission can be calculated by modelling the emitting region as a single hemisphere of plasma with constant density and temperature inside a magnetic field (e.g., Meggitt & Wickramasinghe 1982; Wickramasinghe & Meggitt 1985; Potter et al. 2002). The polarised Stokes parameters (I, Q, U and V) of the emitted radiation are calculated as a function of viewing angle over a grid of points on the modelled region. These calculations can be used to model orbital polarisation light curves by constructing an artificial cyclotron emitting region that consists of a number of these hemispheres. The calculated viewing angle to the artificial region at regular spin phases of the white dwarf is used to look up the corresponding values of the Stokes parameters in a

table of the model calculations. The Stokes parameters are then used to calculate model orbital polarisation light curves that can be compared with the observed light curves. The fit between the model and observed light curves is improved by adjusting the shape, size and location of the artificial region. Stokes imaging uses a genetic algorithm (see Charbonneau 1995, for an overview of genetic algorithms) to optimise the model of the artificial region to obtain the best fit to the observed polarisation light curves. The algorithm starts by generating a set of random solutions, each consisting of a large number of hemispheres in random positions over the surface of the white dwarf. Employing a type of natural selection process that preferentially selects the 'fittest' solutions the algorithm 'breeds' all the solutions. The breeding process continues until the increase in the 'fitness' of the solutions becomes marginal. At this point a more analytical approach is taken to achieve an optimised final solution. Figure 1.13 shows example Stokes images of the polar CP Tuc.

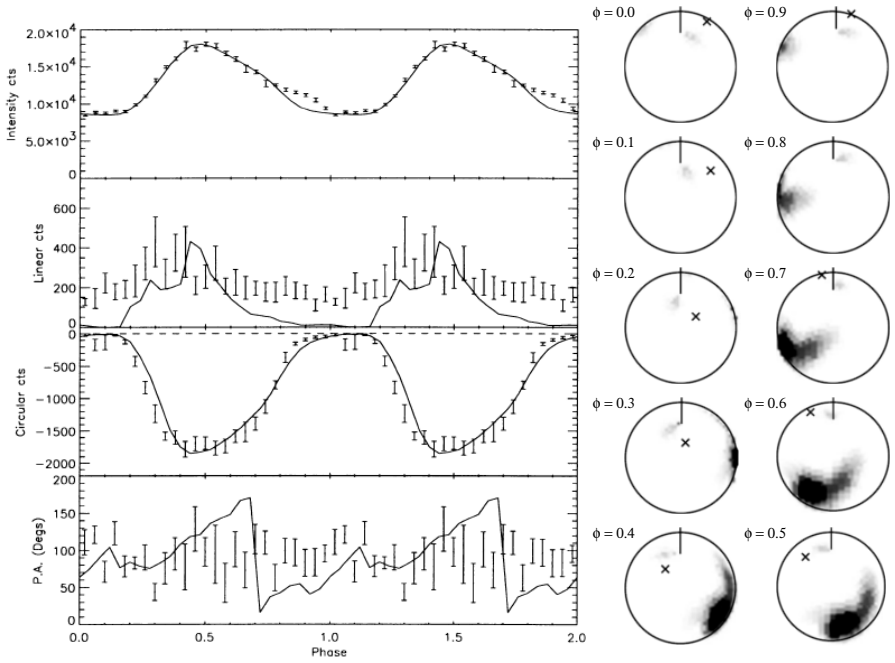

Figure 1.13. Example Stokes images of the polar CP Tuc. The observed polarisation data, that is to say, the light curves of the brightness, the linear and circular polarisation, as well as the polarisation position angle are shown together with the model fit (solid lines). The 10 images on the right show the shape, size and location of the accretion regions, i.e., the cyclotron emitting regions on the surface of the white dwarf, calculated as a function of the spin phase ϕ. The magnetic axis is indicated by the $\times$. The images are in a grey scale with brighter regions being darker. Taken from Ramsay et al. (1999) – Figures 3 and 4.

1.3.4 Accretion stream mapping

Hakala (1995) introduced accretion stream mapping, a technique that constructs a one-dimensional map along a fixed path of the brightness distribution of the accretion stream

of an *eclipsing* polar. Similar to eclipse mapping (Horne 1985, see Section 1.3.1) it utilises the information contained in the eclipse profiles in the photometric light curves of such systems. Harrop-Allin et al. (1999b) refined the original technique with improvements in the optimisation algorithm and the modelled stream trajectory. See also Vrielmann & Schwope (2001) and Hakala et al. (2002) for, respectively, an alternative mapping algorithm and a three-dimensional extension to the technique.

Method: The accretion stream is modelled by evenly spaced emission points along a predetermined stream trajectory. Single emission points with fixed brightnesses are used to model the accretion regions on the surface of the white dwarf. An eclipse of the model stream by the secondary that fills its Roche lobe is then simulated. The summation of the brightnesses of the emission points visible at each orbital phase produces a model light curve that can be compared with the observed light curve. A genetic algorithm* is used to optimise the fit between the model and observed light curves. Figure 1.14 shows example accretion stream maps of the polar HU Aqr.

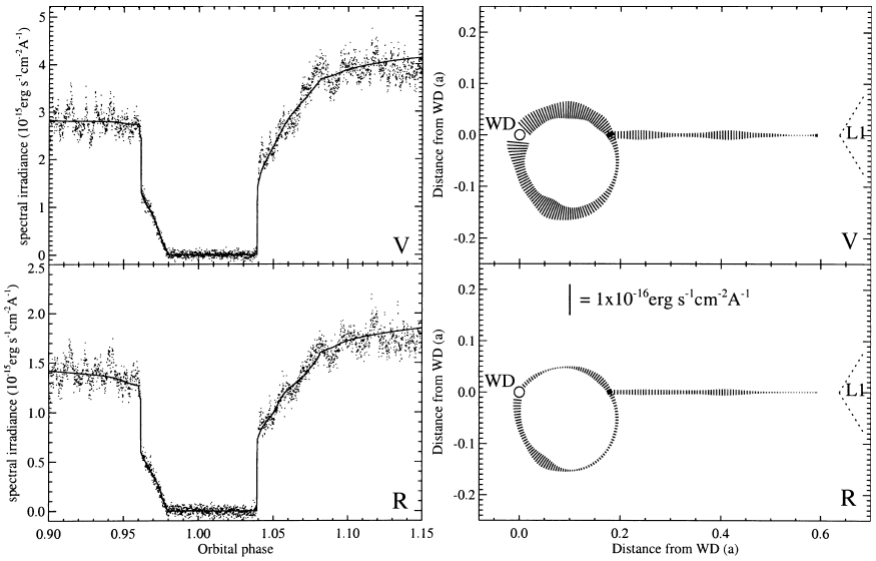

Figure 1.14. Example accretion stream maps of the polar HU Aqr. In the left panels the observed V and R light curves are shown together with the respective model fits (solid lines). The corresponding accretion stream maps are shown in the right panels. The models assume a two-pole accretion configuration along a magnetic dipole field line onto the white dwarf (WD). Each emission point along the accretion stream is represented by a line perpendicular to the stream and with a length that indicates its brightness. Taken from Harrop-Allin et al. (1999a) – Figure 3.

In the next chapter I turn to Doppler tomography, the indirect imaging technique at the core of this thesis. Whereas the aforementioned techniques in this section construct images of specific emission components, Doppler tomography aims to construct a phase-averaged image of all the observed emission line components in a CV.

*See Section 1.3.3 for a minimalistic description of the working of a genetic algorithm.

Chapter 2

Doppler tomography

O for a Muse of fire, that would ascend
The brightest heaven of invention!

– William Shakespeare, *Henry V*, Prologue

Crawford & Kraft (1956) linked the observation of broad and strong emission lines in the spectrum of an interacting binary star with the existence of an accretion flow in the system. Since then it has been recognised that the profile of emission lines in the spectra of interacting binary stars contain information about the kinematics of the accretion flow in such systems (e.g., Smak 1981; Horne & Marsh 1986).

The meaningful extraction of the kinematic information locked-up in the spectral line profiles prompted the development of Doppler tomography as described by Marsh & Horne (1988). Their initial aim was to construct a two-dimensional velocity image of the accretion disc of a CV from a particular emission line in its orbitally phase-resolved spectra. This seminal work has made it possible to visualise the main emission producing regions, such as the irradiated side of the secondary, the accretion disc and other accretion flows, in various types of interacting binary systems. In short, Doppler tomography has revolutionised the interpretation of complex line profiles in phase-resolved spectroscopic observations of interacting binary systems. Significant contributions have been, amongst others, the discovery of two-arm spiral shocks in the accretion disc of the dwarf nova IP Peg (Steeghs et al. 1997) and the mapping of the accretion stream in the polar HU Aqr with evidence of the transition from ballistic to magnetic flow (Schwope et al. 1997b).

In this chapter I strive to establish a modest overview of the standard Doppler tomographic technique. Section 2.1 covers the basic concepts of the standard technique. In Section 2.2 short overviews are given of two extensions to standard Doppler tomography, namely spin-cycle Doppler tomography (Hellier 1997) and modulation Doppler tomography (Steeghs 2003).

2.1 Standard Doppler tomography

In observational astronomy a Doppler tomogram is a two-dimensional image in velocity coordinates of the emission distribution in an interacting binary. The tomographic technique extracts the emission and kinematic information contained in a specific emission line from a set of observed Doppler-shifted spectra and projects it onto a two-dimensional velocity coordinate frame. Effectively, the observed emission line profiles are resolved into discrete emission components which are then characterised by their velocity vector in the co-rotating frame of the binary. The main benefit of using velocity as opposed to spatial coordinates is the close relationship between the observed emission line profiles and the velocity coordinates. This relationship allows the velocity image to be constructed without knowledge of the exact structure of the velocity field. Also, the extracted emission and velocity information cannot be inverted to a unique spatial solution without complete knowledge of the velocity field. For comprehensive reviews of standard Doppler tomography and its applications see Marsh (2001), Schwope (2001), Marsh (2005) and Marsh & Schwope (2016).

In the first part of this section the axioms of standard Doppler tomography are listed and discussed. Next, a short overview of the velocity coordinates in which a standard Doppler tomogram is constructed is given. Then the phase-resolved visualisation of the emission and velocity information from observed spectra is discussed. Finally, the maximum entropy method for constructing a tomogram is described.

2.1.1 Axioms

The Doppler tomographic technique acts within the theoretical model of CVs and therefore an interpretation of Doppler tomograms is only applicable as the model itself. Furthermore, the technique has to apply some approximations, therefore it is necessary to list the underlying axioms. The basic axioms (Marsh 2001) are as follows:

1. all points in the system are equally visible at all times;
2. the flux from each point in the frame of rotation is constant in time;
3. all motion is parallel to the orbital plane and is mapped accordingly;
4. all velocity vectors co-rotate with the system; and
5. the intrinsic line profile width (e.g., thermal) is negligible.

The first axiom is the most difficult to justify because the exact geometry for any given system is, in general, unknown. In high-inclination systems the effect of self-shadowing may be seen as a violation of the first axiom, while in eclipsing systems the violation is obvious.

The second axiom is violated by default if the first axiom is violated. Furthermore, any emission anisotropy in the system, such as that caused by shocks and density waves in the accretion disc, or system outbursts, violates the second axiom.

The third and fourth axioms can be violated in parts of the accretion flows. For example, the third axiom is violated especially in magnetic systems where material is threaded along the magnetic field lines out of the orbital plane onto the primary.

The fifth axiom is, in general, satisfied for most systems. A Doppler shift produced by the orbital motion of the system, and the motion in the accretion flows, typically translates to a velocity of hundreds to thousands of km s^{-1}, whereas the broadening produced by random thermal motions translates to a velocity of only tens of km s^{-1} for typical temperatures in CVs and other interacting binary systems.

These violations do not imply that any resulting tomograms are useless, but they do add a cautionary note for the interpretation of Doppler tomograms. A tomogram must be interpreted as an approximation of the motions projected onto the orbital plane. It provides a time-averaged picture in velocity coordinates of the emission distribution in which any phase-dependent complications are ignored.

It is also possible to exploit the violation of, for example, the first axiom. The assumption that all points in the system are equally visible at all times means a tomogram can be constructed using spectra covering half of a phase only and that tomograms produced from different half-phases will be identical. The violation of this axiom, however, means that tomograms produced from different half-phases will not be identical. This is exploited to great effect in Chapter 5.

2.1.2 Spatial and velocity cartesian coordinates

2.1.2.1 Spatial cartesian coordinates

In order to grasp the layout of the velocity coordinate frame that forms the 'canvas' for a tomogram it is necessary to define a coordinate frame for the accepted theoretical spatial picture of a typical CV as discussed in Section 1.2. The spatial cartesian coordinate frame that *co-rotates* with the system, as described by Marsh & Horne (1988), places

- the origin at the binary's centre of mass (for a low q system this is very close to the primary's centre of mass);
- the x-axis along a line through the centres of the primary and secondary;
- the y-axis along a line parallel to the velocity vector of the secondary, that is, perpendicular to the x-axis; and
- the z-axis along a line through the binary's centre of mass orthogonal to the orbital plane.

The binary orbital phase zero ($\phi = 0.0$) is defined as the point of mid-eclipse of the primary by the secondary, that is, the point in the orbit when the secondary is closest to the point of observation. The orbital motion is anticlockwise around the binary's centre of mass. One of the axioms of Doppler tomography is the assumption that all motion is parallel to the orbital plane (see axiom three in Section 2.1.1). In most CVs Roche lobe overflow is considered to

be the source of the accretion flows in the form of the ballistic stream and the accretion disc. These features are primarily confined to the orbital plane. A two-dimensional layout in the orbital plane, that is, the xy-plane, is therefore sufficient as a model velocity coordinate frame.

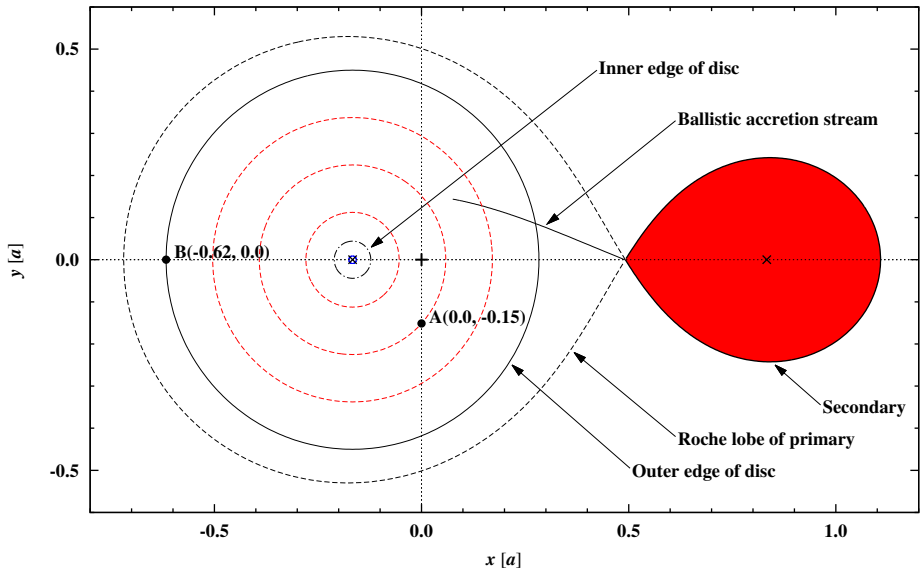

Figure 2.1. Spatial cartesian coordinates for a model CV with an accretion disc. The binary's centre of mass is marked with a plus (+) while that of the primary and secondary are marked with crosses (×). Spatial overlays are shown for the Roche lobe of the primary (black dashed line), the 3:1 resonance radius as the outer edge of the disc (black solid circle) and the inner edge of the disc (black dot-dashed circle) based on an absolute radial velocity of $1800\,\mathrm{km\,s^{-1}}$. Also shown are disc radii at decrements of 0.25 times the outer disc radius (red dashed circles) and two arbitrary reference points, A and B, in the disc. The accretion stream (black solid line) from the secondary towards the primary, shown up to an azimuth angle of 30°, is based on the ballistic trajectory of a single particle.

Figure 2.1 shows the spatial cartesian coordinates (normalised by the binary separation a) for a model CV with an accretion disc as viewed at orbital phase $\phi = 0.25$ (the observer is located below the figure). The assumed system parameters for the model CV are

- orbital period $P_{\mathrm{orb}} = 0.125\,\mathrm{d} = 3\,\mathrm{hr}$;
- mass of the primary $M_1 = 0.85\,M_\odot$; and
- mass ratio $q = 0.2$.

2.1.2.2 Velocity cartesian coordinates

Every spatial point $(x,\, y)$ in the system has a two-dimensional velocity cartesian coordinate $(u_x,\, u_y)$ in the co-rotating spatial coordinate frame. The u_z-component is ignored based

on the same argument as for the spatial coordinate frame. It is important to note that the (u_x, u_y)-coordinate of a point in the system is independent of the orbital phase ϕ. Given the definition of the spatial coordinate frame it follows that, for example, the primary's centre of mass is moving in a negative y-direction (u_y is negative), but with no movement in the x-direction (u_x is zero). Similarly, the secondary's centre of mass is moving in a positive y-direction (u_y is positive), but also with no movement in the x-direction (u_x is zero). Structures such as the accretion stream and disc are more complex because they have structural motion as well, and therefore a velocity other than just the rotational velocity about the binary's centre of mass. However, it is possible to determine the (u_x, u_y)-coordinate for any point in the system based on its rotational velocity *and*, if any, its structural velocity, for example, the ballistic velocity of a point in the accretion stream or the Keplerian velocity of a point in the accretion disc. The projection of all the (u_x, u_y)-coordinates onto the axes of the rotating frame forms the velocity cartesian coordinate frame for the system with (v_x, v_y)-coordinates. The inclination angle i of the system is taken into account in the projection, that is, $v_x = u_x \sin i$ and $v_y = u_y \sin i$. Every spatial point (x, y) in the system therefore has a corresponding velocity point (v_x, v_y) in the velocity coordinate frame.

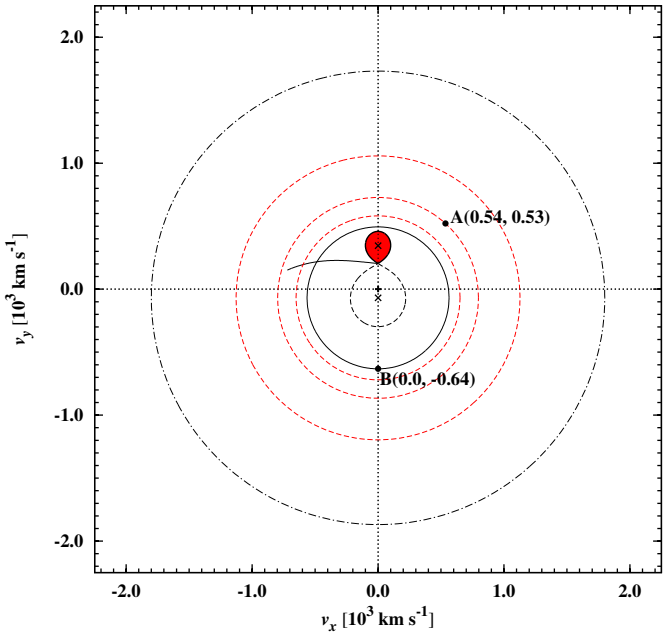

Figure 2.2. Velocity cartesian coordinates for a model CV with an accretion disc (as in Figure 2.1). The binary's centre of mass is the plus (+) at the origin, while that of the primary and secondary are the crosses (×) on the negative and positive y-axis, respectively. The red dashed circles between the velocity profiles of the inner (black dot-dashed circle) and outer disc (black solid circle) are that of radii at decrements of 0.25 times the outer disc radius. The two arbitrary reference points, A and B, in the disc are now shown with their corresponding velocity cartesian coordinates.

Figure 2.2 shows the velocity cartesian coordinates of the model CV based on the co-

rotating spatial coordinate frame defined above (Figure 2.1). The inclination angle i of the system is taken to be 75°. Overlays of the velocity profiles of the secondary, the accretion stream, the inner and outer edges of the accretion disc, as well as radii at decrements of 0.25 times the outer disc radius are shown. The whole of the secondary rotates as a solid body about the binary's centre of mass. Therefore, the projection of its velocity vectors onto the velocity coordinate frame retains the same shape as in the spatial coordinate frame. The increasing velocity along the ballistic trajectory of the accretion stream is clearly seen in the absolute increase in its v_x component. The secondary and the ballistic stream, however, appear to be 'inside' the accretion disc in velocity coordinates. The Keplerian motion in the accretion disc causes its velocity profile to appear inverted, that is to say, the higher velocities of the inner edge of the disc are further from the origin in the velocity coordinate frame and conversely for the lower velocities of the outer edge of the disc. The velocity profiles of the radii at decrements of 0.25 times the outer disc radius further emphasise the Keplerian motion in the disc. These radii do not follow the same linear distribution in velocity coordinates as they do in spatial coordinates.

Now, Figure 2.2 is just a raw theoretical velocity map of the structures in the binary based on the parameters of the model CV. It is important to note that it is not possible to invert this velocity map to reproduce the spatial map in Figure 2.1. In other words, every velocity coordinate does not have a unique spatial coordinate making the inversion from velocity to spatial coordinates impossible without additional information (e.g., Harlaftis et al. 2004). A Doppler tomogram, therefore, is constructed by directly mapping velocity- and phase-resolved spectroscopic observations of a binary onto a velocity coordinate frame which is divided into discrete velocity bins, that is, pixels. Each pixel in the velocity coordinate frame is centred on a velocity coordinate (v_x, v_y) and represents a square velocity bin of size (dv_x, dv_y), where $dv_x = dv_y = dv_p$ for all the velocity bins. The line emission is then mapped onto the applicable pixel according to the extracted velocity and observed phase. In order to do this a link is needed between the velocity- and phase-resolved spectra and the velocity coordinates of the observed system. In the next section this link is established as a first step in the construction of a tomogram.

2.1.3 Velocity-phase space

Most emission components of a CV are moving at a few hundred to a few thousand $\mathrm{km\,s^{-1}}$. Therefore, the shift in emission lines due to the movement, typically a few to tens of angstrom (Å), is easily detectable. Firstly, consider an emission component that has only a rotational velocity about the binary's centre of mass, for example, the secondary. Emission from its irradiated side, for instance, is redshifted when it is moving away along the line of sight of a terrestrial observer, and blueshifted when it is moving towards the observer. If the binary has a circular orbit the shift changes sinusoidally from blue to red and back. Therefore, if a set of spectra taken over an orbit are plotted in order, the single-peaked emission line profile associated with the irradiated side of the secondary moves back and forth in a characteristic 'S-wave' pattern.

Secondly, consider an emission component that has both structural and rotational velocity about the binary's centre of mass, for example, the accretion disc. The disc can be considered to consist of numerous small emission components producing S-waves. The double-peaked emission line profile associated with the disc is therefore a sum of S-waves covering a range of amplitudes according to the difference between the velocity in its outer and inner parts. Because the accretion disc is centred on the white dwarf which has a rotational velocity about the binary's centre of mass, the whole double-peaked profile of the disc executes an S-wave along with the white dwarf.

A specific emission line (e.g., He II λ4686, Hα, etc.) includes the emission from all points in the binary which produce emission at the specific wavelength. The radial (line-of-sight) velocity v_r of these points can be extracted from the spectral wavelength profile of the emission line using the relativistic Doppler shift (Einstein 1905) in its wavelength form, that is,

$$\frac{\lambda}{\lambda_0} = \sqrt{\frac{1+v_r/c}{1-v_r/c}} \;\Rightarrow\; v_r = \left(\frac{\lambda^2-\lambda_0^2}{\lambda^2+\lambda_0^2}\right) c. \tag{2.1}$$

Here λ is the observed wavelength containing the Doppler shift, λ_0 is the 'rest' wavelength as measured in the laboratory for the emission line and c is the speed of light.

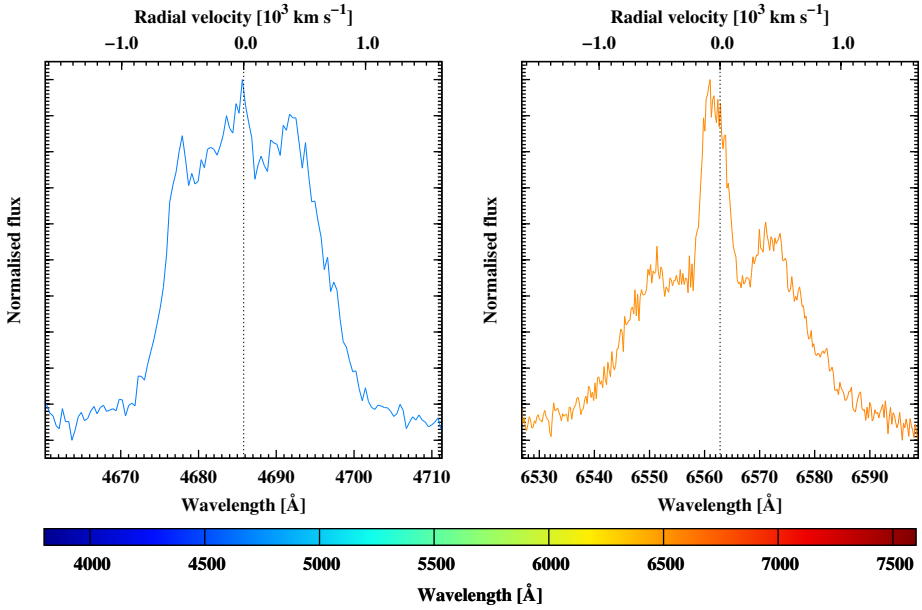

Figure 2.3. Wavelength and radial velocity spectrum profiles. The left and right panels show, respectively, the He II λ4686 and Hα emission lines in spectra of the dwarf nova IP Peg taken at orbital phase $\phi \sim 0.5$ (spectra courtesy of Danny Steeghs).

Figure 2.3 shows the spectrum profiles of an He II λ4686 emission line and an Hα emission line. The flux of the emission is plotted against the wavelength and the corresponding radial velocity. The redshifted emission has a positive radial velocity, while the blueshifted

emission has a negative radial velocity. The profile of an emission line can also be plotted as an intensity 'strip'. The strips from spectra at a number of observed orbital phases can be 'stacked' to form a two-dimensional intensity map of the observed flux density as a function of radial velocity v_r (or wavelength λ) and orbital phase ϕ. Such a map in velocity-phase space is technically a *spectrogram*, that is, a visual representation of the profile of the spectrum as it changes over time. However, more frequently it is referred to as *trailed spectra*. It provides an effective way to visualise the orbital phase variations of the emission line profile. Trailed spectra also help to identify different emission components and the subtle patterns in their orbital phase variations. Figure 2.4 shows a set of trailed velocity- and phase-resolved spectra of the dwarf nova IP Peg. The spectra contain emission components that produce characteristic S-wave patterns with the dominant emission redshifted after orbital phase $\phi = 0.0$ and blueshifted after orbital phase $\phi = 0.5$.

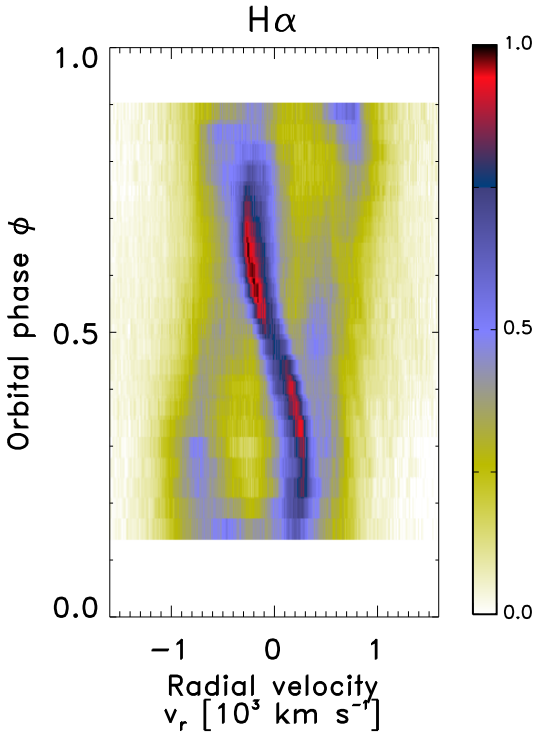

Figure 2.4. Trailed Hα spectra of the dwarf nova IP Peg (spectra courtesy of Danny Steeghs). The spectra have been normalised by the maximum flux in the spectra.

Now, each point of emission in the binary can be defined by its spatial and velocity coordinates, that is, (x, y) and (v_x, v_y), in the co-rotating spatial coordinate frame described in Section 2.1.2. However, the radial (line-of-sight) velocity v_r of the point measured in the inertial frame of an observer changes as the binary rotates, but it has a unique value at the observed orbital phase ϕ of measurement. The radial velocity v_r curve of the point is a function of its velocity coordinate (v_x, v_y) in the co-rotating spatial coordinate frame and

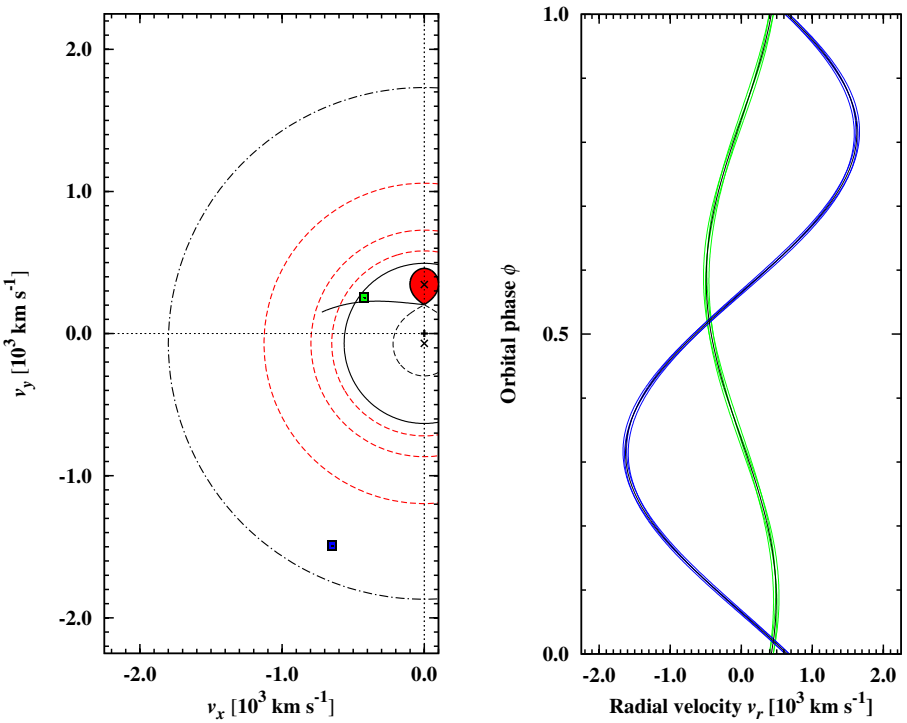

Figure 2.5. Velocity bins (pixels) in the cartesian velocity frame. The left panel shows the positions of a lower velocity green pixel and higher velocity blue pixel in, respectively, the upper and lower left quadrants of the velocity map in Figure 2.2. The right panel shows the corresponding radial velocity v_r curves traced in velocity-phase space by the centre (solid black lines) and corner (solid green and solid blue lines) velocity coordinates of the pixels.

the observed orbital phase ϕ, that is,

$$v_r(\phi) = \gamma - v_x \cos 2\pi\phi + v_y \sin 2\pi\phi, \tag{2.2}$$

where γ is the systemic velocity of the binary.

From Equation 2.2 it follows that the velocity coordinate (v_x, v_y) of each point of emission traces a sinusoidal curve through velocity-phase space over the duration of a complete orbit. The semi-amplitude K of this sinusoidal curve is the magnitude of the corresponding velocity coordinate, that is, $K = \sqrt{v_x^2 + v_y^2}$. At the same time, each of the velocity coordinates in the co-rotating spatial coordinate frame represents a unique coordinate in the velocity coordinate frame that forms the 'canvas' for a Doppler tomogram. Therefore, each square velocity bin (pixel) with width dv_p $(= dv_x = dv_y)$ and centred on a unique velocity coordinate (v_x, v_y) in a tomogram, can be considered to represent a particular S-wave component in velocity-phase space, that is, in the trailed spectra.

This is demonstrated in Figure 2.5 for two pixels with widths $dv_p = 56\,\mathrm{km\,s^{-1}}$ and centred on, respectively, $(v_x, v_y) = (-423, 254)$ and $(-648, -1493)$ $\mathrm{km\,s^{-1}}$. Each pixel in the tomogram represents an area in the trailed spectra bounded by the radial velocity v_r curves

of the velocity coordinates $(v_x \pm 0.5dv_p,\ v_y \pm 0.5dv_p)$. In other words, the intensity in each pixel, that is, $I\,(v_x,\ v_y)$, represents the orbitally phase-averaged emission line flux for the particular bounded emission component in the trailed spectra. A tomogram, therefore, represents a phase-averaged image (map) in velocity coordinates of the emission distribution in the observed system. Conversely, the trailed spectra can be reproduced by summing up the S-wave components from all the pixels in the tomogram. The inclusion of the systemic velocity γ in Equation 2.2 places the radial velocity v_r curves, and consequently the tomogram, in the rest frame of the binary. Therefore, in order to 'align' each pixel with the 'correct' S-wave component in the trailed spectra (and vice versa) the systemic velocity γ of the binary must be known.

According to axioms one and two (Section 2.1.1) each emission component is considered to have a constant contribution to the observed emission line profile at each observed orbital phase. At orbital phase ϕ the observed emission line flux between radial velocities v and $v + dv$ can therefore be recovered by integration over all the pixels in the tomogram that cover the range of radial velocities, that is,

$$\int_{-\infty}^{\infty}\int_{-\infty}^{\infty} I\,(v_x,\ v_y)\,[g\,(v - v_r)\,dv]\,dv_x dv_y. \tag{2.3}$$

Here the function $g\,(v - v_r)$ describes the intensity of the local line profile at a Doppler shift of $v - v_r$. The observed emission line flux *density* at orbital phase ϕ, that is to say, the observed line profile $f\,(v,\ \phi)$, is then given by

$$f\,(v,\ \phi) = \int_{-\infty}^{\infty}\int_{-\infty}^{\infty} I\,(v_x,\ v_y)\,g\,(v - v_r)\,dv_x dv_y. \tag{2.4}$$

Taking $g\,(v - v_r)$ to be a narrow Gaussian profile with a width matching the instrumental resolution, that is to say, almost a delta function, Equation 2.4 isolates all pixels close to

$$v = v_r\,(\phi) = \gamma - v_x \cos 2\pi\phi + v_y \sin 2\pi\phi. \tag{2.5}$$

Equation 2.5 represents a straight line in velocity coordinates (i.e., the tomogram). The gradient (slope) is determined by the orbital phase ϕ while the intercept is dependent on the value of v as well as the orbital phase ϕ. Now, given the definition of the co-rotating spatial coordinate frame and the resulting velocity coordinates it follows that orbital phase $\phi = 0.0$ represents a collapse (projection) of the tomogram in the positive v_y direction. Similarly, orbital phases $\phi = 0.25$, 0.5 and 0.75 represent projections in the positive v_x, negative v_y and negative v_x directions, respectively. At a specific orbital phase ϕ the emission line profile can be seen, therefore, as a projection of the tomogram in a direction determined by that orbital phase. In other words, each trailed phase-resolved spectrum represents a sum view of the intensity in all the pixels in the tomogram that line up along the direction of its specific orbital phase ϕ.

There are, however, an infinite number of emission distributions in velocity coordinates which can produce the same sum view seen in the trailed spectrum. Finding the emission distribution from which all the observed spectra can be reconstructed, poses a linear inverse problem. This problem can be cast in the form of a Fredholm integral equation of the first kind (Lucy 1994):

$$\varphi(x) = \int P(x, t)\, \psi(t)\, dt, \tag{2.6}$$

where $\varphi(x)$ represents a reconstructed spectrum, $\psi(t)$ is the emission distribution to be found and $P(x, t)$ is the kernel (a bounded linear operator) of the integral equation. Solving the linear inverse problem, in other words, finding the emission distribution that is an accurate representation of the observed system, is the objective of Doppler tomography. However, the inversion from the observed spectra to the Doppler tomogram can be accomplished by more than one method. Marsh & Horne (1988) focussed on a maximum entropy method (MEM) of regularised fitting whereas Horne (1991) favoured a filtered back-projection method. Marsh (2001) gives a comparison of the relative merits of both methods which highlights the superiority of the MEM in dealing with noise and artefacts. Together with its flexibility and employment of a χ^2 as a formal goodness-of-fit parameter makes the MEM the preferred inversion method in most cases. Therefore, only the MEM is considered here and it is discussed in the next section.

2.1.4 Maximum entropy method

Jaynes (1957) introduced the concept of a 'maximum-entropy estimate' which is a statistical inference for finding a probability distribution based on partial 'knowledge'. Consider the function $f(x)$ where x can be the discrete values x_i $(i = 1, 2, ..., n)$. The expected value $\langle f(x) \rangle$ of $f(x)$, that is,

$$\langle f(x) \rangle = \sum_{i=1}^{n} f(x_i)\, p_i, \tag{2.7}$$

is known, but the corresponding probabilities p_i are not. It is possible that any of an infinite number of probability distributions may produce the expected value. Jaynes (1957) gives the entropy S* for the probability distribution p_i as

$$S = -K \sum_i p_i \ln p_i, \tag{2.8}$$

where K is a positive constant. Of all the possible probability distributions that satisfy Equation 2.7 the one that has the maximum entropy, based on the given information, is the best estimate possible, that is, "it is maximally non-committal with regard to missing information" (Jaynes 1957).

The 'maximum-entropy estimate' or maximum entropy method (MEM) was originally introduced for statistical mechanics, but it has been adapted for and used extensively in

*Jaynes (1957) uses the notation H for the entropy.

other fields. A review of its use for image restoration in astronomy is given by Narayan & Nityananda (1986). In Doppler tomography (Marsh & Horne 1988) the MEM is applied to find the emission distribution in velocity coordinates (a tomogram) that is consistent with the input data, that is, the Doppler-shifted spectra at a number of observed phases of the target system. The MEM uses an iteration algorithm to achieve this which is best explained by describing a specific algorithm. The algorithm used for this purpose is a slightly modified version of the algorithm described by Lucy (1994), which is related to the Richardson-Lucy iteration (Richardson 1972; Lucy 1974). The modified algorithm, that is, the *fast maximum entropy algorithm*, is described by Spruit (1994) for use in eclipse mapping (Horne 1985), but it is also used in constructing Doppler tomograms (Spruit 1998). It is much faster than other algorithms (e.g., Skilling & Bryan 1984) normally used in MEM applications. The fast maximum entropy algorithm is described here in its specific form for constructing Doppler tomograms. This description is given in reference to and incorporates elements from Lucy (1994), Spruit (1994) and Spruit (1998).

2.1.4.1 Fast maximum entropy algorithm

The input spectra (in velocity profile format) at observed phases ϕ_i are denoted by $\tilde{\varphi}_i$. These need not be at equal phase intervals, but they must provide reasonable coverage over the orbit of the observed system. The aim is to find a tomogram (emission distribution in velocity coordinates), denoted by ψ, from which it is possible to reconstruct the input spectra. The reconstructed spectra are denoted by φ_i. The shape of the tomogram ψ is assumed to be a circle in velocity coordinates with radius equal to the absolute maximum radial velocity extracted from the input spectra. The area of the tomogram ψ is divided into m discrete elements. The reconstructed spectra φ_i are then given by a discrete form of the Fredholm integral equation,

$$\varphi_i = \sum_{j=1}^{m} P_{ij}\psi_j, \tag{2.9}$$

where the kernel P is a *projection matrix* that converts the emission from surface element j to its contribution to the spectrum at observed phase ϕ_i.

The 'entropy' to be maximised during the reconstruction process, in order to determine the tomogram ψ, is the scalar quantity Q, that is, the quality function, given by

$$Q = H + \alpha S, \tag{2.10}$$

where H and S are the likelihood and entropy functions, respectively, and α is the regularisation parameter. The likelihood H is a measure of the difference between the reconstructed spectra φ and the input spectra $\tilde{\varphi}$, with a maximum when the reconstructed spectra are equal to the input spectra. The preferred formulation of the likelihood H is a log-likelihood*

*The log-likelihood is preferred under the assumption that the uncertainties in the data follow Poisson statistics whereas a χ^2-likelihood is preferred if the uncertainties follow normal statistics.

proposed by Lucy (1994) for non-negative images, ($\psi_j \geq 0$ for all j),

$$H = \sum_i \tilde{\varphi}_i \ln \varphi_i. \tag{2.11}$$

The entropy S adds a smoothing bias to the tomogram and is given by

$$S = -\sum_j \left(\psi_j \ln \frac{\psi_j}{\chi_j} + \chi_j \right), \tag{2.12}$$

where χ is a default image constructed from the tomogram ψ using a Gaussian smearing. This simplifies to

$$S = -\sum_j \left(\psi_j \ln \frac{\psi_j}{\chi_j} \right), \tag{2.13}$$

if the default image is normalised $\left(\sum_j \chi_j = 1\right)$. The regularisation parameter α controls the relative contributions of the likelihood H and the entropy S in the quality function Q. In other words, it controls the trade-off between noise and resolution: a too small value will over fit the noise while a larger value produces smoother tomograms. The procedure for selecting it therefore has a critical effect on the quality of the fit to the data and correspondingly the structure of the resulting tomogram.

The maximisation of the quality function Q is done iteratively by adjusting the values of ψ through constructing a sequence of tomograms ψ^k:

$$\psi^{k+1} = \psi^k + \Delta\psi^k, \tag{2.14}$$

where

$$\Delta\psi_j^k = \psi_j^k \left(\frac{\partial Q}{\partial \psi_j^k} - \sum_j \psi_j^k \frac{\partial Q}{\partial \psi_j^k} \right). \tag{2.15}$$

The first term in Equation 2.15 is crucial as it increases the emission contribution of the surface elements j that produce a higher positive change in the quality function Q, while the second term ensures a constant total emission $\sum_j \psi_j$. The iterative correction $\Delta\psi^k$ is split into its likelihood and entropy elements:

$$\Delta\psi^k = \Delta^H\psi^k + \Delta^S\psi^k, \tag{2.16}$$

where

$$\Delta^H\psi_j^k = \psi_j^k \left(\sum_i \frac{\tilde{\varphi}_i}{\varphi_i^k} P_{ij} - 1 \right), \tag{2.17}$$

and

$$\Delta^S\psi_j^k = -\alpha\psi_j^k \left(S + \ln \frac{\psi_j^k}{\chi_j^k} \right). \tag{2.18}$$

An accuracy of convergence δ is specified for the iteration process and the iterations proceed

until

$$\left|\left|\frac{\Delta\psi^k}{|\Delta^H\psi^k| + |\Delta^S\psi^k|}\right|\right| < \delta, \tag{2.19}$$

where $\| \mathbf{A} \|$ is the root mean square norm of a vector $\mathbf{A}$. At the point of convergence the tomogram ψ^k is taken to be the least biased emission distribution in velocity coordinates that is consistent with the observed spectra for the target system.

Figure 2.6 shows an example of a Doppler tomogram constructed with the fast maximum entropy algorithm. A model velocity profile overlay is added to assist with the interpretation of the emission distribution in the tomogram. The tomogram is dominated by a relatively bright accretion disc and the bright spot of the impact region between the ballistic stream and disc. This example is revisited in Chapter 4 where it is discussed in more detail (see Section 4.1).

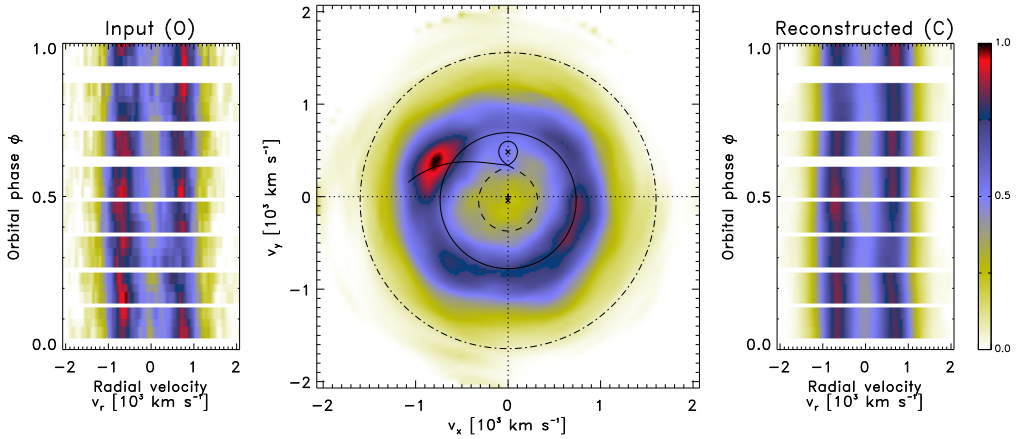

Figure 2.6. Example fast maximum entropy Doppler tomography of a dwarf nova. The normalised Doppler tomogram is shown in the middle panel. The left and right panels show the normalised trailed input and reconstructed spectra, respectively. The binary's centre of mass is at the centre of the tomogram, marked with a plus (+). The centres of mass of the primary and secondary are marked with crosses (×). The model velocity profile overlay includes the Roche lobes of the primary (dashed line), the secondary (solid line) and a single particle ballistic trajectory (solid line) from the L_1 point up to 45° in azimuth around the primary. Also shown are the 3:1 resonance radius as the outer edge of the accretion disc (solid circle) and an inner Keplerian radius (dot-dashed line) based on an absolute radial velocity of 1600 km s^{-1}, that is, the maximum absolute radial velocity seen in the emission line variations.

2.2 Standard Doppler tomography extensions

In the first part of this section an overview is given of spin-cycle Doppler tomography (Hellier 1997) that uses spin-folded spectra to map emission components which are locked on the spin period of the primary of, for example, an intermediate polar. The second part of this section covers modulation Doppler tomography (Steeghs 2003), a notable extension that

maps emission components that vary harmonically as a function of the orbital period.

2.2.1 Spin-cycle Doppler tomography

Hellier (1997, 1999) used spin-cycle Doppler tomography to map the spin-varying emission components in various intermediate polars. This technique was especially successful in exposing the extent and shape of the line-emitting accretion curtains in, for example, PQ Gem.

The first step in spin-cycle Doppler tomography is to resolve the observed spectra on the spin phase as opposed to the orbital phase which is normally the case for Doppler tomography (see Section 2.1). In general, the emission from spin-varying components originates from within the rotating magnetosphere of the primary. On the other hand, the emission from orbitally-varying components is expected to originate further out in the system, for example, from the secondary, ballistic accretion stream and disc. The second step is to subtract a phase-invariant spectrum from each of the spin phase-resolved spectra in order to remove the emission components not varying on the spin phase. According to Hellier (1997) this is achieved by subtracting, at each resolved wavelength, the second lowest flux value from the set of spin phase-resolved spectra at that wavelength. The second lowest value, rather than the lowest, is used because it makes the procedure less sensitive to outlier values. Any residual phase-invariant emission produces azimuthally symmetric rings in the tomogram, hence any such features must be excluded when interpreting the tomogram.

The spin-folded spectra are not corrected for the orbital motion of the primary, because for most intermediate polars the primary's semi-amplitude K_1 and (or) phase-offset are not known. Effectively the orbital motion of the primary will smear the spin-folded emission features in the tomogram. However, in these systems the primary typically has a semi-amplitude $K_1 < 100\text{km s}^{-1}$ which is much less than the infall velocities near the primary. For practical purposes a spin-cycle tomogram can therefore considered to be centred on the rest frame of the primary, but blurred by its orbital motion. See the above mentioned papers for a more complete description of the technique. The spin-cycle Doppler tomography results of PQ Gem, first presented by Hellier (1997), are explored further in Section 4.5.

2.2.2 Modulation Doppler tomography

Axiom two (Section 2.1.1) states that the flux from each point in the frame of rotation is assumed to be constant in time. Observations of CVs and mCvs, however, confirm that the flux from the typical emission components that are mapped in Doppler tomography do modulate in time. Most notable are phased flux modulations that are mostly attributed to the geometry of the system, for example, an eclipse or the aspect variation of an emission component. This is especially common in mid- to high-inclination systems where emission components such as the irradiated side of the secondary and the bright spot where the ballistic stream impacts the accretion disc, can be partially or wholly eclipsed during an orbit. Doppler tomography, however, presents a phase-averaged map in velocity coordinates

of the emission distribution in the system. Phase-dependent details in the observed spectra such as the orbital flux modulation will therefore not be recovered in the reconstructed spectra. Recognising this, Steeghs (2003) introduced modulation Doppler tomography, a technique that maps emission components which modulate sinusoidally as a function of the orbital period. This is achieved through the simultaneous construction of three tomograms, that is, one for the average flux distribution and two for the variable part in terms of its sine and cosine amplitudes.

In Section 2.1.3 it was shown that the flux of a particular emission component is represented by the *single* phase-averaged parameter $I\left(v_x,\, v_y\right)$, that is, the intensity in the pixel centred on the velocity coordinate $(v_x,\, v_y)$ in the tomogram. Now, consider the flux $F\left(\phi\right)$ of an emission component that modulates sinusoidally as a function of the orbital period, that is,

$$F\left(\phi\right) = I_{\rm avg} + I_{\cos}\cos 2\pi\phi + I_{\sin}\sin 2\pi\phi. \tag{2.20}$$

Here $I_{\rm avg}$ is the average flux, and $I_{\cos}$ and $I_{\sin}$ are, respectively, the cosine and sine components of the flux modulation. The total amplitude and the phase of the modulation are given, respectively, by

$$\sqrt{I_{\cos}^2 + I_{\sin}^2} \text{ and } \tan^{-1}\left(I_{\cos}/I_{\sin}\right). \tag{2.21}$$

Three parameters are now used to describe the observed flux of the emission component, that is, $I_{\rm avg}\left(v_x,\, v_y\right)$, $I_{\cos}\left(v_x,\, v_y\right)$ and $I_{\sin}\left(v_x,\, v_y\right)$. The observed line profile $f\left(v,\, \phi\right)$ at orbital phase ϕ is then given by

$$f\left(v,\, \phi\right) = \int_{-\infty}^{\infty}\int_{-\infty}^{\infty}\left[I_{\rm avg}\left(v_x,\, v_y\right) + I_{\cos}\left(v_x,\, v_y\right)\cos 2\pi\phi + I_{\sin}\left(v_x,\, v_y\right)\sin 2\pi\phi\right]\cdot$$
$$g\left(v - v_r\right)dv_x dv_y. \tag{2.22}$$

This extension does not change the basics of the projection from the observed spectra to the tomogram or the reconstruction of the spectra from the tomogram, but three Doppler tomograms are now constructed. One tomogram is constructed in terms of $I_{\rm avg}\left(v_x,\, v_y\right)$ and describes the average flux distribution. This tomogram is equivalent to the conventional tomogram constructed in terms of $I\left(v_x,\, v_y\right)$. The other two tomograms are constructed, respectively, in terms of $I_{\cos}\left(v_x,\, v_y\right)$ and $I_{\sin}\left(v_x,\, v_y\right)$. These tomograms describe the variable component in terms of its sine and cosine amplitudes.

Figure 2.7 shows example modulation tomograms based on the He II λ4686 emission line of the dwarf nova IP Peg during outburst presented by Steeghs (2003). The tomogram of the average emission (upper left panel of Figure 2.7) is similar to the non-modulated standard tomogram presented by Harlaftis et al. (1999), using the same data. The modulation in the emission associated with the accretion disc and secondary is clearly seen in the tomogram of the total modulated emission (upper right panel of Figure 2.7). The tomograms of the cosine and sine amplitudes (bottom left and right panels of Figure 2.7, respectively) show that the modulation is dominated by the sine component. See Steeghs (2003) for a more

complete discussion about the subtleties revealed by the modulation tomograms and the interpretation thereof.

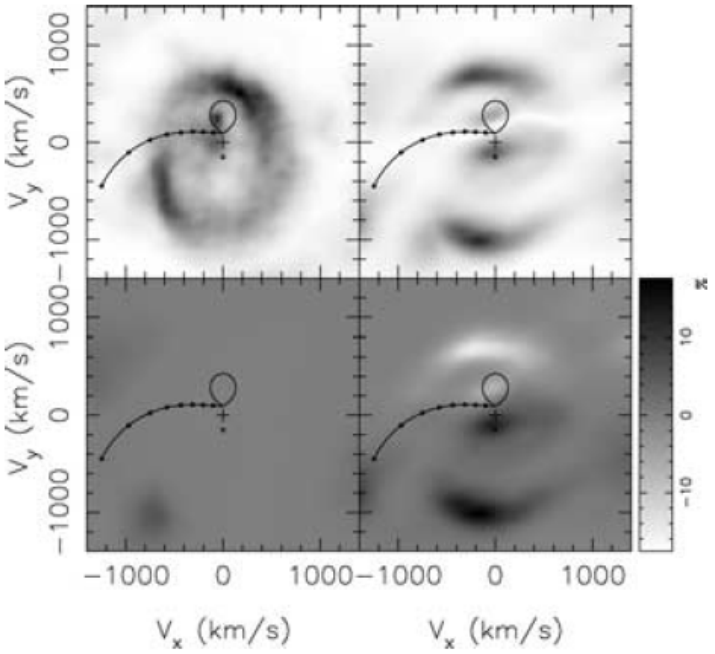

Figure 2.7. Example modulation Doppler tomograms of the dwarf nova IP Peg. The tomograms of the average emission and the total modulated emission are shown in the upper left and right panels, respectively. These tomograms are in a grey scale with brighter regions being darker. The tomograms of the cosine and sine amplitudes are shown in the lower left and right panels, respectively. The grey scale bar on the right shows the fractional modulation amplitudes in these tomograms. Taken from Steeghs (2003) – Figure 4.

Modulation Doppler tomography has been proven to be a sound and well constrained extension to the conventional technique (see, e.g., Papadaki et al. 2008). Recent references in literature to the application of modulation Doppler tomography mostly involve spectroscopic studies of black hole X-ray binaries, e.g., Peris et al. (2015) and Čechura et al. (2015). Building partially on the principles introduced by Steeghs (2003) I developed a variant form of modulation Doppler tomography which I introduce in Chapter 5.

Chapter 3

Inside-out Doppler tomography

Though this be madness, yet there is method in't.

– William Shakespeare, *Hamlet*, Act II, Scene 2

I showed in Chapter 2 how a standard Doppler tomogram is constructed in velocity cartesian coordinates using the velocity and emission information contained in phase-resolved Doppler-shifted spectra. In the cartesian coordinate frame zero velocity is placed at the origin and the maximum velocities at the edge of the coordinate frame. When first encountering such a standard Doppler tomogram of a CV, one may have some difficulty in visualising the accepted spatial geometry of this type of binary based on the velocity geometry of the emission components. This is largely due to the inverted appearance of the emission components in standard velocity coordinates with respect to the spatial direction. The question therefore arises: Is it possible to construct a Doppler tomogram in 'inside-out' velocity coordinates which may present a more intuitive layout to help ease the 'difficulty' associated with standard velocity coordinates? If so, the next question is: Does the distribution of emission component fluxes in the tomogram constructed in 'inside-out' velocity coordinates reveal details not seen in the tomogram constructed in standard velocity coordinates?

In the endeavour to answer the first question I developed a new inside-out velocity projection technique. The second question prompted an extensive investigation into the application of this new technique. While this chapter serves as an introduction to the new inside-out velocity projection technique, the next chapter (Chapter 4) focusses on the investigation involving CVs and mCVs selected for the distinct accretion features apparent in their trailed spectra and exposed through standard Doppler tomography. As a starting point for this chapter I recast the spatial and velocity cartesian coordinate frames, reviewed in the previous chapter (see Section 2.1.2), in polar coordinates in Section 3.1. The resulting standard velocity polar coordinate frame forms the basis for the inside-out velocity polar coordinate frame which I introduce in Section 3.2. Next, in Section 3.3, I revisit velocity-phase space with a comparison between velocity bins in standard and inside-out velocity coordinates. In Section 3.4 I give a short overview of `doptomog`, a refactored fast maximum entropy Doppler

tomography code that incorporates the inside-out projection. It is important to note that this code constructs the inside-out tomogram *independently* of the standard tomogram by directly projecting the phase-resolved spectra onto the inside-out velocity coordinate frame. I end the chapter with a test on a simulated data set of phase-resolved spectra. The results of the inside-out projection are shown alongside that of the standard projection in Section 3.5. Shortened versions of the sections in this chapter have been published as parts of two articles in *Astronomy & Astrophysics* (Kotze et al. 2015, 2016).

3.1 Spatial and velocity polar coordinates

3.1.1 Non-magnetic cataclysmic variables

3.1.1.1 Spatial polar coordinates

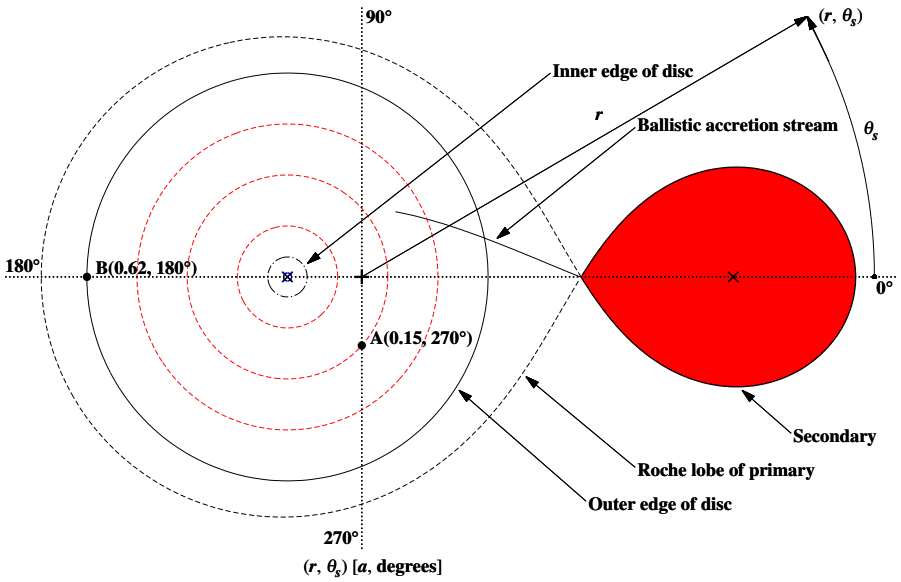

Figure 3.1. Spatial polar coordinates for a model CV with an accretion disc. This figure is the equivalent of Figure 2.1, but in polar coordinates.

Figure 3.1 shows the same model CV shown in Figure 2.1, but in spatial polar coordinates. The radial component r is the distance (normalised by the binary separation a) measured from the binary's centre of mass. The angular component θ_s (also called the polar angle) is measured in an anticlockwise direction from the line between the centres of mass of the binary and secondary. For example, the primary's centre of mass is at $(r,\, \theta_s) = (0.17,\, 180°)$, while that of the secondary is at $(r,\, \theta_s) = (0.83,\, 0°)$. The radial components of the centres of mass of the primary and secondary are functions of the mass ratio q, that is, $r = q/\,(1+q)$

for the primary's centre of mass and $r = 1/(1+q)$ for that of the secondary. The angular component θ_s in the spatial coordinate frame is not to be confused with the angular component θ in the velocity coordinate frame described below.

3.1.1.2 Velocity polar coordinates

Every spatial point (r, θ_s) in the system now has a two-dimensional velocity polar coordinate (u, θ) in the co-rotating spatial coordinate frame. The projection of all the (u, θ)-coordinates onto the rotating frame forms the velocity polar coordinate frame with (v, θ)-coordinates. The inclination angle i is taken into account in the projection, that is, $v = u \sin i$.

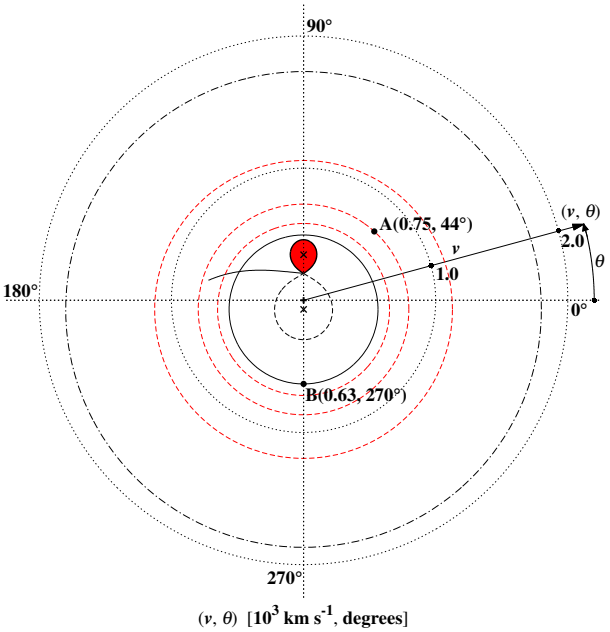

Figure 3.2. Velocity polar coordinates for a model CV with an accretion disc. This figure is the equivalent of Figure 2.2, but in velocity polar coordinates.

Figure 3.2 shows the velocity polar coordinates of the model CV based on the co-rotating spatial polar coordinate frame defined above (Figure 3.1). The inclination angle i of the system is taken to be 75°. The radial component v, that is, the velocity magnitude, increases as a linear function of distance from the origin. The angular component θ, that is, the velocity direction, is measured in an anticlockwise direction from the line drawn from the binary's centre of mass horizontally to the right. For example, the velocity of the secondary's centre of mass is now given by a velocity magnitude $v = 345\,\mathrm{km\,s^{-1}}$ with a velocity direction (angle) $\theta = 90°$ (i.e., $v_x = 0$ and $v_y = 345\,\mathrm{km\,s^{-1}}$ in cartesian coordinates). The velocity coordinate of the primary's centre of mass is now $(v, \theta) = \left(69\,\mathrm{km\,s^{-1}}, 270°\right)$. The advantage of velocity polar coordinates is that a coordinate, that is, (v, θ), *directly* describes its magnitude v and direction θ. In contrast, a velocity cartesian coordinate must be converted to get its magnitude v and direction θ. In general, it is more intuitive to describe velocity in terms of

its magnitude and direction than to describe it in terms of its x- and y-axial components.

At this point it is important to note that the velocity profile of the accretion disc is not centred on the origin of the coordinate frame in Figure 3.2. This is the result of the disc being centred on the *primary's* centre of mass and not on the *binary's* centre of mass. It follows, therefore, that the Keplerian velocities of the disc are offset by an amount corresponding to the orbital motion of the primary. This is clearly seen in the velocity profiles of the inner and outer disc, as well as that of the radii at decrements of 0.25 times the outer disc radius, not being concentric with the velocity grid. The higher the mass ratio q in the binary the further the primary's centre of mass is from the origin and the more noticeable the offset in the velocity profile of the disc will be. It is important to note that the offset in the disc is not the result of using polar coordinates because the offset is also present in cartesian coordinates (see Figure 2.2).

Subtracting the orbital velocity of the primary from the model velocity profile centres the primary and accretion disc on the origin of the coordinate frame (Marsh & Horne 1988). Figure 3.3 shows such a resulting velocity map for the model CV. The velocity profiles of the inner and outer disc, as well as that of the radii at decrements of 0.25 times the outer disc radius, are now concentric with the velocity grid. The velocity coordinates of the centres of mass of the binary and secondary are now $(v,\,\theta) = \left(69\,\mathrm{km\,s^{-1}},\,90°\right)$ and $\left(414\,\mathrm{km\,s^{-1}},\,90°\right)$, respectively. The results of centring Doppler tomograms on the rest frames of the binary and primary, respectively, are compared in Sections 3.5, 4.1 and 4.2.

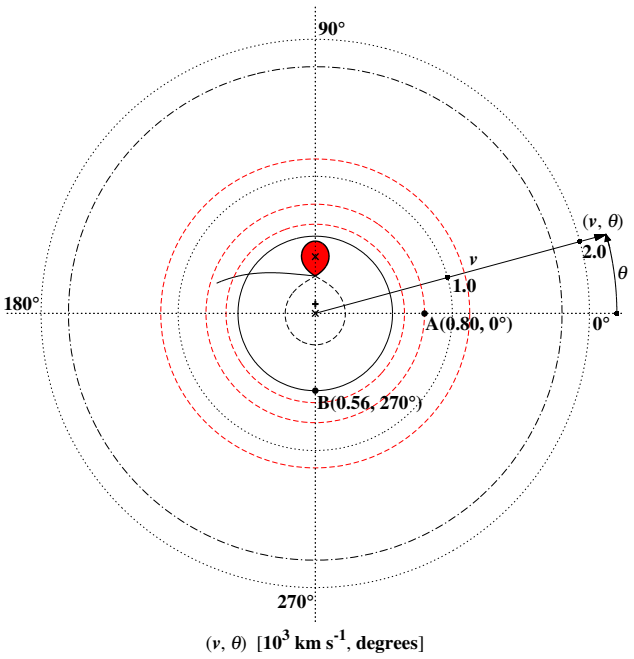

Figure 3.3. Velocity polar coordinates centred on the rest frame of the primary for a model CV with an accretion disc. The primary's centre of mass is the cross ($\times$) at the origin, while that of the binary and secondary are, respectively, the plus ($+$) and cross ($\times$) on the 90°-line.

As noted in Section 2.1.2.2 that due to the Keplerian motion in the accretion disc the velocity profiles of the radii at decrements of 0.25 times the outer disc radius do not follow the same linear distribution in velocity coordinates as they do in spatial coordinates. I explored replacing the linear radial component v with a Keplerian velocity ($\propto 1/\sqrt{r}$) profile in an attempt to produce a more equidistant velocity contour profile for the disc. However, a correct calculation of the Keplerian profile would require knowledge of the mass of the primary of the actual system under investigation. This is rarely known and would introduce a new parameter that would no longer give a map that is simply a direct projection of the observations.

3.1.2 Magnetic cataclysmic variables

3.1.2.1 Spatial polar coordinates

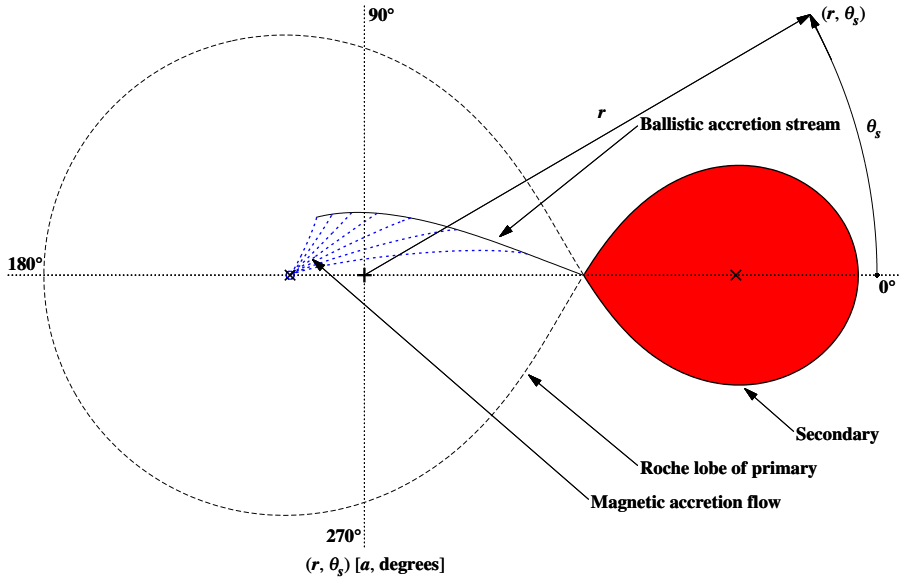

Figure 3.4. Spatial polar coordinates for a model mCV with ballistic and magnetic accretion flows only. Spatial overlays are shown for the Roche lobe of the primary (black dashed line) and ballistic accretion stream (black solid line) up to 65° in azimuth around the primary. Also shown are magnetic dipole field lines (blue dotted lines) at 10° intervals from 5° to 65° in azimuth around the primary. The assumed dipole axis azimuth and co-latitude are 40° and 15°, respectively.

To complete the recasting to polar coordinates a model mCV is also considered. The spatial polar coordinates for a model mCV without an accretion disc, but with a ballistic stream and magnetically confined accretion along the magnetic dipole field lines are shown in Figure 3.4. The model mCV parameters are the same as that for the model CV, that is, a primary mass $M_1 = 0.85\,M_\odot$, a mass ratio $q = 0.2$ and an orbital period $P_{\rm orb} = 0.125\,\mathrm{d}\,(3\,\mathrm{hr})$.

Consequently, the spatial polar coordinates for the centres of mass of the primary and secondary of the model mCV are the same as that of the model CV in Figure 3.1, that is, $(r,\, \theta_s) = (0.17,\, 180°)$ and $(0.83,\, 0°)$, respectively. The modelled single particle ballistic trajectory includes, apart from gravitational and centrifugal effects, a magnetic drag force. This drag force is similar to that employed by Schwope et al. (1997b) and Schwope et al. (2000). It decreases exponentially as a function of the distance from the primary's centre of mass and is included in order to account for the pull of the primary's magnetic field on the partly ionised ballistic stream. The structure of the primary's magnetic field is taken to be a single dipole, but no assumption is made about the strength of the magnetic field.

3.1.2.2 Velocity polar coordinates

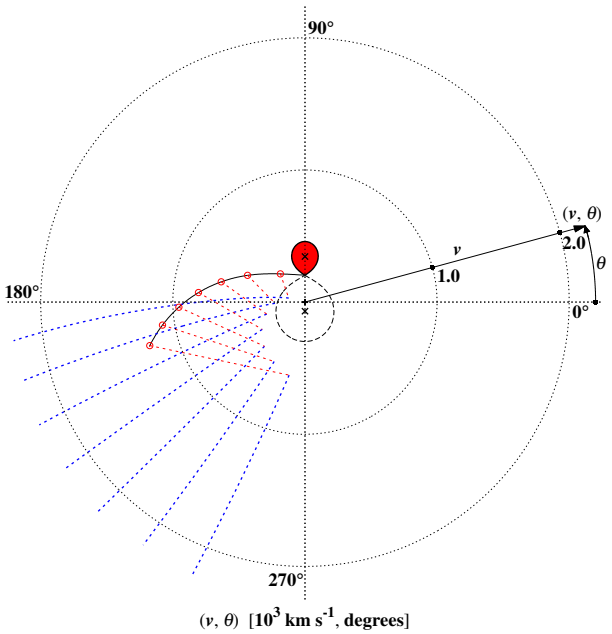

Figure 3.5. Velocity polar coordinates for a model mCV with ballistic and magnetic accretion flows only. The binary's centre of mass is the plus (+) at the origin, while that of the primary and secondary are the crosses (×) on the 270°- and 90°-lines, respectively. The red circles along the ballistic accretion stream (black solid line) mark the points where the magnetic dipole field lines connect. The red dotted lines are non-physical tracers for the change in the line-of-sight velocity as the magnetically confined flows leave the orbital plane along the magnetic dipole field lines. The magnetic dipole field lines (blue dotted lines) *diverge* towards higher velocities.

Following the same procedure discussed above for the model CV the resulting velocity polar coordinates for the model mCV are shown in Figure 3.5. As was the case with their spatial polar coordinates the velocity polar coordinates for the centres of mass of the primary and secondary are the same as that of the model CV in Figure 3.2, that is, $(v,\, \theta) = \left(69\,\mathrm{km\,s^{-1}},\, 270°\right)$ and $\left(345\,\mathrm{km\,s^{-1}},\, 90°\right)$, respectively. The first dipole connection

on the ballistic stream is at $(283\,\mathrm{km\,s^{-1}}, 131°)$, while the first dipole trajectory starts at $(126\,\mathrm{km\,s^{-1}}, 166°)$. Consecutive connections and trajectories are at locations with progressively higher velocities and polar angles. These velocities include the effect of the simulated magnetic drag force described above. The profiles of the dipole trajectories radiate outwards from the lower velocities where they leave the orbital plane towards higher velocities as they approach the primary, in other words, they *diverge* towards higher velocities.

3.2 Inside-out velocity polar coordinates

The aim now is to construct an inside-out velocity coordinate frame with zero velocity on the outer circumference and the maximum velocities around the centre of the coordinate frame. The standard velocity polar coordinate frame defined in Section 3.1 forms the basis for such an inside-out velocity polar coordinate frame. In the inside-out velocity polar coordinate frame the velocity direction (angular component) θ of a point remains unchanged, that is to say, it is measured in an anticlockwise direction from the line drawn from the binary's centre of mass horizontally to the right. However, the velocity magnitude (radial component) v now increases as a linear function of distance from the zero velocity outer circumference towards the centre of the coordinate frame with the said direction θ.

For the inside-out coordinate frame to be complementary to the standard coordinate frame, and to facilitate a direct comparison between them, the default centre of the inside-out coordinate frame is set to the maximum radial velocity (plus a small arbitrary velocity element δv) used to construct the standard coordinate frame. This maximum radial velocity is effectively the maximum velocity v_{max} extracted for an emission (or absorption) line from observed phase-resolved spectra, that is to say, the 'edge' of the data projected onto the coordinate frame to construct the tomogram. The centre and the outer circumference of the inside-out coordinate frame are therefore essentially a transposition of, respectively, the zero velocity origin and the maximum outer velocities (plus the small arbitrary velocity element δv) of the standard coordinate frame. The set of maximum velocities at the small arbitrary velocity element δv from the centre of the inside-out coordinate frame (i.e., *around* the centre) is described by

$$(v, \theta) = (v_{max}, \theta)\,, \tag{3.1}$$

for all values of θ. This means the 'edge' of the data is projected around the centre of the inside-out coordinate frame. Consequently, the centre represents a discontinuity and the inner four velocity bins (pixels) around it are not used in the projection.

Placing zero velocity at the edge of the inside-out coordinate frame means that where it used to be only one point in the standard coordinate frame, it now becomes a set of zero values described by

$$(v, \theta) = (0, \theta)\,, \tag{3.2}$$

for all values of θ.

3.2.1 Non-magnetic cataclysmic variables

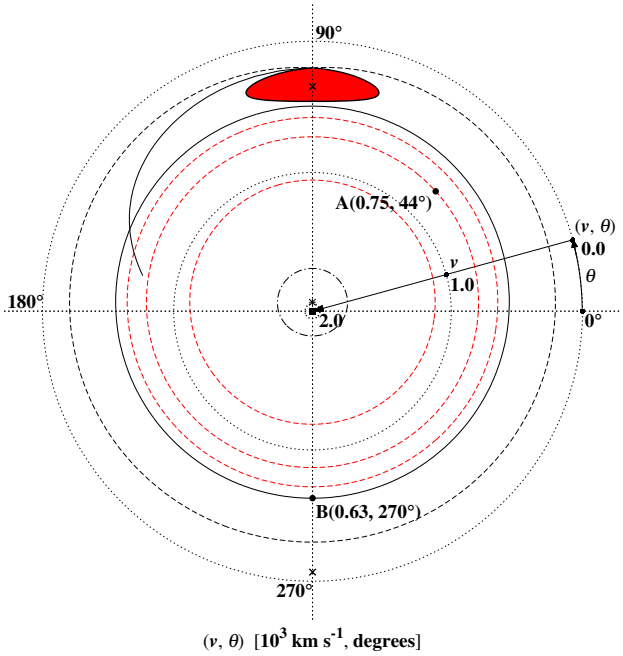

Figure 3.6. Inside-out velocity polar coordinates for a model CV with an accretion disc. The velocity map is centred on the rest frame of the binary. The binary's centre of mass is effectively the zero velocity outer circumference while those of the primary and secondary are the crosses (×) on the 270°- and 90°-lines, respectively. The centre of the disc is the asterisk on the 90°-line.

Figure 3.6 shows the equivalent inside-out velocity map of the standard velocity map presented in Figure 3.2. In the inside-out coordinate frame the binary's centre of mass effectively becomes the outer circumference of zero velocity. The inner and outer edges of the accretion disc are now orientated in accordance to the spatial orientation. In addition, the ballistic accretion stream is on the *outside* of the disc and it 'curves' inwards as it accelerates towards the disc and primary. The secondary is also on the outside of the disc albeit upside down. It is projected upside down because it orbits as a solid body which means that the side furthest from the binary's centre of mass moves faster than the side closest to the binary's centre of mass. This is in contrast to the Keplerian velocities of the accretion disc and the ballistic velocities of the accretion stream. The Roche lobe of the primary is now the outer bounded area between zero velocity and the dashed line that contains the primary's centre of mass (indicated by a ×). The Keplerian velocities in the accretion disc are still visibly apparent as can be seen in the radial velocity profiles of the equidistant disc radii contours (red dashed circles). In the inside-out velocity map the offset in the Keplerian velocities of the disc is more apparent than in the standard velocity map (i.e., Figure 3.2).

Figure 3.7 shows the inside-out velocity map with the orbital motion of the primary subtracted from the model velocity profile. Now the velocity map is centred on the rest

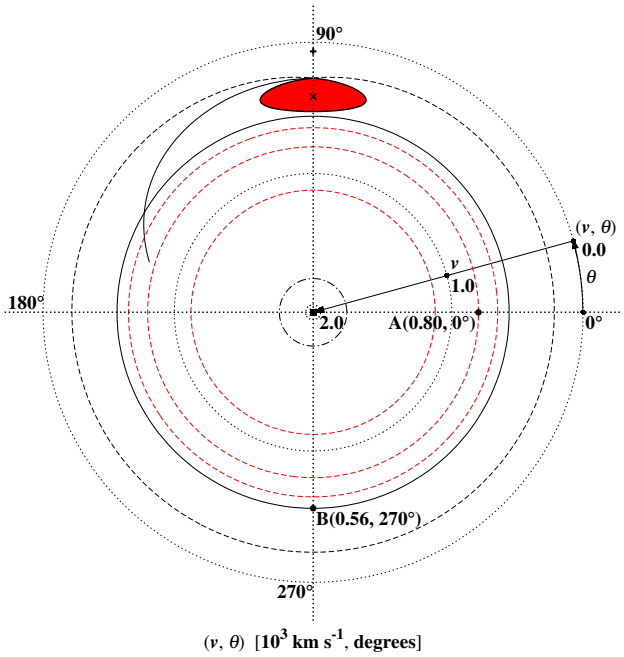

Figure 3.7. Inside-out velocity polar coordinates centred on the rest frame of the primary for a model CV with an accretion disc. The primary's centre of mass is the zero velocity outer circumference while those of the binary and secondary are the plus (+) and cross (×) on the 90°-line, respectively.

frame of the primary and the primary's centre of mass is effectively the outer circumference of zero velocity. As was the case for the equivalent standard velocity map presented in Figure 3.3, the velocity profiles of the inner and outer disc, as well as that of the radii at decrements of 0.25 times the outer disc radius, are now concentric with the velocity grid. The results of centring Doppler tomograms on the rest frame of the binary and the primary, respectively, are compared in Sections 3.5, 4.1 and 4.2.

3.2.2 Magnetic cataclysmic variables

The equivalent inside-out velocity map of the standard velocity map of the model mCV presented in Figure 3.5 is shown in Figure 3.8. Compared to the profiles in the standard velocity map the profiles of the dipole trajectories now radiate inwards from the lower velocities where they leave the orbital plane towards higher velocities as they approach the primary, in other words, they *converge* towards higher velocities.

3.3 Velocity-phase space revisited

In Section 2.1.2 the velocity cartesian coordinate frame was discussed. It was noted that the velocity coordinate frame is divided into discrete square velocity bins (pixels) each of which is centred on a unique velocity coordinate (v_x, v_y). Now, each coordinate in the velocity

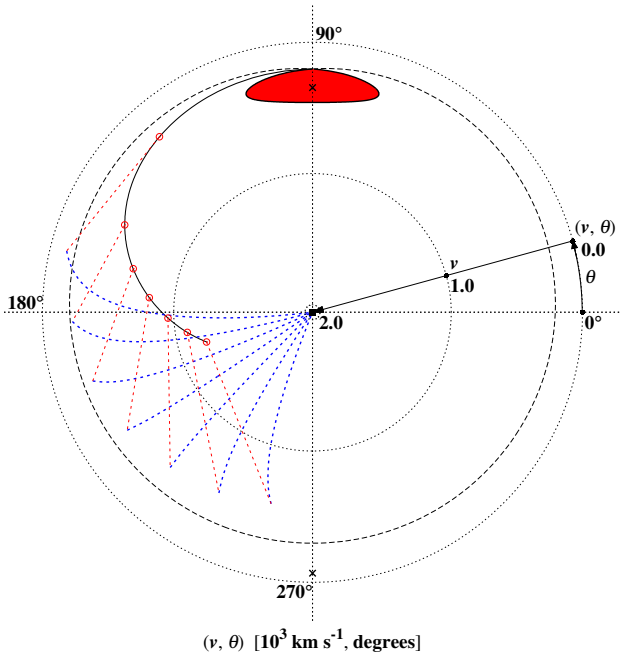

Figure 3.8. Inside-out velocity polar coordinates for a model mCV with ballistic and magnetic accretion flows only. The velocity map is centred on the rest frame of the binary. The binary's centre of mass is effectively the zero velocity outer circumference while those of the primary and secondary are the crosses (×) on the 270°- and 90°-lines, respectively. The magnetic dipole field lines (blue dotted lines) *converge* towards higher velocities.

coordinate frame describes a velocity vector that has both a magnitude v and direction (angle) θ. In the standard and inside-out polar coordinate frames each pixel is centred on a velocity coordinate (v, θ) which directly describes the magnitude v and angle θ of the corresponding centre velocity vector $\vec{v} = (v, \theta)$. Similar to the cartesian coordinate frame, each pixel represents a square velocity bin which has sides of magnitude dv_p.

The left panel of Figure 3.9 is the equivalent of the left panel of Figure 2.5, but in standard velocity polar coordinates. It shows the same lower velocity green pixel and higher velocity blue pixel in the upper and lower left quadrants, respectively, of the Doppler map with the equivalent velocities in polar coordinates $(v, \theta) = \left(493\,\mathrm{km\,s^{-1}}, 149.0°\right)$ and $\left(1627\,\mathrm{km\,s^{-1}}, 246.5°\right)$, respectively. As is the case for the cartesian layout, both pixels represent square velocity bins which have sides of magnitude $dv_p = 56\,\mathrm{km\,s^{-1}}$. In standard velocity coordinates the lower velocity pixels are closer to the centre of the coordinate frame while the higher velocity pixels are further away. Consequently, and as expected, the range in velocity angle $d\theta$ for the lower velocity green pixel is larger than that for the high velocity blue pixel, that is, 9.0° for the green pixel compared to 2.6° for the blue pixel. The range in velocity angle $d\theta$, in other words, the angle subtended by a pixel, therefore decreases as the pixel's velocity magnitude v increases. For the lower velocity green pixel the range in velocity magnitude dv is $77\,\mathrm{km\,s^{-1}}$ compared to $74\,\mathrm{km\,s^{-1}}$ for the higher velocity blue pixel. The maximum range in velocity magnitude dv is the diagonal magnitude dm of a pixel, that is,

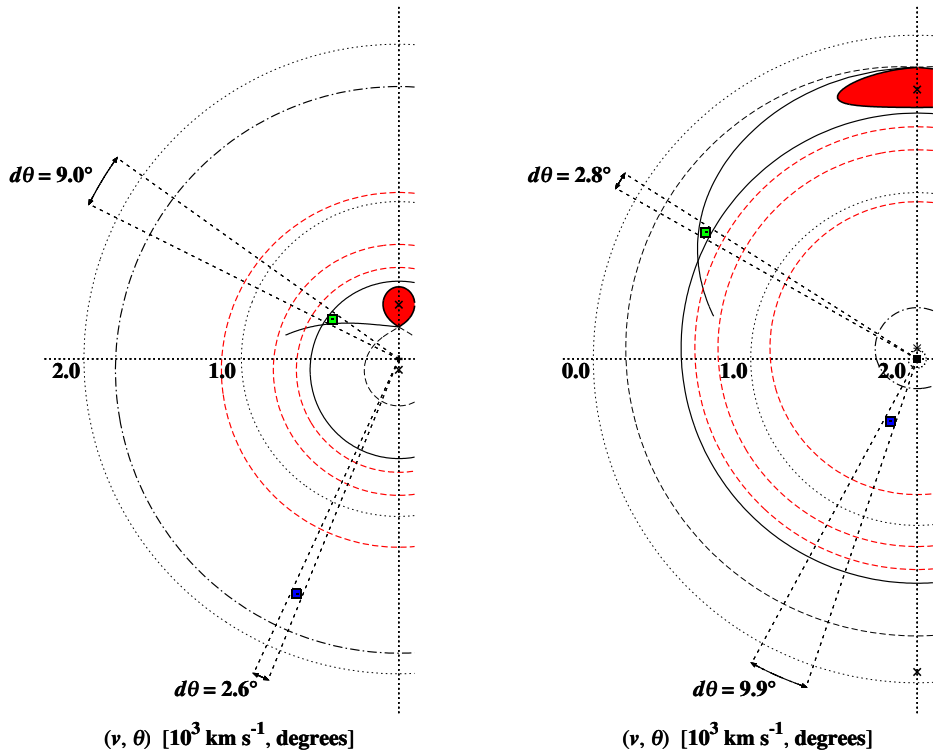

Figure 3.9. Velocity bins (pixels) in standard and inside-out polar velocity coordinates. The left panel shows the positions of a lower velocity green pixel and a higher velocity blue pixel in, respectively, the upper and lower left quadrants of the standard velocity map. The right panel shows the equivalent pixels in the inside-out velocity map.

$dm = \sqrt{2} \cdot dv_p$, which holds for *all* pixels with a velocity angle θ that coincides with the diagonals of the coordinate frame quadrants, that is, $\theta \in \{45°, 135°, 225°, 315°\}$. The minimum range is $\sim dv_p$ which holds when a pixel is close to the $(0° - 180°)$- or $(90° - 270°)$-lines *and* it is close to the outer circumference of the coordinate frame, that is to say, its velocity magnitude v is close to v_{max}. In general therefore, in the standard coordinate frame the lower velocity pixels sample a larger velocity vector range than the higher velocity pixels, in other words, the velocity vector range sampled by a pixel *decreases* as a function of radial distance from the centre of the coordinate frame.

To demonstrate this for the inside-out coordinate frame the equivalent lower velocity green and higher velocity blue pixels shown in the left panel of Figure 3.9 are shown in inside-out velocity polar coordinates in the right panel of Figure 3.9. In inside-out velocity coordinates the higher velocity pixels are closer to the centre of the coordinate frame while the lower velocity pixels are further away. Now the range in velocity angle $d\theta$ for the lower velocity green pixel is smaller than that for the high velocity blue pixel, that is, 2.8° for the green pixel compared to 9.9° for the blue pixel. The range in velocity angle $d\theta$ now increases as its velocity magnitude v increases. The range in velocity magnitude dv for both pixels, however, is unchanged compared to the standard coordinate frame, that is, $77\,\mathrm{km\,s^{-1}}$ for the

lower velocity green pixel compared to $74\,\mathrm{km\,s^{-1}}$ for the high velocity blue pixel. Therefore, in the inside-out coordinate frame the higher velocity pixels sample a larger velocity vector range than in the standard coordinate frame and conversely for the lower velocity pixels. This can be seen clearly by comparing the left and right panels of Figures 3.9.

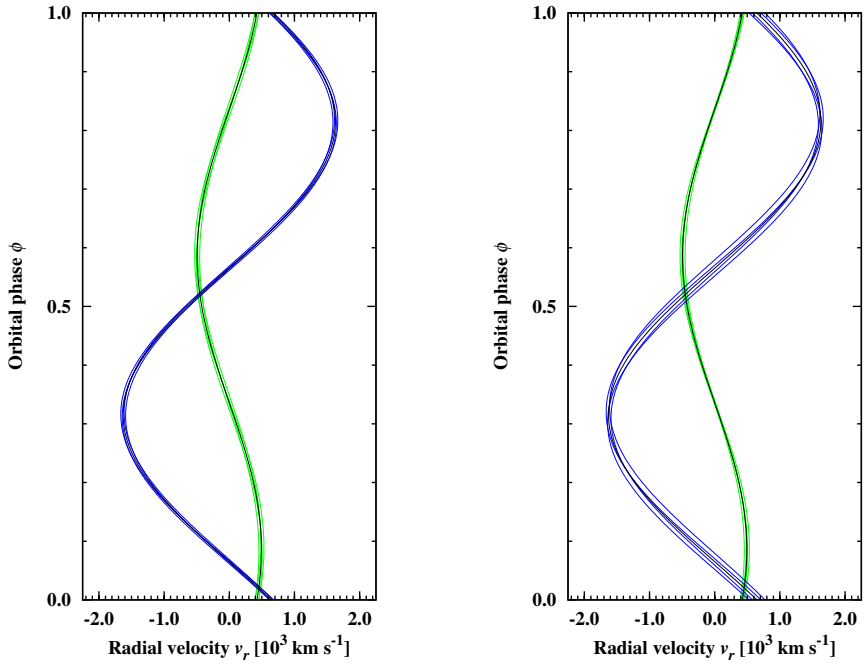

Figure 3.10. Radial velocity curves in velocity-phase space. The left and right panels show the radial velocity v_r curves traced by the centre (solid black lines) and corner (solid green and solid blue lines) velocity coordinates of the example pixels in, respectively, the standard and inside-out coordinate frames (i.e., the left and right panels of Figure 3.9, respectively).

The difference in velocity vector range sampling in the standard and inside-out coordinate frames is further demonstrated by the sinusoidal radial velocity curves traced in the velocity-phase space by velocity coordinates in each coordinate frame. The sinusoidal radial velocity v_r (Equation 2.2) is equally given in polar coordinates, that is,

$$v_r \quad = \quad \gamma - v\cos(\theta + 2\pi\phi), \tag{3.3}$$

where v is the velocity magnitude and θ is the velocity angle of the velocity vector described by the velocity coordinate. Figure 3.10 shows the radial velocity curves traced by the centre and corner velocity coordinates of the lower velocity (green) pixel and the higher velocity (blue) pixel. Each of these velocity coordinates has a different sinusoidal amplitude and phase-offset. This is seen in the five radial velocity curves traced for each pixel in both the standard and inside-out coordinate frames. The ranges in the amplitudes and phase-offsets of opposite pixel corners are, respectively, the ranges in velocity magnitude dv and angle $d\theta$. The range in phase-offset, however, plays a larger role in determining the total area bounded by a pixel in velocity-phase space. A pixel with a larger $d\theta$ therefore bounds a

larger area in velocity-phase phase compared to a pixel with a smaller $d\theta$. In the standard coordinate frame lower velocity pixels with larger $d\theta$'s therefore represent the flux from a larger area in the trailed spectra than higher velocity pixels with smaller $d\theta$'s. Conversely, in the inside-out coordinate frame higher velocity pixels with larger $d\theta$'s represent the flux from a larger area in the trailed spectra than lower velocity pixels with smaller $d\theta$'s. The implications of this are highlighted in Section 3.5 and Chapter 4.

3.4 Inside-out Doppler tomography code: doptomog

Spruit (1998) presented a fast maximum entropy (FME) Doppler mapping code (`dopmap`) for constructing standard Doppler tomograms of CVs. The `dopmap` code uses the FME algorithm discussed in Section 2.1.4. It is a well established code that has been referenced in ~ 60 refereed articles in the period February 1999 to February 2017. This code consists of two Fortran 77 programs. The main calculation program `dop` performs the Doppler tomography. The output of `dop` includes the calculated standard tomogram as well as the reconstructed spectra. The program `lobe` calculates spatial and velocity profiles of the Roche lobe of the secondary and a single particle ballistic trajectory based on the mass ratio q of the binary. Its output is used in the model velocity profile overlay which can be added to the tomogram to assist with the interpretation of the calculated emission distribution. The code also includes a number of Interactive Data Language (IDL) scripts. One of these scripts, `foldspec`, is used to phase-fold the input spectra and, if necessary, to interpolate each spectrum to the same wavelength range and resolution. The script `dopin` is used to extract a specified emission (or absorption) line from the phase-folded input spectra. The scripts `dopmap` and `stream` are used to visualise the input and output produced by the code, that is to say, the trailed input and reconstructed spectra as well as the standard tomogram with (or without) an applicable model velocity profile overlay in a cartesian coordinate frame.

I have refactored and extended the code described above into a new code which consists of three Fortran 90/95/2003 programs and various IDL and GNUPlot scripts. The program `dop` was refactored into the program `pdoptomog`. This program was extended to calculate tomograms in the standard *and* inside-out velocity coordinate frames. The inside-out tomogram is constructed independently of the standard tomogram by directly projecting the input spectra onto the inside-out velocity coordinate frame. The program `pdoptomog` was also extended to calculate a specified number of consecutive half-phase tomograms and the resulting flux modulation mapping (see Chapter 5). The program `lobe` was refactored into the program `pbinarymodel` which was extended to calculate also the spatial and velocity profiles of the primary. Also, it was extended for non-magnetic CVs to calculate profiles for the 3:1 resonance radius and a specified inner Keplerian radius as the outer and inner edges of the accretion disc, respectively. For magnetic CVs it was extended to calculate magnetic dipole trajectories and to include a simulated magnetic drag force (described in Section 3.1.2.2) in the single particle ballistic trajectory. The functionality of the IDL scripts `foldspec` and `dopin` was refactored into the Fortran program `pspectra`. The scripts

`dopmap` and `stream` were refactored into the scripts `doptomogplotpre` and `doptomogplot`, respectively. These scripts were extended to produce the visualisation of the tomograms, as well as the flux modulation mapping output, in standard and inside-out *polar* coordinate frames. The basic plotting functionality repeated in the scripts `dopmap` and `stream` were refactored into a number of reusable IDL scripts. The GNUPlot script `binarymodel3d` was added for the three-dimensional visualisation of the model spatial profile calculated by the program `pbinarymodel` based on the specified binary parameters. Figure 3.11 shows the main components and a simplified flow of this new refactored and extended code which I named, collectively, the `doptomog` code. In the spirit of open access, I made the `doptomog` code publicly accessible. It can be downloaded from

http://cdsarc.u-strasbg.fr/viz-bin/qcat?J/A+A/595/A47

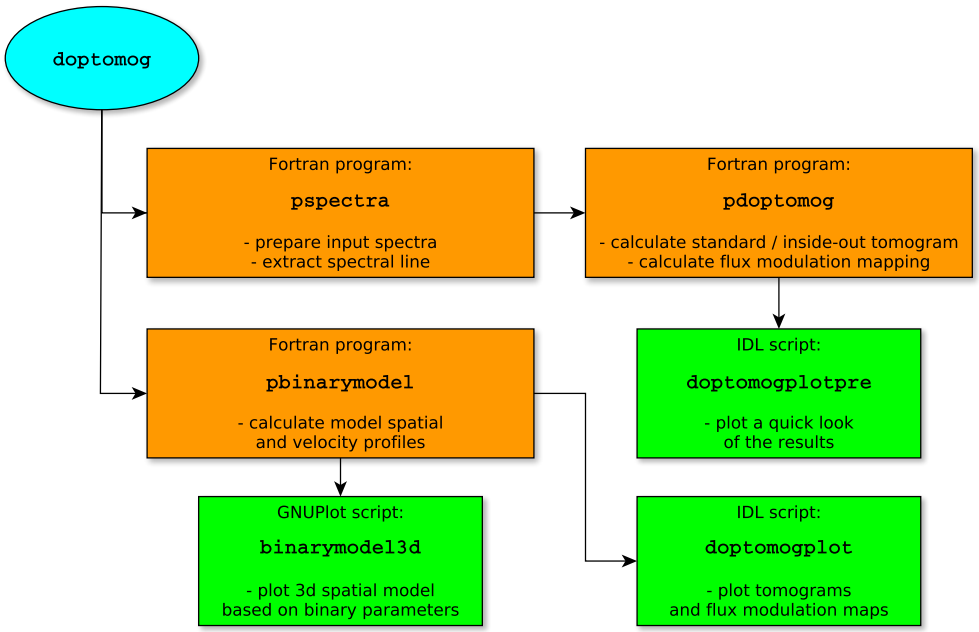

Figure 3.11. Main components of `doptomog`.

3.5 Standard and inside-out Doppler tomography of simulated data

I start the investigation into the inside-out projection technique by applying it to a simulated data set. This allows for a controlled first look at how the technique distributes the fluxes of defined emission components in the inside-out velocity coordinate frame. A typical single emission line profile, like that seen in the spectra of a disc-accreting CV, was calculated by combining simulated line profiles that represent an accretion disc, the bright spot of the stream-disc impact region and the irradiated face of a secondary star. A broad double peaked

profile represents the emission from the disc, while two relatively narrow Gaussian profiles represent the emission from the bright spot and the irradiated secondary. Appropriate phase-dependent Doppler shifts were applied to each simulated line profile based on the binary parameters previously used for the model CV, that is, an orbital period $P_{\rm orb} = 0.125\,{\rm d}\,(3\,{\rm hr})$, a primary mass $M_1 = 0.85\,M_\odot$, a mass ratio $q = 0.2$ and an inclination angle $i = 75°$. All the simulated line profiles, that is, the spectra, include some artificial random noise. The data set consists of 50 phase-resolved simulated spectra and each spectrum has 100 velocity points in the radial velocity range used ($n = 5000$, i.e., the number of spectra times the number of velocity points in each spectrum).

I used the `doptomog` code described in Section 3.4 to perform standard and inside-out Doppler tomography on the simulated spectra of the model CV described above. In Sections 3.5.1 and 3.5.2 I show the results centred on the rest frames of, respectively, the *binary* and the *primary*. The normalised standard and inside-out tomograms are shown for each scenario. The model velocity profile overlay shown in all the tomograms was calculated using the same system parameters listed above. Also shown are the trailed normalised input and reconstructed spectra, as well as *absolute* input-minus-reconstructed (O − C) residuals. The input and reconstructed spectra are normalised by the maximum flux in the input spectra. The absolute O − C spectra are shown in order to have all the displayed trailed spectra on a comparable colour scale. The relative success the two projection techniques have in reproducing the features in the input spectra is measured by means of a simple root mean square (rms) value of the residuals, that is,

$$\mathrm{rms} = \sqrt{\frac{1}{n}\sum_{i=1}^{n}(\mathrm{O}_i - \mathrm{C}_i)^2}, \tag{3.4}$$

where n is the total number of data points.

All the standard and inside-out tomograms, in this section and the rest of this thesis, were constructed using 3996 discrete velocity bins (pixels). I choose a slightly higher value for the regularisation parameter α, that is, 0.003 as opposed to the default value of ~ 0.002, as described by Spruit (1998). This was used for all the tomograms, standard and inside-out, so that all are on the same comparable measure of regularisation. Also, it produces solutions that reproduce the detail in the observed spectra, but it does not over-fit the noise.

3.5.1 Doppler tomography centred on the rest frame of the binary

Figure 3.12 shows the standard and the inside-out Doppler tomography based on the simulated spectra of the model CV described above. The tomograms are centred on the rest frame of the binary.

Trailed spectra: The three simulated emission features are easily distinguished in the trailed input spectra (middle panel of Figure 3.12). The emission from the disc presents as two broad features, one redshifted and the other blueshifted. Because the disc is centred

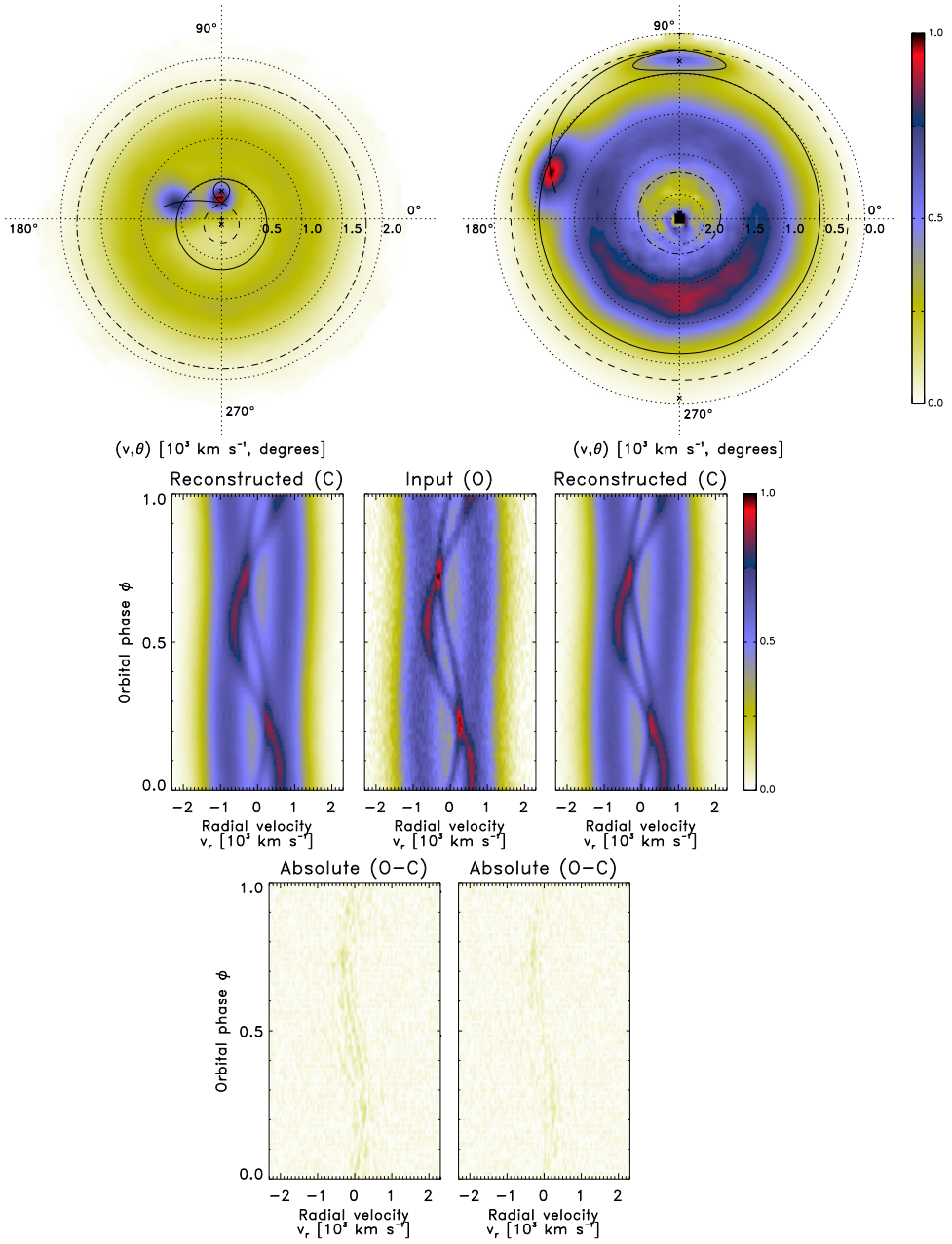

Figure 3.12. Doppler tomography of a simulated CV: centred on the rest frame of the binary. The standard and inside-out tomograms are shown in the top left and right panels, respectively. The middle panel shows the trailed input spectra with the trailed reconstructed spectra for the corresponding tomogram to the left and right of it. The bottom left and right panels show the trailed absolute residual spectra for the corresponding tomogram. The rms values of the standard and inside-out residuals (i.e., absolute O − C) are 0.087 and 0.078, respectively. See Section 3.5.1 for more details.

on the primary the whole double-peaked profile of the disc executes an S-wave due to the orbital motion of the primary. The higher the mass ratio q in the binary the more noticeable

this 'wobble' is in the trailed spectra (e.g., see middle panel of Figure 4.3 for a system with $q \sim 0.5$). The emissions from the secondary and bright spot are the narrow low- and mid-velocity features, respectively.

For both the standard and the inside-out projections all three emission features seen in the input spectra are reproduced in the respective trailed reconstructed spectra (panels to the left and right of the middle panel of Figure 3.12). This is confirmed by a visual inspection of the trailed absolute O − C spectra (bottom panels of Figure 3.12). The rms value of the standard projection residuals is 0.087 while that of the inside-out projection residuals is 0.078. The inside-out projection therefore has a slightly better level of success than the standard projection in reproducing the input spectra for this scenario. This is primarily due to the inside-out projection producing a better reconstruction of the lower velocity emission components such as the secondary and bright spot (see discussion below).

Tomograms: The binary's centre of mass, marked with a plus (+), is at the centre of the standard tomogram (top left panel of Figure 3.12). In the inside-out tomogram (top right panel of Figure 3.12), however, the binary's centre of mass is effectively the zero velocity outer circumference while the centre of the disc is marked with an asterisk (∗) only partially visible on the 90°-line above the centre discontinuity. In both tomograms the centres of mass of the primary and secondary are marked with crosses (×). Overlays are shown for the Roche lobes of the primary (dashed line), the secondary (solid line) and a single particle ballistic trajectory (solid line) from the L_1 point up to 30° in azimuth around the primary. Also shown are the 3:1 resonance radius as the outer edge of the disc (solid circle) and an inner Keplerian radius (dot-dashed line) based on an absolute radial velocity of $1800\,\mathrm{km\,s^{-1}}$, that is, the maximum absolute radial velocity seen in the emission line variations.

Most striking in the standard tomogram are the two bright emission regions at the locations of the irradiated face of the secondary and the bright spot of the stream-disc impact region. The emission from the secondary dominates the brightness scale of the tomogram. The ring-like feature seen in the tomogram corresponds to the emission from the disc. The disc's higher velocity emission, that is to say, that from closer to the inner part of of the disc, is only discernible up to velocities $\sim 1500\,\mathrm{km\,s^{-1}}$.

In the inside-out tomogram the brightness distribution between the emission features has changed significantly compared to the standard tomogram. This can be understood in terms of the discussion in Section 3.3. In the inside-out tomogram lower velocity emissions are distributed over more pixels covering a larger surface area further from the centre of the tomogram. Conversely, higher velocity emissions are compacted into fewer pixels covering a smaller surface area closer to the centre of the tomogram. It is important to note that despite the change in the brightness distribution the total integrated brightness of the various emission features is the same in both tomograms.

As expected from the model velocity profile presented in Figure 3.6 the emission of the secondary is now located on the outside of the disc in the inside-out tomogram. However, this emission is now distributed over more pixels and consequently it is less bright (i.e., it has a smaller maximum brightness) than in the standard tomogram. The emission from

the bright spot is still projected on the disc's outer edge. Even though this emission is also distributed over more pixels it now dominates the brightness scale of the tomogram. The projection of the secondary and bright spot emissions into more pixels gives them an increased velocity resolution compared to the standard projection. This allows these features to be reproduced with greater accuracy in the reconstructed spectra.

The emission from the disc is still a ring-like feature in the inside-out tomogram. However, the disc's radial emission profile has changed from a more even distribution in the standard tomogram to a more inner disc concentration. In the standard tomogram the disc's higher velocity emission is distributed over more pixels covering a larger surface area in the tomogram, but in the inside-out tomogram this emission is compacted into fewer pixels closer to the centre of the tomogram and hence it appears brighter. This is perhaps more consistent with what is expected from disc emission, that is, the hotter inner disc is brighter even though the emitting area in the inner edges is much smaller than that in the outer edges of the disc. Overall, the whole disc is brighter in the inside-out tomogram than in the standard tomogram.

As noted previously the Keplerian velocity centre of the disc is offset from the origin of the tomogram by an amount corresponding to the orbital velocity of the primary. In a standard tomogram this typically results in an asymmetric artefact for a disc with an even circular emission distribution in which it appears that at lower velocities the part of the disc in the upper half of the tomogram contains more emission, that is to say, it appears brighter than the part in the lower half of the tomogram. This type of artefact arises because the same level of emission is being projected into fewer pixels closer to the origin of the tomogram for the upper half of the disc compared to the lower half. However, given that the simulated binary's mass ratio is only 0.2 and that the emission from the secondary dominates the low-velocity part of the tomogram, this artefact is diminished in the standard tomogram of this simulation. In the inside-out tomogram, however, for velocities $> 1000\,\mathrm{km\,s^{-1}}$ it appears that the lower half of the disc contains more emission than the upper half. As noted for the standard tomogram, the offset in the Keplerian velocities of the disc results in an asymmetric artefact. However, in the inside-out tomogram the effect of the offset is clearly seen due to the brightening of the higher velocity pixels closer to the centre of the tomogram. This brightening of high-velocity pixels also enhances the high-velocity ($> 2000\,\mathrm{km\,s^{-1}}$) noise present at the edge of the spectra.

3.5.2 Doppler tomography centred on the rest frame of the primary

Figure 3.13 shows the standard and the inside-out Doppler tomography centred on the rest frame of the primary. In order to centre the tomograms on the rest frame of the primary the orbitally phased velocity of the primary ($K_1 \sim 69\,\mathrm{km\,s^{-1}}$; phase zero offset ~ 0.0) was subtracted from the original simulated phase-resolved spectra.

Trailed spectra: As expected, the disc's double peak emission has been 'straightened' in the trailed input spectra (middle panel of Figure 3.13), that is, with the orbital velocity

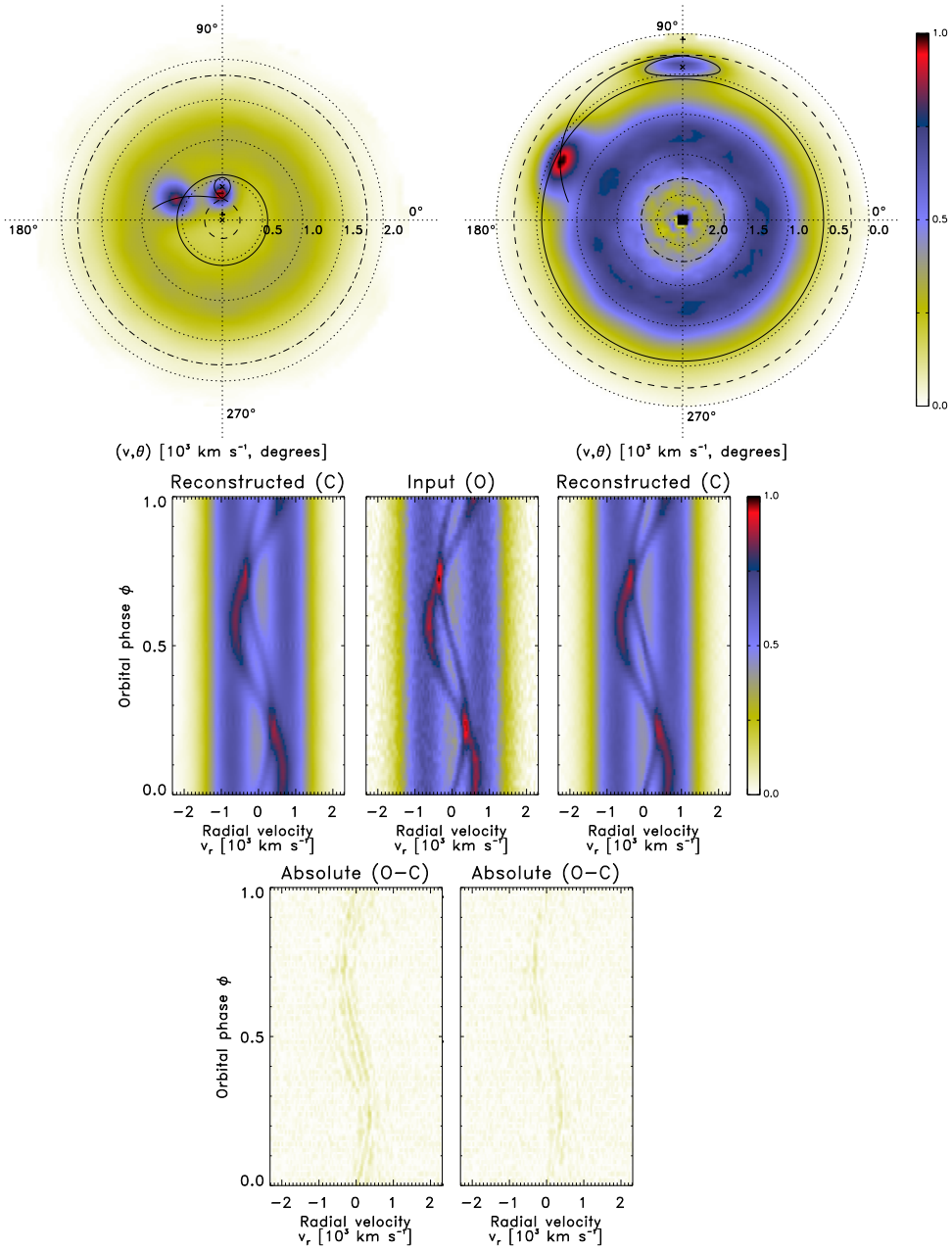

Figure 3.13. Doppler tomography of a simulated CV: centred on the rest frame of the primary. Same layout as Figure 3.12. The rms values of the standard and inside-out residuals (i.e., absolute O − C) are 0.078 and 0.066, respectively. See Section 3.5.2 for more details.

of the primary removed, emission from a given radius in the disc shows a constant radial velocity in the trailed spectra. All three emission features seen in the trailed input spectra are reproduced in the trailed reconstructed spectra of both the standard and the inside-out projections (panels to the left and right, respectively, of the middle panel of Figure 3.13). There is a noticeable improvement in the rms values of both sets of residuals (bottom panels

of Figure 3.13). For the standard projection residuals the rms value is 0.078 while the inside-out projection residuals have an rms value of 0.066. The inside-out projection again has a slightly better level of success than the standard projection in reproducing the input spectra.

Tomograms: The primary's centre of mass is now the zero velocity origin in the standard tomogram (top left panel of Figure 3.13) while the binary's centre of mass is the plus (+) on the 90°-line. The disc is now centred in the tomogram and it appears slightly brighter than in the tomogram centred on the rest frame of the binary. The emissions from the secondary and bright spot still dominate the brightness scale of the standard tomogram.

In the inside-out tomogram (top right panel of Figure 3.13) the primary's centre of mass is now effectively the zero velocity outer circumference while the binary's centre of mass is the plus (+) on the 90°-line. The disc is also centred in the inside-out tomogram and, as expected, the asymmetric artefact previously seen in the disc emission is no longer present.

Chapter 4

Exploring inside-out Doppler tomography

There are more things in Heaven and Earth, Horatio, than are dreamt of in your philosophy.

– William Shakespeare, *Hamlet*, Act I, Scene 5

I introduced inside-out Doppler tomography, a new technique for constructing Doppler tomograms in inside-out velocity coordinates, in the previous chapter (Chapter 3). In this chapter I pursue an investigation into the application of this new technique. The main aim of the investigation is to establish if the inside-out velocity projection can reveal details in the tomogram not exposed by the standard velocity projection.

Various sets of spectra from real CVs and mCVs are employed to aid in the investigation. These were selected for the distinct accretion features that are apparent in their trailed spectra and that are exposed through standard Doppler tomography. For example, the standard tomogram of the non-eclipsing dwarf nova WZ Sge (e.g., Spruit & Rutten 1998) shows a prominent accretion disc and bright spot where the ballistic accretion stream impacts the outer edge of the disc while the standard tomogram of the eclipsing dwarf nova IP Peg (e.g., Steeghs et al. 1997; Harlaftis et al. 1999) shows a prominent spiral structure in its accretion disc. The emission associated with a ballistic accretion stream is very prominent in the standard tomogram of the eclipsing polar HU Aqr (Schwope et al. 1997b). On the other hand, in the standard tomogram of the non-eclipsing polar V834 Cen (Potter et al. 2004) emission associated with a magnetically confined accretion flow is prominent. The standard spin-cycle tomograms of the intermediate polar PQ Gem (Hellier 1997, 1999) exclusively show emission associated with a magnetically confined accretion flow locked on the spin period of the primary.

I showcase the results of applying the inside-out projection to the Doppler tomography of the dwarf novae WZ Sge (Section 4.1) and IP Peg (Section 4.2) alongside the results of the standard projection. I do the same for the Doppler tomography of the polars HU Aqr (Section 4.3), V834 Cen (Section 4.4) and the intermediate polar PQ Gem (Section 4.5).

The `doptomog` fast maximum entropy Doppler tomography code described in Section 3.4 was used to construct all the tomograms, standard and inside-out, presented hereafter. The results of the Doppler tomography are presented in the same layout established in Section 3.5. Shortened versions of the sections in this chapter have been published as parts of two articles in *Astronomy & Astrophysics* (Kotze et al. 2015, 2016).

4.1 WZ Sge: a non-eclipsing dwarf nova

WZ Sge is a prototypical member of the CV subclass referred to as WZ Sge-type dwarf novae (Bailey 1979). Doppler tomography of WZ Sge (e.g., Spruit & Rutten 1998) has revealed a prominent accretion disc and bright spot where the ballistic accretion stream impacts the outer edge of the disc. This makes it an ideal first real test case for inside-out Doppler tomography. The tomography is based on the Hα emission line from spectroscopic observations included with the original fast maximum entropy Doppler tomography code described by Spruit (1998). There are 17 spectra and each spectrum has 82 velocity points in the extracted radial velocity range around the Hα emission line ($n = 1394$). The model velocity profile overlay shown in all the tomograms was calculated using the orbital period $P_{\rm orb} = 0.056687846\,{\rm d}\,(\sim 82\,{\rm min})$ determined by Patterson et al. (1998), the inclination angle $i = 77^\circ$ obtained by Spruit & Rutten (1998) and the mass parameters preferred by Steeghs et al. (2007), that is, a primary mass $M_1 = 0.85 M_\odot$ and a mass ratio $q = 0.09$.

4.1.1 Doppler tomography centred on the rest frame of the binary

The standard and inside-out Doppler tomography results for WZ Sge in quiescence are shown in Figure 4.1. The tomograms are centred on the rest frame of the binary.

Trailed spectra: Two distinct emission components are visible in the trailed input spectra (middle panel of Figure 4.1). The first component presents as two prominent broad features, one redshifted and the other blueshifted. This component is associated with emission from the accretion disc. The second component is less prominent and is seen in the red-to-blue crossover at phase 0.3 and again in the blue-to-red crossover at phase 0.8. This component is associated with the emission from the bright spot where the ballistic accretion stream impacts the disc. All the emission features in the trailed input spectra are reproduced in the trailed reconstructed spectra of both the standard and the inside-out projections (panels to the left and right, respectively, of the middle panel of Figure 4.1). Both sets of residuals (bottom panels of Figure 4.1) have an rms value of 0.164.

Tomograms: In the standard tomogram (top left panel of Figure 4.1) the binary's centre of mass, marked with a plus (+), is at the centre of the tomogram. In the inside-out tomogram (top right panel of Figure 4.1) the binary's centre of mass is effectively the zero velocity outer circumference while the centre of the disc is hidden behind the centre discontinuity. The centres of mass of the primary and secondary are marked with crosses ($\times$) in both tomograms. Overlays are shown for the Roche lobes of the primary (dashed line), the

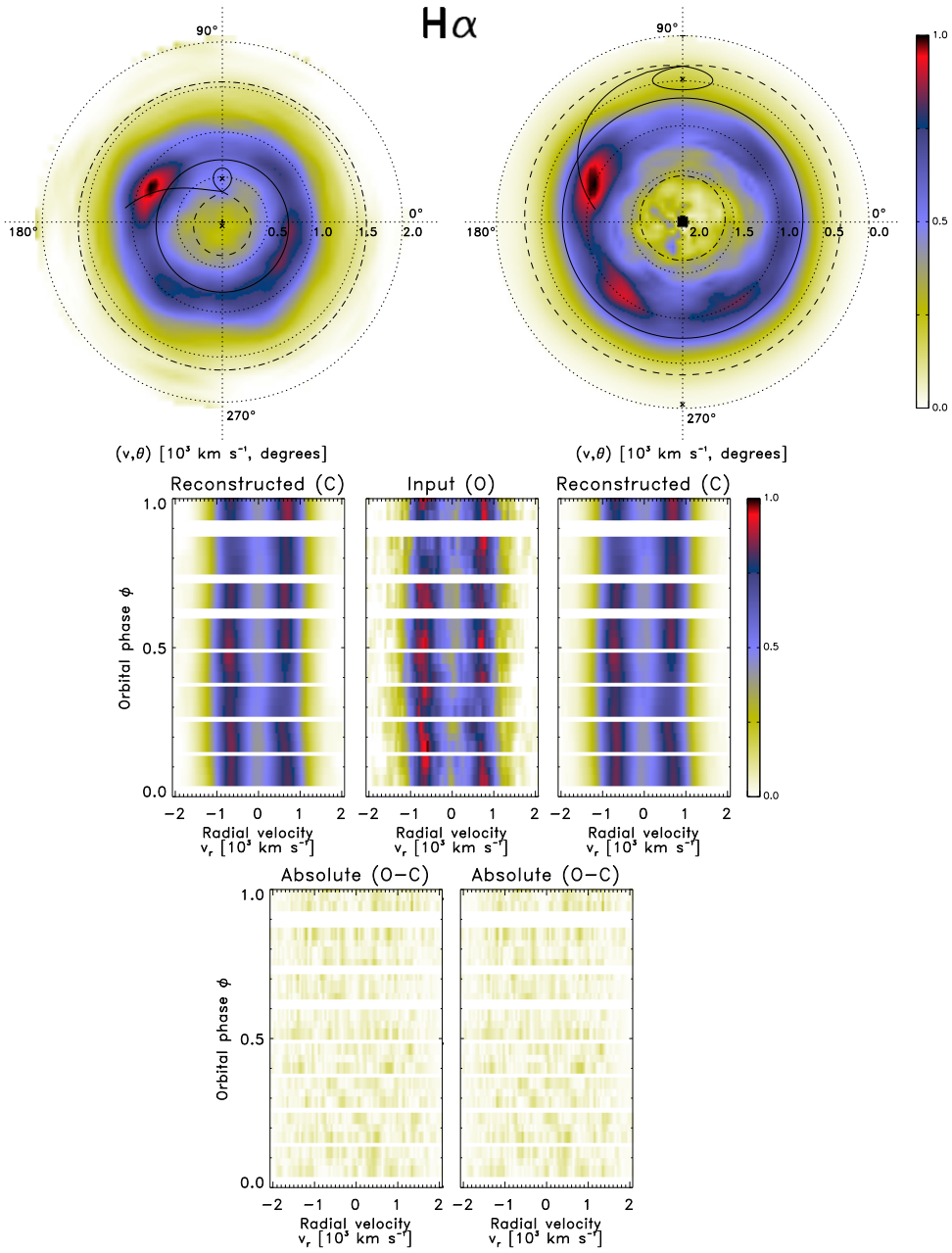

Figure 4.1. Doppler tomography of WZ Sge: centred on the rest frame of the binary. The standard and inside-out tomograms are shown in the top left and right panels, respectively. The middle panel shows the trailed input spectra with the trailed reconstructed spectra for the corresponding tomogram to the left and right of it. The bottom left and right panels show the trailed absolute residual spectra for the corresponding tomogram. Both the standard and inside-out residuals (i.e., absolute O − C) have an rms value of 0.164. See Section 4.1.1 for more details.

secondary (solid line) and a single particle ballistic trajectory (solid line) from the L_1 point up to 45° in azimuth around the primary. Also shown are the 3:1 resonance radius as the

outer edge of the disc (solid circle) and an inner Keplerian radius (dot-dashed line) based on an absolute radial velocity of 1600 km s^{-1}, that is, the maximum absolute radial velocity seen in the emission line variations.

The most distinct features in the standard tomogram are the relatively bright accretion disc and the bright spot of the impact region between the ballistic stream and disc. The disc appears brighter around the assumed outer edge (velocities $< 1000\,\mathrm{km\,s^{-1}}$) while it becomes more diffused towards the assumed inner edge (velocities $> 1000\,\mathrm{km\,s^{-1}}$). The extended nature of the bright spot (stream impact region) in velocity coordinates is considered to be the result of the mixing of stream and disc material with different velocities (Marsh et al. 1990). The model stream lines up well with the brightest part of the impact region located at (820 km s^{-1}, 150°). There is only a slight enhancement in the emission at the expected velocity of the secondary (400 km s^{-1}, 90°).

In the inside-out tomogram the brighter disc emission is now occurring at generally higher velocities ($> 1000\,\mathrm{km\,s^{-1}}$). Due to the effect of the off-centre projection of the disc there is a slight enhancement in the brightness of the disc in the lower half. Although given WZ Sge's low mass ratio this effect is fairly minimal. Similar to the standard tomogram the bright spot (stream impact region) also dominates the brightness scale of the inside-out tomogram. However, it is now located towards the disc's outer edge in velocity coordinates and has acquired an extended enhancement in the lower left quadrant covering (1000 km s^{-1}, 180 − 250°). The brightest part of the impact region it is now located at (1050 km s^{-1}, 165°), a slightly different velocity position than in the standard tomogram. This shift is caused by the redistribution of the relative contrast levels throughout the tomogram. The model stream, however, still lines up well with the brightest part of the impact region. The secondary is not discernible within the low-velocity emission covering ($0 - 700\,\mathrm{km\,s^{-1}}$, 0 − 360°). This is expected because it was barely discernible in the standard tomogram and is projected into more pixels in the inside-out tomogram. Similar to the simulated system in Section 3.5, the high-velocity ($\sim 2000\,\mathrm{km\,s^{-1}}$) noise present at the edge of the spectra is enhanced by the brightening of the high-velocity pixels around the centre of the tomogram.

4.1.2 Doppler tomography centred on the rest frame of the primary

Figure 4.2 shows the standard and the inside-out Doppler tomography centred on the rest frame of the primary. The orbitally phased velocity of the primary ($K_1 \sim 47\,\mathrm{km\,s^{-1}}$; phase zero offset ~ 0.12; Steeghs et al. 2007) was subtracted from the original phase-resolved spectra in order to centre the tomograms on the rest frame of the primary.

Trailed spectra: Given the relatively low velocity of the primary with which the spectra were shifted, the 'straightening' of the double peak emission from the disc in the trailed input spectra (middle panel of Figure 4.2) is less pronounced compared to the case of the simulated system in the previous section. The trailed reconstructed spectra (panels to the left and right of the middle panel of Figure 4.2) of both projections reproduce all the emission features in the trailed input spectra. The rms values of both sets of residuals (bottom panels

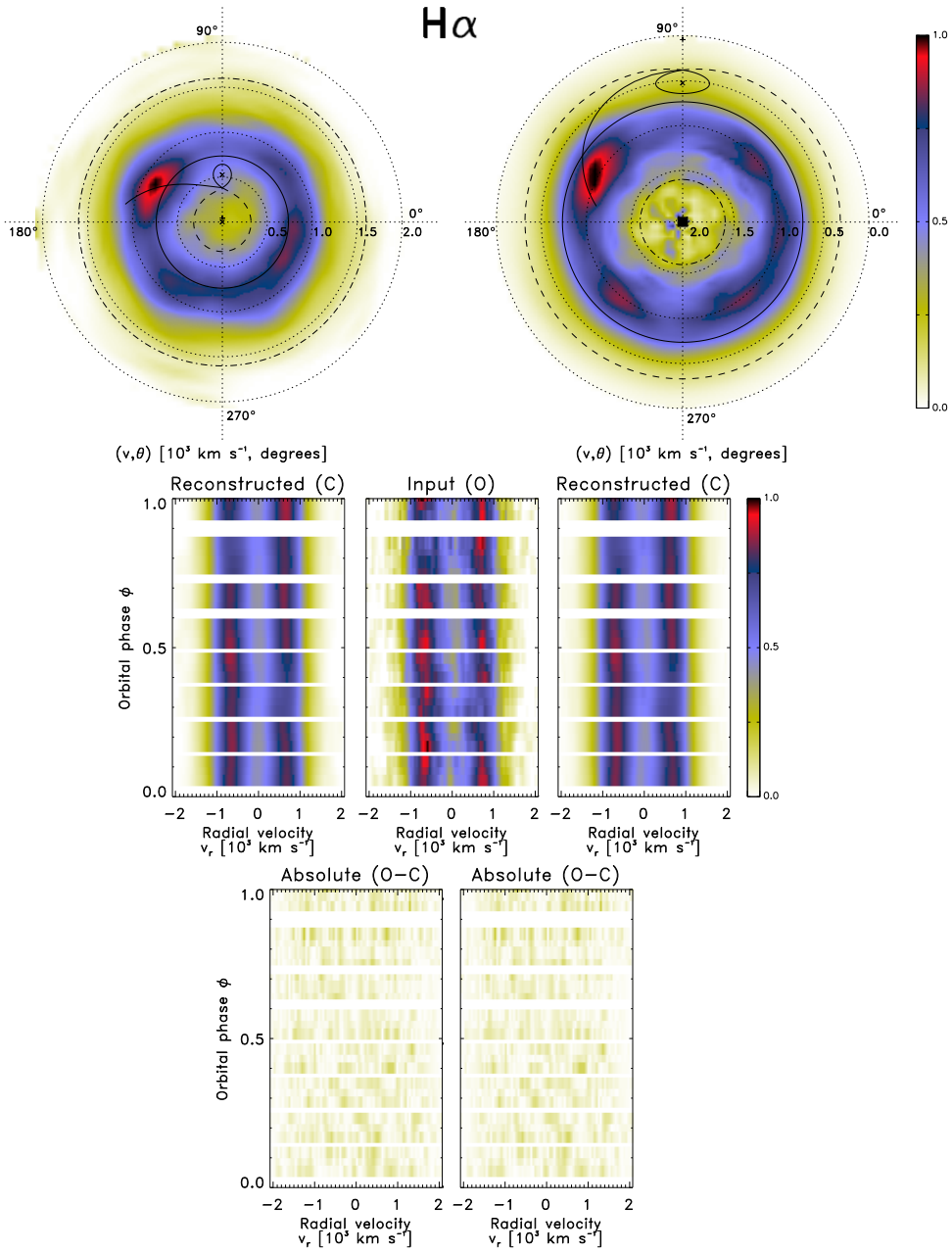

Figure 4.2. Doppler tomography of WZ Sge: centred on the rest frame of the primary. Same layout as Figure 4.1. Both the standard and inside-out residuals (i.e., absolute O − C) have an rms value of 0.160. See Section 4.1.2 for more details.

of Figure 4.2) show only a marginal improvement to 0.160.

Tomograms: In the standard tomogram (top left panel of Figure 4.2) the primary's centre of mass is now the zero velocity origin while the binary's centre of mass is the plus (+) on the 90°-line. Due to the relatively low mass ratio of WZ Sge ($q \sim 0.1$) there is not a significant change in the emission distribution of the standard tomogram.

The primary's centre of mass is now effectively the zero velocity outer circumference in the inside-out tomogram (top right panel of Figure 3.13) while the binary's centre of mass is the plus (+) on the 90°-line. With the effect of the off-centre projection of the disc removed a more uniform circularly symmetric appearance of the disc is recovered. The extended enhancement of the bright spot in the lower left quadrant covering ($1000\,\mathrm{km\,s^{-1}}$, $180-250°$) is also less pronounced. It is, however, not possible to trace its origin unequivocally in the trailed spectra and is therefore probably not a real emission feature.

4.2 IP Peg: an eclipsing dwarf nova

IP Peg is an eclipsing member of the dwarf nova subclass of CVs. Outbursts lasting $10-12$ days occur every $70-100$ days during which it brightens by $2-3$ magnitudes. The spiral shocks observed in the accretion disc of IP Peg during an outburst (Steeghs et al. 1997) favour the disc instability model (Osaki 1974) as the cause of the recurrent outbursts. Because the disc expands during the outburst the outer disc will experience an increased gravitational attraction from the secondary. This causes perturbations in the circular Keplerian orbits of the disc material in the outer disc, leading to the formation of spiral arms in the disc. The spiral structure in the accretion disc of IP Peg makes it an ideal test case for inside-out Doppler tomography. The tomography is based on the He II λ4686 emission line from the 1996 November spectroscopic observations taken during outburst maximum. These observations were presented first by Harlaftis et al. (1999) and the reader is referred to that paper for a detailed description of the data set and reduction procedures. The data set, courtesy of Danny Steeghs, consists of 61 spectra that cover the orbital phase range $0.09-0.86$ with smallish gaps around phases 0.3 and 0.57. The spectra are evenly spaced and each spectrum has 119 velocity points in the extracted radial velocity range around the He II λ4686 emission line ($n = 7259$). The binary system parameters as calculated by Copperwheat et al. (2010), that is, an orbital period $P_{\mathrm{orb}} = 0.1582061029\,\mathrm{d}$ ($\sim 228\,\mathrm{min}$), a primary mass $M_1 = 1.16 M_\odot$, a mass ratio $q = 0.48$ and an inclination angle $i = 83.8°$ were used to calculate the model velocity profile overlay shown in all the tomograms.

4.2.1 Doppler tomography centred on the rest frame of the binary

Figure 4.3 shows the standard and the inside-out Doppler tomography for IP Peg during outburst maximum. The tomograms are centred on the rest frame of the binary.

Trailed spectra: The trailed input spectra (middle panel of Figure 4.3) display a very complex structure (Harlaftis et al. 1999). The most distinct emission component is the broad asymmetric feature with a prominent narrowing at phase 0.5. This component is associated with emission from the accretion disc. Another obvious emission component is the bright narrow component with a low-velocity amplitude and a red-to-blue crossover at phase 0.5. This component is associated with emission from the irradiated secondary. The complex structure in the trailed input spectra is fairly well reproduced in the respective

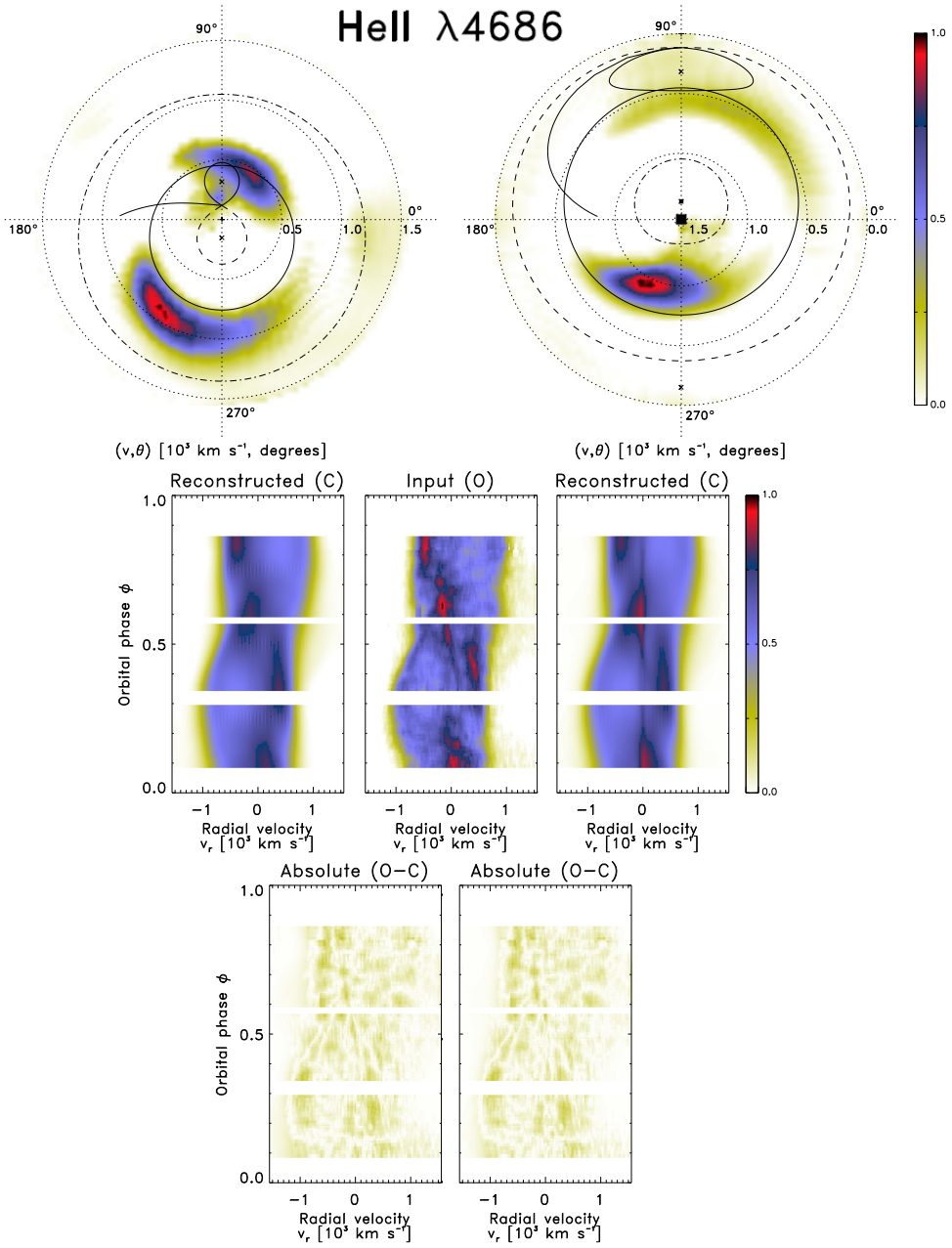

Figure 4.3. Doppler tomography of IP Peg: centred on the rest frame of the binary. Same layout as Figure 4.1. Only the non-axisymmetric emission, that is to say, the remaining emission after subtracting the axisymmetric average of the emission at each radius around the centres of the tomograms, is shown. The rms values of the standard and inside-out residuals (i.e., absolute O − C) are 0.135 and 0.130, respectively. See Section 4.2.1 for more details.

trailed reconstructed spectra of both the standard and the inside-out projections (panels to the left and right, respectively, of the middle panel of Figure 4.3). The inside-out projection, however, reproduces a spurious stationary feature at zero velocity that is not apparent in

the input spectra. The standard projection residuals (bottom left panel of Figure 4.3) have an rms value of 0.135 while the inside-out projection residuals (bottom right panel of Figure 4.3) have a value of 0.130.

Tomograms: The binary's centre of mass, marked with a plus (+), is at the centre of the standard tomogram (top left panel of Figure 4.3). In the inside-out tomogram (top right panel of Figure 4.3) the binary's centre of mass is effectively the zero velocity outer circumference while the centre of the disc is marked with an asterisk (∗) on the 90°-line above the centre discontinuity. In both tomograms the centres of mass of the primary and secondary are marked with crosses (×). Overlays are shown for the Roche lobes of the primary (dashed line), the secondary (solid line) and a single particle ballistic trajectory (solid line) from the L_1 point up to 45° in azimuth around the primary. Also shown are the 3:1 resonance radius as the outer edge of the disc (solid circle) and an inner Keplerian radius (dot-dashed line) based on an absolute radial velocity of $1200\,\mathrm{km\,s^{-1}}$, that is, the maximum absolute radial velocity seen in the emission line variations.

In the standard tomogram the emission from the leading side of the irradiated secondary is seen as a bright spot at ($200\,\mathrm{km\,s^{-1}}$, 95°) which appears to be 'inside' the disc. There is also a low-velocity component visible at ($0-300\,\mathrm{km\,s^{-1}}$, 140 − 250°). This low-velocity component has been seen in other dwarf novae during outburst, but its origin is not understood (Steeghs et al. 1996). The origin of the high-velocity component seen as a diffuse patch of emission at ($1000-1500\,\mathrm{km\,s^{-1}}$, 0°) is also uncertain. The tomogram is dominated by the emission from the shocks in the accretion disc that creates an extended two-armed spiral structure. The two spiral shocks have a clear asymmetry in both brightness and velocity. The observed velocity asymmetry of the material in the shocks suggests a highly non-Keplerian flow in the disc because circular rings of emission are expected from a purely Keplerian disc. The shocks appear to be spiralling 'outwards' from lower to higher velocities. The upper spiral shock extends to velocities lower than our velocity profile overlay of the outer disc radius. This supports the suggestion by Steeghs et al. (1997) that the disc possibly expanded beyond its tidal radius early on in the outburst as a result of it being triggered by a disc instability.

The mass ratio of IP Peg is fairly high ($q \sim 0.5$). Consequently the primary's centre of mass is significantly offset from the binary's centre of mass. In the inside-out tomogam this can be clearly seen in the offset of the model overlay with respect to the centre of the tomogram. As expected the secondary is seen as an extended diffuse patch of emission 'outside' the disc in the inside-out tomogam. However, the low-velocity component visible at ($0-300\,\mathrm{km\,s^{-1}}$, 140 − 250°) in the standard tomogram is no longer discernible. The high-velocity patch of emission at ($1000-1500\,\mathrm{km\,s^{-1}}$, 0°) has become more enhanced and compact given its new projection closer to the origin. The two-armed spiral structure associated with the shocks in the disc is still clearly present in the inside-out tomogram. However, the asymmetry in the brightness of the shocks caused by the off-centre projection of the disc is more pronounced than in the standard tomogram. The upper shock is more extended and diffuse while the lower shock is more compact and brighter.

4.2.2 Doppler tomography centred on the rest frame of the primary

Figure 4.4 shows the standard and the inside-out Doppler tomography centred on the rest frame of the primary. In order to centre the tomograms on the rest frame of the primary the orbitally phased velocity of the primary ($K_1 \sim 152\,\mathrm{km\,s^{-1}}$; phase zero offset ~ 0.0; Copperwheat et al. 2010) was subtracted from the original simulated phase-resolved spectra.

Trailed spectra: Given the complex structure of the trailed input spectra (middle panel of Figure 4.4) the 'straightening' of the double peak emission from the disc is primarily seen in the blue peak. The trailed reconstructed spectra (panels to the left and right of the middle panel of Figure 4.4) of both projections again reproduce the complex structure in the trailed input spectra fairly well. However, the inside-out projection again reproduces a spurious stationary feature at zero velocity that is not apparent in the input spectra. The rms values of the residuals (bottom panels of Figure 4.4) are unchanged at 0.135 and 0.130 for the standard and the inside-out projections, respectively.

Tomograms: The primary's centre of mass is now the zero velocity origin in the standard tomogram (top left panel of Figure 4.4) while the binary's centre of mass is the plus (+) on the 90°-line. The standard tomogram is still dominated by the emission from the extended two-armed spiral structure. However, the asymmetry in brightness has switched around with the upper shock appearing brighter. The emission associated with the irradiated secondary as well as the low-velocity ($< 300\,\mathrm{km\,s^{-1}}$) component in the upper left quadrant also appear brighter.

In the inside-out tomogram (top right panel of Figure 4.4) the primary's centre of mass is now effectively the zero velocity outer circumference while the binary's centre of mass is the plus (+) on the 90°-line. The secondary has become more compact and brighter. This is because the position of the secondary has moved significantly closer to the centre of the tomogram leading to its enhancement. Similarly, the patch of high-velocity emission at $(1000 - 1500\,\mathrm{km\,s^{-1}}, 0°)$ has become slightly more enhanced. Although the origin of this feature is unknown it is associated with the low brightness emission seen in the input trailed spectra at high radial velocity ($> 1000\,\mathrm{km\,s^{-1}}$) between phases 0.4 and 0.8. In addition an extended low-velocity component is now visible at $(0 - 250\,\mathrm{km\,s^{-1}}, 110 - 150°)$. This low-velocity component is part of the low-velocity component of unknown origin (Steeghs et al. 1996) covering $(0-300\,\mathrm{km\,s^{-1}}, 140-250°)$ in the standard tomogram. The asymmetry between the brightness of the two shocks caused by the off-centre projection of the disc has also been removed. The spiral nature of the shocks is clearly evident and is more intuitive to interpret in respect that it shows how they begin at the outer edges of the disc and curve inwards towards the primary as they increase in velocity.

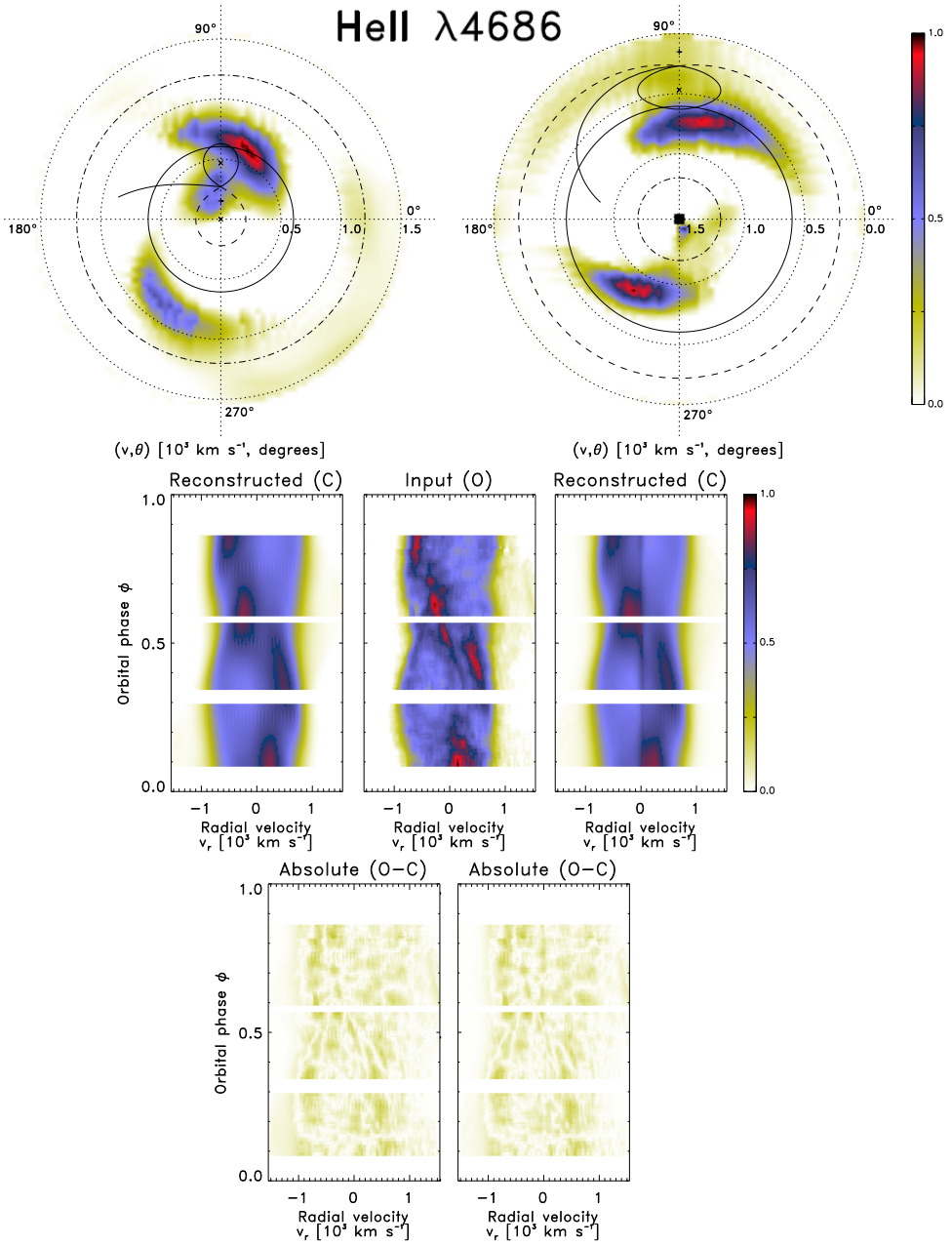

Figure 4.4. Doppler tomography of IP Peg: centred on the rest frame of the primary. Same layout as Figure 4.1. Only the non-axisymmetric emission is shown in the tomograms. The rms values of the standard and inside-out residuals (i.e., absolute O − C) are 0.135 and 0.130, respectively. See Section 4.2.2 for more details. Note that the 'stripy' appearance of the emission distributions in the tomograms is an artefact introduced by the combined effect of subtracting both the orbitally phased velocity of the primary from the input spectra and the axisymmetric average of the emission at each radius around the centres of the tomograms.

4.3 HU Aqr: an eclipsing polar

HU Aqr is a bright eclipsing polar. Standard Doppler tomography of HU Aqr presented by Schwope et al. (1997b) showed an extraordinary prominent ballistic stream, at least compared to other polars, distinct emission from the secondary and a diffuse patch of emission thought to be associated with the magnetically confined accretion flow. HU Aqr is therefore an excellent candidate as a test case for inside-out Doppler tomography.

Figure 4.5 shows the results of applying standard and inside-out Doppler tomography to the He II λ4686 emission line from 1993 August spectroscopic observations of the high accretion state of HU Aqr. These observations were presented first by Schwope et al. (1997b) and the reader is referred to that paper for a description of the data set and reduction procedures. Because HU Aqr is an eclipsing system, a small range around phase 0.0 is excluded and only the 92 spectra covering the orbital phase range $0.06 - 0.97$ are used in constructing the tomograms. The spectra are evenly spaced and each spectrum has 72 velocity points in the extracted radial velocity range around the He II λ4686 emission line ($n = 6624$). The model velocity profile overlay shown in both tomograms is based on one of the models used by Schwope et al. (1997b) with an orbital period $P_{\rm orb} = 0.086820446\,{\rm d}$ ($\sim 125\,{\rm min}$), a primary mass $M_1 = 0.875 M_\odot$, a mass ratio $q = 0.40$ and an inclination angle $i = 84°$.

Trailed spectra: The trailed input spectra (middle panel of Figure 4.5) show three distinct emission components. The first component is the prominent narrow line which is brightest around phase 0.5 and which has zero radial velocity at phase 0.0. This component has a low-velocity amplitude and is associated with emission from the irradiated secondary. The second component is also relatively narrow, but it has a high velocity amplitude. It has a maximum redshift around phase 0.95 and a maximum blueshift around phase 0.45. This component crosses the first component around phases 0.2 and 0.7. The third component is relatively broad and visible throughout the covered phase range. It has a maximum blueshift around phase 0.40. Both the second and third component are associated with emission produced in different parts of the ballistic and magnetically confined accretion flows.

The three distinct line components identified in the trailed input spectra are reproduced fairly well in the trailed reconstructed spectra from both the standard and inside-out tomograms (panels to the left and right, respectively, of the middle panel of Figure 4.5). However, neither of the projections is able to reproduce the observed flux distribution in the prominent narrow line component associated with emission from the irradiated secondary. This is clearly seen in both sets of trailed absolute O − C spectra (bottom panels of Figure 4.5). Overall, the two projections performed equally well in reproducing the input spectra, that is, the residuals of both have rms values of 0.172. In Section 5.3.1 it is shown how the flux modulation mapping technique improves the reproduction of the narrow feature.

Tomograms: In the standard tomogram (top left panel of Figure 4.5) the binary's centre of mass is at the centre of the tomogram, marked with a plus (+). The binary's centre of mass is effectively the zero velocity outer circumference in the inside-out tomogram (top right

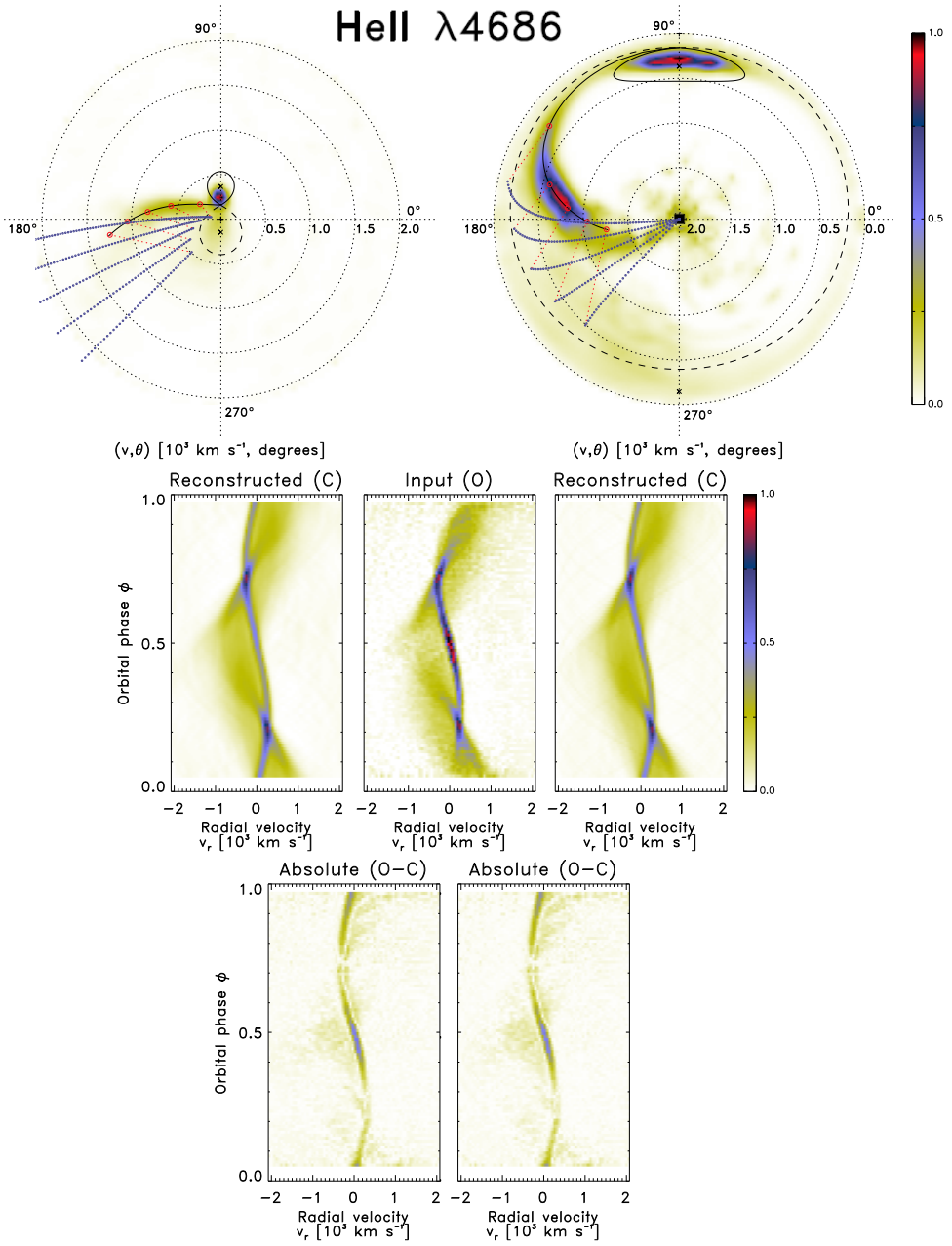

Figure 4.5. Doppler tomography of HU Aqr. Same layout as Figure 4.1. Both the standard and inside-out residuals (i.e., absolute O − C) have an rms value of 0.172. See Section 4.3 for more details.

panel of Figure 4.5). In both tomograms the centres of mass of the primary and secondary are marked with crosses (×). The model velocity profile overlay shown in both tomograms includes the Roche lobes of the primary (dashed line) and the secondary (solid line) as well as a single particle ballistic trajectory from the L_1 point up to 45° in azimuth around the primary (solid line). Magnetic dipole trajectories are calculated at 10° intervals from 5° to

45° in azimuth around the primary (thin dotted lines). The first dipole connection on the ballistic stream (small red circles) is at ($287\,\mathrm{km\,s^{-1}}$, 145°). The first dipole trajectory starts at ($111\,\mathrm{km\,s^{-1}}$, 167°), with consecutive trajectories starting at locations with progressively higher velocities and polar angles. The dipolar axis azimuth and co-latitude, as modelled by Heerlein et al. (1999), are $\sim 38°$ and $\sim 12°$, respectively.

In both the standard and the inside-out tomograms the emission associated with the irradiated secondary is seen as a bright spot at ($360\,\mathrm{km\,s^{-1}}$, 90°). This feature in the tomograms is well traced by the velocity profile of the Roche lobe of the secondary. In the standard tomogram the secondary dominates the brightness scale due to its compact projection. In contrast, its more extended projection in the inside-out tomogram allows other emission features to appear brighter.

In the standard tomogram the emission associated with the ballistic part of the accretion stream is a prominent, slightly downward-sloping horizontal ridge with an apparent relatively constant brightness. However, a closer inspection reveals that at first, as the stream leaves L_1 at ($200\,\mathrm{km\,s^{-1}}$, 90°), it is faint, but it becomes brighter as it reaches ($300\,\mathrm{km\,s^{-1}}$, 135°). It keeps a relatively consistent brightness up to ($750\,\mathrm{km\,s^{-1}}$, 170°) before it starts to become fainter. It stays clearly discernible up to ($1000\,\mathrm{km\,s^{-1}}$, 180°). After this point it becomes more diffused and almost no detail is discernible at velocities above $1000\,\mathrm{km\,s^{-1}}$. In the inside-out tomogram the distribution in brightness along the ballistic stream is more prominent, that is, the lower velocity part is even fainter, whereas the mid- and high-velocity parts are significantly brighter. As in the standard tomogram, the stream appears faint as it leaves L_1 at ($200\,\mathrm{km\,s^{-1}}$, 90°) and it becomes brighter as it reaches ($300\,\mathrm{km\,s^{-1}}$, 135°). It progressively increases in brightness, reaching maximum brightness around ($750\,\mathrm{km\,s^{-1}}$, 170°), before it becomes fainter again. The lower velocity emission appears fainter as the emission is re-binned in a larger area with more pixels. The mid-velocity emission, especially in the range ($500-1000\,\mathrm{km\,s^{-1}}$, $160-180°$), appears brighter because overall the relative contrast levels changed due to the more extended projection of the secondary. Modelling done by Heerlein et al. (1999) on the magnetic stripping of the ballistic stream showed that it is possible for the stream to 'survive' up to a distance of $0.5a$ along its trajectory. This is equivalent to a velocity of $\sim 1250\,\mathrm{km\,s^{-1}}$. It is therefore possible that part of the emission visible in the inside-out tomogram along the extended ballistic trajectory in the velocity range ($1000-1500\,\mathrm{km\,s^{-1}}$, $180-220°$) can be ascribed to the ballistic stream. This tenuous higher velocity ($> 1000\,\mathrm{km\,s^{-1}}$) emission is not clearly discernible in the standard tomogram. Resolving it in the inside-out tomogram is possible as the emission is re-binned in a smaller area with fewer pixels. In both tomograms the brighter part of the ballistic stream is well traced by the modelled velocity profile for the threading region, that is, the region where the ballistic stream is threaded onto the magnetic field lines, but before it leaves the orbital plane.

The diffuse patch of emission seen in the standard tomogram in the velocity range ($0-500\,\mathrm{km\,s^{-1}}$, $180-270°$) is considered to be associated with the magnetically confined accretion flow after it has left the orbital plane. In the inside-out tomogram this

patch of emission is exposed to extend to even higher velocities, covering a velocity range of $(0-1000\,\mathrm{km\,s^{-1}}, 180-270^{\circ})$. Also discernible in the inside-out tomogram is the funnelling of the emission associated with the magnetically confined accretion flow along the dipole trajectories close to the primary at velocities above $1500\,\mathrm{km\,s^{-1}}$. This tenuous higher velocity emission is not discernible in the standard tomogram. It is resolved in the inside-out tomogram because the emission is re-binned in a smaller area with fewer pixels.

4.4 V834 Cen: a non-eclipsing polar

V834 Cen is a bright non-eclipsing polar. Potter et al. (2004) presented standard Doppler tomography of V834 Cen that exposed dominant emission from the secondary and (or) from around L_1, less discernible emission from the ballistic stream and extended diffuse emission considered to be consistent with the magnetically confined accretion flow. In the standard Doppler tomography, however, the lower velocity emission from these components presents as a compact blended, almost blob-like, patch of emission. It is therefore an ideal candidate as a test case to investigate, for example, how inside-out Doppler tomography distributes such compact lower velocity emission.

Figure 4.6 shows standard and inside-out Doppler tomography based on the He II λ4686 emission line from the 2000 August spectroscopic observations of V834 Cen presented by Potter et al. (2004). The reader is referred to that paper for more information on the data set and reduction procedures. All 59 spectra from the original data set, which covers the whole orbital phase range, are used in constructing the tomograms. Each spectrum covers 0.05 of the phase with some overlap and has 73 velocity points in the extracted radial velocity range around the He II λ4686 emission line ($n = 4307$). The model velocity profile overlay shown in both tomograms is based on the model used by Potter et al. (2004) with an inclination angle $i = 50^{\circ}$, a primary mass $M_1 = 0.85 M_{\odot}$, a mass ratio $q = 0.154$ and an orbital period $P_{\mathrm{orb}} = 0.070497518\,\mathrm{d}$ ($\sim 101.5\,\mathrm{min}$; Schwope et al. 1993).

Trailed spectra: The trailed input spectra (middle panel of Figure 4.6) have a complex structure with at least three emission components. There is a blended low- to mid-velocity component which is brightest between phases $0.0-0.2$. It is fainter, but separated between phases $0.2-0.55$, and again blended and brighter between phases $0.55-1.0$. This component is associated with blended emission from the irradiated secondary and the low- to mid-velocity part of the ballistic accretion stream. Also discernible is a fainter high-velocity broad base component underlying the whole phase range. The broad base component is associated with emission produced in different parts of the accretion flow. There is also a striking brighter blueshifted wing that follows closely the high-velocity edge of the underlying broad base component between phases $0.4-0.55$. This high-velocity component is associated specifically with emission produced in the magnetically confined accretion flow as it falls towards the primary.

The basic structure of the emission components seen in the trailed input spectra is repro-

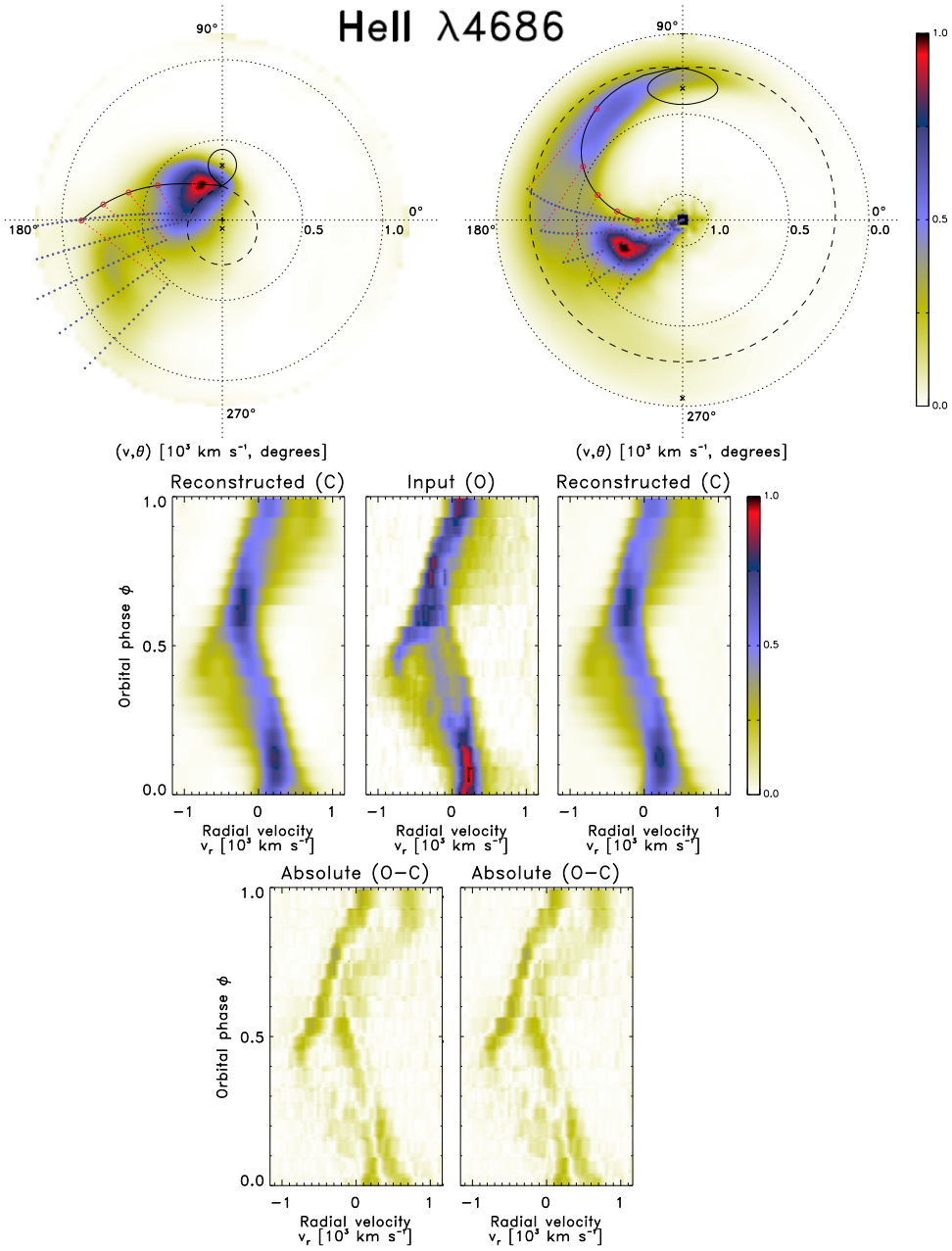

Figure 4.6. Doppler tomography of V834 Cen. Same layout as Figure 4.1. Both the standard and inside-out residuals (i.e., absolute O − C) have an rms value of 0.165. See Section 4.4 for more details.

duced in the trailed reconstructed spectra from both the standard and inside-out tomograms (panels to the left and right, respectively, of the middle panel of Figure 4.6). However, the more complex structure between phases $0.2 - 0.55$ and the observed flux distribution in the narrower component between phases $0.0 - 0.2$ and $0.55 - 1.0$ are not reproduced by either of the projections. The trailed absolute O − C spectra of both projections (bottom panels

of Figure 4.6) clearly show the incomplete reconstructed parts. Both projections, however, achieved the same level of overall success, that is, the residuals of both have rms values of 0.165. It is shown in Section 5.3.2 that the flux modulation mapping technique is able to reproduce the complex structure and the flux distribution.

Tomograms: The binary's centre of mass, marked with a plus (+), is at the centre of the standard tomogram (top left panel of Figure 4.6). In the inside-out tomogram (top right panel of Figure 4.6) the binary's centre of mass is effectively the zero velocity outer circumference. The centres of mass of the primary and secondary are marked with crosses (×) in both tomograms. The Roche lobes of the primary (dashed line) and the secondary (solid line) as well as a single particle ballistic trajectory from the L_1 point up to 45° in azimuth around the primary (solid line), are included in the overlay shown in both tomograms. Magnetic dipole trajectories are calculated from 5° to 45° in azimuth around the primary (thin dotted lines) at 10° intervals using a dipolar axis azimuth and co-latitude of $\sim 36°$ and $\sim 20°$ (Potter et al. 2004), respectively. The first of the dipole connections (small red circles) is at ($284\,\mathrm{km\,s^{-1}}$, 127°) and the first dipole trajectory starts at ($174\,\mathrm{km\,s^{-1}}$, 169°). Consecutive trajectories start at locations with progressively higher velocities and polar angles.

In the standard tomogram the emission from the irradiated secondary is blended with emission from the ballistic stream. This overly compact blended emission creates an extremely bright ridge in the velocity range ($250-500\,\mathrm{km\,s^{-1}}$, $90-150°$) and dominates the brightness scale of the standard tomogram. In the inside-out tomogram this blended emission is more separated: the secondary is seen as a diffused patch at ($340\,\mathrm{km\,s^{-1}}$, 90°), while the stream forms a brighter ridge along the model stream trajectory in the velocity range ($300-400\,\mathrm{km\,s^{-1}}$, $115-140°$). Separating this lower velocity emission in the inside-out tomogram is possible as the emission is re-binned in a larger area with more pixels.

The emission associated with the magnetically confined accretion as it leaves the orbital plane in the threading region is seen in both tomograms in the velocity range ($0-500\,\mathrm{km\,s^{-1}}$, $170-230°$). In the inside-out tomogram, however, the separation between the lower velocity emission from the ballistic stream and that from the magnetically confined accretion is more pronounced. Also, in both tomograms the emission considered to be consistent with the magnetically confined accretion as it flows down to the primary is centred on the ridge of brightness covering the velocity range ($700-1000\,\mathrm{km\,s^{-1}}$, $185-235°$). However, in the inside-out tomogram the funnelling of the emission as it falls towards the primary along the dipole trajectories, especially those with azimuth angles 35° and 45°, is significantly more apparent than in the standard tomogram.

4.5 PQ Gem: a non-eclipsing intermediate polar

PQ Gem is a bright, low-inclination ($i \sim 30°$; Hellier 1997) intermediate polar. Hellier (1997, 1999) presented spin-cycle Doppler tomography of PQ Gem. Spin-cycle tomography (see Section 2.2.1) is uniquely geared to produce velocity maps of the emission components

that are locked on the spin period of the primary, for example, the accretion curtains of the magnetically confined accretion flow falling onto the primary of an intermediate polar.

Figure 4.7 shows standard and inside-out spin-cycle Doppler tomography based on the spin-folded He II λ4686 emission line from the 1993 December spectroscopic observations of PQ Gem presented first by Hellier (1997). The reader is referred to that paper for a detailed description of the data set and reduction procedures. In short, a phase-invariant spectrum is subtracted from each of the spin phase-resolved spectra in order to remove the emission components not varying on the spin period (~ 13.9 min; Hellier 1997). All 15 spectra from the original spin-folded data set, which covers the whole spin phase range, are used for our calculations. The spectra are evenly spaced and each spectrum has 361 velocity points in the extracted radial velocity range around the He II λ4686 emission line ($n = 5415$). The model velocity profile overlay shown in both tomograms is based on an inclination angle of 30° (Hellier 1997) and a dipolar axis co-latitude of 30° (Potter et al. 1997). As proposed by Hellier (1997) a maximum absolute radial velocity amplitude of $\sim 500\,\mathrm{km\,s^{-1}}$ is used for the magnetic co-rotation and the upper magnetic pole points towards the observer at spin phase 0.87 (dipolar axis azimuth $\sim 47°$). I assume the upper curtain (blue dotted lines) extends over spin phase $0.63 - 0.96$ and the lower curtain (red dotted lines) $0.13 - 0.46$.

Trailed spectra: At least two distinct emission components are seen in the trailed spin-folded input spectra (middle panel of Figure 4.7). The first component has a maximum blueshift around phase 0.4 and a maximum redshift around phase 0.9. It is bright at phases 0.3 and 0.65, but the expected blue-to-red crossover is not clear. The second component has a lower velocity amplitude with a maximum redshift around phase 0.4 and a maximum blueshift around phase 0.9. Although the red-to-blue crossover is visible for this component, the blue-to-red crossover is again not clear. Both the components are associated with emission produced in the spin-locked magnetically confined accretion flow.

The basic structure of the components identified in the trailed input spectra is reproduced in the trailed reconstructed spectra from both the standard and inside-out tomograms (panels to the left and right, respectively, of the middle panel of Figure 4.7). However, the observed flux distribution, especially between phases $0.5 - 1.0$, is not reproduced by either of the projections. This partial reproduction is evident in the excess seen in both sets of trailed absolute O − C spectra (bottom panels of Figure 4.7). The inside-out projection achieved a marginal better overall result, that is, its residuals have a rms value of 0.365 compared to the 0.371 of the standard projection. In Section 5.3.3 it is shown how the flux modulation mapping technique improves the reproduction of the flux distribution.

Tomograms: The standard tomogram of PQ Gem is dominated by two bright spots, one in the upper right quadrant and the other in the lower left quadrant. Hellier (1997, 1999) suggested that these two spots are associated with emission from the accretion curtains flowing towards, respectively, the lower and upper magnetic poles of the primary. The accretion curtains are considered to be formed by material at the magnetosphere flowing onto the magnetic field lines at an azimuth $30 - 50°$ ahead of the accretion region on the

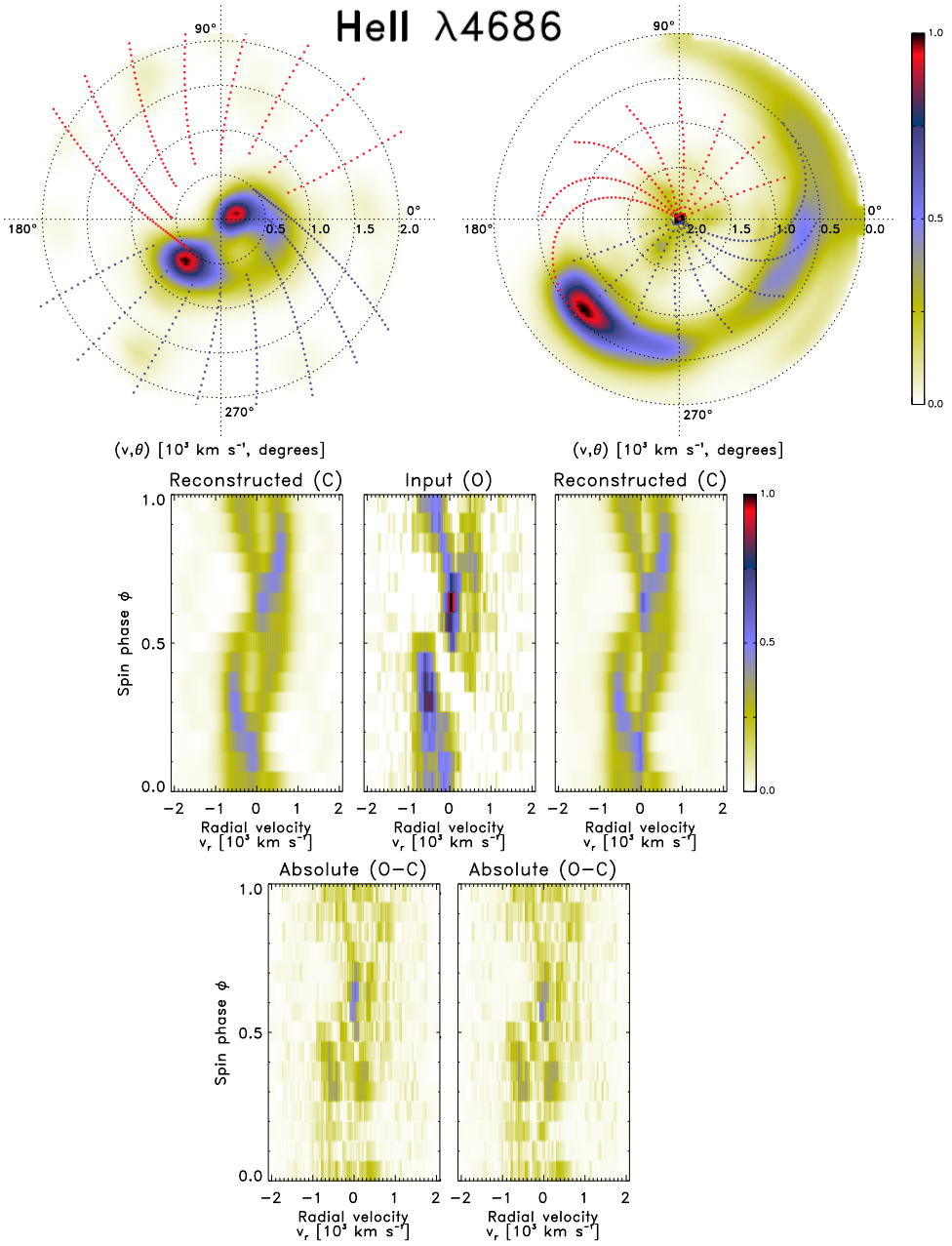

Figure 4.7. Spin-cycle Doppler tomography of PQ Gem. The standard and inside-out spin-cycle tomograms are shown in the top left and right panels, respectively. The middle panel shows the trailed input spectra with the trailed reconstructed spectra for the corresponding spin-cycle tomogram to the left and right of it. The bottom left and right panels show the trailed absolute residual spectra for the corresponding spin-cycle tomogram. The rms values of the standard and inside-out residuals (i.e., absolute O − C) are 0.371 and 0.365, respectively. See Section 4.5 for more details.

primary (Hellier 1997). In the inside-out tomogram the spot seen in the upper right quadrant of the standard tomogram, is projected as an extended, more diffused feature. The brighter

of the two spots seen in the standard tomogram, that is to say, the one in the lower left quadrant, is also more extended, but still the most prominent feature. The inside-out projection significantly changes the apparent flux distribution between these two emission features. This places greater emphasis on the difference in the velocities of the two features.

If the model velocity profile is considered it is found that in the inside-out projection the magnetic dipole lines converge while in the standard projection they diverge towards higher velocities. Compared to the standard projection the inside-out projection creates a far more intuitive representation of the curving accretion curtains as they fall down onto the primary.

Chapter 5

Flux modulation mapping

For there is nothing either good or bad, but thinking makes it so.

– William Shakespeare, *Hamlet*, Act II, Scene 2

In Section 2.2.2 I gave an overview of modulation Doppler tomography (Steeghs 2003), a technique that maps emission components that vary harmonically as a function of the orbital period. Potter et al. (2004) exploited the violation of the first axiom of Doppler tomography (as listed in Section 2.1.1) and successfully used ten consecutive half-phase tomograms of the polar V834 Cen to illustrate how different emission components in the system modulate in flux during an orbit. Building on the principles introduced by Steeghs (2003) and Potter et al. (2004) I developed a variant form of modulation Doppler tomography. The aim is to extract more information from the phase-resolved spectra of especially mCVs and present it in a useful, easily interpretable format. This new technique of flux modulation mapping extracts any phased modulation in the observed flux from consecutive half-phase standard and inside-out tomograms. From the extracted phased modulation it is possible to map how the flux from a specific emission component modulates over a complete phase. The flux modulation mapping is presented in velocity maps that represent the amplitude and average of the modulated emission, as well as the observed phase of maximum flux.

In this chapter I introduce this new flux modulation mapping technique. I discuss the use of consecutive half-phase tomograms to identify how the observed emission distribution changes with phase, that is to say, how the flux modulates with phase, in Section 5.1. I describe the new technique to map the identified flux modulation in Section 5.2. In Section 5.3 I showcase the results of applying the flux modulation mapping technique to ten consecutive half-phase standard and inside-out tomograms based on the same spectra of the three mCVs, namely HU Aqr, V834 Cen and PQ Gem, presented in Chapter 4. A shortened version of this chapter has been published as part of an article in *Astronomy & Astrophysics* (Kotze et al. 2016).

5.1 Identifying flux modulation

The first axiom of Doppler tomography (as listed in Section 2.1.1), states that all points in the binary system being mapped are equally visible at all times. Therefore, a tomogram can be produced from spectra that cover half of the binary cycle. If this axiom is not violated then tomograms produced from different half-phases are identical. However, if this axiom is violated, in other words, all points in the system are *not* equally visible at all times, then the tomograms are not identical. Given that the tomogram for a specific half-phase is the phase-averaged map in velocity coordinates of the emission distribution in the system at the mid-value of the half-phase, it follows that only the emission components visible during the half-phase are present in the tomogram. This lays the foundation for a simple but effective technique to probe how the observed emission distribution changes with phase, that is to say, how the emission features modulate in flux with phase. For example, in a mid- to high-inclination system it is reasonable to assume that the emission from the irradiated side of the secondary appears brightest around orbital phase 0.5. Consequently, in all half-phase tomograms that include phase 0.5 this emission will be a dominant feature whereas in those that exclude phase 0.5 it will not. Therefore, by using half-phase spectra only, it is possible to selectively eliminate dominant emission components in the system from a tomogram, thus allowing otherwise less obvious features to become more enhanced (e.g., Potter et al. 2004).

Figure 5.1 illustrates this concept clearly for the high-inclination polar HU Aqr. In both the standard and inside-out half-phase tomograms that include phase 0.5 the most dominant feature is the emission from the irradiated side of the secondary. On the other hand, in the half-phase tomograms that exclude phase 0.5 the emission from the irradiated side of the secondary is less discernible and the tomograms are dominated by emission from the ballistic accretion stream.

5.2 Mapping flux modulation: method

In this section a simple, but effective technique is introduced for mapping the type of phased flux modulation illustrated in the previous section. As noted previously, a specific half-phase tomogram gives the phase-averaged emission distribution of only the emission components visible during that half-phase. Now, let F_{ij} and Φ_i be, respectively, the flux in the j-th pixel and the mid-phase value of the i-th half-phase tomogram in a set of m consecutive half-phase tomograms. Under the assumption that the flux from an emission component modulates sinusoidally over the orbital (or spin) period then the amplitude A_j, phase-offset φ_j and average B_j of the flux modulation in the j-th pixel can be extracted from a simple sinusoidal fit, that is,

$$F_{ij} = A_j \sin\left[2\pi\left(\Phi_i - \varphi_j\right)\right] + B_j. \tag{5.1}$$

These fitted variables for each pixel are presented in separate velocity maps. The amplitude map, that is, the fitted amplitude for each pixel A_j, represents the strength of the flux

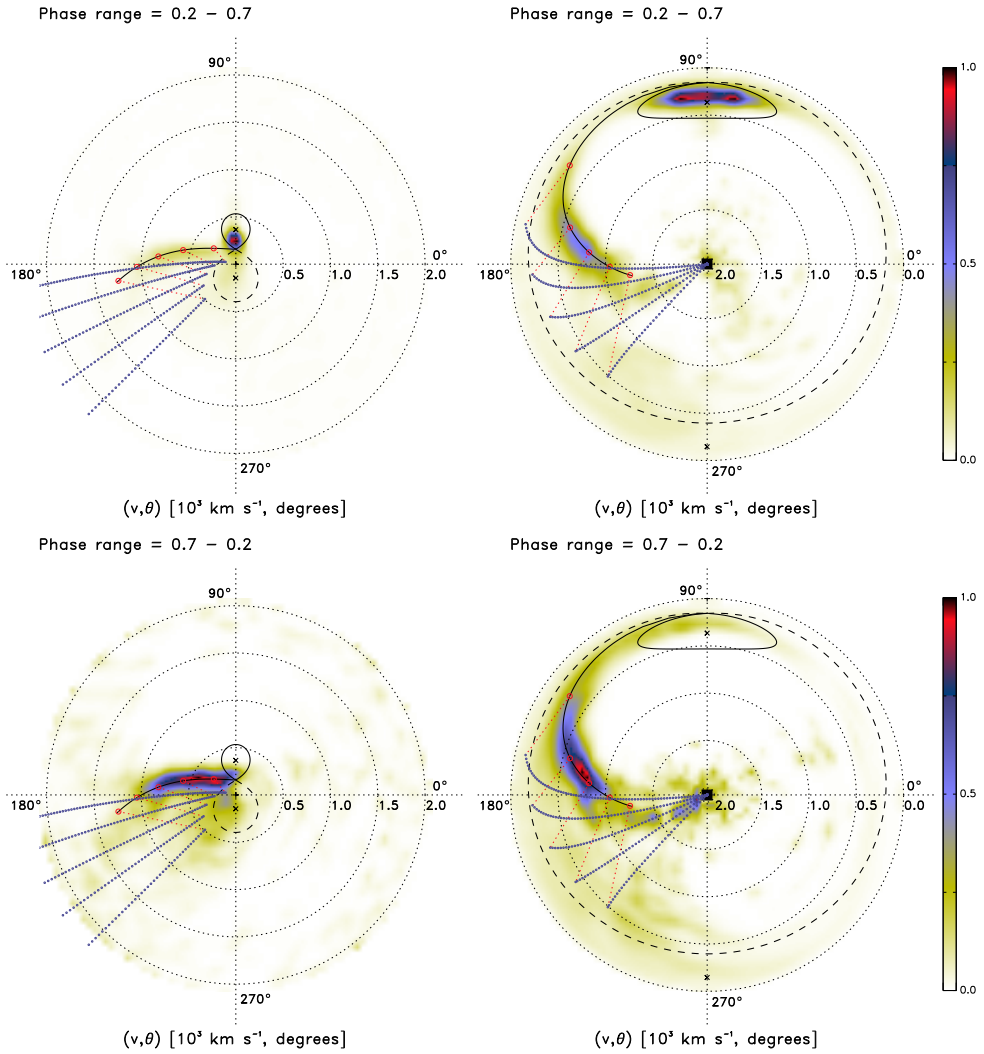

Figure 5.1. Example half-phase standard and inside-out tomograms of HU Aqr. The left top and bottom panels show standard tomograms for the half-phases $0.2-0.7$ and $0.7-0.2$, respectively. The right top and bottom panels show the equivalent inside-out tomograms.

modulation and can be used to identify which emission components are modulated. Adding 0.25 to the fitted phase-offset for each pixel φ_j produces a *phase of maximum flux* map, that is, the phase at which an emission component appears brightest to an observer. It is important to note that if the sine function in Equation 5.1 is replaced by a cosine function then the fitted phase-offset φ_j is the phase of maximum flux for each pixel without having to add 0.25. Effectively, the average map, that is, the fitted average for each pixel B_j, is the conventional tomogram in the standard and inside-out projections.

A simple multivariate least squares procedure is used to calculate the sinusoidal fit. By making use of the sine sum identity, Equation 5.1 is re-written as

$$y_i = a_0 + a_1 \sin(2\pi\Phi_i) + a_2 \cos(2\pi\Phi_i), \tag{5.2}$$

where $y_i = F_{ij}$, $a_0 = B_j$, $a_1 = A_j \cos(2\pi\varphi_j)$ and $a_2 = -A_j \sin(2\pi\varphi_j)$. Having solved for a_0, a_1 and a_2, it then follows that

$$A_j = \sqrt{a_1^2 + a_2^2},\ \varphi_j = \frac{1}{2\pi}\tan^{-1}\left(-\frac{a_2}{a_1}\right) \text{ and } B_j = a_0. \tag{5.3}$$

The sinusoidal fitting process described above can be demonstrated at the hand of the set of ten consecutive half-phase standard and inside-out tomograms of the mid-inclination polar V834 Cen shown in Figures 5.2 to 5.11 (see Appendix A.2 for the complete consecutive half-phase standard and inside-out Doppler tomography of V834 Cen for the ten half-phases 0.0−0.5, ..., 0.4−0.9, 0.5−0.0, 0.6−0.1, ..., 0.9−0.4). A closer examination of the half-phase tomograms reveals that each tomogram has a unique emission distribution. The dominant emission features in each tomogram also tend to differ from tomogram to tomogram. Now, consider four example pixels at different velocity coordinates in the set of half-phase tomograms. The positions of these example pixels are indicated on all the half-phase tomograms in Figures 5.2 to 5.11. The first pixel maps to the trailing hemisphere of the irradiated side of the secondary. The second and third pixels map roughly to parts of, respectively, the ballistic and magnetic accretion flows. The fourth pixel maps to an 'empty' part of the tomogram. The extracted flux values from the ten half-phase tomograms for each pixel and the calculated sinusoidal fits are plotted in Figure 5.12. The values of the fitted amplitude A_j and average B_j, as well as the phase-offset φ_j, for both the standard and inside-out projections are listed in Table 5.1. The extracted flux values, as well as the fitted amplitude A_j and average B_j are normalised by the maximum flux value from the half-phase tomograms.

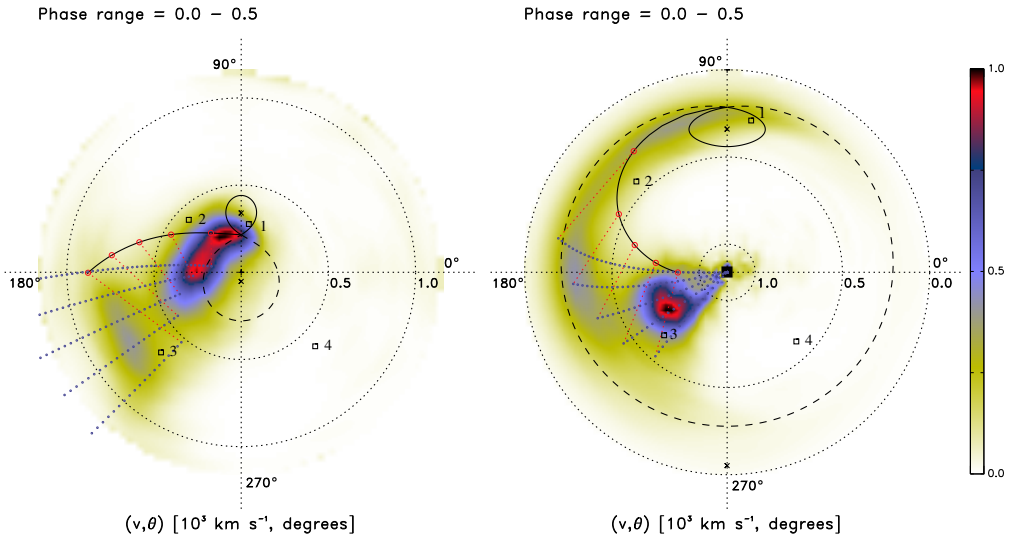

Figure 5.2. Half-phase standard and inside-out tomograms of V834 Cen: orbital phase range 0.0 − 0.5. The standard and inside-out tomograms are shown on the left and right, respectively. The four equivalent example pixels in the tomograms are marked with small squares and numbered 1 to 4 for easy reference.

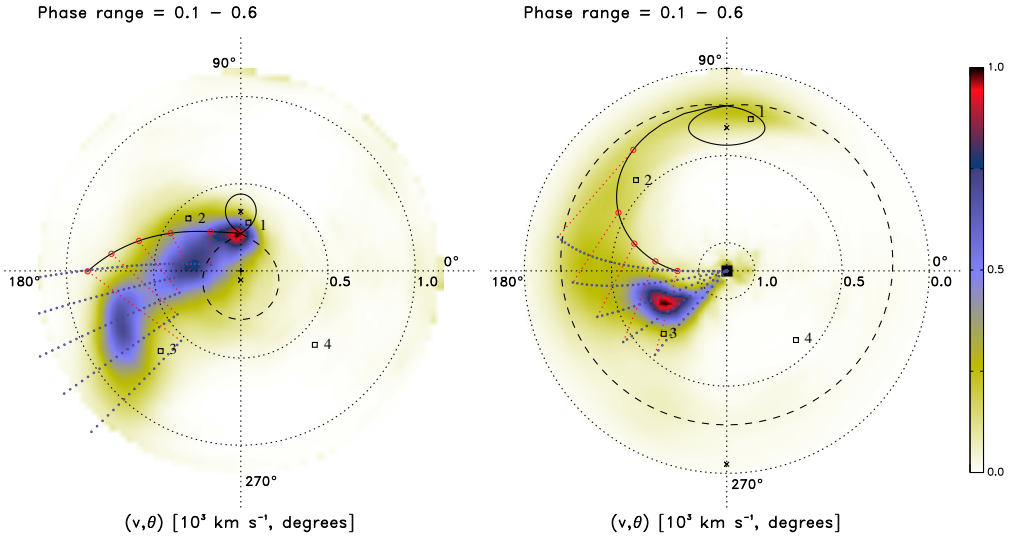

Figure 5.3. Half-phase standard and inside-out tomograms of V834 Cen: orbital phase range $0.1 - 0.6$. Same layout as Figure 5.2.

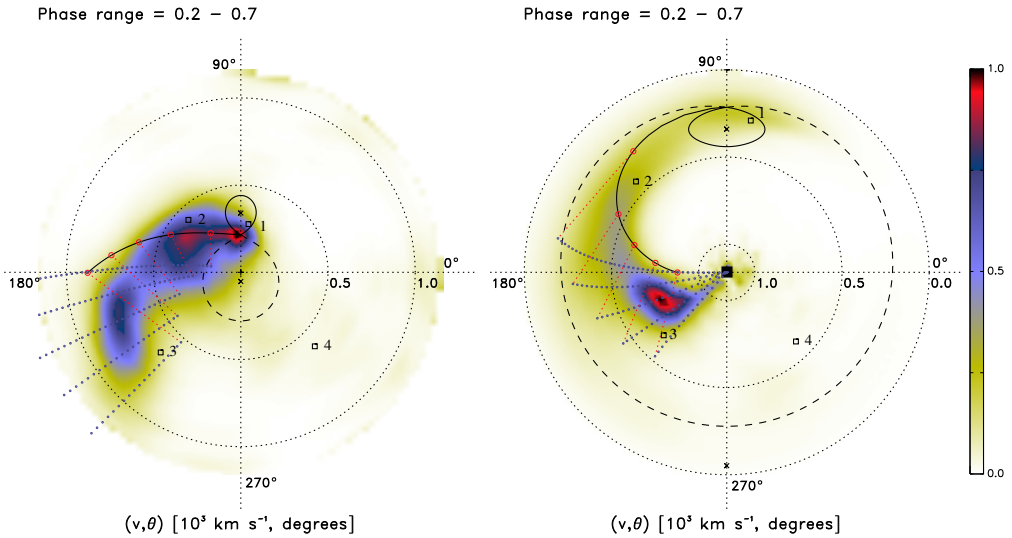

Figure 5.4. Half-phase standard and inside-out tomograms of V834 Cen: orbital phase range $0.2 - 0.7$. Same layout as Figure 5.2.

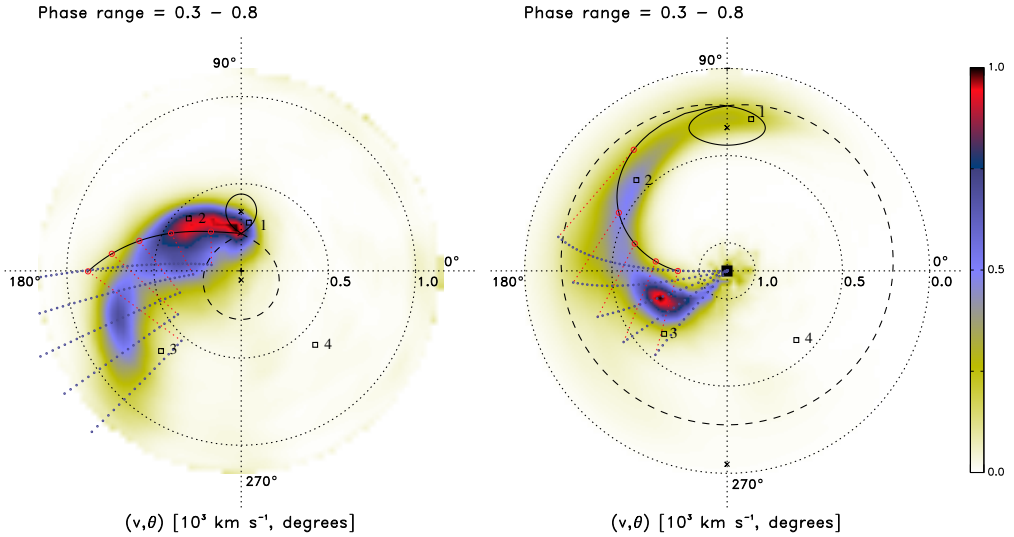

Figure 5.5. Half-phase standard and inside-out tomograms of V834 Cen: orbital phase range $0.3 - 0.8$. Same layout as Figure 5.2.

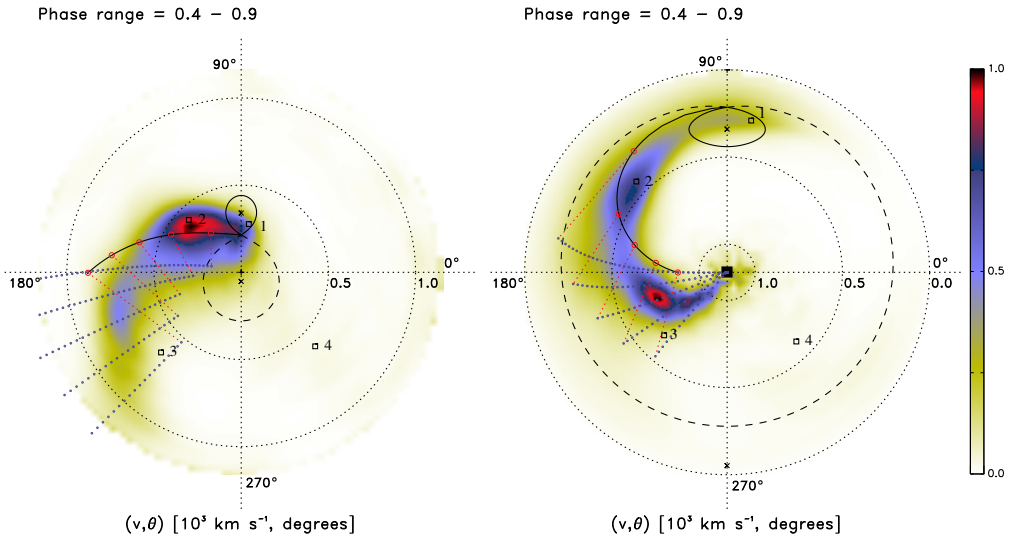

Figure 5.6. Half-phase standard and inside-out tomograms of V834 Cen: orbital phase range $0.4 - 0.9$. Same layout as Figure 5.2.

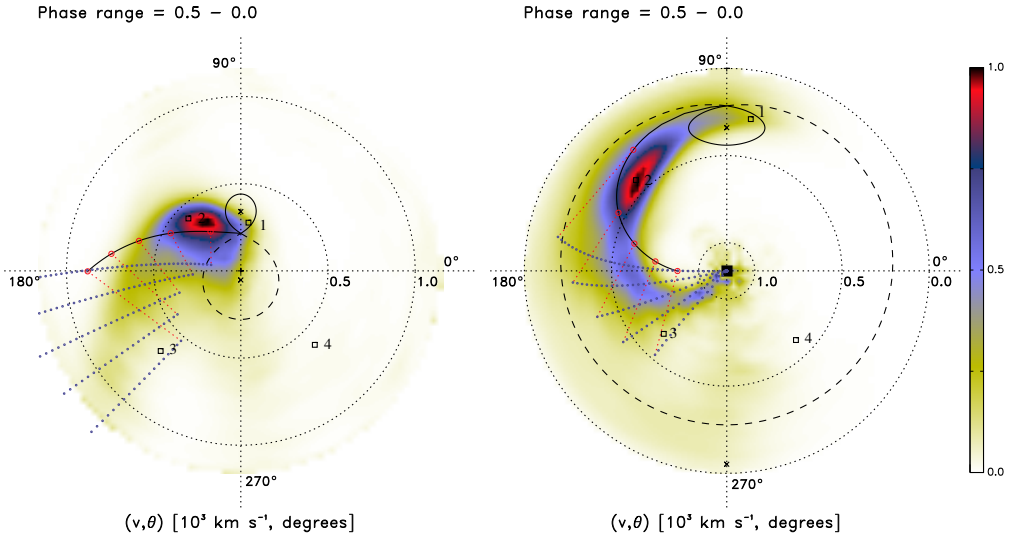

Figure 5.7. Half-phase standard and inside-out tomograms of V834 Cen: orbital phase range $0.5 - 0.0$. Same layout as Figure 5.2.

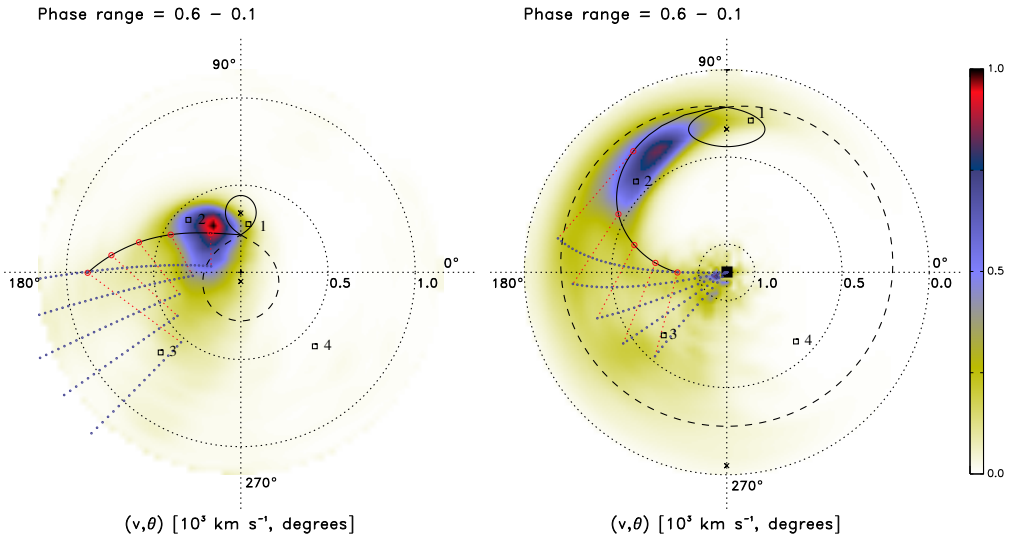

Figure 5.8. Half-phase standard and inside-out tomograms of V834 Cen: orbital phase range $0.6 - 0.1$. Same layout as Figure 5.2.

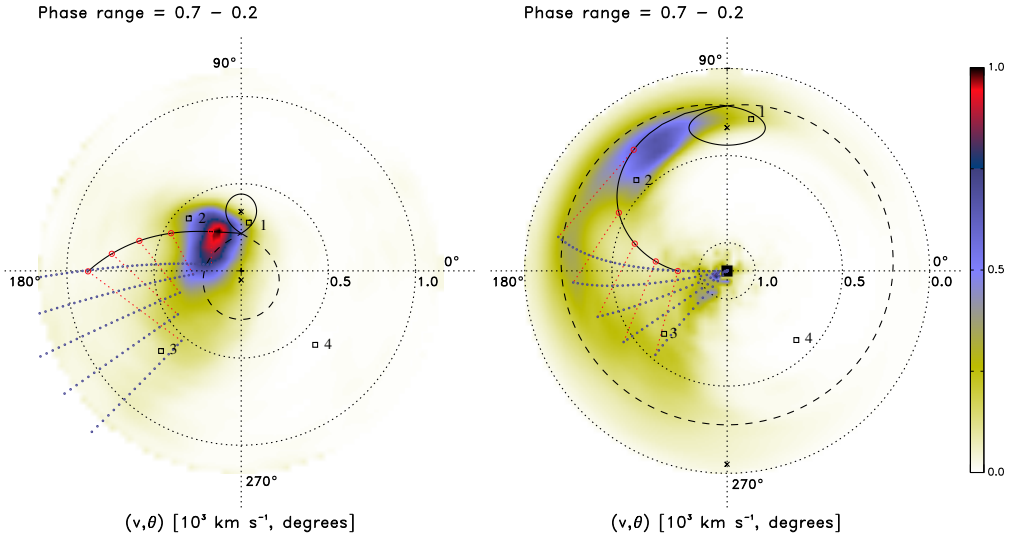

Figure 5.9. Half-phase standard and inside-out tomograms of V834 Cen: orbital phase range 0.7 – 0.2. Same layout as Figure 5.2.

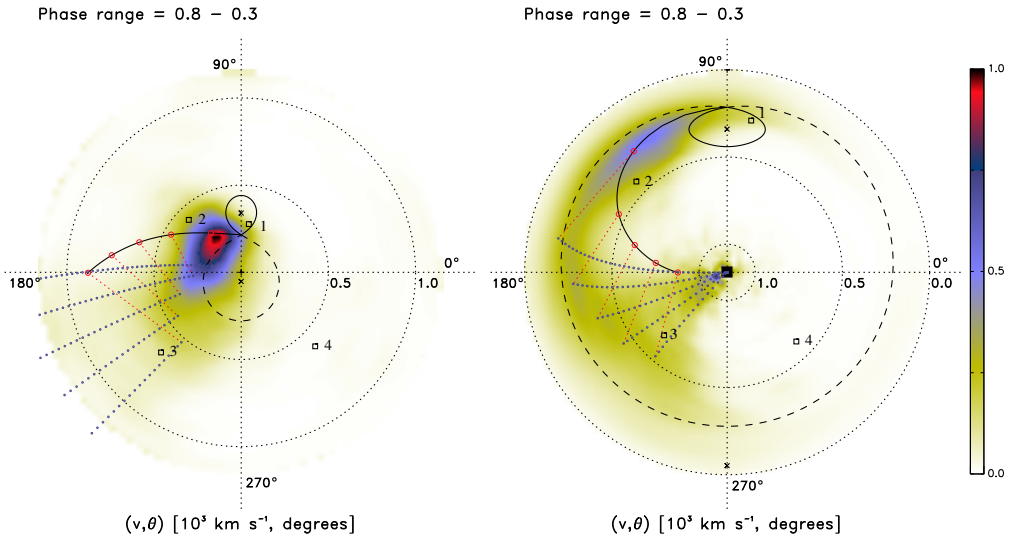

Figure 5.10. Half-phase standard and inside-out tomograms of V834 Cen: orbital phase range 0.8 – 0.3. Same layout as Figure 5.2.

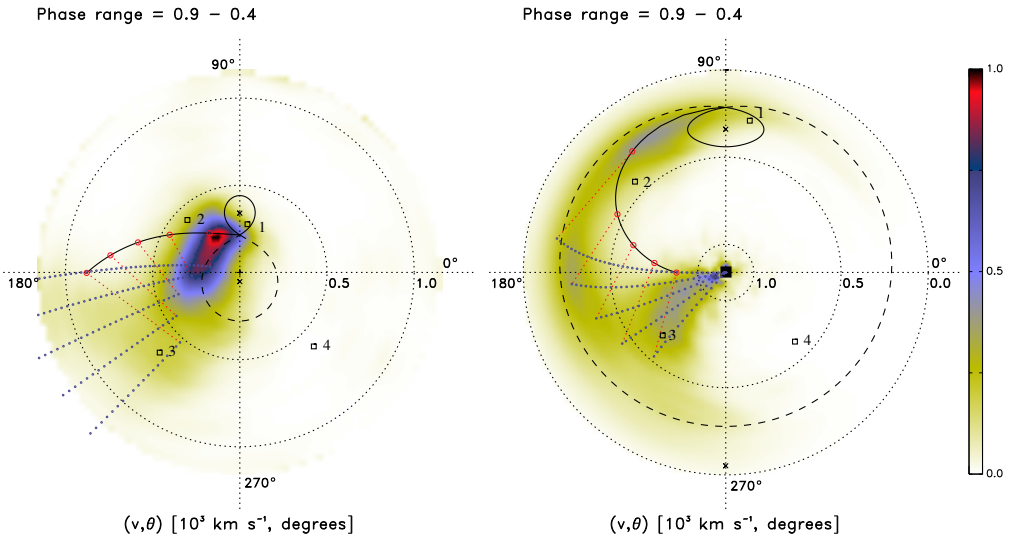

Figure 5.11. Half-phase standard and inside-out tomograms of V834 Cen: orbital phase range $0.9 - 0.4$. Same layout as Figure 5.2.

Table 5.1. Example flux modulation sine fit variables from the half-phase tomograms of V834 Cen. The amplitude A_j and average B_j are normalised by the maximum flux value from the half-phase tomograms. The sine fits of the four example pixels are displayed in Figure 5.12.

Pixel	Amplitude A_j		Phase-offset φ_j		Average B_j	
	Standard	Inside-out	Standard	Inside-out	Standard	Inside-out
1	0.070	0.052	0.244	0.266	0.426	0.126
2	0.244	0.193	0.450	0.448	0.424	0.271
3	0.067	0.082	1.010	1.027	0.098	0.126
4	0.005	0.003	0.345	0.355	0.008	0.003

Pixel 1: The phase-offset φ_j calculated for both the standard and inside-out sets of half-phase tomograms is ~ 0.25. The fitted sinusoids must therefore have their maxima at phase $\phi \sim 0.5$, which is confirmed in both the plotted fits for the pixel. The amplitude A_j and average B_j calculated for the standard tomograms are higher than that calculated for the inside-out tomograms. This is expected because the low-velocity emission associated with the irradiated side of the secondary is projected into fewer pixels close to the centre of each standard tomogram whereas it is projected into more pixels close to the outer edge of each inside-out tomogram. In other words, in the standard projection this one pixel holds more emission than the one pixel in the inside-out projection.

Pixel 2: The calculated phase-offset φ_j for both the standard and inside-out sets of half-phase tomograms is ~ 0.45. The maxima of the fitted sinusoids must therefore be at phase $\phi \sim 0.7$, which is confirmed in both the plotted fits for the pixel. This pixel contains emission associated with the *lower* velocity part of the ballistic accretion flow. Hence, for the same

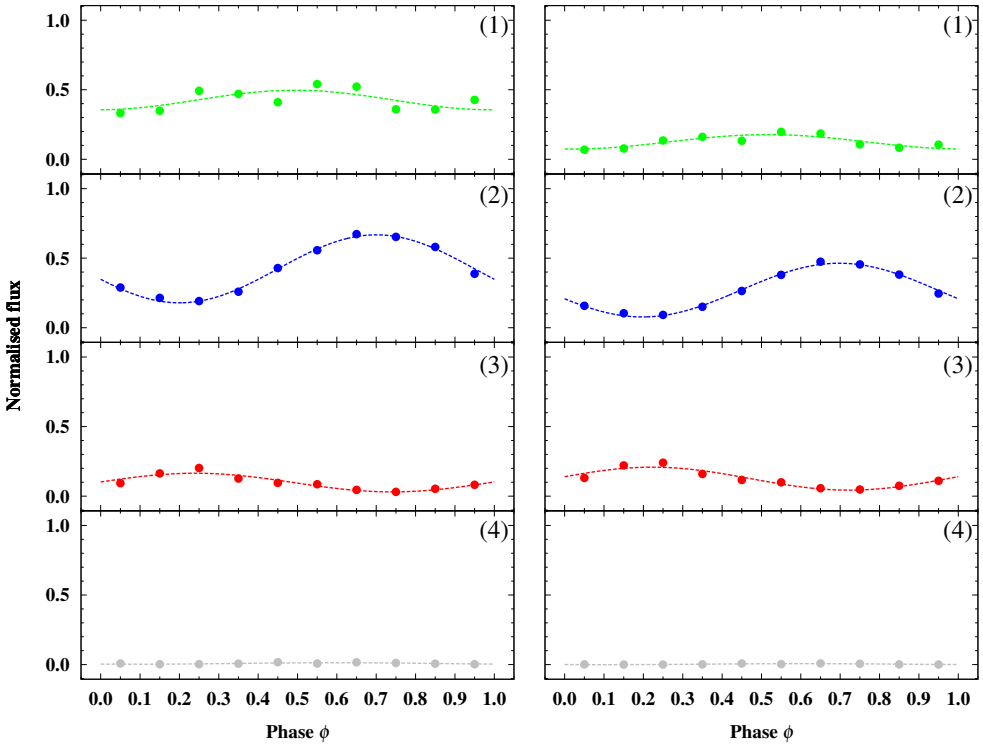

Figure 5.12. Example flux modulation sine fits from the half-phase tomograms of V834 Cen. The left panel shows the extracted flux values (solid dots) from the set of standard half-phase tomograms and the calculated sinusoidal fits (dashed lines) for the four example pixels (numbered 1 to 4). The equivalent from the set of inside-out half-phase tomograms are shown on the right. The sine fit variables are listed in Table 5.1.

reason that applies to pixel 1, the calculated amplitude A_j and average B_j for this pixel in the standard tomograms are higher than in the inside-out tomograms.

Pixel 3: The phase-offset φ_j calculated for both the standard and inside-out sets of half-phase tomograms is ~ 0.0. The fitted sinusoids must therefore have their maxima at phase $\phi \sim 0.25$, which is confirmed in both the plotted fits for the pixel. This pixel contains emission associated with part of the magnetic accretion flow which is at a *higher* velocity than the emission in the first two pixels. Higher velocity emission is projected into more pixels closer to the outer edge of a standard tomogram and into fewer pixels closer to the centre of an inside-out tomogram. Consequently, in the inside-out projection this one pixel holds more emission than the one pixel in the standard projection. For this pixel then, as expected, the calculated amplitude A_j and average B_j for the inside-out tomograms are slightly higher than for the standard tomograms.

Pixel 4: Even though this pixel appears to be 'empty' the fitting procedure does calculate values for the amplitude A_j, average B_j and phase-offset φ_j. However, the value of the amplitude A_j is very small and therefore does not represent any significant flux modulation. In order to ignore such spurious modulations in the phase of maximum flux map it typically suffices to exclude pixels with amplitudes less than 10% of the maximum amplitude determined for all the pixels. This percentage, however, may be set lower to probe more marginal modulations or it may be set higher to isolate the dominant modulations.

It was shown in the previous chapter that the standard and inside-out projections produce different distributions of the relative brightness of emission components in a tomogram. Consequently, the fitted amplitude A_j and average B_j of the flux modulation per pixel are dependent on the projection used and the values from the two projections are therefore not directly comparable. The phase-offset φ_j of any phased flux modulation, however, is determined by the physical position of the emission component in the system and does not depend on the projection used, as was shown for the example pixels. In other words, a modulating emission component may exhibit a differing amplitude or average, but it should present the same phase-offset for the standard and inside-out projections. In the next section I apply the same flux modulation mapping technique described above to ten consecutive half-phase standard and inside-out tomograms of the three mCVs HU Aqr, V834 Cen and PQ Gem.

5.3 Flux modulation mapping: standard and inside-out projections

The flux modulation mappings presented hereafter are based on ten consecutive half-phases (i.e., $0.0-0.5$, ..., $0.4-0.9$, $0.5-0.0$, $0.6-0.1$, ..., $0.9-0.4$). The normalised amplitude map is presented with the same colour scheme as the conventional tomogram. The map for the phase of maximum flux, which shows at which phase an emission component appears brightest to an observer, is colour-coded according to phase: 0.0 - black, 0.25 - red, 0.5 - green and 0.75 - blue. The average map is effectively the conventional tomogram in the standard and inside-out projections and is not shown here. Also shown are trailed summed normalised input and reconstructed spectra, as well as absolute O − C spectra for all the test cases in a similar way as in the previous chapter.

5.3.1 HU Aqr: an eclipsing polar

Figure 5.13 shows standard and inside-out flux modulation mapping of HU Aqr. These results are based on the consecutive half-phase standard and inside-out Doppler tomography of HU Aqr for the ten half-phases $0.0-0.5$, ..., $0.4-0.9$, $0.5-0.0$, $0.6-0.1$, ..., $0.9-0.4$ presented in Appendix A.1. The standard and inside-out velocity maps are shown left and right, respectively. The top two panels show the modulation amplitude maps and the middle

two panels show the phase of maximum flux maps. The phase of maximum flux map shows only pixels where the corresponding modulation amplitude is at least 10% of the maximum amplitude. This map is colour coded to represent phase: black (0.0), red (0.25), green (0.5) and blue (0.75). The middle panel below the phase of maximum flux maps shows the trailed input spectra with the trailed summed reconstructed spectra for the ten consecutive half-phase standard and inside-out tomograms to the left and right of it, respectively. The bottom panels show the corresponding trailed summed absolute residual spectra. The model velocity profile overlay shown in all the velocity maps is the same as the one in Figure 4.5.

Trailed spectra: When compared with the reconstructed spectra in Figure 4.5 the summed reconstructed spectra better reproduce the input spectra. Most striking is the almost complete absence of the bright narrow line flux between phases 0.0−0.2 and 0.8−1.0. This narrow line is associated with emission from the irradiated side of the secondary. It is expected to be absent in the range around phase 0.0 when the non-irradiated side of the secondary is pointing towards the observer as it eclipses the primary. The brightening around phase 0.5 in the same bright narrow emission is also slightly better reproduced. The improvement achieved for both projections is clearly seen in their absolute O − C spectra with rms values of 0.108 compared to the non-modulated rms values of 0.172.

Model schematic: Figure 5.14 shows a model spatial schematic of HU Aqr which is a useful aid in the interpretation of both the amplitude of the phased modulation and the phase of maximum flux. The model spatial schematic is based on the same system parameters used in the calculation of the model velocity profile overlay used in all the tomograms of HU Aqr.

Amplitude maps: In both the standard and inside-out amplitude maps the secondary is the most flux modulated component. The flux from the ballistic stream is also shown to modulate, but more so in the inside-out map. HU Aqr is a high-inclination eclipsing system and it is therefore expected that the flux from the irradiated side of the secondary and the ballistic stream will modulate over the orbital phase of the system due to their changing aspect angle.

Phase of maximum flux maps: In the phase of maximum flux maps most of the secondary appears brightest around orbital phase 0.5 (green), when the irradiated side of the secondary is pointing towards the observer. The trailing and leading hemispheres of the irradiated side of the secondary appears brightest at orbital phases 0.25 (red) and 0.75 (blue), respectively. This is expected because the observer has full views of the trailing and leading hemispheres at orbital phases 0.25 and 0.75, respectively. The ballistic stream appears brightest between orbital phases 0.75 and 0.0 (mixture of blue and black), that is to say, between when the observer has a full view of the leading side of the stream and when the stream is flowing away from the observer. The standard amplitude map and the phase of maximum flux map hold amplitude and phase information for the ballistic stream up to velocities of ~ 500 km s^{-1} whereas the inside-out versions expose information up to velocities of $\sim 1000\,\mathrm{km\,s^{-1}}$.

5.3.2 V834 Cen: a non-eclipsing polar

The standard and inside-out flux modulation mapping results for V834 Cen are shown in Figure 5.15 (same layout as Figure 5.13; see Section 5.3.1 for details). These results are based on the consecutive half-phase standard and inside-out Doppler tomography of V834 Cen for the ten half-phases 0.0−0.5, ..., 0.4−0.9, 0.5−0.0, 0.6−0.1, ..., 0.9−0.4 presented in Appendix A.2. The phase of maximum flux map shows only pixels where the corresponding modulation amplitude is at least 10% of the maximum amplitude. The model velocity profile overlay shown in all the velocity maps is the same as the one in Figure 4.6.

Trailed spectra: The summed reconstructed spectra better reproduce the input spectra when compared with the reconstructed spectra in Figure 4.6. Most prominent is the considerable brightening in the narrower line flux between phases $0.0 - 0.2$ and $0.55 - 1.0$. Also, the more complex, multiple flux components between phases $0.2 - 0.55$, and the flux level of the striking high-velocity blue wing at phase $0.4 - 0.55$ are better reproduced. Both sets of absolute O − C spectra clearly show the significant improvement achieved with rms values of 0.074 and 0.078 for the standard and the inside-out projections, respectively, compared to the non-modulated rms values of 0.165.

Model schematic: A model spatial schematic of V834 Cen is shown in Figure 5.16. This schematic is very useful when interpreting both the amplitude of the phased modulation and the phase of maximum flux. The same system parameters used in the calculation of the model velocity profile overlay used in all the tomograms of V834 Cen were used to construct the model spatial schematic.

Amplitude maps: The most prominent flux modulated components in both the standard and inside-out amplitude maps are the ballistic and the magnetically confined accretion flows. In both amplitude maps it almost looks like the ballistic stream is 'split' into two parts, that is, one with velocities less than and the other with velocities greater than $250\,\mathrm{km\,s^{-1}}$. This is a neat separation of the magnetically confined accretion flow as it leaves the orbital plane along the early part of the ballistic stream (velocities $< 250\,\mathrm{km\,s^{-1}}$) and the mid-velocity part of the 'real' ballistic stream (velocities $> 250\,\mathrm{km\,s^{-1}}$). The secondary is also flux modulated, but because V834 Cen is a mid-inclination non-eclipsing system the amplitude of the modulation is not as dominant as that of the secondary of HU Aqr, which is a high-inclination eclipsing system.

Phase of maximum flux maps: In both the standard and inside-out phase of maximum flux maps the lower velocity part of the real ballistic stream (before the first dipole connection) appears brightest at orbital phase 0.0 (black) when it is pointing away from the observer, while the mid-velocity part appears brightest at orbital phase 0.75 (blue) when the observer has a full view of the outer side of the stream. The phase of maximum flux interpretation for the higher velocity part of the ballistic stream is ambiguous because emission from this part is blended with emission from the magnetically confined accretion flow. The mid- to high-velocity part of the threading region in both maps appears brightest at orbital

phase 0.25 (predominantly red) when the observer has a full view of the inner sides of the ballistic and magnetically confined accretion flows. The low-velocity part of the threading region, on the other hand, appears brightest between orbital phases 0.0 (black) and 0.25 (red) when it is predominantly flowing away from the observer. The higher velocity part of the magnetically confined accretion flow appears brightest around orbital phase 0.5 (green) when the observer has a full view of the outer side of the magnetically confined accretion flow with most of it flowing towards the observer.

5.3.3 PQ Gem: a non-eclipsing intermediate polar

The standard and inside-out flux modulation mapping results for PQ Gem are shown in Figure 5.17 (same layout as Figure 5.13; see Section 5.3.1 for details). These results are based on the consecutive half-phase standard and inside-out spin-cycle Doppler tomography of PQ Gem for the ten half-phases $0.0-0.5$, ..., $0.4-0.9$, $0.5-0.0$, $0.6-0.1$, ..., $0.9-0.4$ presented in Appendix A.3. The phase of maximum flux map shows only pixels where the corresponding modulation amplitude is at least 10% of the maximum amplitude. The model velocity profile overlay shown in all the velocity maps is the same as the one in Figure 4.7.

Trailed spectra: Compared to the reconstructed spectra in Figure 4.7 the summed reconstructed spectra better reproduce the input spectra. Even though the flux levels between phases $0.25-0.75$ are not as high as required, the flux distribution in the two distinct emission components is significantly improved. This is especially apparent in the split of the two components between phases $0.5-1.0$. The absolute O$-$C spectra of both projections clearly show the improvement in the reproduction of the input spectra with rms values of 0.276 and 0.257 compared to the non-modulated rms values of 0.371 and 0.365 for the standard and the inside-out projections, respectively.

Model schematic: Figure 5.18 shows a model spatial schematic of PQ Gem, based on the same system parameters used in the calculation of the model velocity profile overlay used in all the tomograms of PQ Gem. The model spatial schematic is a useful aid when interpreting both the amplitude of the phased modulation and the phase of maximum flux.

Amplitude maps: In both the standard and inside-out amplitude maps most of the emission components seen in the Doppler tomograms are heavily flux modulated. In the standard amplitude map the emission associated with the lower accretion curtain (represented by the spot in the upper right quadrant) appears to be the most flux modulated component. The emission associated with the upper accretion curtain (represented by the spot in the lower left quadrant) is also flux modulated, but it is split into two modulating components. In the inside-out amplitude map this emission is also split into two components, but now they appear to be the most modulated. There is, however, no clear evidence in the trailed spectra that there are multiple components that can produce this and therefore it is probably not real.

Phase of maximum flux maps: In both the standard and inside-out phase of maximum flux maps the proposed upper curtain appears brightest at spin phase 0.5 (green) when the observer has a lateral view of the curtain. In the inside-out map the low ($< 500\,\mathrm{km\,s^{-1}}$) and high ($> 1500\,\mathrm{km\,s^{-1}}$) velocity parts of the proposed upper curtain, that is to say, the 'start' (as it leaves the orbital plane) and 'end' (as it falls onto the primary) of the curtain, appear brightest at spin phase 0.75 (blue) when these parts flow, respectively, towards and away from the observer. The proposed lower curtain, in both phase of maximum flux maps, appears brightest at spin phase 0.75 (blue) when the curtain is predominantly flowing towards the observer. In the inside-out map the high velocity ($> 1200\,\mathrm{km\,s^{-1}}$) part of the proposed lower curtain (as it falls onto the primary) appears brightest at spin phase 0.25 (red) when this part is predominantly flowing away from the observer. The arc of emission running through the lower right quadrant that 'connects' the proposed upper and lower curtains appears brightest around spin phases $0.0 - 0.25$ (black – red). Most striking is the clockwise progression in the phase of maximum flux starting from the proposed lower curtain at spin phase 0.75 (blue; in the upper right quadrant) along the arc of emission through spin phases $0.0 - 0.25$ (black – red; in the lower right and left quadrants) to the proposed upper curtain at spin phase 0.5 (green; in lower left quadrant).

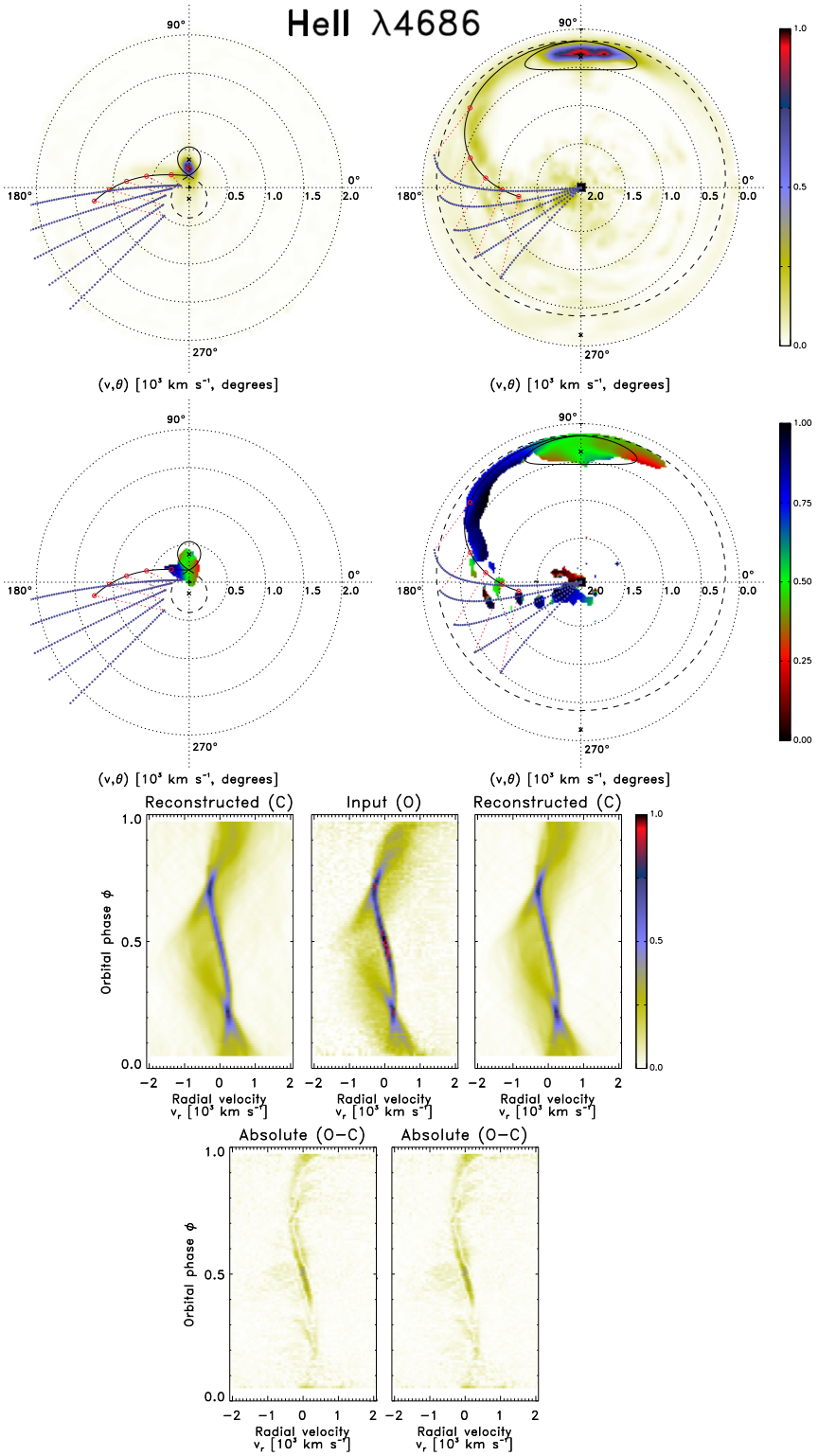

Figure 5.13. Flux modulation mapping of HU Aqr. Both the standard and inside-out residuals (i.e., absolute O − C) have an rms value of 0.108. See Section 5.3.1 for more details.

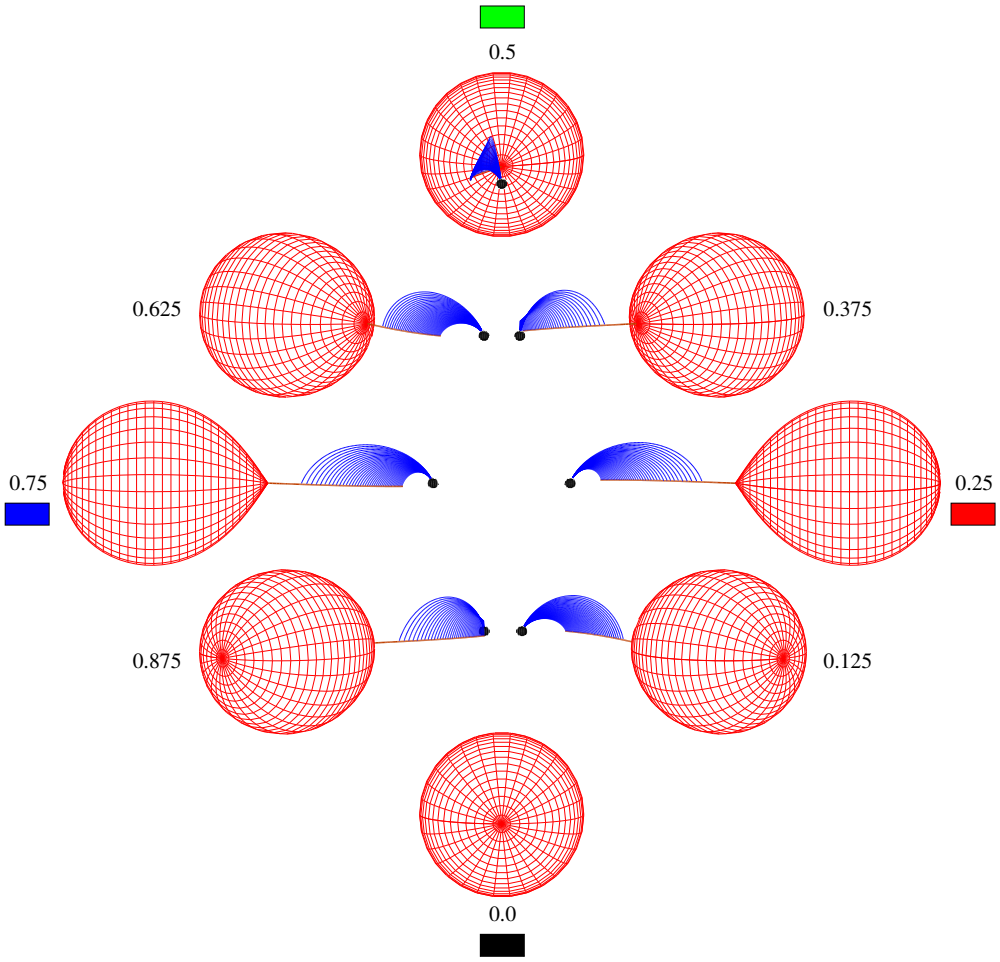

Figure 5.14. A schematic illustration of HU Aqr: An eclipsing polar. The system is viewed at eight orbital phases, namely 0.0, 0.125, 0.25, 0.375, 0.5, 0.625, 0.75 and 0.875. To aid the interpretation of the phase of maximum flux maps the corresponding colour codes are displayed for phases 0.0, 0.25, 0.5 and 0.75. The system parameters are the same as in Section 4.3. The radius of the primary has been exaggerated to twice the calculated radius based on the assumed system parameters.

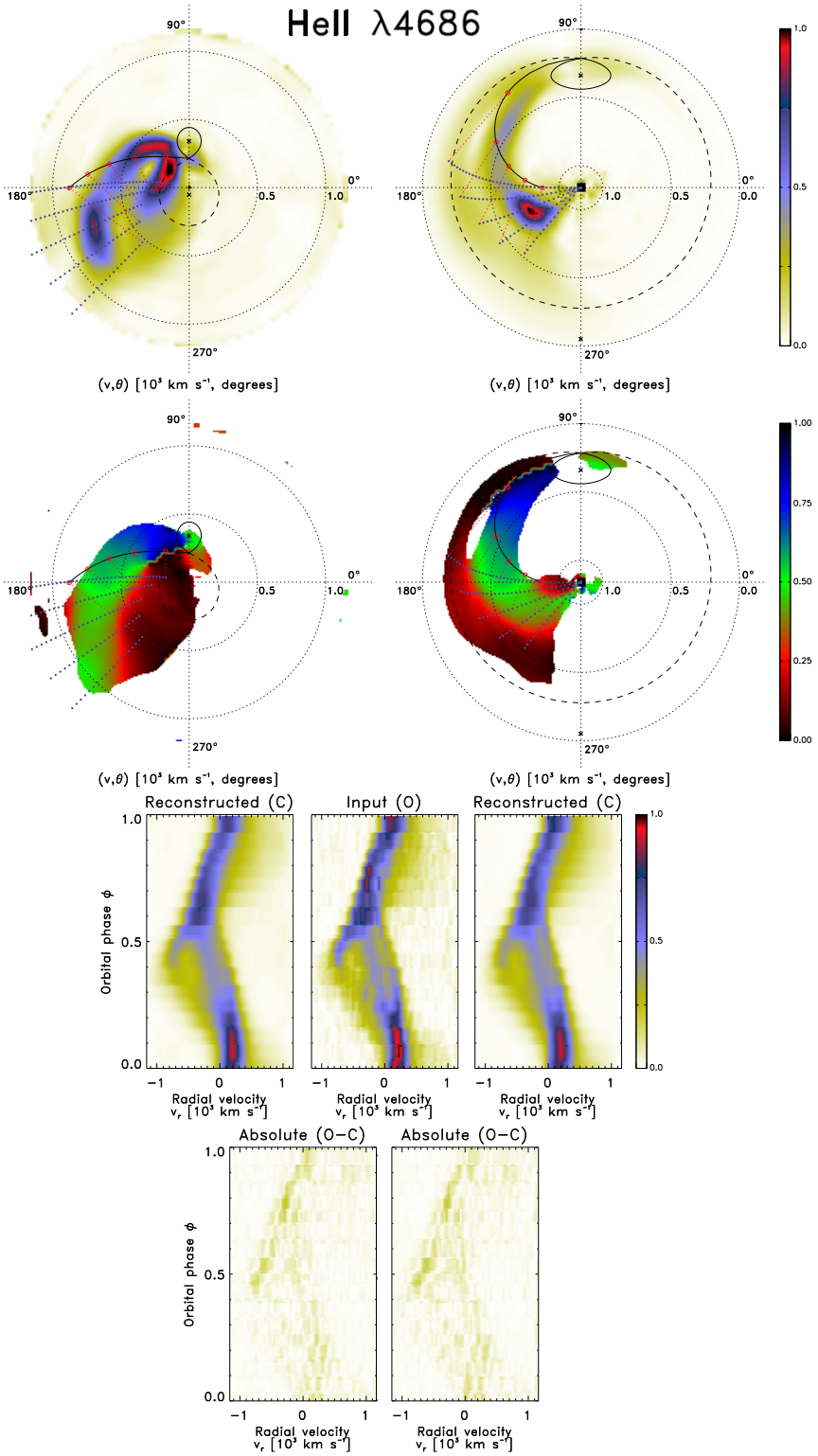

Figure 5.15. Flux modulation mapping of V834 Cen. The rms values of the standard and inside-out residuals (i.e., absolute O − C) are 0.074 and 0.078, respectively. See Section 5.3.2 for details.

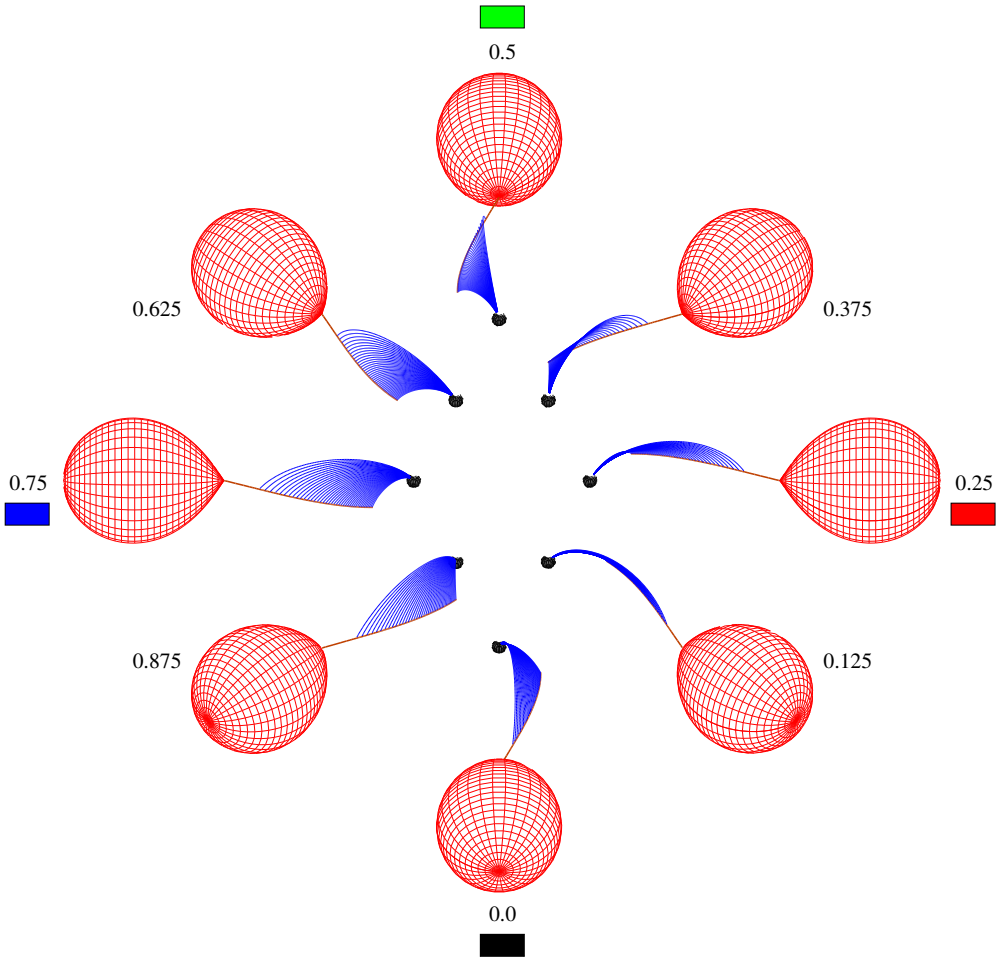

Figure 5.16. A schematic illustration of the non-eclipsing polar V834 Cen. The system is viewed at eight orbital phases, namely 0.0, 0.125, 0.25, 0.375, 0.5, 0.625, 0.75 and 0.875. To aid the interpretation of the phase of maximum flux maps the corresponding colour codes are displayed for phases 0.0, 0.25, 0.5 and 0.75. The system parameters are the same as in Figure 4.6. The radius of the primary has been exaggerated to twice the calculated radius based on the assumed system parameters.

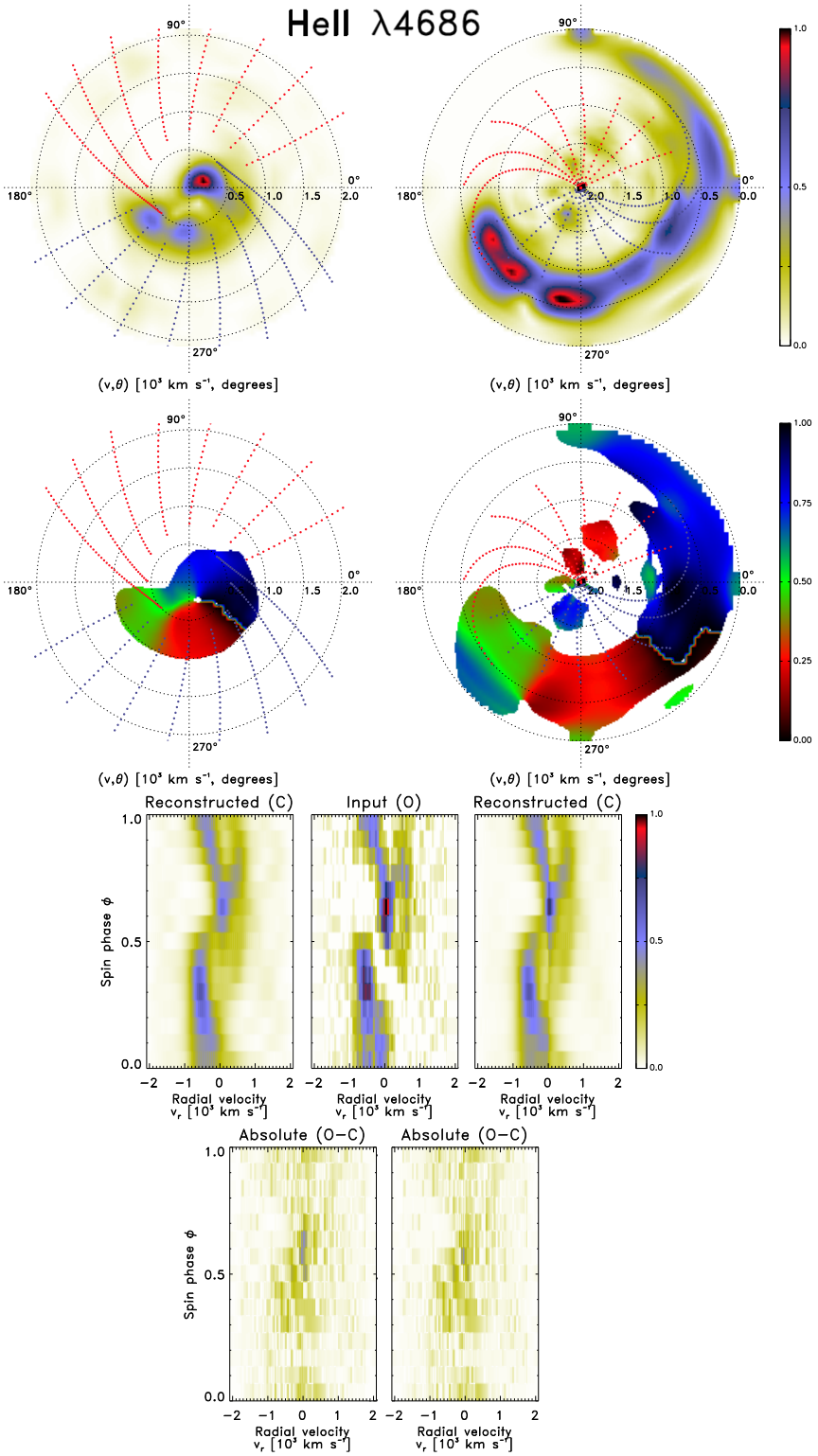

Figure 5.17. Flux modulation mapping of PQ Gem. The rms values of the standard and inside-out residuals (i.e., absolute O − C) are 0.276 and 0.257, respectively. See Section 5.3.3 for details.

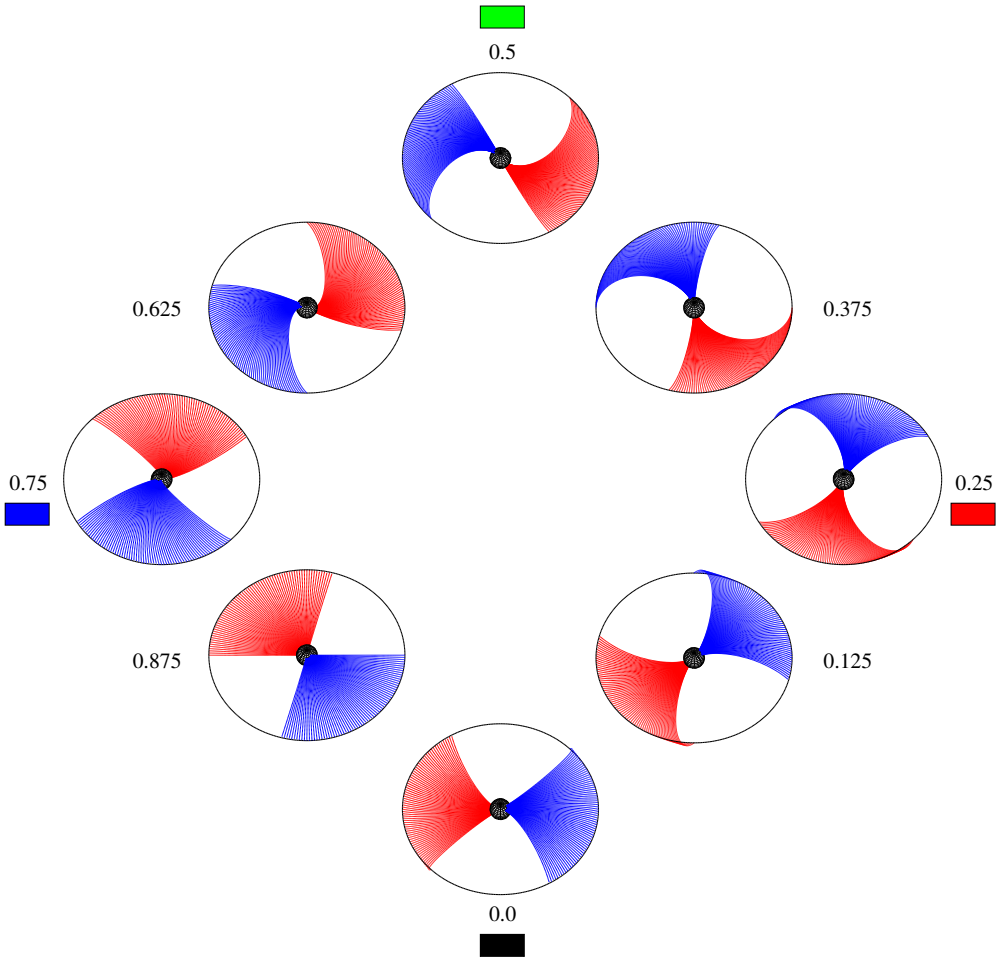

Figure 5.18. A schematic illustration of the non-eclipsing intermediate polar PQ Gem. The system is viewed at eight spin phases, namely 0.0, 0.125, 0.25, 0.375, 0.5, 0.625, 0.75 and 0.875. To aid the interpretation of the phase of maximum flux maps the corresponding colour codes are displayed for phases 0.0, 0.25, 0.5 and 0.75. The system parameters are the same as in Figure 4.7. The radius of the primary has been exaggerated to one and a half times the calculated radius based on the assumed system parameters. The upper curtain is coloured blue while the lower curtain is coloured red.

Chapter 6

Unravelling the accretion flows in the polar CTCV J1928–5001

Though she be but little, she is fierce!

– William Shakespeare, *A Midsummer Night's Dream*, Act III, Scene 2

In Chapters 3 and 5 I introduced the new techniques of inside-out Doppler tomography and flux modulation mapping, respectively. These two techniques were shown to be complementary to the established technique of standard Doppler tomography when interpreting phase-resolved spectroscopic observations of interacting binary systems. Together with flux modulation mapping the inside-out projection forms a useful addition for unravelling the different emission line components in the observed spectra of especially mCVs.

In this chapter I focus mainly on applying standard and inside-out Doppler tomography, together with flux modulation mapping, to new phase-resolved spectra of the eclipsing polar CTCV J1928−5001 obtained with the Southern African Large Telescope (SALT). The aim is to unravel the contributions of the different emission components which add to the complex emission structure seen in the trailed phase-resolved spectra. Section 6.1 is a short introduction on CTCV J1928−5001. In Section 6.2 the relevant observations and data reductions are presented. Apart from the spectroscopy, the observations also include high-speed photometry for calculating an accurate ephemeris for the phasing of the spectra. Section 6.3 starts with a basic analysis of the results from the photometry and spectroscopy before it culminates in a comprehensive tomographic analysis. A summary and conclusions are given in Section 6.4. This chapter will form the basis for a future publication to be submitted to an appropriate peer-reviewed international journal (see Section 7.2.1).

6.1 Introduction

Based on time-series photometry and optical spectroscopy Tappert et al. (2004) identified CTCV J1928−5001 as a polar candidate in a search for cataclysmic variables in the Calán–

Tololo Survey. Its status as a polar with an orbital modulation of ~ 101 min was confirmed by subsequent high-speed photometric and polarimetric observations presented by Potter et al. (2005). These polarimetric observations revealed two accretion regions on a primary with a magnetic field strength of ~ 20 MG. The light curves presented in both the above mentioned works are characterised by deep, short eclipses with extremely sharp ingresses and egresses. From their high-speed photometry Potter et al. (2005) were able to show that the eclipse lasts ~ 177 s with the ingresses and egresses lasting typically $2-3$ s. Their calculated linear eclipse ephemeris, in heliocentric Julian date (HJD), is

$$T\,(\mathrm{HJD}) = 2452879.2813386\,(58) + 0.070162312\,(9)\,E, \tag{6.1}$$

where E is the cycle number.

6.2 Observations and data reduction

6.2.1 High-speed photometry

CTCV J1928−5001 was observed for $\sim 4\frac{1}{2}$ hr on 2013 June 5 with the HIgh-speed Photo-POlarimeter (HIPPO; Potter et al. 2010) on the South African Astronomical Observatory (SAAO) 1.9 m telescope as part of an ongoing photo-polarimetric monitoring campaign of mCVs. The HIPPO has superachromatic half- and quarter-wave plates. It utilises a Thompson beam-splitter to produce the s-polarised ordinary beam (channel 1) and the p-polarised extraordinary beam (channel 2). Two photo-multiplier tubes act as detectors. This unique polarimeter produces high-speed photo-polarimetry.

Part of the above mentioned campaign involves the photometric monitoring of observable eclipsing mCVs to measure precise mid-eclipse times with the aim of detecting any orbital period variations. The high-speed (i.e., 1 ms interval) photometric data stream that is obtained as part of an observation with the HIPPO is ideal for this purpose. The 2013 June 5 observation was unfiltered and covered three full eclipses. Measurements of the sky background were taken at frequent intervals (every ~ 30 min) during the observation. The 1 ms photometric data stream obtained was sorted into channel 1 and channel 2 counts, co-added and binned into 1 s bins. The binned sky background stream was subtracted from the binned target stream. For this work the polarimetric data stream is not used, but it will be included in future work (see Section 7.2.1).

The measured mid-eclipse times from this observation were intended to be used in calculating an ephemeris to accurately phase the spectroscopic observations discussed in Section 6.2.2. However, in Section 6.3.1 it is shown that, even after more than 50000 cycles, the linear eclipse ephemeris from Potter et al. (2005), that is to say, Equation 6.1, is remarkably accurate as it produces very small (~ 100 ms) observed minus calculated (O − C) times for the eclipses from this observation.

6.2.2 Long-slit spectroscopy

CTCV J1928−5001 was successfully observed on three occasions in 2013 with the Robert Stobie Spectrograph (RSS; Burgh et al. 2003; Kobulnicky et al. 2003) on the queue-scheduled Southern African Large Telescope (SALT; Buckley et al. 2006; O'Donoghue et al. 2006) under programme 2013-1-RSA-006 (PI: Potter). The RSS uses a mosaic of three CCDs, each with 2048×4096 pixels. The width of a pixel is $15\,\mu$m. The two gaps between the three CCDs are each 15 pixels ($225\,\mu$m) wide. Each CCD has two amplifiers to aid faster readout. The effective field of view is $8'$ in diameter and the spatial plate scale is $0\farcs127$ per unbinned pixel. For the 2013 observations the RSS was configured with a $1\farcs5$ wide slit and the `pg2300` volume phase holographic grating at a rotation angle (i.e., position angle) of 32°. This configuration gives a spectral range $\sim 4050 - 5100$ Å and resolution $R \approx 2340$ at a central wavelength of ~ 4600 Å. Using a column binning factor of two for the exposures produced a reciprocal dispersion of 0.34 Å per binned pixel. The spectral ranges for the gaps between the CCDs were $\sim 4405 - 4425$ Å and $\sim 4766 - 4786$ Å. During the three observations a total of 21 spectra, covering $\sim 85\%$ of the orbit, were obtained. Each spectrum was exposed for 250 s. A thorium argon lamp reference spectrum and a set of quartz tungsten halogen flat-field frames were obtained at the end of each set of target observations.

The primary data reductions were performed in the standard way with the SALT science pipeline (Crawford et al. 2010)*. The basic pre-processing reductions applied by this pipeline include correcting the images for gain and amplifier cross talk, trimming the overscan regions from the images, and finally mosaicking the CCD amplifier images and applying a distortion correction. Correcting for the bias level is achieved through the overscan subtraction.

All secondary reductions were done with applicable `IRAF`† tasks. Cosmic ray events were cleaned with the task `lacos_spec` (Van Dokkum 2001). The wavelength calibration of the lamp reference spectra was done with the tasks `identify`, `reidentify`, `fitcoords` and `transform`. Wavelength solutions with a root mean square value less than 0.1 Å were obtained for all the reference spectra. Each set of flat-field frames was median combined with the task `imcombine` into a master flat-field frame which was illumination corrected with the task `mkillumflat`. The target spectra were divided by the applicable master flat-field frame in order to correct for pixel-to-pixel sensitivity variations of the detector. The task `background` was used to do the background subtraction from the target spectra. The sensitivity of the detector as a function of wavelength was determined by using the task `sensfunc` on a spectrum of the southern spectrophotometric standard star LTT 2415 (Hamuy et al. 1994) and taking into account the Sutherland extinction curve. This sensitivity curve was used to apply a relative flux calibration‡ to the target spectra with the task `calibrate`. The calibrated target spectra were continuum normalised with the task `continuum`. The

*`http://pysalt.salt.ac.za/`

†IRAF: the Image Reduction and Analysis Facility is distributed by the National Optical Astronomy Observatory, which is operated by the Association of Universities for Research in Astronomy, Inc. (AURA) under cooperative agreement with the National Science Foundation (NSF).

‡The variable nature of the SALT pupil (and any changing conditions during an observation) does not allow for the absolute flux calibration of the target spectra.

final one-dimensional target spectra were extracted with the task `apall`. To facilitate the phasing of the target spectra (see Section 6.3.4) the task `setjd` was used to calculate the Julian date (JD) and the heliocentric Julian date (HJD) of the mid-exposure of each target spectrum.

6.3 Results and analysis

6.3.1 Eclipse profiles

The profiles of the three observed eclipses are shown in Figure 6.1. The observed as well as the predicted or calculated times of mid-eclipse are shown in Table 6.1. The observed times were determined by using the mid-point between the sharp ($2-3$ s) ingresses and egresses of the eclipses. The width of each of the three eclipses is 177 ± 1 s. The linear eclipse ephemeris from Potter et al. (2005), that is to say, Equation 6.1, was used for the calculated times. The O $-$ C times for all three eclipses are remarkably small (~ 100 ms) despite the number of cycles (~ 50900) used in the ephemeris for the calculated times.

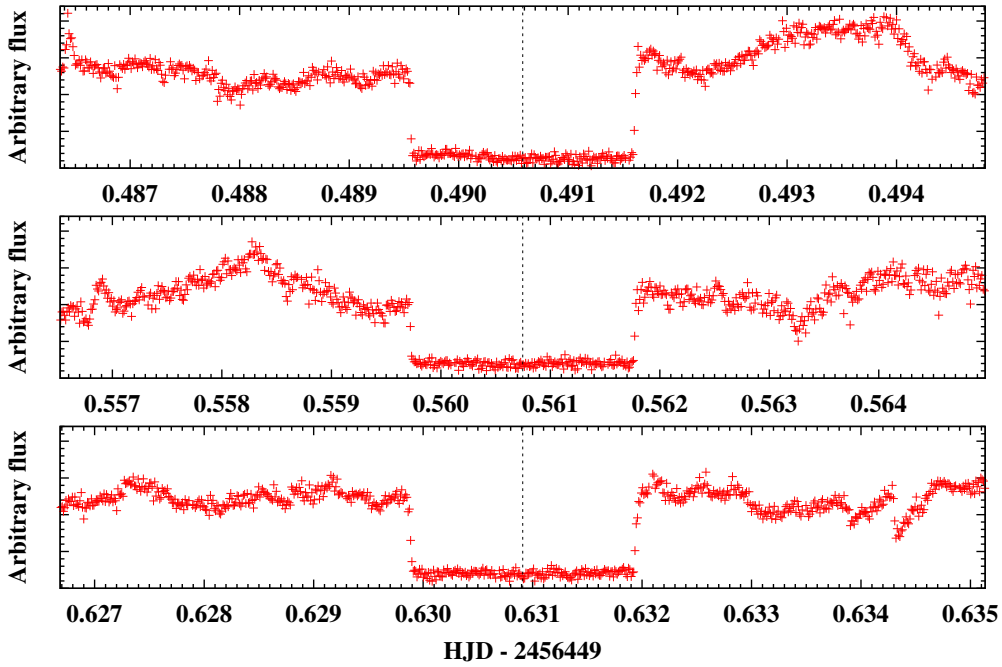

Figure 6.1. Eclipse profiles from the 2013 June 5 photometry of CTCV J1928−5001 binned into 1 s bins. The dashed black lines indicate the calculated mid-eclipse times using the linear eclipse ephemeris from Potter et al. (2005), i.e., Equation 6.1.

The stability in the HJD-based linear eclipse ephemeris of CTCV J1928−5001 warrants further investigation given the reported deviations in the HJD-based linear eclipse ephemerides of other eclipsing polars, for example, UZ For (e.g., Ramsay 1994; Dai et al.

Table 6.1. Heliocentric corrected eclipse timings from the 2013 June 5 photometry of CTCV J1928−5001. The ingresses, egresses and mid-eclipses are HJD − 2456449. Also listed are the observed minus calculated (O − C) time and the absolute *accumulated* error $\Sigma s_{\rm C}$ ($= s_{T_0} + s_{P_{\rm orb}} \times E$) in the calculated mid-eclipse, using Equation 6.1.

Ingress	Egress	Mid-eclipse	Cycle (E)	O − C (s)	$\Sigma s_{\rm C}$ (s)
0.489561(12)	0.491610(12)	0.490586(16)	50885	0.1	40.1
0.559727(12)	0.561776(12)	0.560752(16)	50886	−0.1	40.1
0.629892(12)	0.631941(12)	0.630917(16)	50887	0.1	40.1

2010; Potter et al. 2011), HU Aqr (e.g., Schwope et al. 2001; Qian et al. 2011) and DP Leo (e.g., Schwope et al. 2002; Qian et al. 2010; Beuermann et al. 2011). A complete investigation is beyond the scope of this work, but it will be pursued in future work (see Section 7.2.1). As a prelude to such an investigation I calculate a new eclipse ephemeris in the next section.

6.3.2 Eclipse ephemeris

The mid-eclipse times calculated by Potter et al. (2005), as well as those listed in Table 6.1 are all based on Coordinated Universal Time (UTC). The UTC system, however, add leap seconds irregularly and the heliocentric correction does not take into account the influence of the major planets on the movement of the centre of the Sun. In order to correct all the mid-eclipse times for the light-travel time to the barycentre of the Solar system I converted the HJD mid-eclipse times to Barycentric Julian Date (BJD) in the barycentric dynamical time (TDB) system using the time utilities described in Eastman et al. (2010). The $\rm BJD_{TDB}$ mid-eclipse times are listed in Table 6.2. Given the accuracy of the HJD-based linear eclipse ephemeris (Equation 6.1) it is possible to assign distinct cycle numbers to all the observed eclipses. A least-squares linear fit to the $\rm BJD_{TDB}$ mid-eclipse times yields the following eclipse ephemeris:

$$T\,(\mathrm{BJD_{TDB}}) = 2452879.4913750\,(92) + 0.0701623125\,(2)\,E. \tag{6.2}$$

The O − C times obtained with the new BJD-based ephemeris (Equation 6.2) are also listed in Table 6.2 and the O − C diagram is shown in Figure 6.2. Overall these O − C times are very similar to those obtained with the HJD-based ephemeris (Equation 6.1). The larger O − C times for the 1996 July eclipses are expected given the larger errors in the mid-eclipse times. At face value the mostly small O − C times suggest that the orbital period of CTCV J1928−5001 is remarkably stable. Also, a second degree polynomial fit to the mid-eclipse times does not yield a quadratic term.

As yet there is insufficient data on CTCV J1928−5001 to confirm the apparent stability of its orbital period and more high-speed observations are needed to establish a better understanding of this system. It has been included in an observing campaign at the SAAO that involves the ongoing monitoring of observable eclipsing mCVs to measure precise mid-

Table 6.2. Barycentric corrected mid-eclipse timings of CTCV J1928−5001. The observed mid-eclipses, as listed in Table 2 of Potter et al. (2005), as well as the new observations listed in Table 6.1, have been converted to BJD_{TDB}. Also listed are the observed minus calculated (O − C) time and the absolute accumulated error Σs_C in the calculated mid-eclipse, using Equation 6.2.

Mid-eclipse	ΔMid-eclipse	Cycle (E)	O − C (s)	Σs_C (s)
2450273.734079	0.005500	−88021	−33.5	2.0
2450273.804279	0.002300	−88020	−30.2	2.0
2450274.716379	0.001900	−88007	−31.1	2.0
2450274.786879	0.001900	−88006	−1.9	2.0
2450274.857179	0.001900	−88005	10.0	2.0
2450295.625179	0.001200	−87709	6.1	2.0
2450295.695379	0.001200	−87708	9.4	2.0
2452879.282085	0.000160	−50885	−1.6	1.4
2452879.352265	0.000016	−50884	−0.1	1.4
2452879.492591	0.000016	−50882	0.1	1.4
2452880.264379	0.000016	−50871	0.3	1.4
2452880.334542	0.000016	−50870	0.3	1.4
2452880.404699	0.000016	−50869	−0.1	1.4
2452880.474860	0.000016	−50868	−0.2	1.4
2452881.316775	0.000120	−50856	−3.1	1.4
2452881.386978	0.000016	−50855	0.4	1.4
2452881.457131	0.000016	−50854	−0.4	1.4
2456449.491375	0.000016	0	0.0	0.5
2456449.561536	0.000016	1	−0.1	0.5
2456449.631701	0.000016	2	0.1	0.5

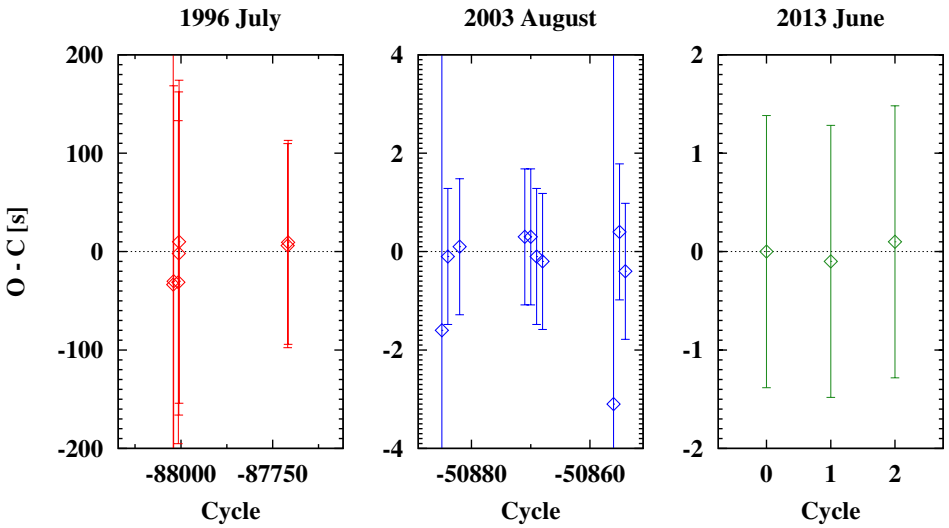

Figure 6.2. O − C diagram of CTCV J1928−5001. The O − C times were calculated using the new BJD-based ephemeris, i.e., Equation 6.2.

eclipse times with the aim of detecting any orbital period variations. As noted in Section 6.3.1 a more complete investigation of the mid-eclipse times of CTCV J1928−5001 will be pursued in future work (see Section 7.2.1). Such an investigation will incorporate all new observations obtained with the above mentioned observing campaign.

6.3.3 Mean orbital spectrum

The mean continuum-normalised orbital spectrum of the 2013 long-slit spectroscopic observations is shown in Figure 6.3. Some of the emission lines that characterise polars, for example, lines from the Balmer series, as well as some neutral (He I) and singly ionised (He II) helium lines, are present in the wavelength range of the spectrum. The Balmer lines Hβ (λ4861), Hγ (λ4340) and Hδ (λ4102) are the most prominent features in the spectrum. The helium lines are significantly weaker, but He I λ4471 and He II λ4686, as well as He I λ4921 and He I λ5015, are easily identifiable.

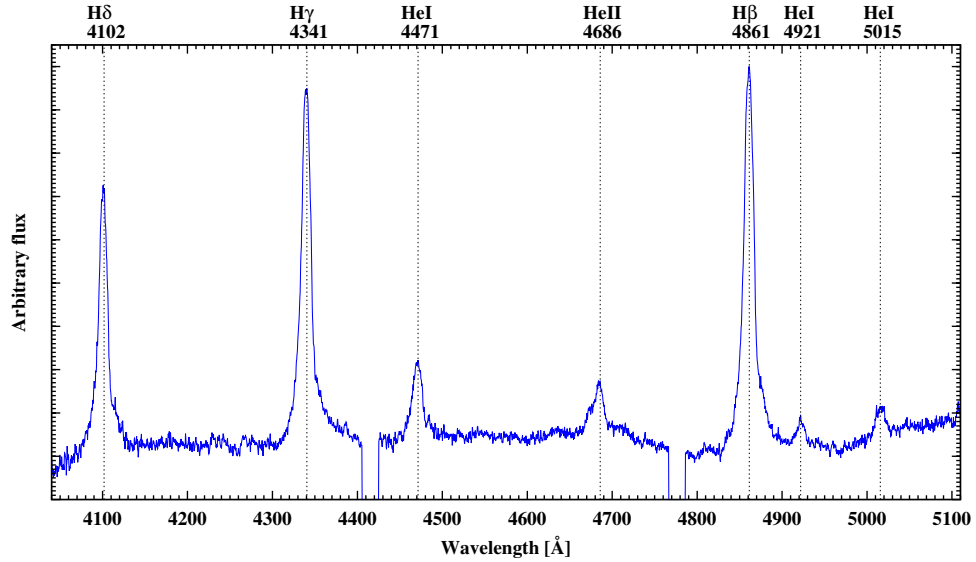

Figure 6.3. Mean continuum-normalised spectrum of the 2013 long-slit spectra of CTCV J1928−5001. The most prominent emission lines are indicated for easy reference. The gaps between the CCDs are clearly visible between $\sim 4405 - 4425$ Å and $\sim 4766 - 4786$ Å.

Normally in the spectra of polars the strength of He II λ4686 is comparable to that of Hβ (Mukai 1988; Warner 2003), but here the strength ratio is only $\sim$ 1:5. The doubly ionised carbon (C III) and nitrogen (N III) Bowen fluorescence complex at $4640 - 50$ Å commonly seen in polars (Schachter et al. 1991, and references therein) is barely visible. Schwope et al. (1993) attributed a similar weakness of He II λ4686 and absence of the Bowen blend in their spectroscopic observations of the polar V834 Cen to the object being in an intermediate high state. Also notable is the flattish Balmer decrement (Hγ/H$\beta \simeq 1$). According to Williams (1991) this is indicative of a temperature of $\sim 10^4$ K in the emission region. The work of Williams focussed on emission regions in accretion discs, but Gerke et al. (2006) notes that

the same should hold for emission regions in the accretion flow of polars. The Hγ/Hβ ratio for an optically thin gas (case B) is $\simeq 0.5$ (Brocklehurst 1971), therefore the Balmer emission lines are interpreted to be optically thick.

It is important to note that the mean spectra of the 3 individual observing epochs (not shown) exhibit the same structure described above for the mean of all the spectra. This confirms that CTCV J1928−5001 was in the same accretion state during the 3 observations.

6.3.4 Trailed phase-resolved spectra

Table 6.3. Orbital phasing of the 2013 long-slit spectra of CTCV J1928−5001.

Date (2013)	Spectrum	Mid-exposure	Cycle (E)	Orbital phase (ϕ)
May 2	1	2456413.509544	−513	0.1630
	2	2456413.512440	−513	0.2043
	3	2456413.515334	−513	0.2455
	4	2456413.518227	−513	0.2867
	5	2456413.521121	−513	0.3280
	6	2456413.524015	−513	0.3692
	7	2456413.526908	−513	0.4105
	8	2456413.529802	−513	0.4517
	9	2456413.532696	−513	0.4930
June 17	1	2456461.386480	169	0.5370
	2	2456461.389374	169	0.5782
	3	2456461.392268	169	0.6195
	4	2456461.395161	169	0.6607
July 16	1	2456490.303907	581	0.6874
	2	2456490.306802	581	0.7286
	3	2456490.309695	581	0.7699
	4	2456490.312589	581	0.8111
	5	2456490.315482	581	0.8524
	6	2456490.318376	581	0.8936
	7	2456490.321269	581	0.9348
	8	2456490.324163	581	0.9761

The orbital phasing of the spectroscopic observations is shown in Table 6.3. This phasing was produced by using Equation 6.2, that is, the BJD-based linear eclipse ephemeris calculated in Section 6.3.2. I note that the same phasing is produced when using Equation 6.1, that is, the HJD-based linear eclipse ephemeris calculated by Potter et al. (2005). The orbital phase range covered by the 21 spectra is $0.1427 - 0.9967$ with each spectrum covering 0.0412. Near perfect continuity in phase coverage in the cross-over from one observation to the next was obtained. The phase gap between the last and first spectrum taken on May 2 and June 17, respectively, is 0.044. For the last and first spectrum taken on June 17 and July 16, respectively, the phase gap is 0.0267.

The trailed phase-resolved spectra of the main emission lines are shown in Figure 6.4. The trailed spectra of the three helium emission lines, that is, He I λ4471, He II λ4686 and

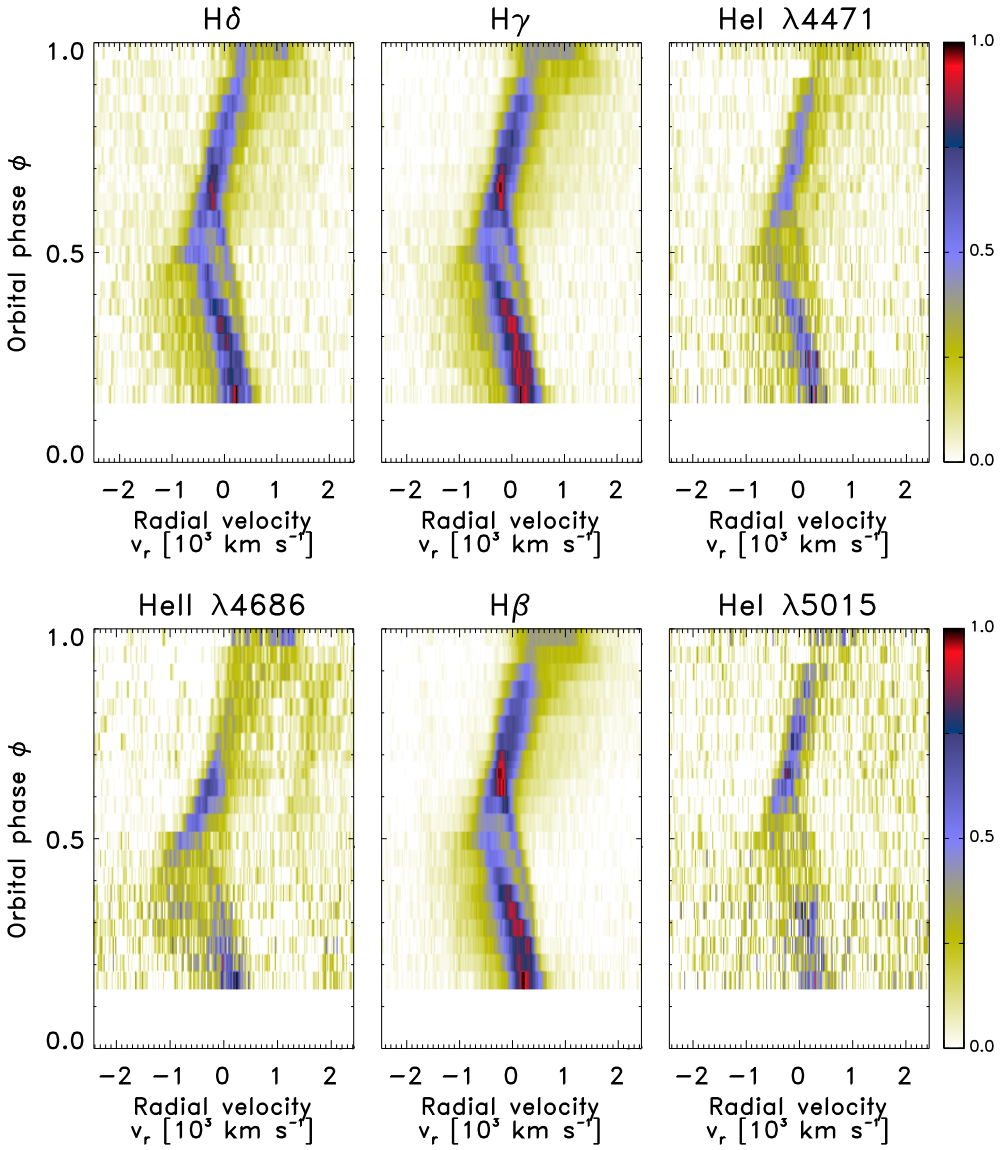

Figure 6.4. Trailed phase-resolved spectra of the main emission lines of CTCV J1928−5001.

He I λ5015 are relatively noisy compared to that of the three Balmer emission lines Hδ, Hγ and Hβ. Also, the He II λ4686 trailed spectra are contaminated with low level emission from He I λ4713. The same complex structure is visible in the trailed spectra of all the lines and at least two emission components are discernible in the trailed spectra of the Balmer and the neutral helium lines*. There is a blended low- to mid-velocity component which is bright between phases $0.15 - 0.4$. It becomes separated at phase 0.3 and is fainter between phases $0.4 - 0.6$. At phase 0.6 it becomes blended again and is bright between phases $0.6 - 0.7$. After this it gradually becomes fainter. A fainter high-velocity broad base component underlying

*The trailed spectra of He II λ4686 are excluded from the discussion as it is too noisy and contaminated.

the whole phase range is also discernible. The complex structure and the two emission components are best seen in the trailed spectra of the Balmer lines. Given the low signal-to-noise of the helium lines and the overall similarities in the trailed spectra of the Balmer lines, only the Hβ emission line, which has the highest signal-to-noise ratio, will be used for the tomographic analysis that follows in the next section.

6.3.5 Doppler tomography: standard and inside-out projections

Figure 6.5 shows standard and inside-out Doppler tomography based on the Hβ emission line from the 2013 spectroscopic observations of CTCV J1928 − 5001. All 21 spectra, which covers the orbital phase range $\sim 0.14 - 1.0$, were used to construct the tomograms. Each spectrum covers 0.0412 of the phase and has 236 velocity points in the extracted radial velocity range around the Hβ emission line ($n = 4956$). The model velocity profile overlay shown in both tomograms is based on one of the models used by Potter et al. (2005) with an inclination angle $i = 78°$, a primary mass $M_1 = 0.5 M_\odot$, a mass ratio $q = 0.2$ and an orbital period $P_{\rm orb} = 0.070162312\,{\rm d}\,(\sim 101\,{\rm min})$.

Trailed spectra: The features seen in the trailed input spectra (middle panel of Figure 6.5) were discussed in the previous section (see Section 6.3.4). The blended low- to mid-velocity component is associated with blended emission from the low- to mid-velocity part of the ballistic accretion stream and the irradiated hemisphere of the secondary. The broad base component can be associated with emission that is produced in different parts of the accretion flow.

CTCV J1928−5001 is an eclipsing polar and to some extent one expects that its emission structure might resemble that of HU Aqr, another eclipsing polar. However, the overall structure in the trailed spectra is more reminiscent of that of the mid-inclination, non-eclipsing polar V834 Cen, albeit without the striking blueshifted wing at the edge of the base component between phases $0.4 - 0.55$ (see Section 4.4). The idea of inclination as a driver for the observed emission structure of a polar can therefore be discarded. Instead, it serves to highlight the intrinsic differences in the accretion geometries of these polars.

The trailed reconstructed spectra from both the standard and inside-out tomograms (panels to the left and right, respectively, of the middle panel of Figure 6.5) reproduce the basic structure of the broad base component seen in the trailed input spectra. Where the trailed reconstructed spectra from the standard tomogram fail to reproduce the more complex structure of the blended low- to mid-velocity component, the trailed reconstructed spectra from the inside-out tomogram do reproduce partially the separation seen in this component between phases $0.3 - 0.6$. The overall observed flux distribution is also better reproduced in the trailed reconstructed spectra from the inside-out tomogram, especially the bright parts. Compared to its compact projection in the standard tomogram the lower velocity emission is projected into more pixels in the inside-out tomogram which better separates the contributing elements of the blended emission component (see discussion below). This allows the inside-out projection to reproduce the blended low- to mid-velocity component in the trailed reconstructed spectra better than the standard projection. The incomplete

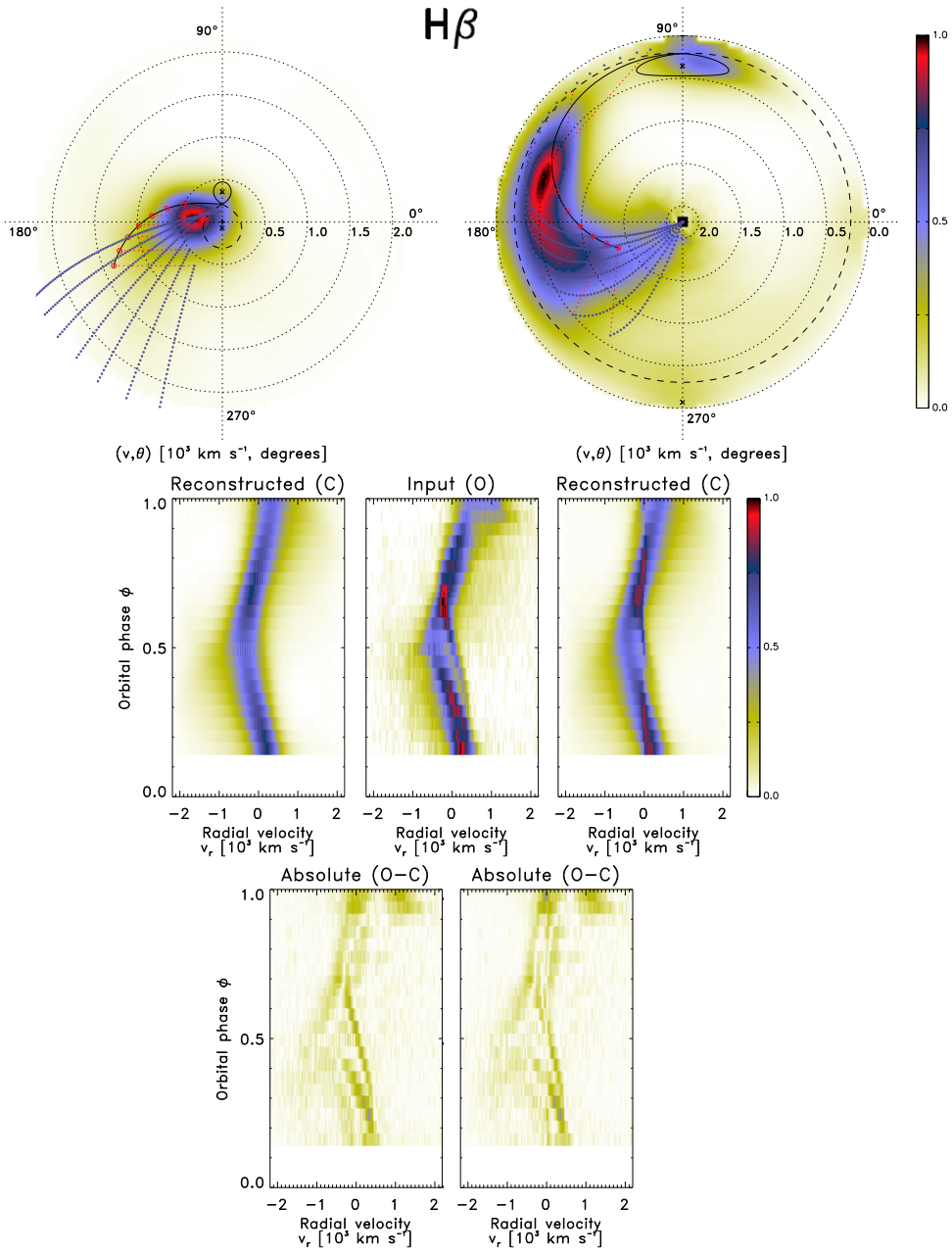

Figure 6.5. Doppler tomography of CTCV J1928−5001. The standard and inside-out tomograms are shown in the top left and right panels, respectively. The middle panel shows the trailed input spectra with the trailed reconstructed spectra for the corresponding tomogram to the left and right of it. The bottom left and right panels show the trailed absolute residual spectra for the corresponding tomogram. The rms values of the standard and inside-out residuals (i.e., absolute O − C) are 0.257 and 0.244, respectively. See Section 6.3.5 for details.

reconstructed parts from both projections, however, are clearly seen in the respective trailed absolute O − C spectra (bottom panels of Figure 6.5). The rms values of the residuals of

the standard and inside-out projections are 0.257 and 0.244, respectively, which confirms the greater success of the inside-out projection in reproducing the input spectra. In Section 6.3.6 it is shown that the flux modulation mapping technique is able to improve on the reproduction of the complex structure and the flux distribution even further.

Tomograms: In the standard tomogram (top left panel of Figure 6.5) the binary's centre of mass is at the centre of the tomogram, marked with a plus (+). The binary's centre of mass is effectively the zero velocity outer circumference in the inside-out tomogram (top right panel of Figure 6.5). In both tomograms the centres of mass of the primary and secondary are marked with crosses (×). The model velocity profile overlay shown in both tomograms includes the Roche lobes of the primary (dashed line) and the secondary (solid line) as well as a single particle ballistic trajectory from the L_1 point up to 75° in azimuth around the primary (solid line). Magnetic dipole trajectories are calculated at 10° intervals from 15° to 75° in azimuth around the primary (thin dotted lines). The first dipole connection on the ballistic stream (small red circles) is at ($493\,\mathrm{km\,s^{-1}}$, 155°). The first dipole trajectory starts at ($128\,\mathrm{km\,s^{-1}}$, 101°), with consecutive trajectories starting at locations with progressively higher velocities and polar angles. The dipolar axis azimuth and co-latitude, also taken from Potter et al. (2005), are 108° and 15°, respectively. A one-pole accretion configuration is assumed, in order to prevent an overcrowded velocity profile.

The standard tomogram is dominated by a large patch of blended emission which covers most of the low- to mid-velocity parts of the upper and lower left quadrants. This blended emission is compact and is almost symmetrically centred on $\sim$($330\,\mathrm{km\,s^{-1}}$, 180°). It contains contributions from the irradiated secondary and the ballistic accretion stream. It probably also contains emission from the lower velocity part of the magnetically confined accretion flow, as is alluded to by the model velocity profile overlay. However, none of these emission components is clearly discernible in this almost blob-like emission distribution in the standard tomogram. The higher velocity ($> 1000\,\mathrm{km\,s^{-1}}$) part of the broad base component seen in the trailed spectra appears very diffused in the lower left quadrant. This emission can be associated with the higher velocity part of the magnetically confined accretion flow as indicated by the model velocity profile overlay.

In the inside-out tomogram the different emission components that contribute to the total emission are neatly separated. There is a separate bright patch of emission clearly visible at $\sim$($350\,\mathrm{km\,s^{-1}}$, 90°) which is fairly well traced by the velocity profile of the Roche lobe of the secondary. The trailing hemisphere is noticeably brighter than the leading hemisphere. A probable explanation for this is that the irradiation from the primary in the direction of the leading hemisphere of the secondary is partially blocked by the ballistic accretion stream. In other words, the ballistic stream is probably casting a shadow on the leading hemisphere making it appear less bright than the trailing hemisphere. It is worth to note that an offset in the emission associated with a specific emission component may be ascribed to an offset in the phasing of the spectra. However, given the accuracy of the mid-eclipse ephemeris used to phase the input spectra on mid-exposure it is highly unlikely to be the reason in this case.

The ballistic stream is now also discernible as a faint arc of emission along the velocity profile of the model stream trajectory in the velocity range $(200 - 300\,\mathrm{km\,s^{-1}}, 105 - 135°)$. After this point the ballistic stream becomes blended with emission associated with the low-velocity part of the magnetically confined accretion flow as it leaves the orbital plane in the threading region. The ability of the inside-out projection to separate the lower velocity emission components which appear overly compacted in the standard projection, was already demonstrated in especially the case of the polar V834 Cen (see Section 4.4). This separation of the lower velocity emission is possible as the emission is re-binned in a larger area with more pixels in the inside-out tomogram.

The emission associated with the magnetically confined accretion flow forms a bright curtain-like feature in the inside-out tomogram that covers a large part of the upper and bottom left quadrants. It stretches from the low velocities associated with the magnetically confined accretion as it leaves the orbital plane in the threading region to the high velocities associated with the magnetically confined accretion flowing down to the primary. This curtain-like feature is fairly well traced by the velocity profile of the model dipole trajectories.

6.3.6 Flux modulation mapping: standard and inside-out projections

Figure 6.6 shows the standard and inside-out flux modulation mapping results based on the 2013 long-slit spectra of CTCV J1928−5001. These results are based on the consecutive half-phase standard and inside-out Doppler tomography of CTCV J1928−5001 for the ten half-phases $0.0 - 0.5$, ..., $0.4 - 0.9$, $0.5 - 0.0$, $0.6 - 0.1$, ..., $0.9 - 0.4$ presented in Appendix A.4. The standard and inside-out velocity maps are shown left and right, respectively. The top two panels show the modulation amplitude maps and the middle two panels show the phase of maximum flux maps. The phase of maximum flux map shows only pixels where the corresponding modulation amplitude is at least 20% of the maximum amplitude. This map is colour coded to represent phase: black (0.0), red (0.25), green (0.5) and blue (0.75). The middle panel below the phase of maximum flux maps shows the trailed input spectra with the trailed summed reconstructed spectra for the ten consecutive half-phase standard and inside-out tomograms to the left and right of it, respectively. The bottom panels show the corresponding trailed summed absolute residual spectra. The model velocity profile overlay shown in all the velocity maps is the same as the one in Figure 6.5.

Trailed spectra: The summed reconstructed spectra show a slight improvement in reproducing the input spectra when compared with the reconstructed spectra in Figure 6.5, even though it is not apparent at face value. The improvement is, however, more noticeable in the sets of absolute $O - C$ spectra, now with rms values of 0.180 and 0.160 for the standard and the inside-out projections, respectively, compared to the non-modulated rms values of 0.257 and 0.244. Both projections better reproduce the flux levels in the broad base component, but there is only a marginal improvement in the more complex structure of the blended

component. As indicated by the rms values of the residuals the inside-out projection fares better overall.

Model schematic: The model spatial schematic in Figure 6.7 is a great aid in the interpretation of both the amplitude of the phased modulation and the phase of maximum flux. The model spatial schematic is based on the same system parameters used in the calculation of the model velocity profile overlay used in all the tomograms of CTCV J1928−5001. As previously noted, a one-pole accretion configuration is assumed.

Amplitude maps: In the standard amplitude map most of the blob-like emission distribution seen in the standard tomogram is shown to be flux modulated. Similar to the emission distribution the amplitude distribution is compact and blended between the contributions of the secondary and both the ballistic and the magnetically confined accretion flows. There is, however, a clear separation between the ballistic stream, which forms an arc in the velocity range ($300-1500\,\mathrm{km\,s^{-1}}$, $120-210°$), and the rest of the amplitude distribution. This arc follows closely the velocity profile of the model stream trajectory, albeit at slightly higher velocities.

On the other hand, in the inside-out amplitude map the emission components that are flux modulated are even more neatly separated. The irradiated side of the secondary is the most prominent flux modulated component which is expected because CTCV J1928−5001 is a high-inclination eclipsing system. The ballistic and magnetically confined accretion flows are separated into two arcs and a funnel. The ballistic stream forms an arc in the low- to mid-velocity range ($300-1000\,\mathrm{km\,s^{-1}}$, $120-180°$), while the low-velocity part of the magnetically confined accretion flow as it leaves the orbital plane, forms an arc in the velocity range ($300-500\,\mathrm{km\,s^{-1}}$, $140-220°$). The high-velocity ($> 1500\,\mathrm{km\,s^{-1}}$) part of the magnetically confined accretion flow as it falls towards the primary, forms a striking funnel along the velocity profiles of the model dipole trajectories. There is also an indication of flux modulation around the primary's centre of mass. However, this feature extends to a velocity of $\sim 500\,\mathrm{km\,s^{-1}}$, which is well beyond that of the primary. It is probably not an actual modulation in the emission of the primary, but rather related to the modulation in some unidentified lower velocity emission component(s).

Phase of maximum flux maps: In both the phase of maximum flux maps the secondary appears brightest around orbital phase 0.5 (green), when the irradiated side of the secondary is pointing towards the observer. The lower velocity part of the ballistic stream appears brightest at orbital phase 0.25 (red) when the observer has a full view of its inner side. The interpretation of the phase of maximum flux for the higher velocity part of the ballistic stream is ambiguous because emission from this part is blended with emission from the magnetically confined accretion flow. The low-velocity ($< 500\,\mathrm{km\,s^{-1}}$) part of the threading region appears brightest between orbital phases 0.5 (green) and 0.75 (blue) when it is predominantly flowing towards the observer. The mid- to high-velocity ($> 500\,\mathrm{km\,s^{-1}}$) part of the magnetically confined accretion flow appears brightest between orbital phases 0.75 (blue) and 0.0 (black) when the observer has a full view of it as it predominantly flows away from him or her.

6.4 Summary

I presented results from new high-speed photometric and phase-resolved spectroscopic observations of the eclipsing polar CTCV J1928−5001. The mid-eclipse timings determined from the photometric observations confirmed that the HJD-based linear eclipse ephemeris from Potter et al. (2005) is remarkably stable. As a prelude to a future work involving deeper investigation into the stability of the ephemeris I calculated a new BJD-based eclipse ephemeris. Both the HJD- and BJD-based ephemerides yielded the same phasing of the spectroscopic observations. The mean orbital spectrum is dominated by the Balmer emission lines Hβ (λ4861), Hγ (λ4340) and Hδ (λ4102). Notably, the He II λ4686 emission line is relative weak compared to Hβ. Together with the absence of the Bowen fluorescence complex at $4640-50$ Å commonly seen in polars, this suggests that CTCV J1928−5001 was observed in an intermediate high state.

I performed standard and inside-out Doppler tomography on the Hβ emission line extracted from the phase-resolved spectroscopic observations. The standard tomogram is dominated by a large blob-like patch of emission associated with contributions from the irradiated secondary, as well as the ballistic and magnetically confined accretion flows. However, none of these emission components is clearly discernible. In the inside-out tomogram, as expected, given especially the results obtained for the polars HU Aqr and V834 Cen (see Sections 4.3 and 4.4, respectively) these emission components are neatly separated.

I also applied flux modulation mapping, in both the standard and inside-out projections, to the consecutive half-phase Doppler tomography of CTCV J1928−5001. The compactness of the emission distribution in the standard projection puts a limit on the information that can be derived for this projection from the amplitude of the phased modulation. However, in both projections the modulating low-velocity parts of the ballistic and the magnetically confined accretion flows are neatly separated. In the inside-out projection the modulating higher velocity part of the magnetically confined accretion flow is also exposed. This greatly emphasises the funnelling of the emission as it falls towards the primary. Furthermore, the inside-out projection clearly exposed the modulation in the secondary, which is expected due to the high inclination angle of CTCV J1928−5001.

In both projections the phase of maximum observed flux satisfies the expected modulation based on the modelled geometry of CTCV J1928−5001. In the standard projection, however, the phasing of the modulating high-velocity emission is lost due to it being too tenuous in this projection. In the inside-out projection the phasing of most of the modulating low-velocity emission is preserved despite it being more tenuous in this projection.

Overall, these results establish that the inside-out projection exposes low-velocity emission details that are overly compacted and enhances high-velocity emission details that are overly tenuous in the standard projection. The extra emission information obtained with the inside-out projection for CTCV J1928−5001 is extremely valuable to get a more complete picture of the emission components in this system.

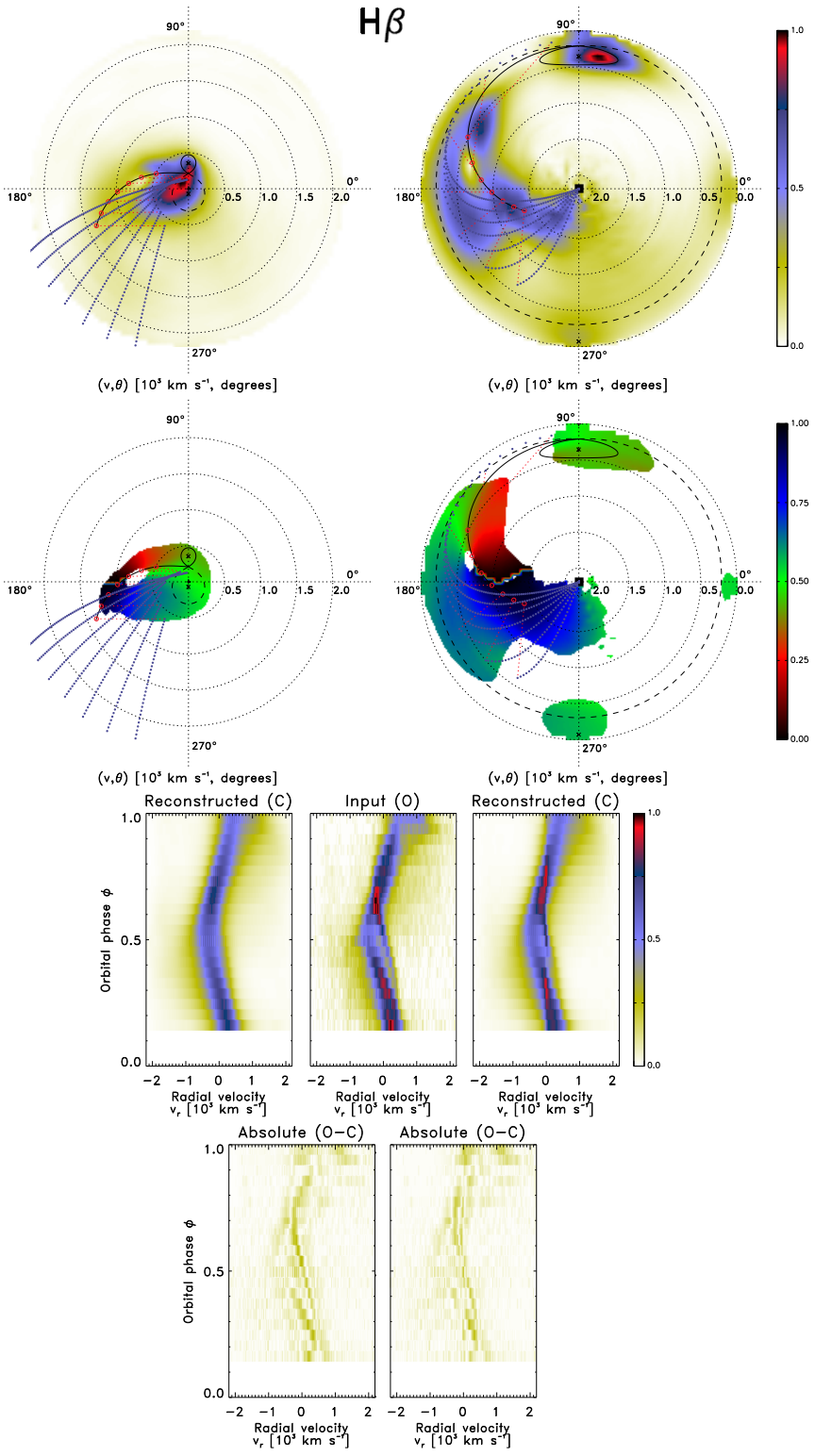

Figure 6.6. Flux modulation mapping of CTCV J1928−5001. The rms values of the standard and inside-out residuals (i.e., absolute O − C) are 0.180 and 0.160, respectively. See Section 6.3.6 for details.

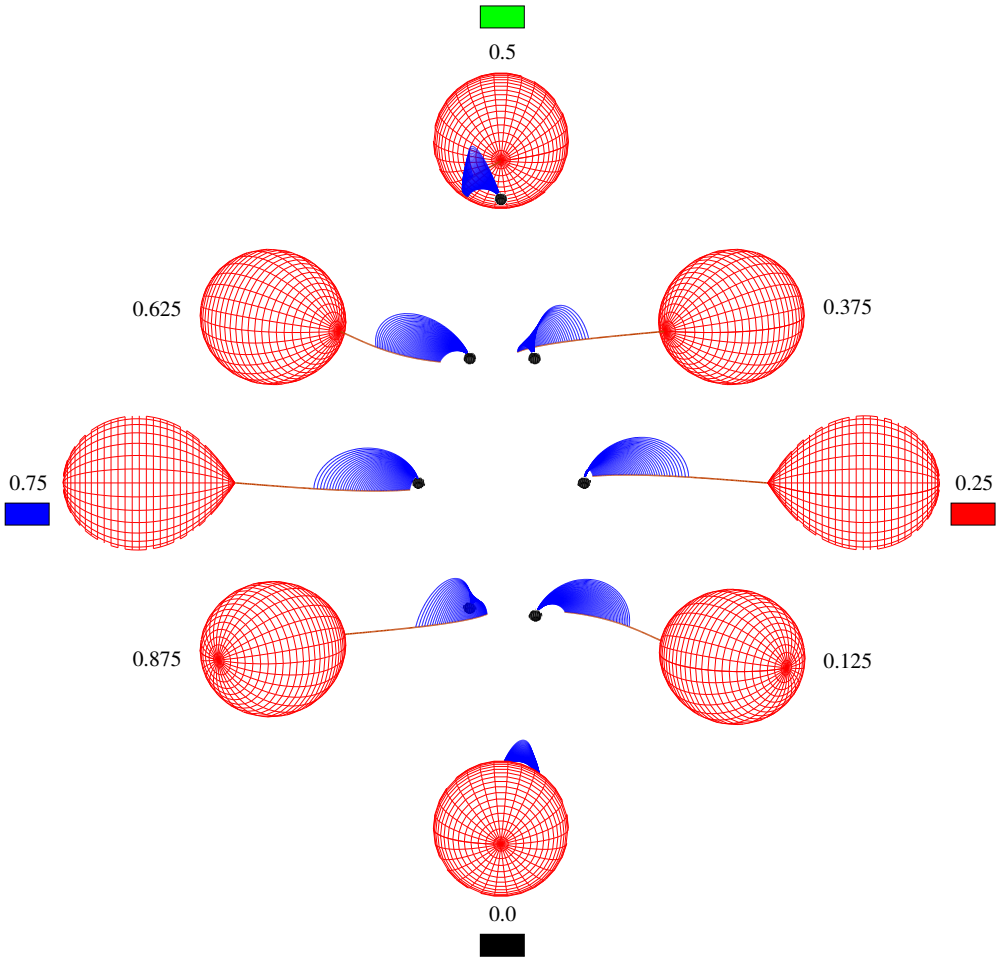

Figure 6.7. A schematic illustration of the eclipsing polar CTCV J1928−5001. The system is viewed at eight orbital phases, namely 0.0, 0.125, 0.25, 0.375, 0.5, 0.625, 0.75 and 0.875. To aid the interpretation of the phase of maximum flux maps the corresponding colour codes are displayed for phases 0.0, 0.25, 0.5 and 0.75. The system parameters are the same as in Figure 6.5. The radius of the primary has not been exaggerated.

Chapter 7

Summary and future work

Mary, this is the short and the long of it: ...

– William Shakespeare, *The Merry Wives of Windsor*, Act II, Scene 2

In this chapter I summarise the results that were obtained during my investigation of inside-out Doppler tomography and flux modulation mapping. Finally, I conclude with an overview of some of the exciting future work that will build on the work done for this thesis.

7.1 Summary of results

7.1.1 Inside-out Doppler tomography

I have developed an inside-out projection for, and investigated its application in the Doppler tomograms of cataclysmic variables. The inside-out tomogram is constructed by projecting the observed phase-resolved spectra directly onto the inside-out coordinate frame with zero velocity transposed to the outer circumference and the maximum velocities to the centre of the tomogram. I refactored and extended the fast maximum entropy Doppler tomography code presented by Spruit (1998) to incorporate the inside-out projection in order to construct the inside-out tomogram independently of the standard tomogram. I applied the inside-out projection to published data of a number of CVs and mCVs which were selected for the distinct accretion features that are apparent in their trailed spectra and that are exposed through standard Doppler tomography. I also applied the inside-out projection to new data obtained with the SALT for the eclipsing polar CTCV J1928−5001.

7.1.1.1 Non-magnetic cataclysmic variables

WZ Sge (Section 4.1): The standard tomogram of the non-eclipsing dwarf nova WZ Sge shows a prominent accretion disc and bright spot where the ballistic accretion stream impacts the outer edge of the disc. In the inside-out tomogram there is a redistribution of disc brightness, that is, in the standard tomogram the disc appears to brighten for lower

velocities whereas in the inside-out tomogram the disc brightens for higher velocities. The difference arises because the higher velocity emission emanating from the inner regions of the disc are spread out over a larger area with more pixels in the standard tomogram, whereas it is concentrated in a smaller area with fewer pixels in the inside-out tomogram as is more in line with the expected brightness distribution caused by the disc temperature profile. Given the relatively low mass ratio ($q \sim 0.1$) of WZ Sge this data set only marginally highlighted the vertical asymmetry in the brightness distribution in a tomogram with an off-centre projection of the accretion disc, that is, with the tomogram centred on the rest frame of the binary. The asymmetry is somewhat enhanced in the inside-out tomogram, but it can be removed by subtracting the orbitally induced Doppler velocity of the primary from the phase-resolved input spectra.

IP Peg (Section 4.2): The standard tomogram of the eclipsing dwarf nova IP Peg shows a prominent spiral structure in its accretion disc and emission associated with the irradiated secondary. The inside-out tomogram also shows these features, albeit with a change in the relative contrast levels of the features. The emission associated with the secondary is now placed 'outside' the disc in velocity coordinates. The dominant spiral structure of the shocks in the disc is clearly seen and the shocks are now spiralling 'inwards' from lower to higher velocities. Due to the relatively high mass ratio ($q \sim 0.5$) of IP Peg the vertical asymmetry in the brightness distribution in the tomogram centred on the rest frame of the binary is more pronounced than in the case of WZ Sge. This implies that it is crucial to consider the mass ratio (q) of the system when interpreting the brightness distribution in a tomogram. The asymmetry in the brightness distribution is removed in the tomogram centred on the rest frame of the primary resulting in a more circularly symmetric brightness distribution. This, together with the 'inwards' spiralling appearance of the shocks, creates a velocity image which is perhaps more intuitive with the expected radial disc profile of the shocks.

7.1.1.2 Magnetic cataclysmic variables

HU Aqr (Section 4.3): The emission associated with a ballistic accretion stream is very prominent in the standard tomogram of the eclipsing polar HU Aqr, but the emission associated with the irradiated secondary dominates the brightness scale due to its compact projection. In the inside-out tomogram the more extended projection of the emission associated with the secondary allows other emission features to appear brighter. The distribution in brightness along the ballistic stream is more prominent compared to the standard tomogram, that is, the lower velocity part is even fainter, whereas the mid- and high-velocity parts are significantly brighter. The lower velocity emission appears fainter as the emission is re-binned in a larger area with more pixels. The mid-velocity emission appears brighter because overall the relative contrast levels changed due to the more extended projection of the secondary. The high-velocity emission appears brighter as it is re-binned in a smaller area with fewer pixels. This allows the ballistic accretion stream to be discernible to one and a quarter times its velocity extent in the standard tomogram. Also, the diffuse emission

associated with the magnetically confined accretion flow that has left the orbital plane, is discernible to twice its velocity extent in the standard tomogram.

V834 Cen (Section 4.4): In the standard tomogram of the non-eclipsing polar V834 Cen the emission associated with a magnetically confined accretion flow is prominent, but the brightness scale is dominated by the blended emission associated with the irradiated secondary and ballistic stream. In the inside-out tomogram this blended emission is more separated. This allows the separation between the lower velocity emission from the ballistic accretion stream and that from the magnetically confined accretion to be more pronounced compared to the standard tomogram. More striking in the inside-out tomogram, however, is the funnelling of the emission associated with the magnetically confined accretion flow as it falls towards the primary.

PQ Gem (Section 4.5): The standard spin-cycle tomogram of the intermediate polar PQ Gem exclusively shows emission associated with a magnetically confined accretion flow locked on the spin period of the primary. As expected, the inside-out tomogram of PQ Gem shows an extended projection of the lower velocity ($< 1000\,\mathrm{km\,s^{-1}}$) emission associated with the accretion curtains. This significantly changes the apparent flux distribution between these two emission features which places greater emphasis on the difference in their velocities.

CTCV J1928–5001 (Section 6.3.5): A large blob-like patch of emission dominates the standard tomogram of the eclipsing polar CTCV J1928−5001. This emission is associated with contributions from the irradiated secondary, as well as the ballistic and magnetically confined accretion flows, but none of these emission components is clearly discernible. In the inside-out tomogram, however, these emission components are neatly separated. The secondary presents as a separate bright patch of emission at its expected position in the tomogram. The ballistic stream is now also discernible and presents as a faint arc of emission along the velocity profile of the model stream trajectory. The emission associated with the magnetically confined accretion flow forms a bright curtain-like feature which covers a large part of the tomogram.

7.1.2 Flux modulation mapping

I also applied the new flux modulation mapping technique, in both the standard and inside-out projections, to the above mentioned mCVs (HU Aqr – Section 5.3.1, V834 Cen – Section 5.3.2, PQ Gem – Section 5.3.3, CTCV J1928−5001 – Section 6.3.6). I found that the technique neatly extracts how the emission components in these systems modulate over an observed orbital or spin phase. The information obtained through the amplitude of the phased modulation and the phase of maximum observed flux greatly adds to our understanding of different accretion configurations in polars, especially. Also, the flux modulation mapping technique gives a significant improvement in reproducing the input spectra adding more confidence in the interpretation of the modulation maps.

A notable result obtained with the modulation maps is the clear separation of the ballistic

stream from the magnetically confined accretion flow as it leaves the orbital plane. The separation is especially prominent in both the standard and inside-out modulation maps of V834 Cen and CTCV J1928−5001. It is worth noting that a similar separation is not seen in the emission distribution of their non-modulated Doppler tomograms. This underscores the value of the flux modulation mapping technique as a useful aid in the tomographic analysis of the accretion flows of mCVs.

7.1.3 Conclusion

The Doppler tomographic results presented in this work show that the standard projection tends to concentrate and enhance lower velocity features while higher velocity features are more separated and dispersed. Conversely, the results show that the inside-out projection tends to concentrate and enhance higher velocity features while lower velocity features are more separated and dispersed. In the inside-out tomogram lower velocity emissions are distributed over more pixels covering a larger surface area further from the centre of the tomogram, whereas higher velocity emissions are compacted into fewer pixels covering a smaller surface area closer to the centre of the tomogram. This is perhaps more consistent with the spatial emission distribution in disc-accreting CVs where the high- and low-velocity disc emissions are produced in, respectively, smaller and larger fractions of the total disc volume.

I also note that the results, especially for the polars, show that the inside-out projection exposes low-velocity emission details which are overly compacted in the standard projection. Similarly, it enhances high-velocity emission details which are washed out in the standard projection. This is apparent for the polars where the blob-like low-velocity emission in their standard tomograms is more exposed in their inside-out tomograms, making it easier to distinguish between the ballistic and magnetic accretion flows that are evident in their trailed spectra. Also, for all the polars investigated the high-velocity magnetic accretion flows not seen in their standard tomograms are revealed in their inside-out tomograms. Essentially, the inside-out projection has the ability to reveal emission details not discernible in the standard projection.

Both the ‘expanded’ view of the lower velocity, higher intensity emissions and the ‘enhanced’ view of the higher velocity, lower intensity emissions obtained with the inside-out projection are uniquely geared to investigate the different configurations of the contributing emission components in the respective regimes. The extra information obtained with the inside-out projection is extremely valuable to form a more complete picture of these emission components, broadening our knowledge of the accretion dynamics in these systems. I conclude that my new technique of inside-out Doppler tomography complements the existing standard technique. Together with flux modulation mapping, it forms a useful addition for unravelling the different emission line components in the observed spectra of especially polars.

7.2 Future work

7.2.1 Investigating the polar CTCV J1928–5001

The photometric and spectroscopic results presented for CTCV J1928−5001 in Chapter 6, as well as the polarimetric observations (see Section 7.2.1.1) and the investigation into the apparent lack of any orbital period variations (see Section 7.2.1.2), are in preparation to be submitted to an appropriate peer-reviewed international journal.

7.2.1.1 Polarimetric observations

The 2013 June 5 observation of CTCV J1928−5001 was done with the HIPPO (Potter et al. 2010) on the SAAO 1.9 m telescope. See Section 6.2.1 for a more complete description of the observation. Only the photometric data stream produced by the HIPPO was used in the eclipse analyses presented in Sections 6.3.1 and 6.3.2. I am in the process of reducing the polarimetric data stream (in accordance to Potter et al. 2010) and Stokes imaging (see Potter et al. 1998, 2004) will be used to model the polarimetric observations. Together with any detected polarimetric variations the modelling will provide a comprehensive view of the accretion region(s) on the surface of the white dwarf. This should facilitate a useful comparison with the results presented by Potter et al. (2005), thereby providing an insight into the changes (if any) in the accretion dynamics of the system over nearly a decade.

7.2.1.2 Searching for orbital period variations

It was shown in Section 6.3.1 that the HJD-based linear ephemeris (Equation 6.1; Potter et al. 2005) produce remarkably small O − C times (~ 100 ms) for the 2013 June 5 eclipses, despite the number of cycles (~ 50900) used in the ephemeris for the calculated times. This prompted the calculation of a BJD-based linear ephemeris (Equation 6.2) that includes the 2013 June 5 mid-eclipse times. According to Eastman et al. (2010) $\mathrm{BJD_{TDB}}$ provides the most practical absolute time stamp for astronomical observations. It cancels out the unpredictable accumulation of leap seconds associated with UTC and it takes into account the influence of the major planets on the movement of the centre of the Sun. For all the observed eclipses the O − C times obtained with both the HJD- and BJD-based ephemeris are very similar and remarkably small, hinting at a notable lack of variation in the orbital period of CTCV J1928−5001.

Several new eclipse observations have been obtained as part of an ongoing observing campaign at the SAAO that involves the monitoring of observable eclipsing mCVs to measure precise mid-eclipse times with the aim of detecting any orbital period variations. These new observations will be incorporated in the recalculation of the BJD-based ephemeris and an extensive O − C analysis. Such an analysis will include a comprehensive comparison with other similar eclipsing systems that show significant orbital period variations, for example, UZ For (e.g., Ramsay 1994; Dai et al. 2010; Potter et al. 2011), HU Aqr (e.g., Schwope et al.

2001; Qian et al. 2011) and DP Leo (e.g., Schwope et al. 2002; Qian et al. 2010; Beuermann et al. 2011).

7.2.2 Simulated accretion flows in polars

Hydrodynamic and magnetohydrodynamic (MHD) simulations have been used extensively to study the accretion flow structure in CVs and other accreting systems like classical T Tauri stars and millisecond X-ray pulsars (e.g., Bisikalo et al. 2008; Boneva et al. 2009; Zhilkin & Bisikalo 2011; Kononov et al. 2012; Zhilkin et al. 2012; Bisikalo et al. 2013; Ustyugov et al. 2013; Romanova & Owocki 2015; Blinova et al. 2016; Ju et al. 2016). Some of these authors (Bisikalo et al. 2008; Boneva et al. 2009; Kononov et al. 2012) have shown that such simulations can be combined with real Doppler tomograms to identify the main features in the flow structure in a CV (e.g., the dwarf nova SS Cyg). They also showed that synthetic tomograms produced from the simulations can be used to fill in some of the 'missing' information in the real tomograms caused by observational constraints (e.g., system geometry, instrument limitations, etc.).

The full three-dimensional (3D) MHD simulations of ten separate polar models (Zhilkin et al. 2012, see Section 7.2.2.1) present an unprecedented opportunity to investigate different configurations of the accretion flows in polars. Dmitry Bisikalo graciously made available to me the full density, temperature and velocity solutions of all ten simulations. These exhaustive solutions allow for a controlled investigation into the structure of the simulated accretion flows. As a prelude to a more complete exploitation of these solutions I present the preliminary results from my exploratory investigation of using the solutions to generate synthetic spectra for which standard and inside-out Doppler tomography are then performed. The resulting tomograms can be compared with those of real systems with similar geometries in order to establish a better understanding of the accretion flows in polars.

7.2.2.1 Full 3D MHD simulations

Zhilkin et al. (2012) carried out full 3D MHD simulations of the accretion flow structure in polars using the supercomputer facility of the Russian Academy of Sciences. The simulations were done with the well established Nurgush 3D parallel numerical code (Zhilkin 2007; Zhilkin & Bisikalo 2009; Zhilkin 2010; Zhilkin & Bisikalo 2010a,b) which employs adaptive meshes and is based on a finite-difference Godunov-type scheme with a high approximation order. They obtained a single asynchronous polar model for BY Cam by putting together ten separate polar models. The basic system parameters assumed by Zhilkin et al. (2012) for the models are

- mass of the primary $M_1 = 1\,M_\odot$;
- mass ratio $q = 0.5$; and
- orbital period $P_{\rm orb} = 0.14\,{\rm d} = 3.36\,{\rm hr}$.

The magnetic field of the white dwarf primary is assumed to be a combination of a dipolar and quadrupolar field with a coincident axis. The magnetic axis co-latitude is set at 30°. Essentially, the ten simulations are of the same polar, but each simulation assumes a different azimuth for the magnetic axis. The phase reference that Zhilkin et al. (2012) use to distinguish between the different simulations equates phase 0 to a magnetic axis azimuth of 180° measured in an anticlockwise direction from the line between the centres of mass of the binary and secondary. Each subsequent phase is an increment of 0.1 which is equivalent to an increment of 36° in the magnetic axis azimuth. For example, phases 0.2, 0.4, 0.6 and 0.8 place the magnetic axis azimuth at 216°, 324°, 36° and 108°, respectively.

The solutions for each simulation consists of the computed density $\rho(x, y, z)$, temperature $T(x, y, z)$ and velocity $V(x, y, z)$. Figure 7.1 shows the accretion flow structure in terms of density obtained from the simulation with a magnetic axis azimuth of 36° (phase 0.6). I chose this particular simulation for my exploratory investigation because of its relative simple accretion flow structure.

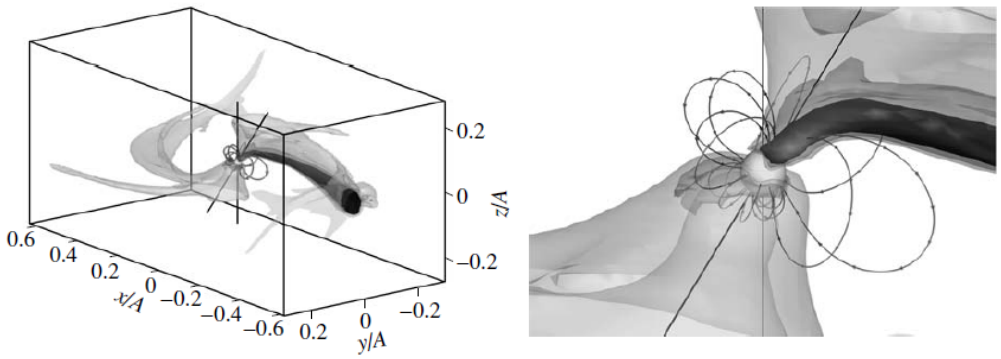

Figure 7.1. Accretion flow structure for a magnetic axis azimuth of 36° (phase 0.6). The left panel shows the full flow structure in the computational domain for a polar with the specified magnetic axis azimuth. The right panel shows the flow structure in the vicinity of the primary. The flow structure is presented in surfaces of constant logarithmic density, in units of the assumed gas density at L_1, for values of -6, -5 and -4. The straight and inclined lines are, respectively, the spin axis of the primary and the magnetic axis. A number of magnetic field lines of the combined dipolar and quadrupolar fields are shown also. Figure 9 from Zhilkin et al. (2012).

7.2.2.2 Synthetic spectra

I used an experimental code provided by Pavel Kaygorodov to generate synthetic spectra from the solutions (density, temperature and velocity) of the simulation with a magnetic axis azimuth of 36° (phase 0.6). In order to keep this exploratory investigation simple I focussed mainly on the higher density part of the accretion flow and therefore used only the part with logarithmic density greater than -5 (i.e., $\log \rho(x, y, z) > -5$). The monochromatic emission from this part of the accretion flow was synthesised as a simple temperature power law. A more complete wavelength dependent synthesis of the emission will form part of the planned

future work on more of the simulations. The synthesised emission from the accretion flow is the only emission component included in the line profiles. The calculated line profiles also include Doppler broadening, as well as the appropriate phase-dependent Doppler shifts based on the basic system parameters previously listed and an assumed inclination angle $i = 85°$. A total of 40 evenly spaced phase-resolved spectra were generated with each spectrum having 288 velocity points in the extracted radial velocity range ($n = 11520$).

7.2.2.3 Standard and inside-out Doppler tomography of synthetic spectra

Figure 7.2 shows the standard and the inside-out Doppler tomography based on the synthetic monochromatic emission spectra. The model velocity profile overlay shown in both tomograms is based on the system parameters listed in Section 7.2.2.1 and the assumed inclination angle $i = 85°$ used in the generation of the spectra.

Trailed spectra: The simulated emission from the higher density accretion flow (see Section 7.2.2.2) produces a relatively broad feature in the trailed input spectra (middle panel of Figure 7.2). It has maximum blueshift and redshift around phases 0.40 and 0.90, respectively. This feature is reproduced fairly well in the trailed reconstructed spectra from both the standard and inside-out tomograms (panels to the left and right, respectively, of the middle panel of Figure 7.2). The inside-out projection achieved a marginal better overall result, that is, its residuals have a rms value of 0.095 compared to the 0.122 of the standard projection.

Tomograms: In the standard tomogram (top left panel of Figure 7.2) the binary's centre of mass is at the centre of the tomogram, marked with a plus (+). The binary's centre of mass is effectively the zero velocity outer circumference in the inside-out tomogram (top right panel of Figure 7.2). In both tomograms the centres of mass of the primary and secondary are marked with crosses (×). For comparison purposes I added a model velocity profile of a single particle ballistic trajectory from the L_1 point up to 45° in azimuth around the primary (solid line). This trajectory includes, apart from gravitational and centrifugal effects, a magnetic drag force (see Section 3.1.2.1). Also, only magnetic *dipole* trajectories (thin dotted lines) are shown at 10° intervals from 5° to 45° in azimuth around the primary. A dipolar axis azimuth and co-latitude of 36° and 30°, respectively, are assumed. The dipolar axis azimuth of 36° is equivalent to phase 0.6 from Zhilkin et al. (2012) (see Figure 7.1). The first dipole connection on the ballistic stream (small red circles) is at ($243\,\mathrm{km\,s^{-1}}$, 150°). The first dipole trajectory starts at ($188\,\mathrm{km\,s^{-1}}$, 168°), with consecutive trajectories starting at locations with progressively higher velocities and polar angles.

In the standard tomogram the emission associated with the ballistic part of the accretion flow is a prominent horizontal ridge. As the stream leaves L_1 at ($110\,\mathrm{km\,s^{-1}}$, 90°), it is faint, but it increases rapidly in brightness. Maximum brightness coincides with the first dipole connection at ($243\,\mathrm{km\,s^{-1}}$, 150°). It then decreases in brightness, but is clearly discernible up to the third dipole connection at ($751\,\mathrm{km\,s^{-1}}$, 177°). After this point the discernible emission is more diffused and slopes downwards away from the single particle ballistic trajectory. This

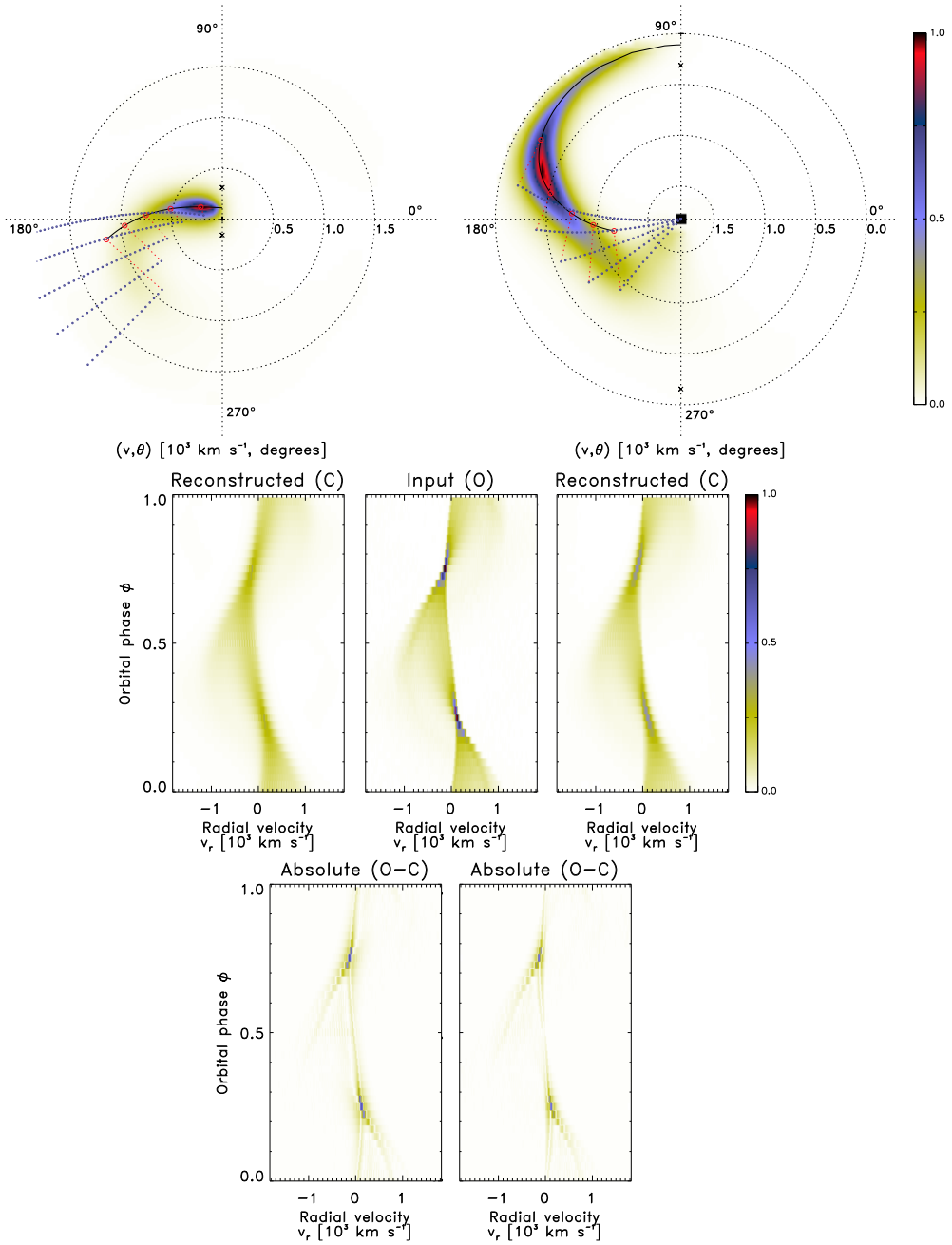

Figure 7.2. Doppler tomography of the simulated accretion flows of a polar. The standard and inside-out tomograms are shown in the top left and right panels, respectively. The middle panel shows the trailed input spectra with the trailed reconstructed spectra for the corresponding tomogram to the left and right of it. The bottom left and right panels show the trailed absolute residual spectra for the corresponding tomogram. The rms values of the standard and inside-out residuals (i.e., absolute O − C) are 0.122 and 0.095, respectively. See text for details.

diffused emission is associated with the magnetically confined accretion flow after it has left the orbital plane and is discernible up to velocities of $\sim 1000\,\mathrm{km\,s^{-1}}$.

The distribution in brightness along the ballistic flow is more prominent in the inside-out tomogram, that is, the lower velocity part is even fainter, whereas the mid- and high-velocity parts are significantly brighter. It appears brightest between the first and second dipole connections which is at ($243\,\mathrm{km\,s^{-1}}$, 150°) and ($519\,\mathrm{km\,s^{-1}}$, 169°), respectively. As was the case in the standard tomogram, the discernible (albeit now brighter) emission slopes downwards away from the single particle ballistic trajectory after the third dipole connection at ($751\,\mathrm{km\,s^{-1}}$, 177°). The emission associated with the magnetically confined accretion flow that has left the orbital plane is clearly discernible to velocities well above $1000\,\mathrm{km\,s^{-1}}$. Also discernible, but more diffused, is the emission associated with the funnelled accretion flowing towards the primary along the magnetic field lines at velocities above $\sim 1200\,\mathrm{km\,s^{-1}}$. This diffused higher velocity emission is not discernible in the standard tomogram. It is resolved in the inside-out tomogram because the emission is re-binned in a smaller area with fewer pixels. In both tomograms the ballistic part of the accretion flow is well traced by the single particle ballistic trajectory.

The emission structure in the trailed input spectra and the resulting emission distribution for the ballistic and magnetically confined accretion flows in both tomograms bear a striking resemblance to those of HU Aqr (see Figure 4.5). This highlights the enormous potential of this type of MHD simulation as an aid in the tomographic study of polars. For example, the solution of a specific simulation can be used to obtain an accurate velocity profile of the accretion flow which takes the MHD effects in the flow into account. Such a 'comprehensive' profile can then be used to replace the 'simple' single particle trajectory profile in the tomogram of a real system with similar system parameters, providing a more realistic view of the velocity field in the accretion flow. This is just one example of how the MHD simulations can be exploited to aid the interpretation of Doppler tomograms. These tantalising preliminary results serve as an impetus to pursue an extensive comparative analysis between the MHD simulations and observations of real polars.

Appendix A

Consecutive half-phase Doppler tomography

Can one desire too much of a good thing?

– William Shakespeare, *As You Like It*, Act IV, Scene 1

This appendix contains the complete half-phase Doppler tomography used in the flux modulation mapping presented for HU Aqr (Section 5.3.1), V834 Cen (Section 5.3.2), PQ Gem (Section 5.3.3) and CTCV J1928−5001 (Section 6.3.6). In all the figures the standard and inside-out half-phase tomograms are shown in the top left and right panels, respectively. The middle panel shows the trailed input spectra with the trailed reconstructed spectra for the corresponding half-phase tomogram to the left and right of it. The bottom left and right panels show the trailed absolute residual spectra for the corresponding half-phase tomogram.

A.1 HU Aqr: an eclipsing polar

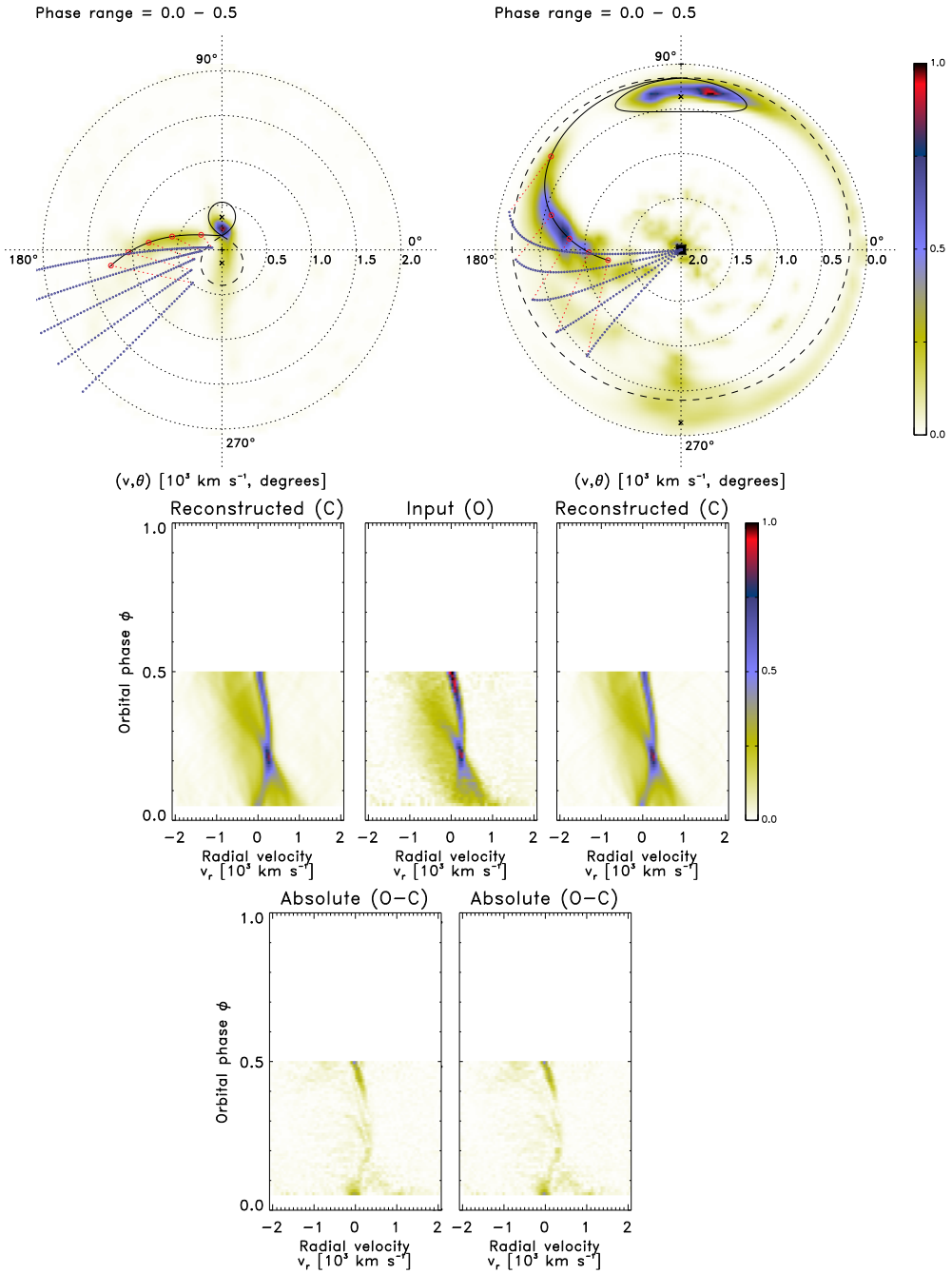

Figure A.1. Half-phase Doppler tomography of HU Aqr: orbital phase range $0.0 - 0.5$.

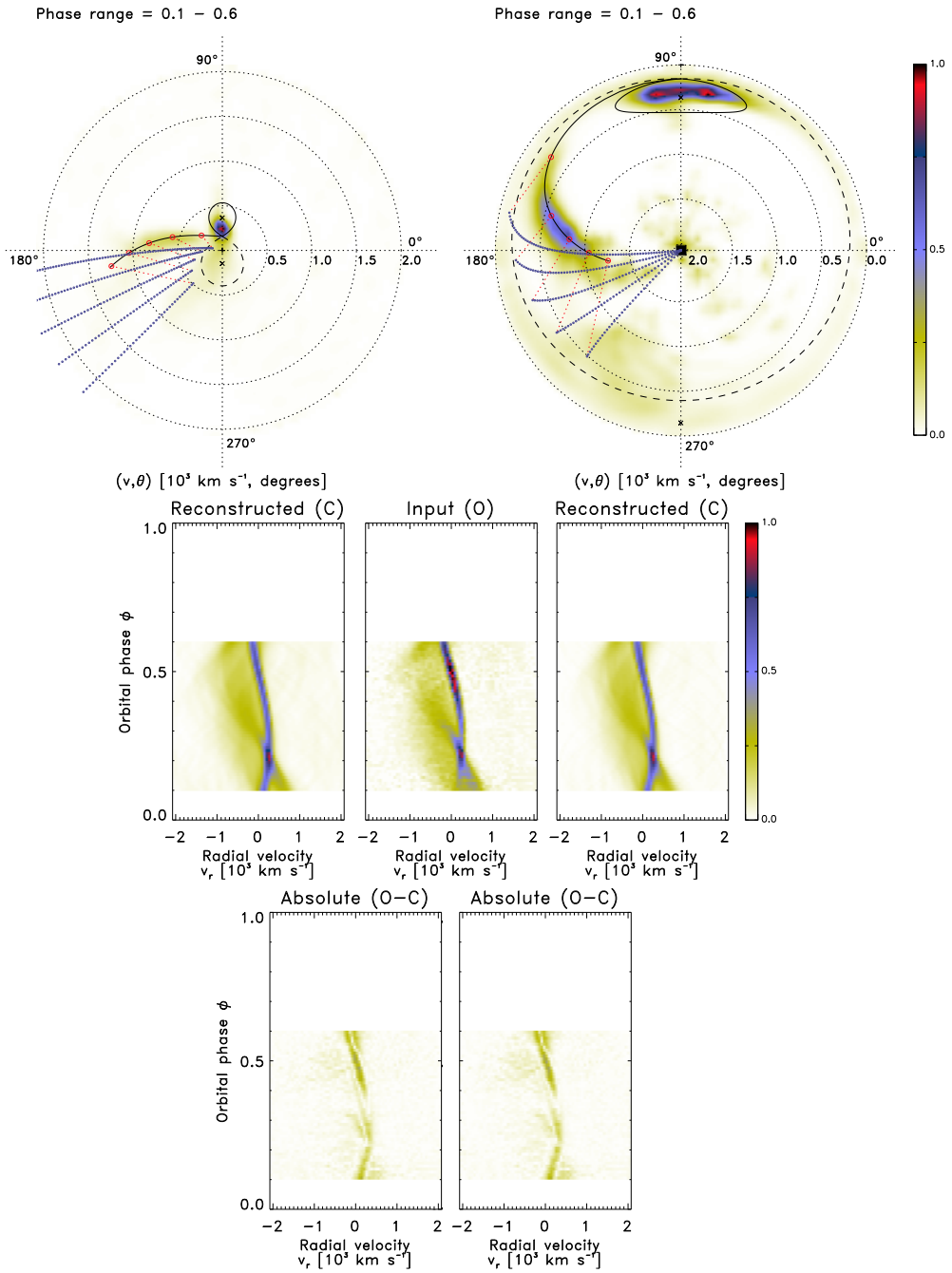

Figure A.2. Half-phase Doppler tomography of HU Aqr: orbital phase range 0.1 – 0.6.

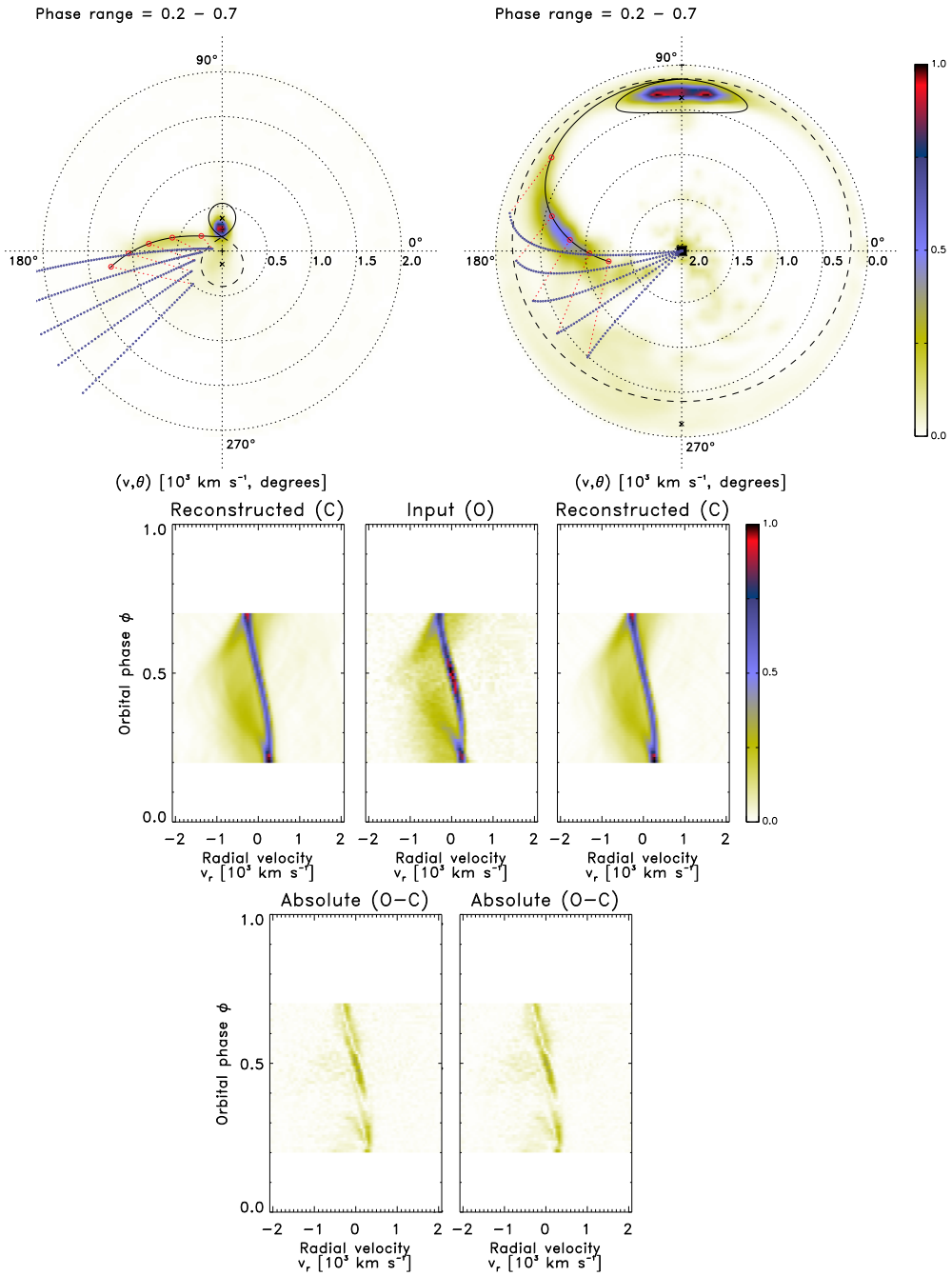

Figure A.3. Half-phase Doppler tomography of HU Aqr: orbital phase range $0.2 - 0.7$.

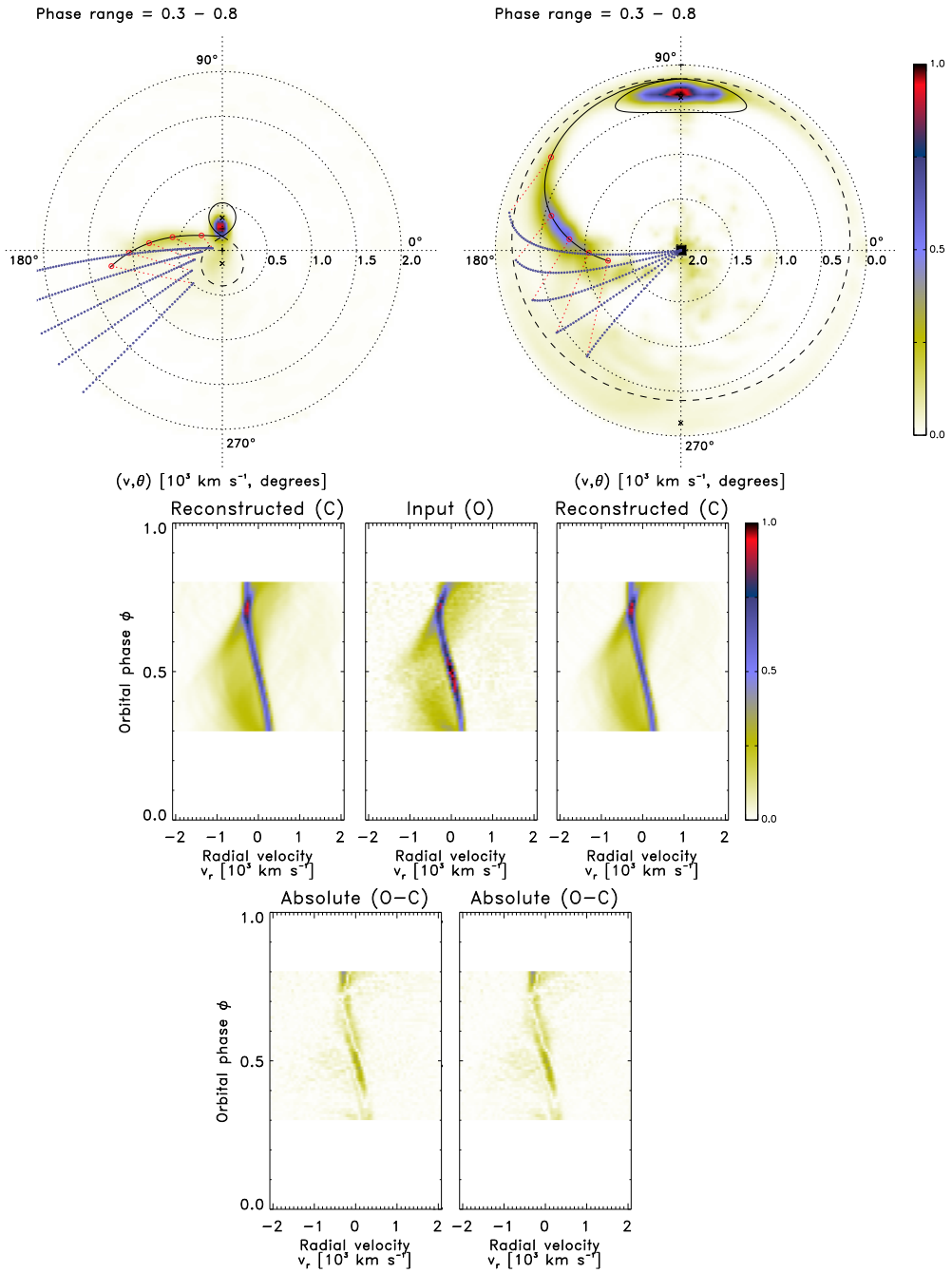

Figure A.4. Half-phase Doppler tomography of HU Aqr: orbital phase range $0.3 - 0.8$.

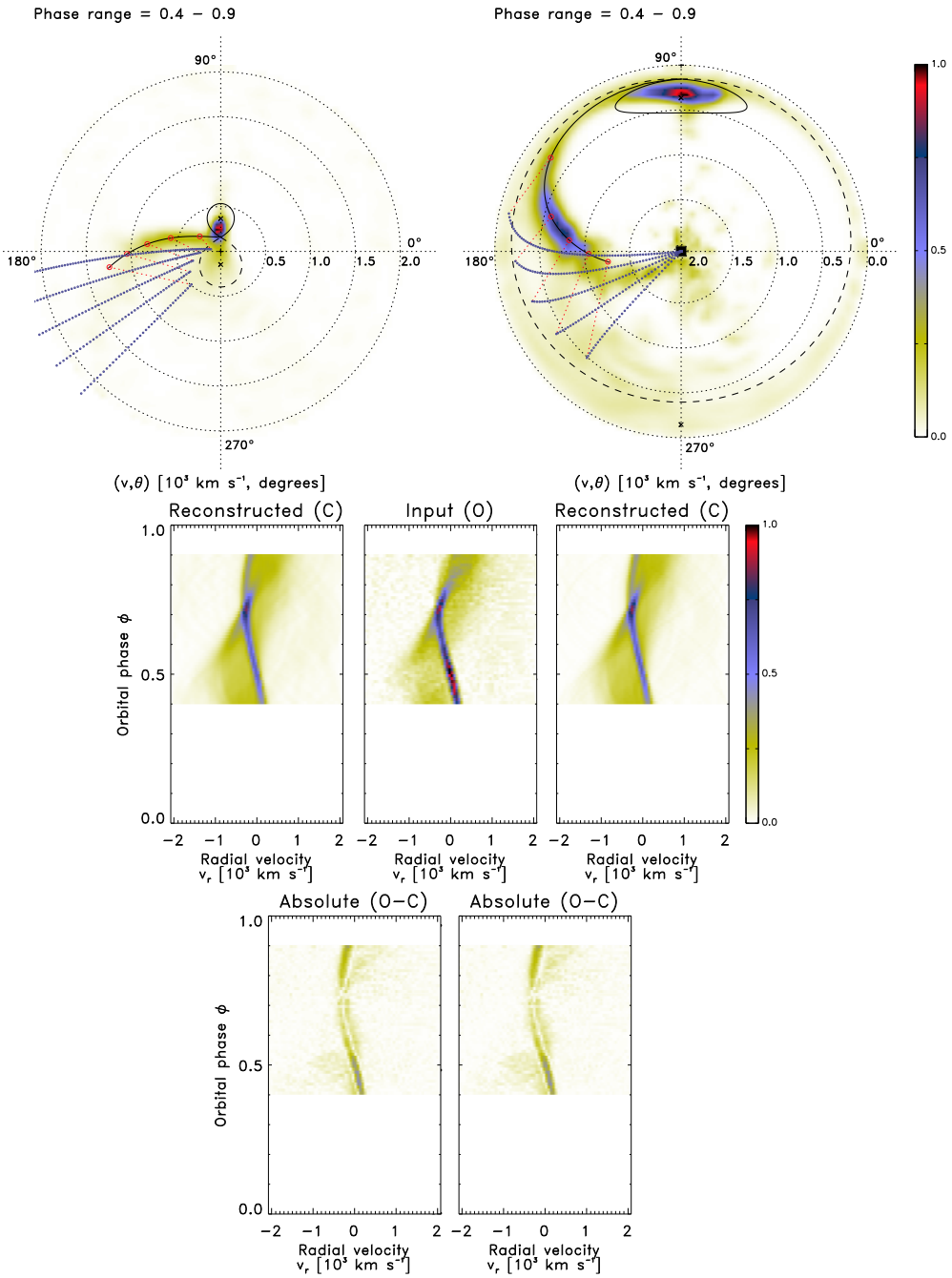

Figure A.5. Half-phase Doppler tomography of HU Aqr: orbital phase range $0.4 - 0.9$.

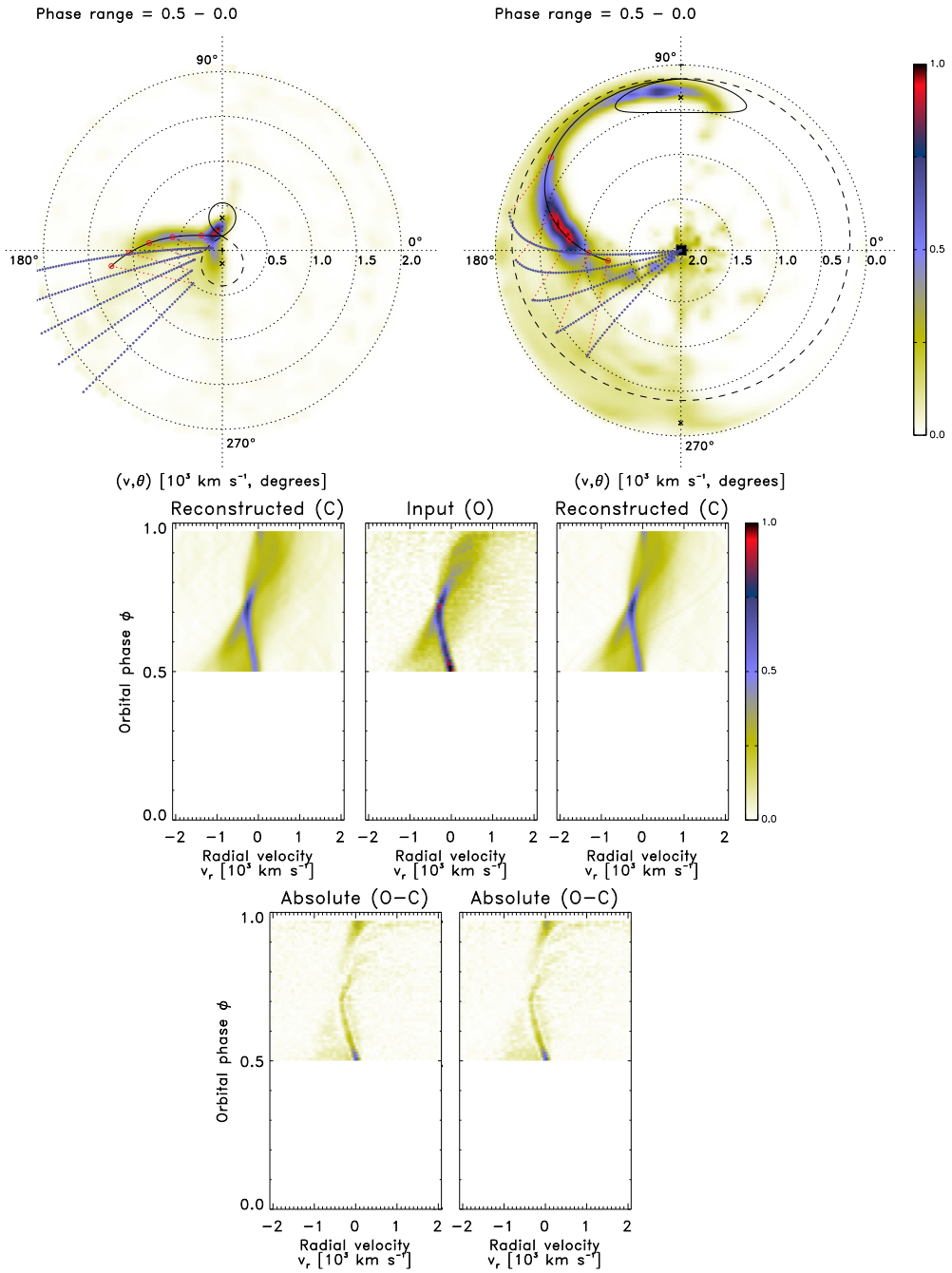

Figure A.6. Half-phase Doppler tomography of HU Aqr: orbital phase range 0.5 – 0.0.

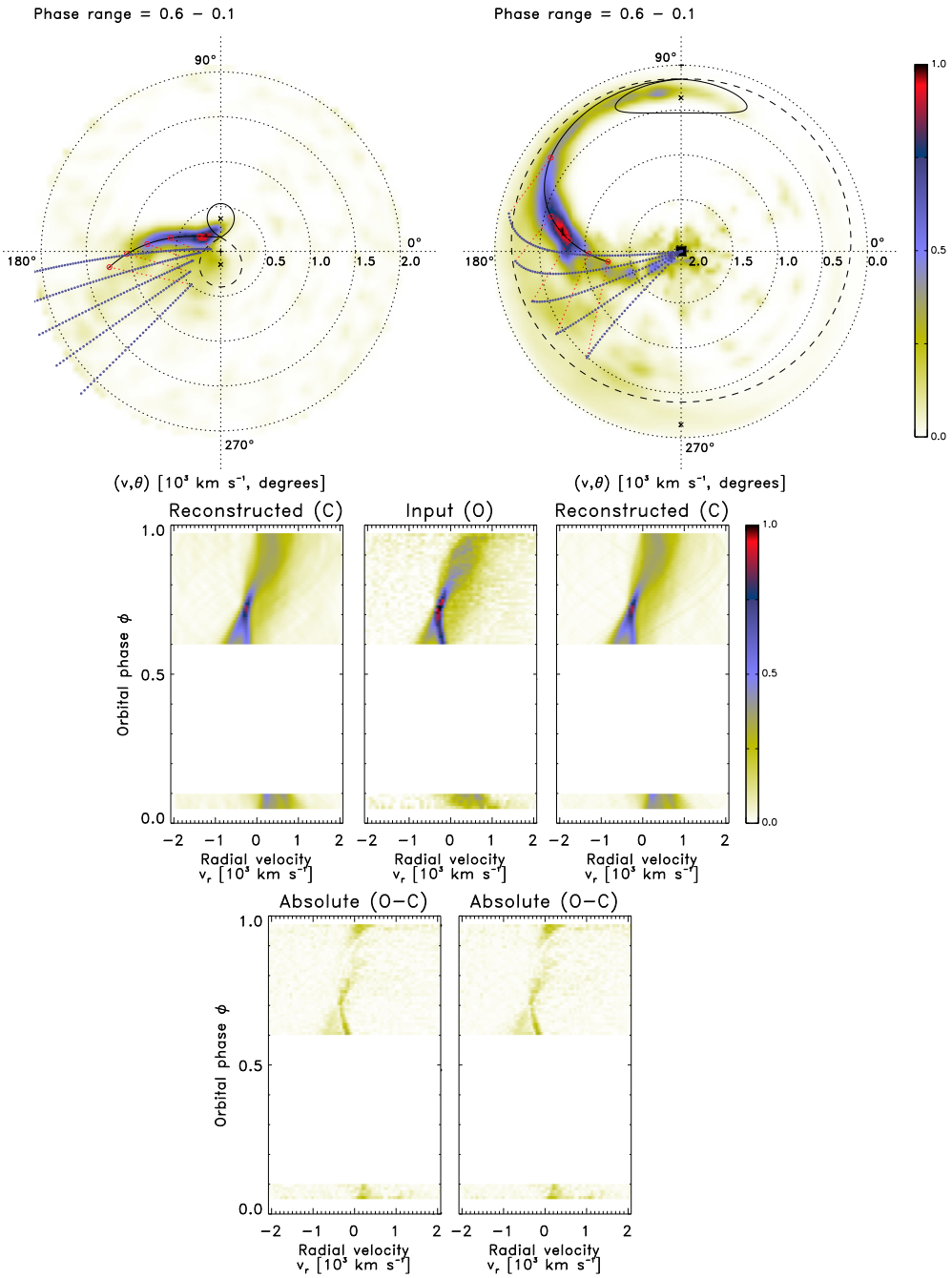

Figure A.7. Half-phase Doppler tomography of HU Aqr: orbital phase range 0.6 – 0.1.

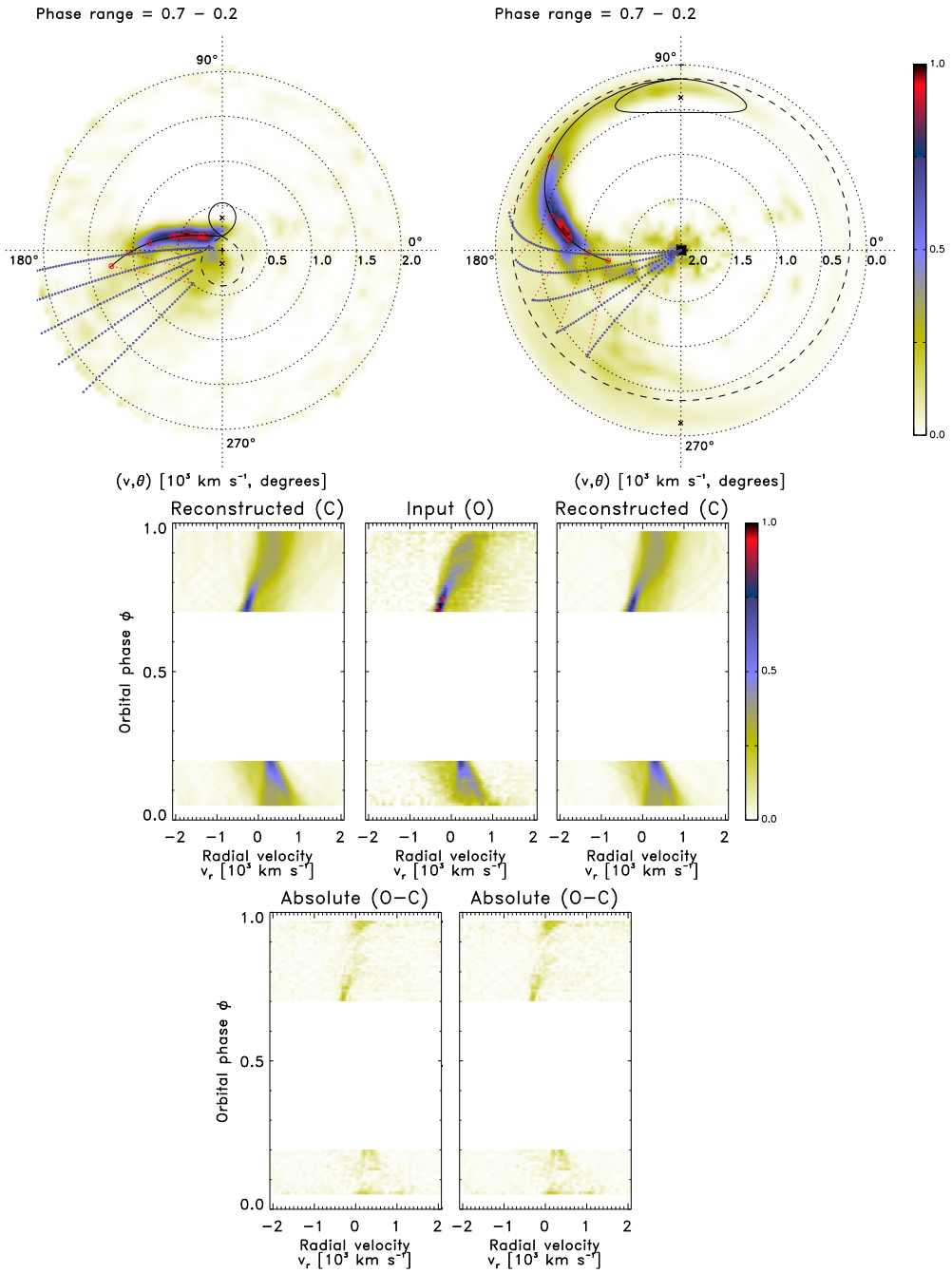

Figure A.8. Half-phase Doppler tomography of HU Aqr: orbital phase range 0.7 – 0.2.

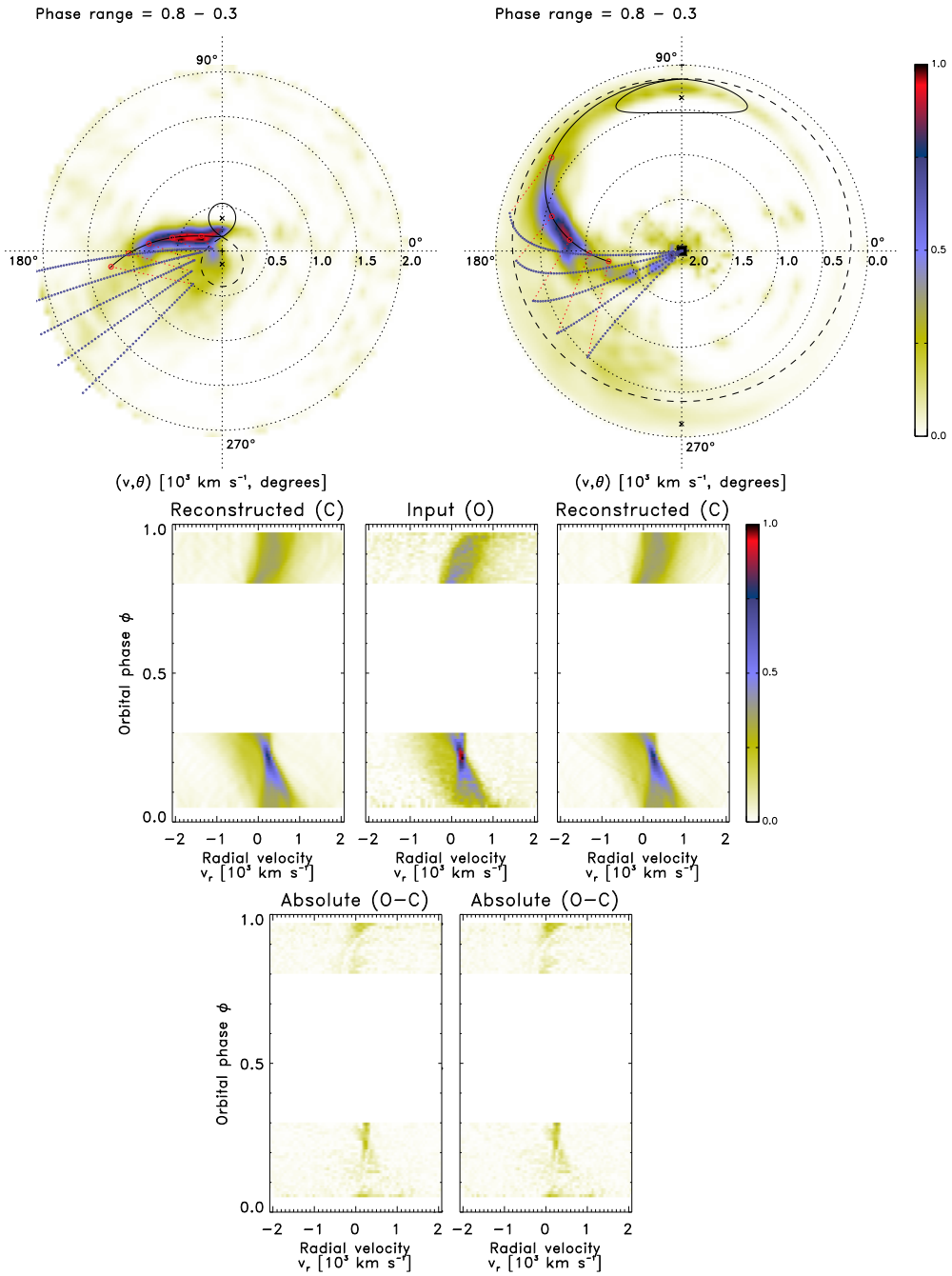

Figure A.9. Half-phase Doppler tomography of HU Aqr: orbital phase range $0.8 - 0.3$.

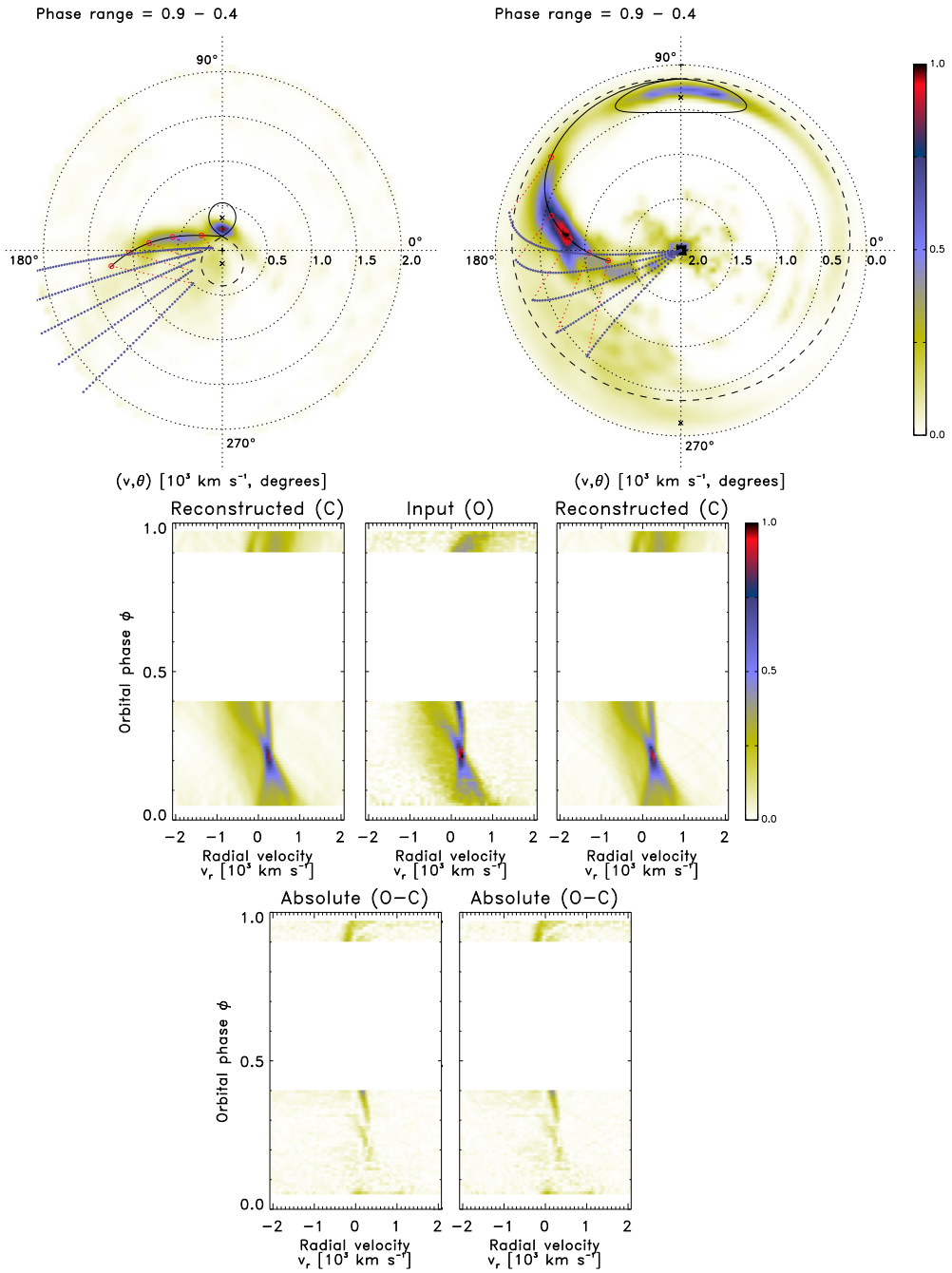

Figure A.10. Half-phase Doppler tomography of HU Aqr: orbital phase range $0.9 - 0.4$.

A.2 V834 Cen: a non-eclipsing polar

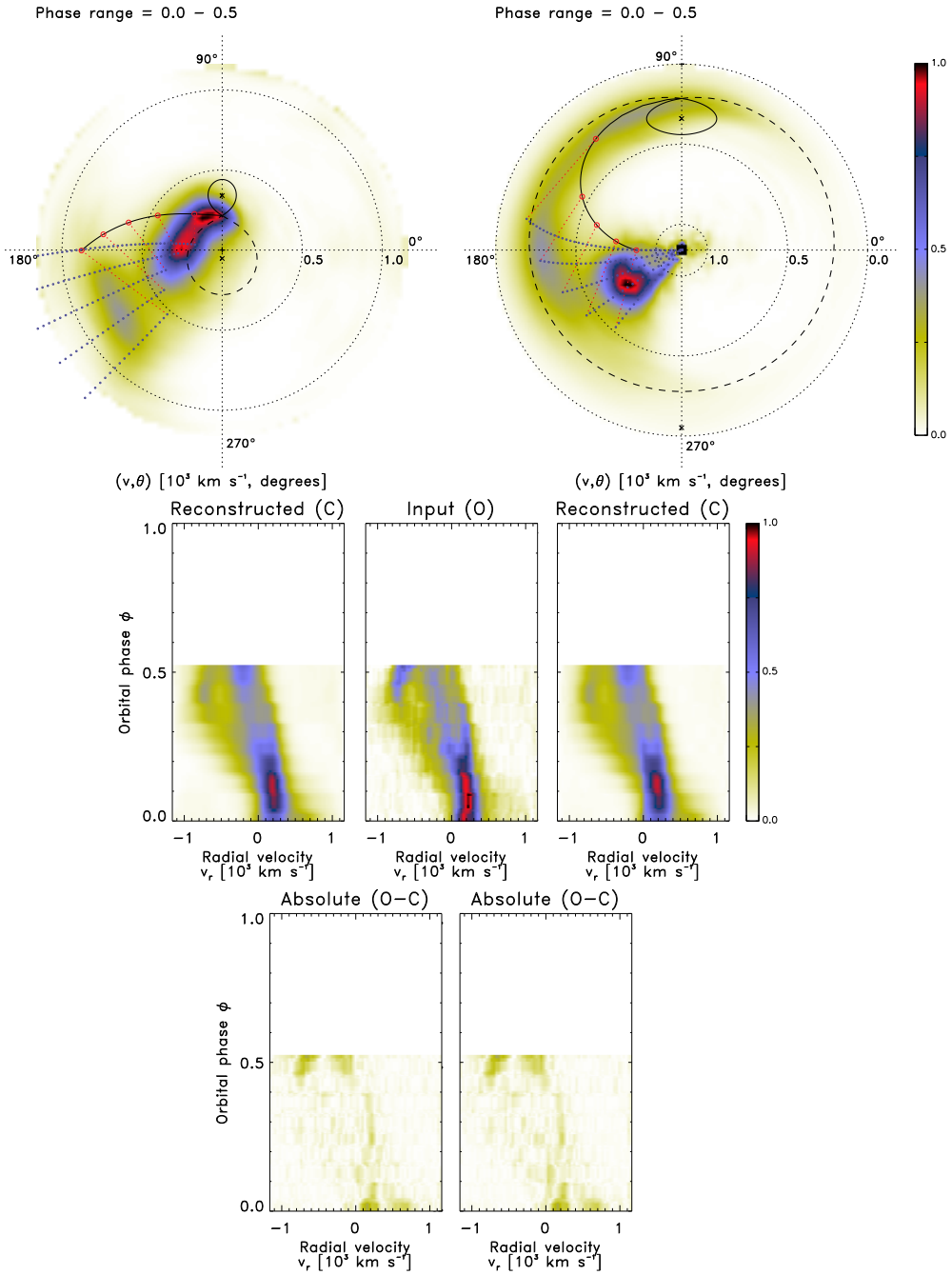

Figure A.11. Half-phase Doppler tomography of V834 Cen: orbital phase range $0.0 - 0.5$.

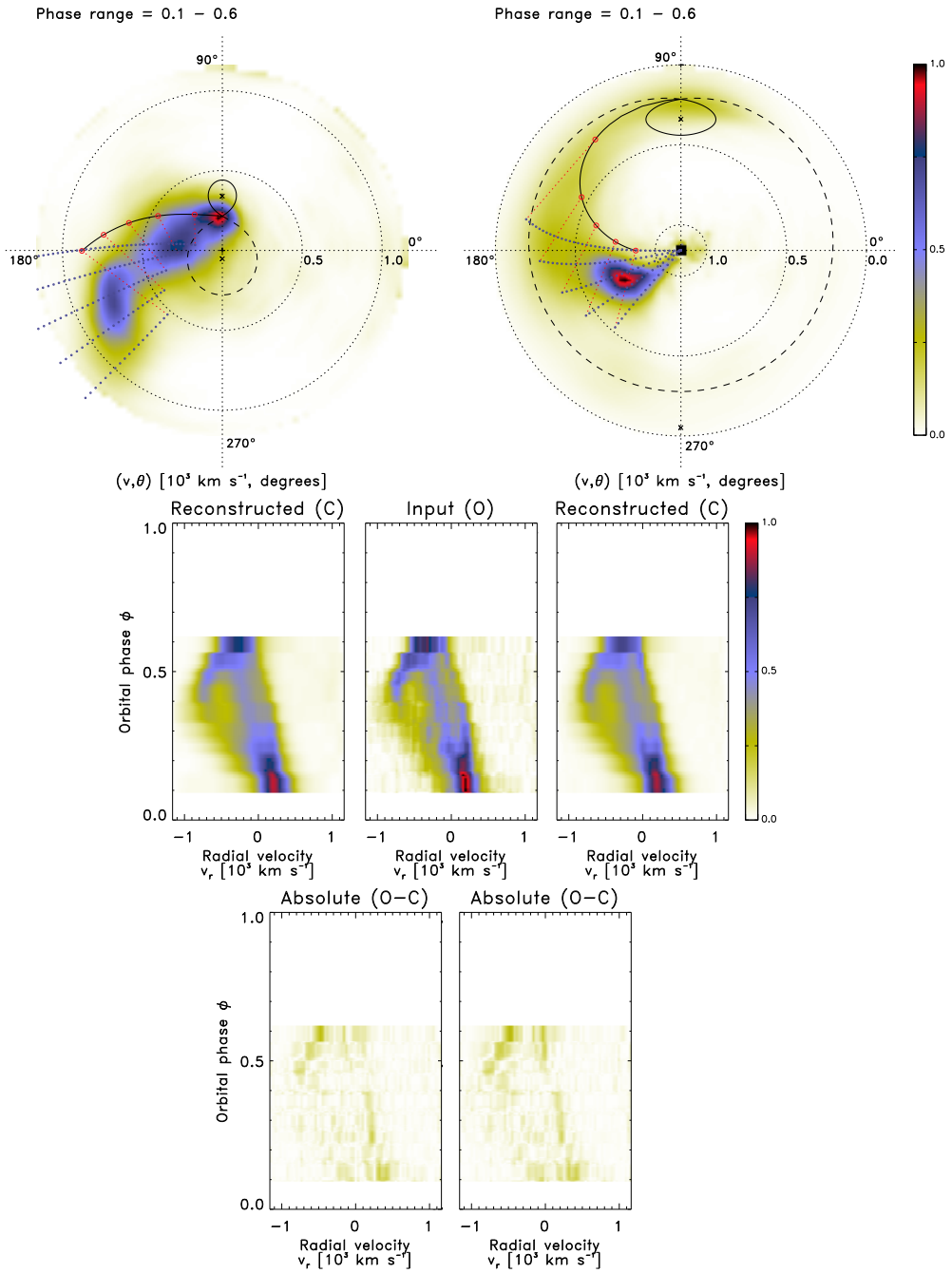

Figure A.12. Half-phase Doppler tomography of V834 Cen: orbital phase range $0.1 - 0.6$.

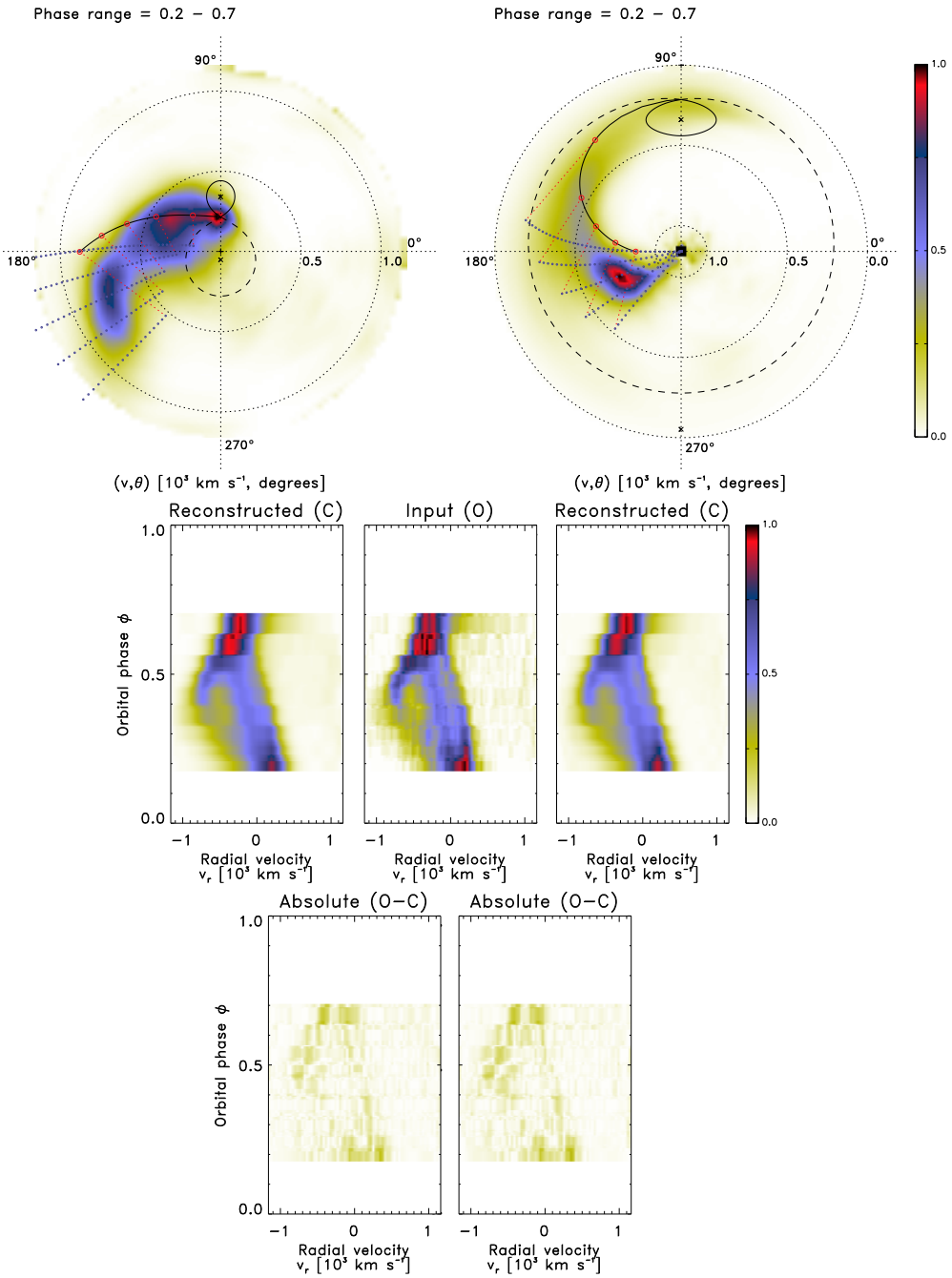

Figure A.13. Half-phase Doppler tomography of V834 Cen: orbital phase range $0.2 - 0.7$.

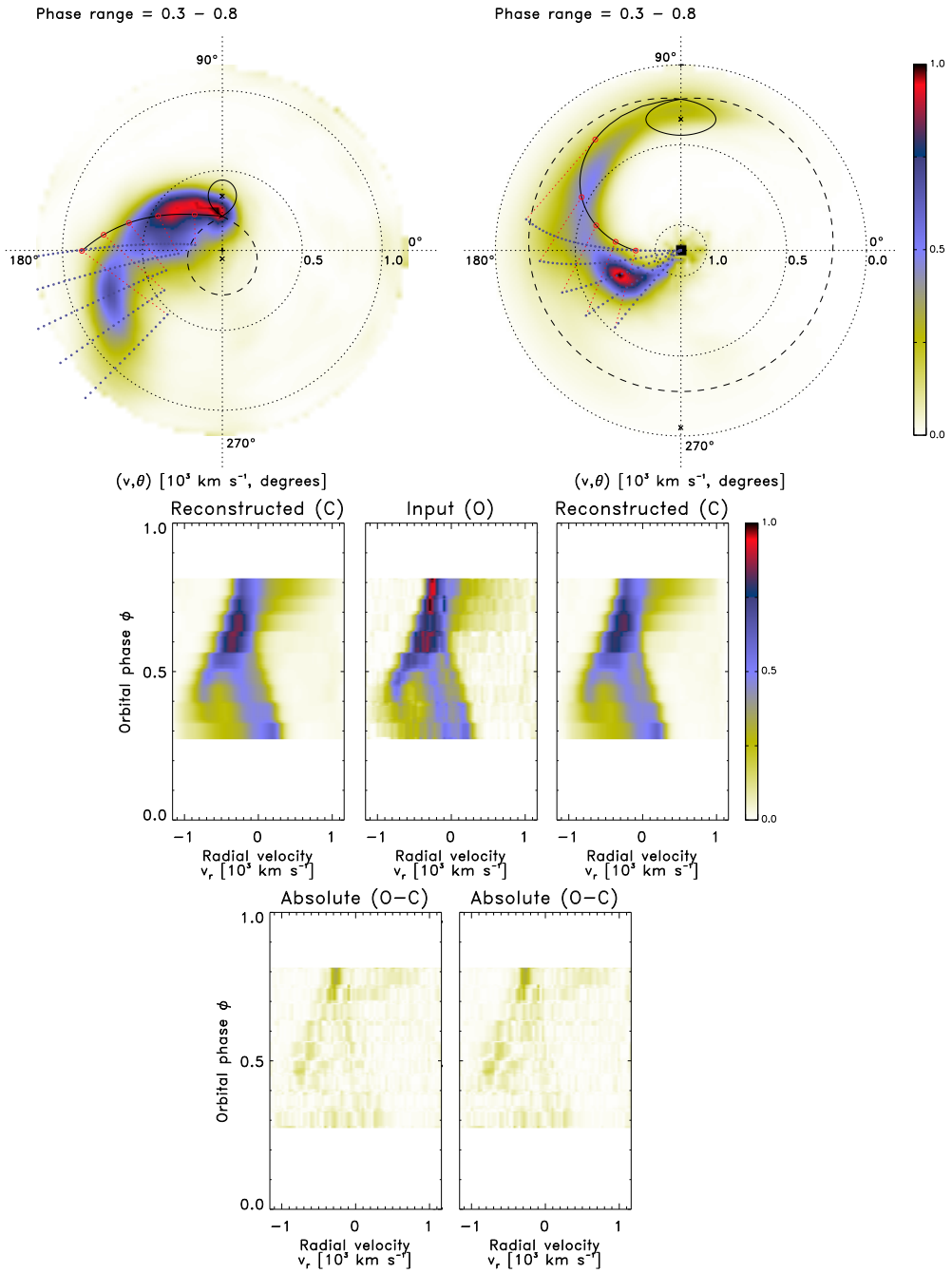

Figure A.14. Half-phase Doppler tomography of V834 Cen: orbital phase range $0.3 - 0.8$.

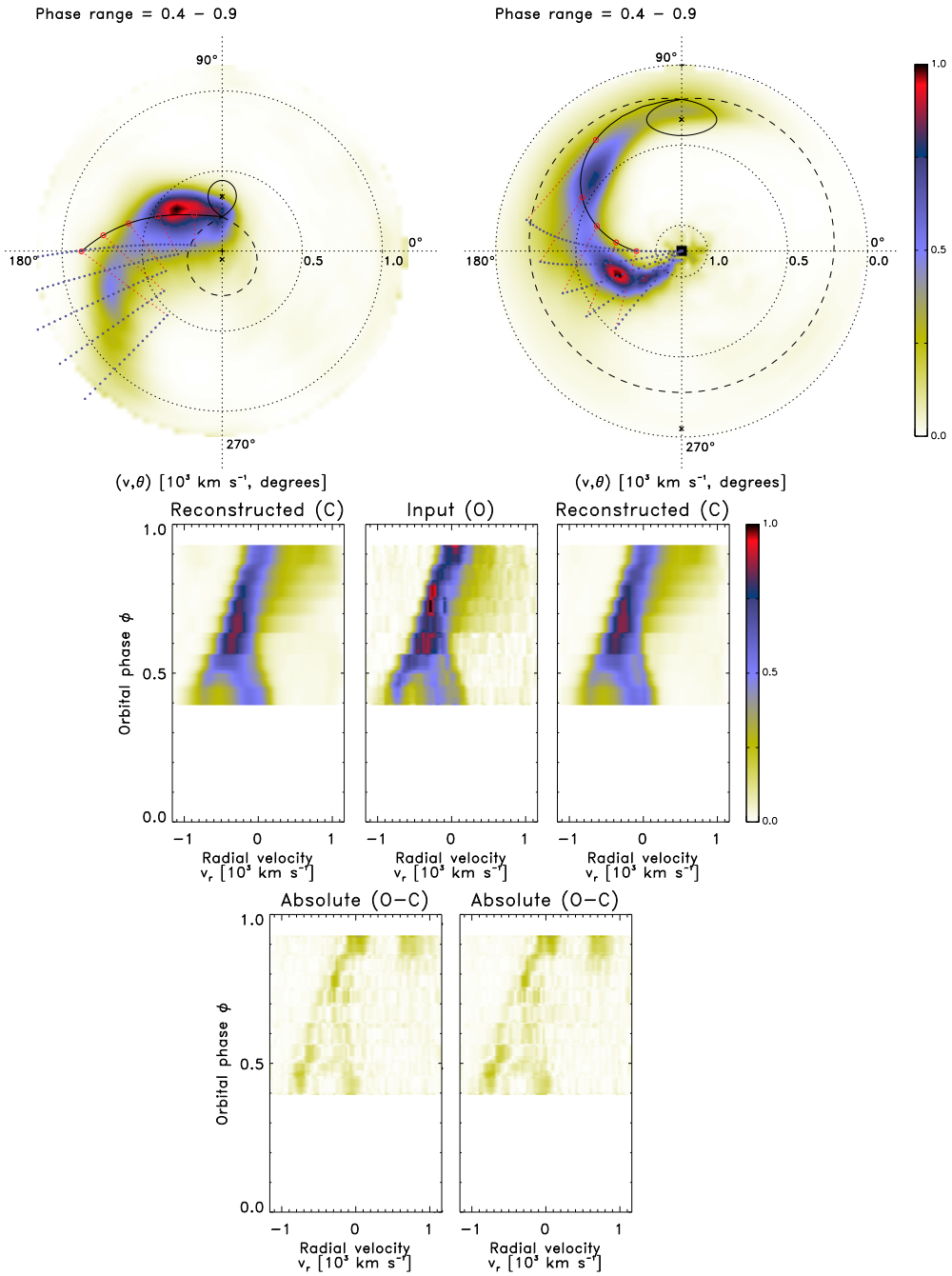

Figure A.15. Half-phase Doppler tomography of V834 Cen: orbital phase range $0.4 - 0.9$.

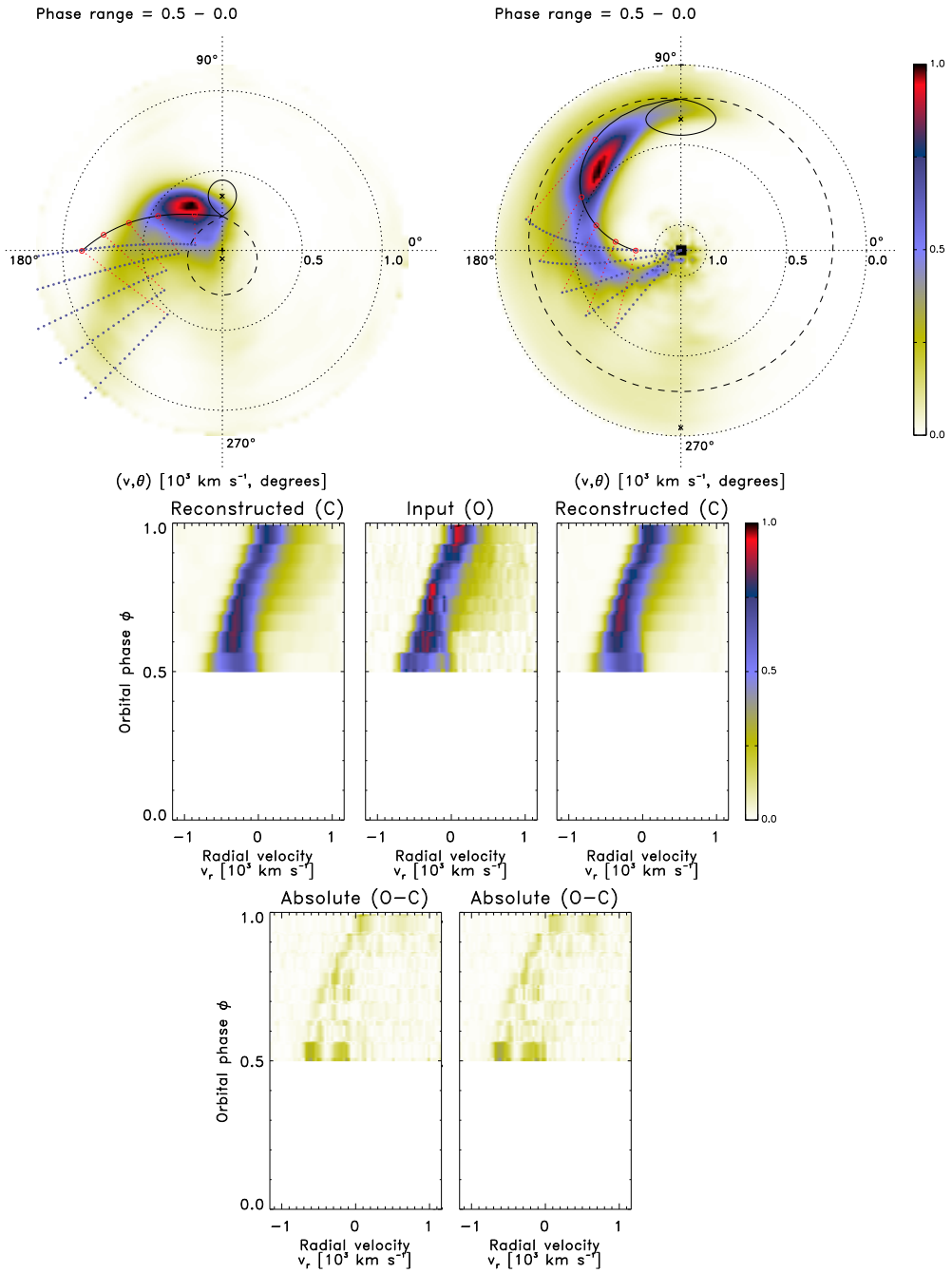

Figure A.16. Half-phase Doppler tomography of V834 Cen: orbital phase range $0.5 - 0.0$.

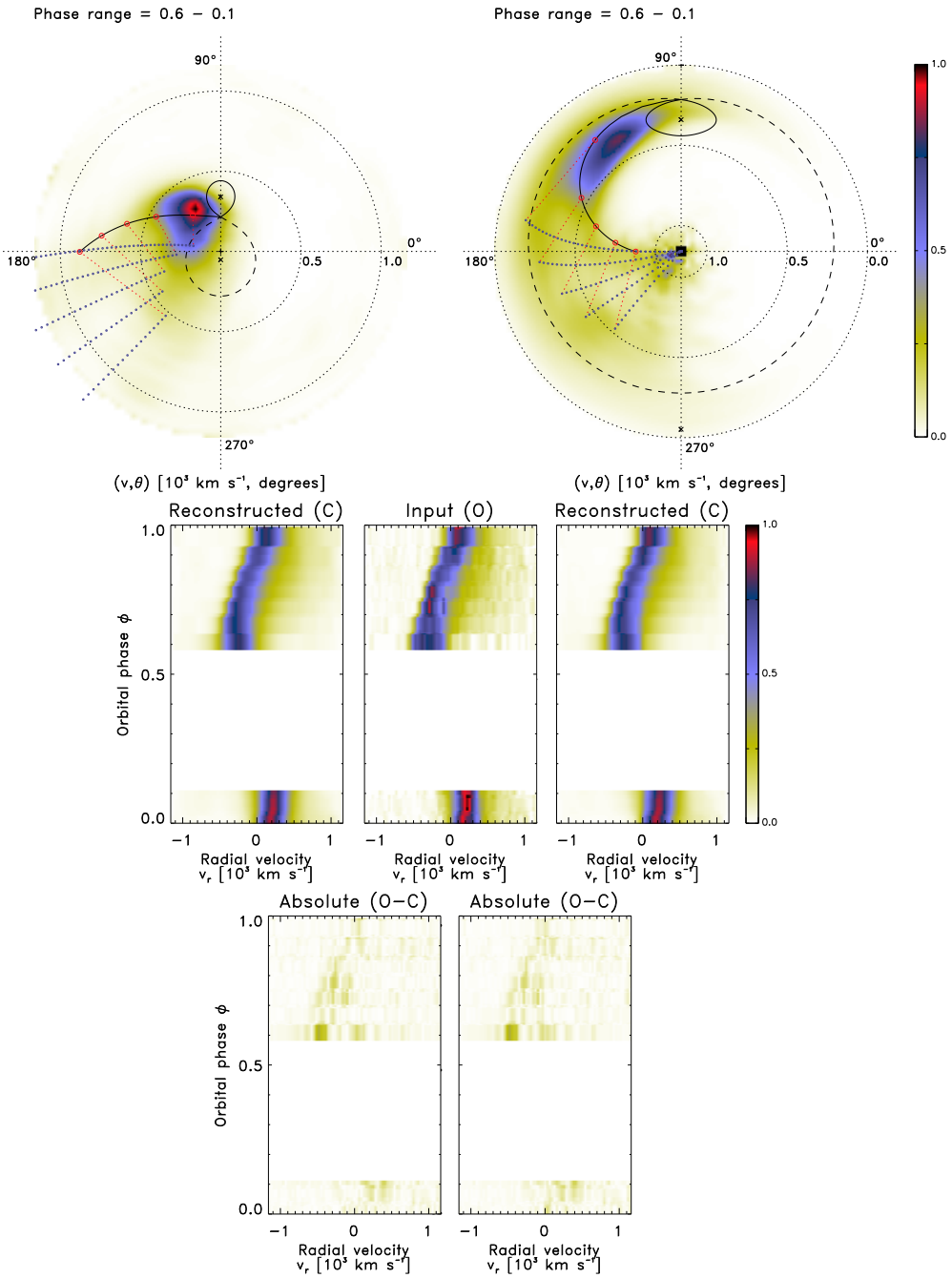

Figure A.17. Half-phase Doppler tomography of V834 Cen: orbital phase range $0.6 - 0.1$.

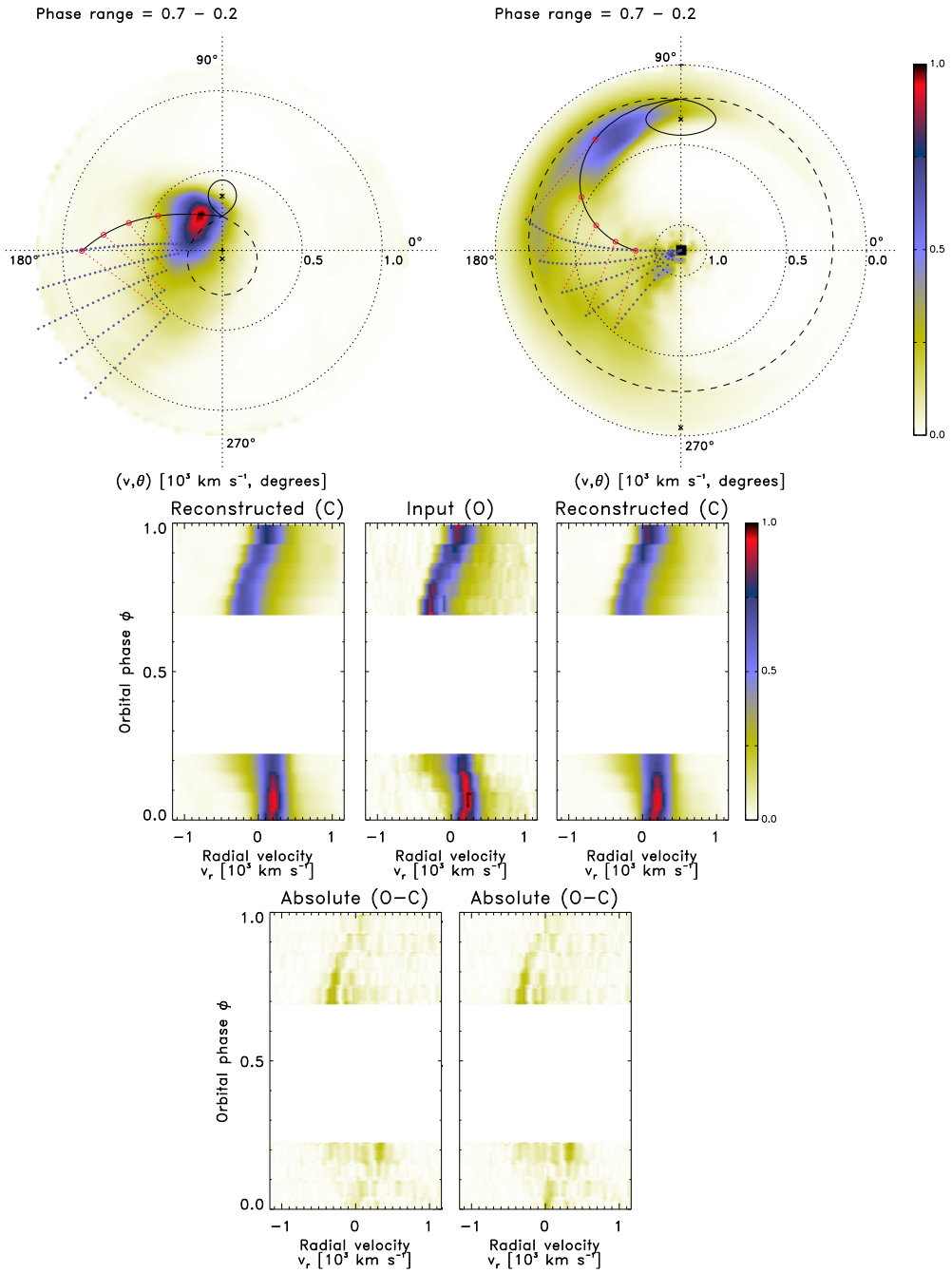

Figure A.18. Half-phase Doppler tomography of V834 Cen: orbital phase range $0.7 - 0.2$.

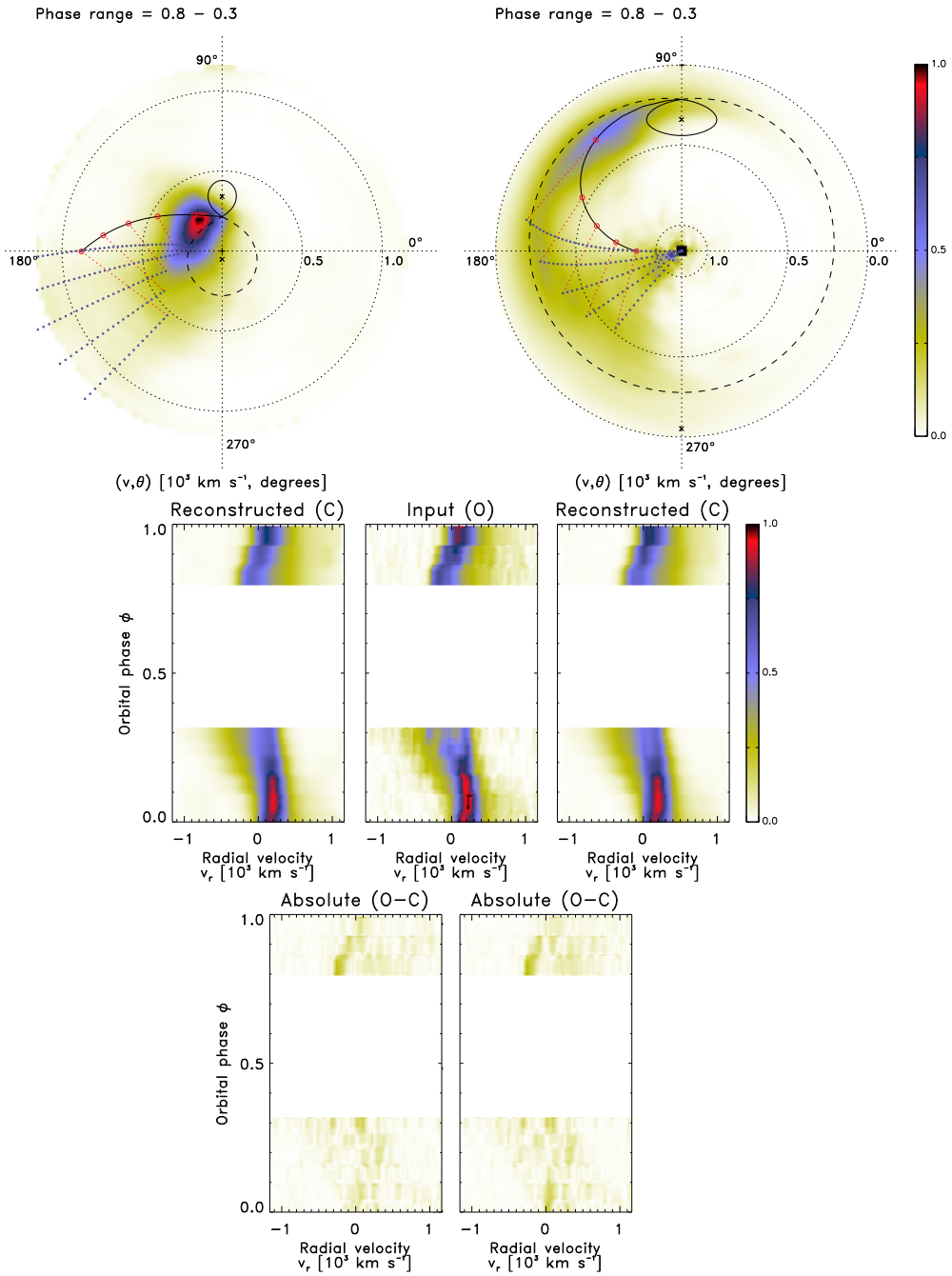

Figure A.19. Half-phase Doppler tomography of V834 Cen: orbital phase range $0.8 - 0.3$.

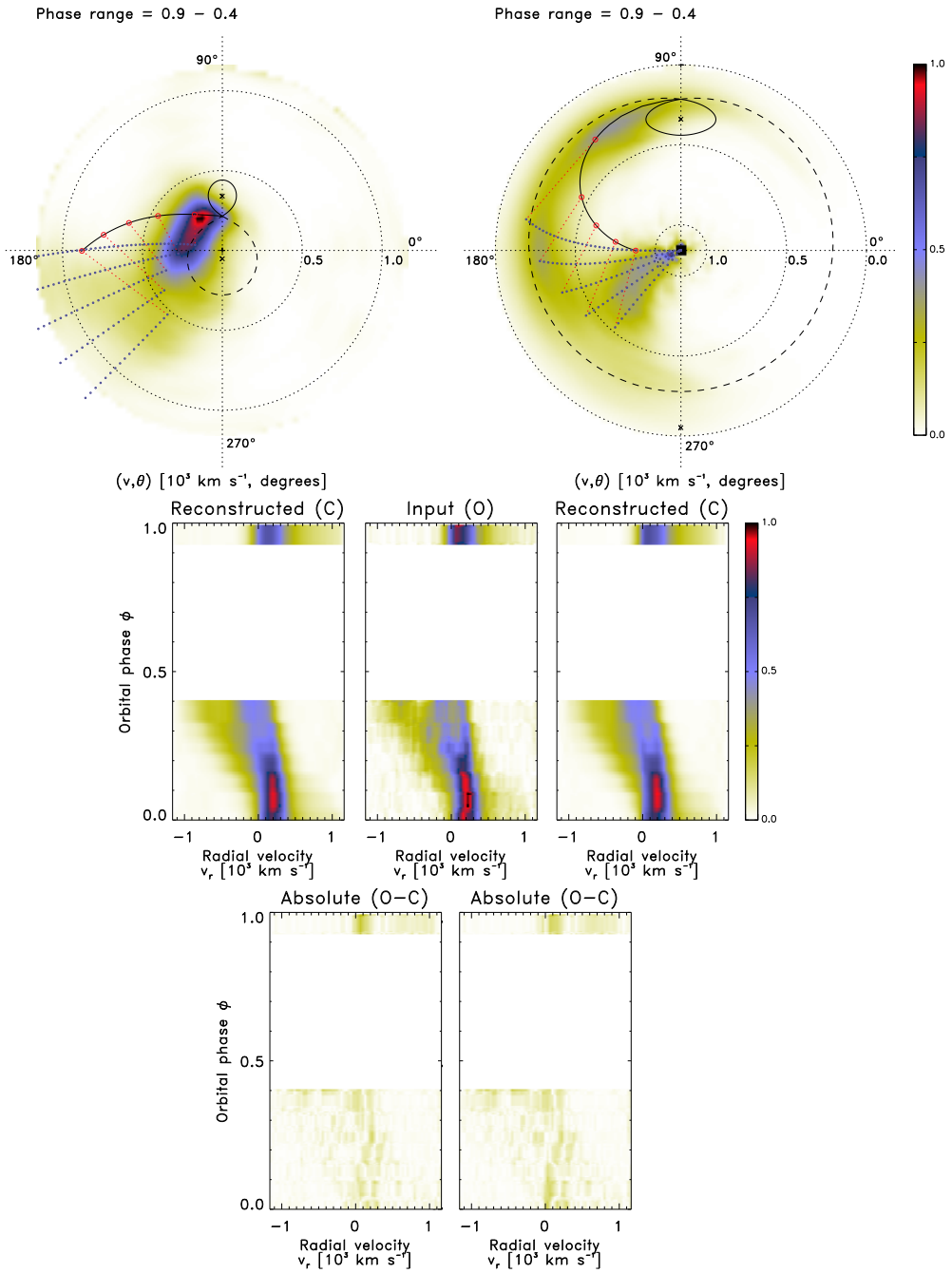

Figure A.20. Half-phase Doppler tomography of V834 Cen: orbital phase range $0.9 - 0.4$.

A.3 PQ Gem: a non-eclipsing intermediate polar

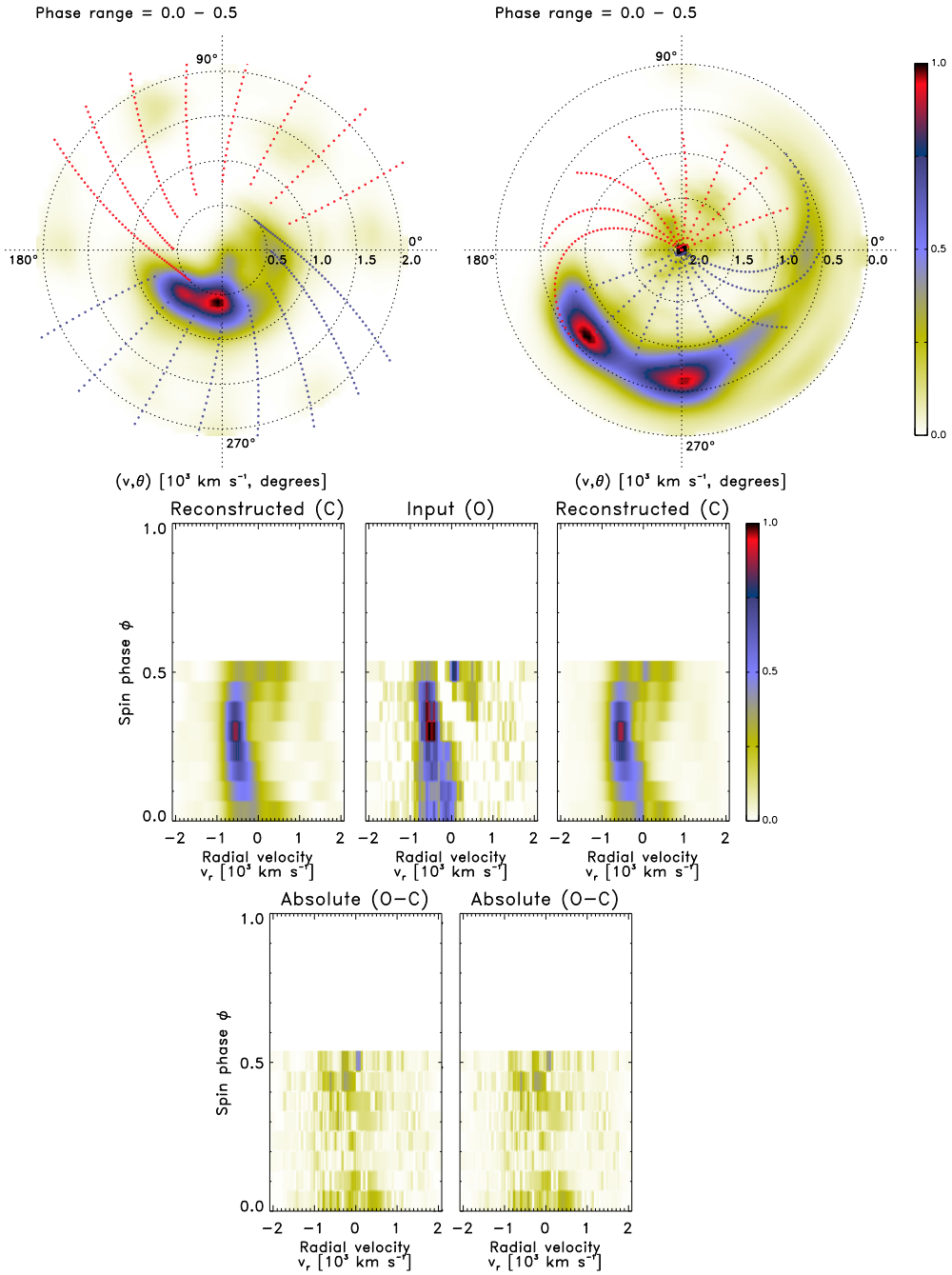

Figure A.21. Half-phase Doppler tomography of PQ Gem: orbital phase range 0.0 – 0.5.

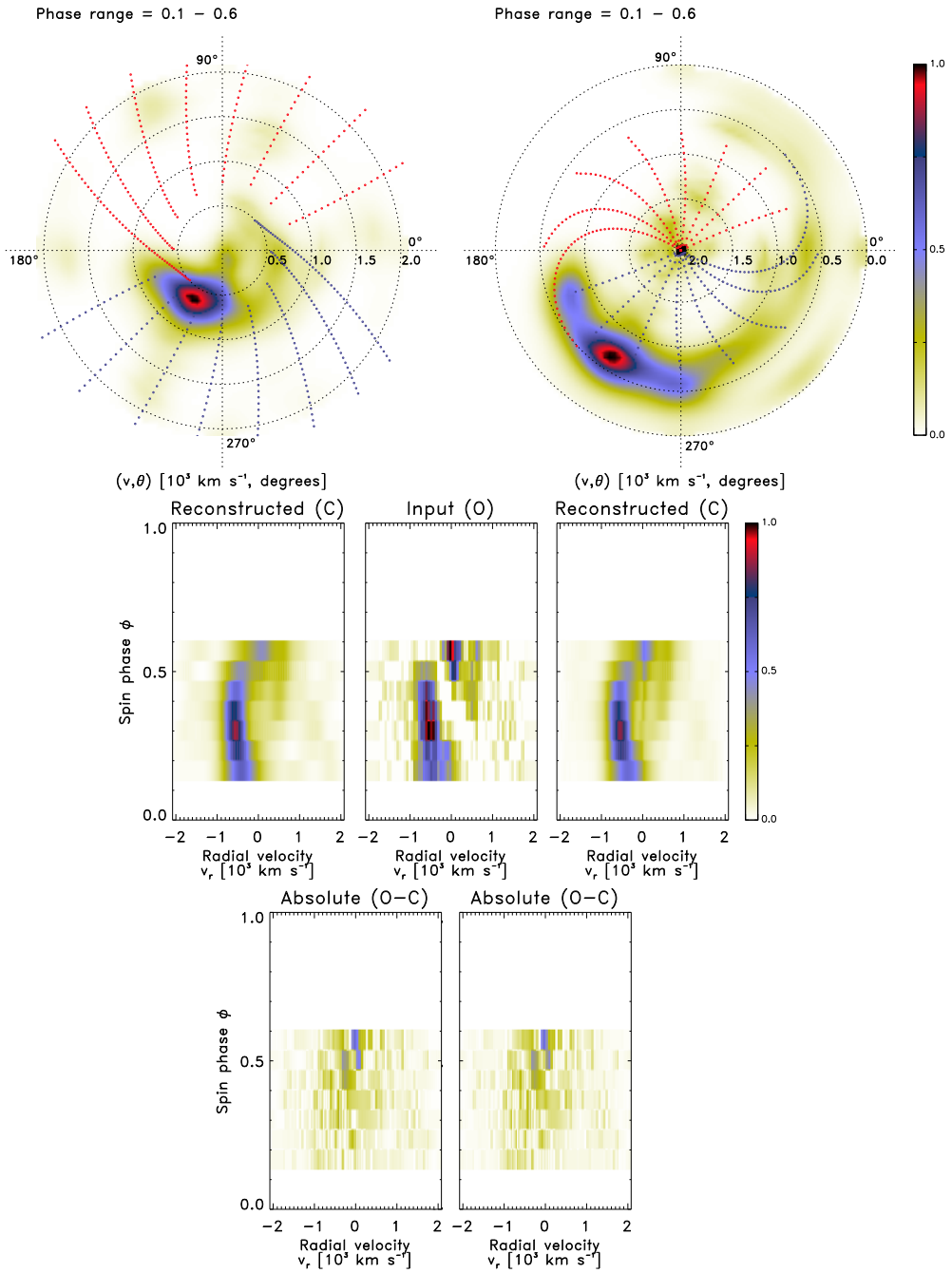

Figure A.22. Half-phase Doppler tomography of PQ Gem: orbital phase range 0.1 – 0.6.

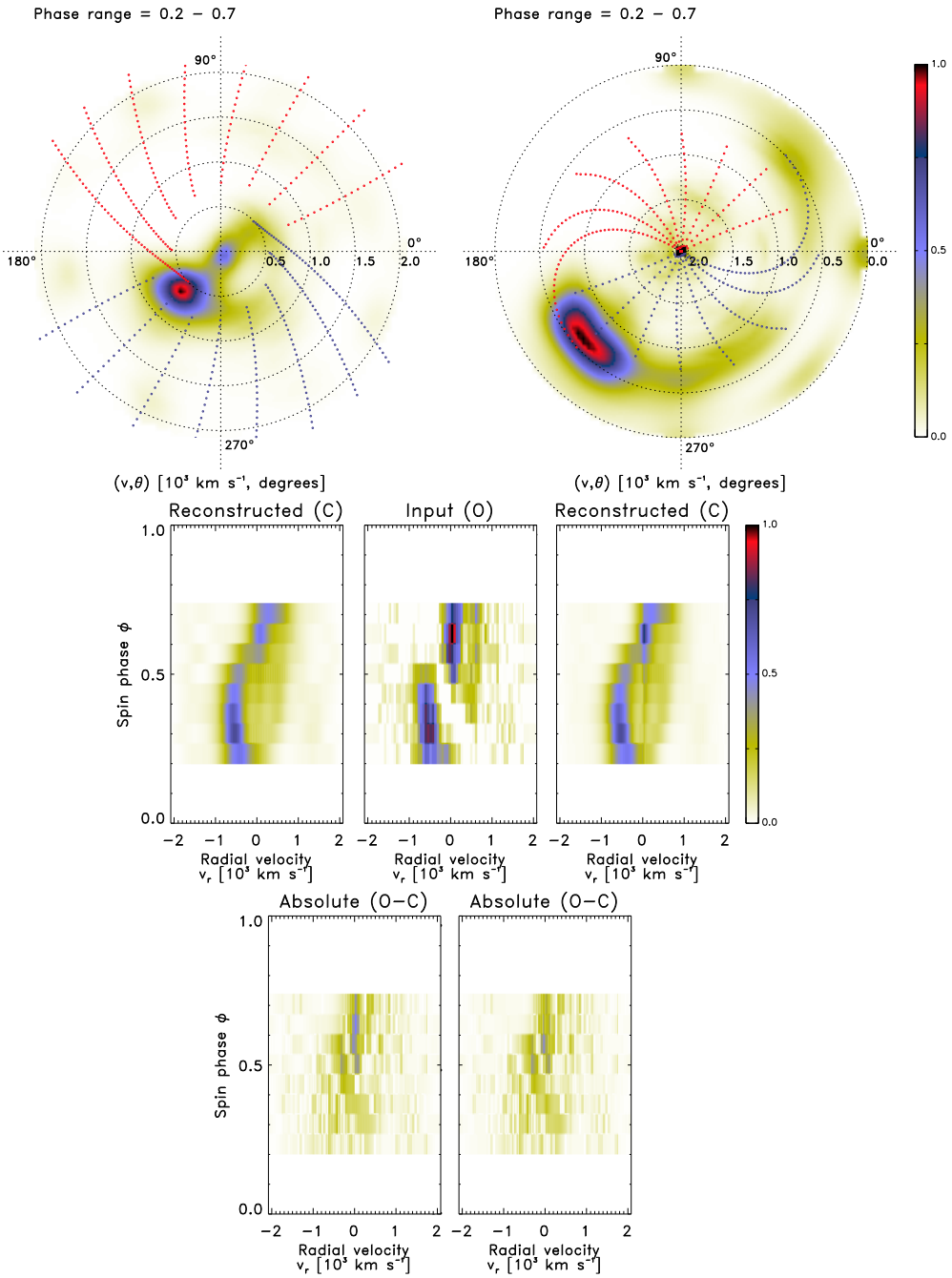

Figure A.23. Half-phase Doppler tomography of PQ Gem: orbital phase range $0.2 - 0.7$.

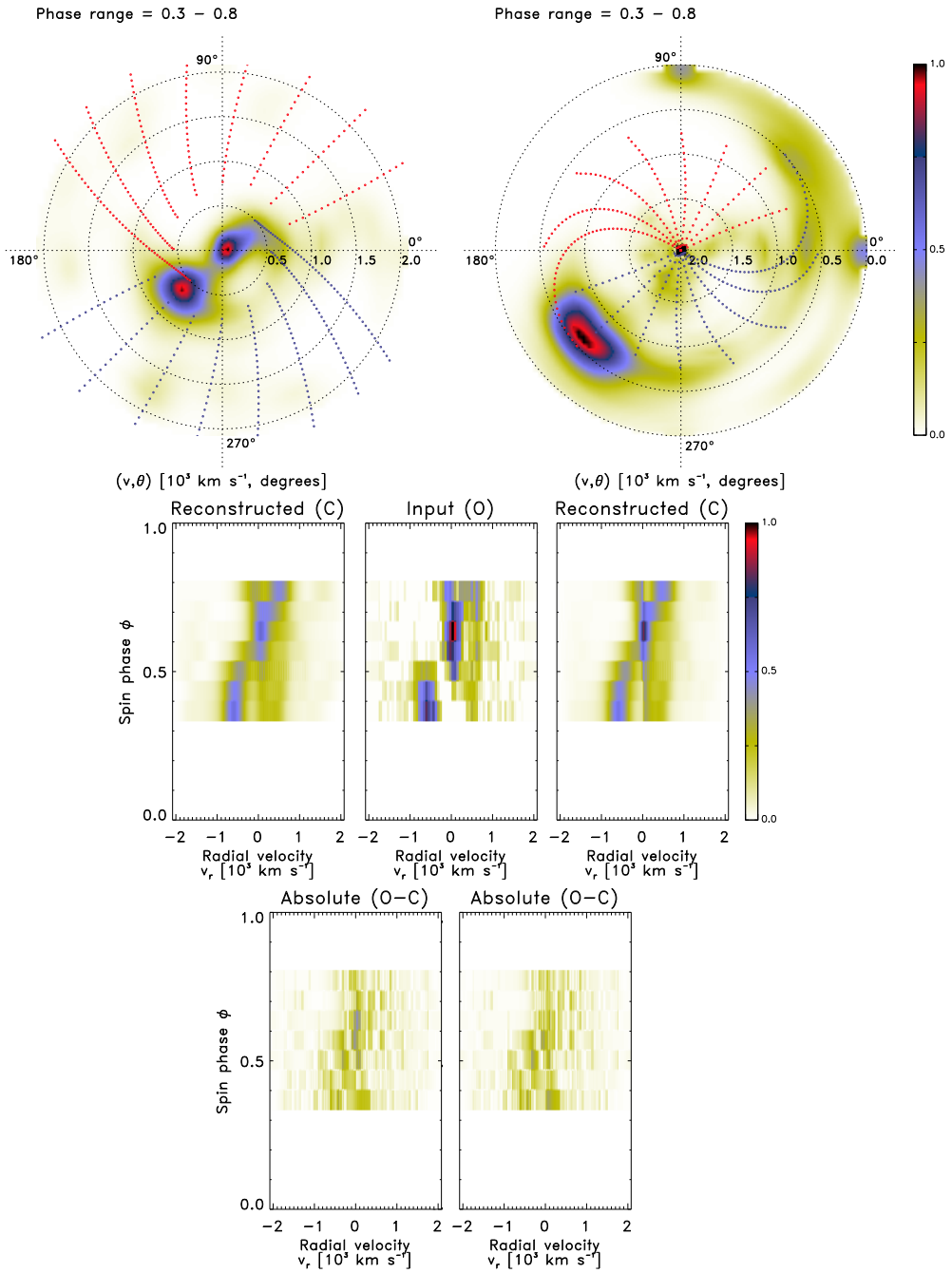

Figure A.24. Half-phase Doppler tomography of PQ Gem: orbital phase range 0.3 – 0.8.

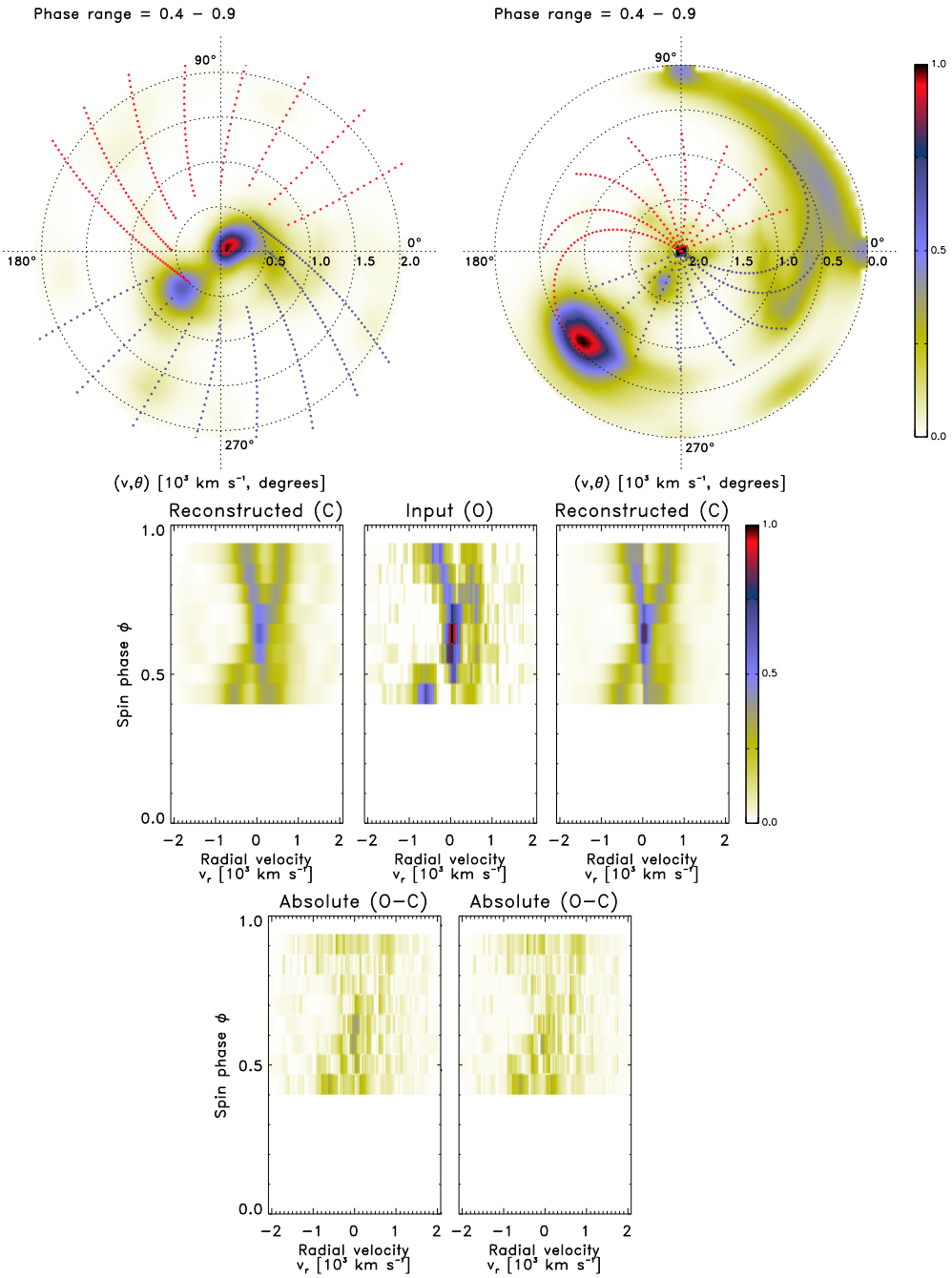

Figure A.25. Half-phase Doppler tomography of PQ Gem: orbital phase range $0.4 - 0.9$.

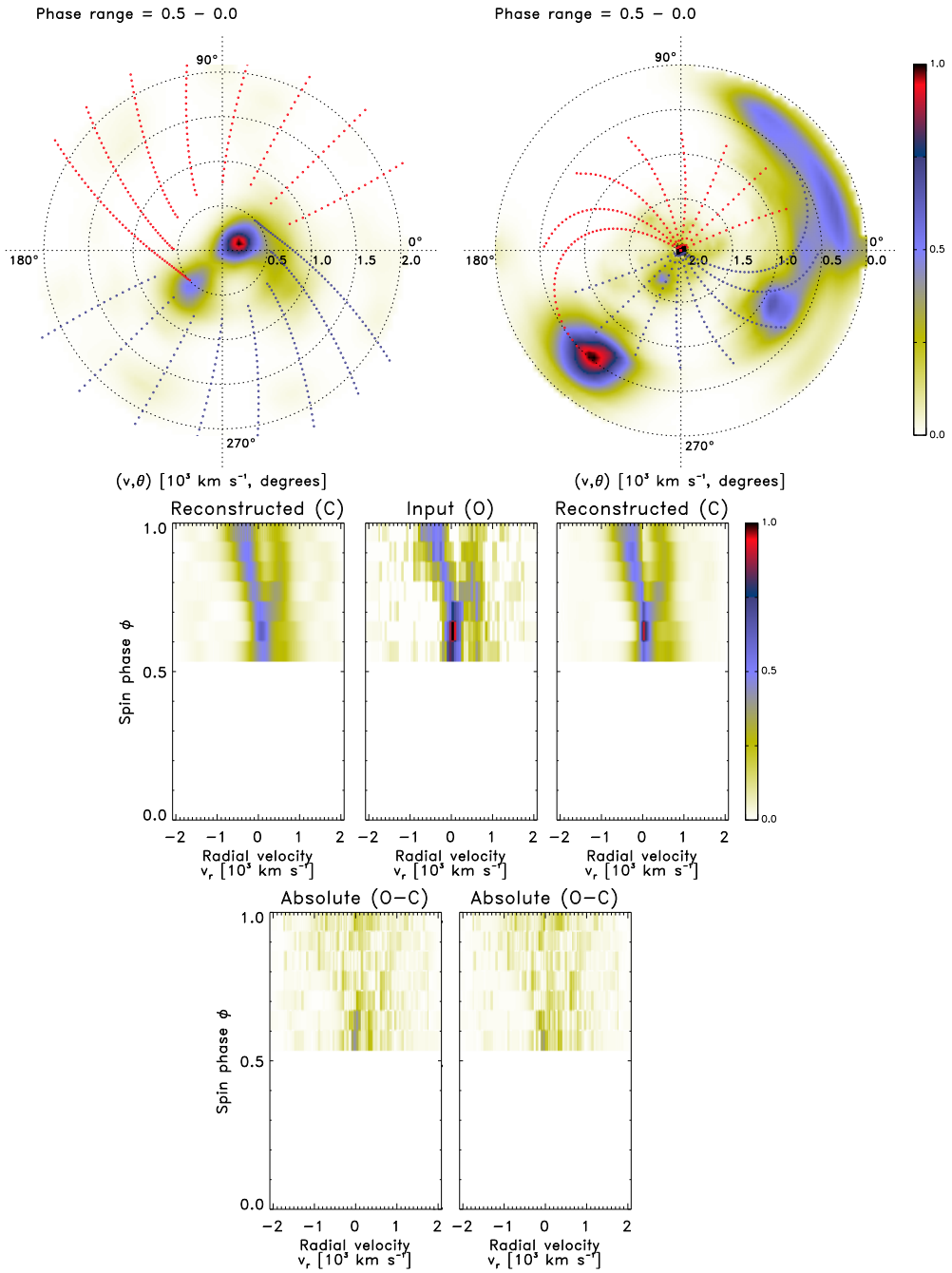

Figure A.26. Half-phase Doppler tomography of PQ Gem: orbital phase range 0.5 – 0.0.

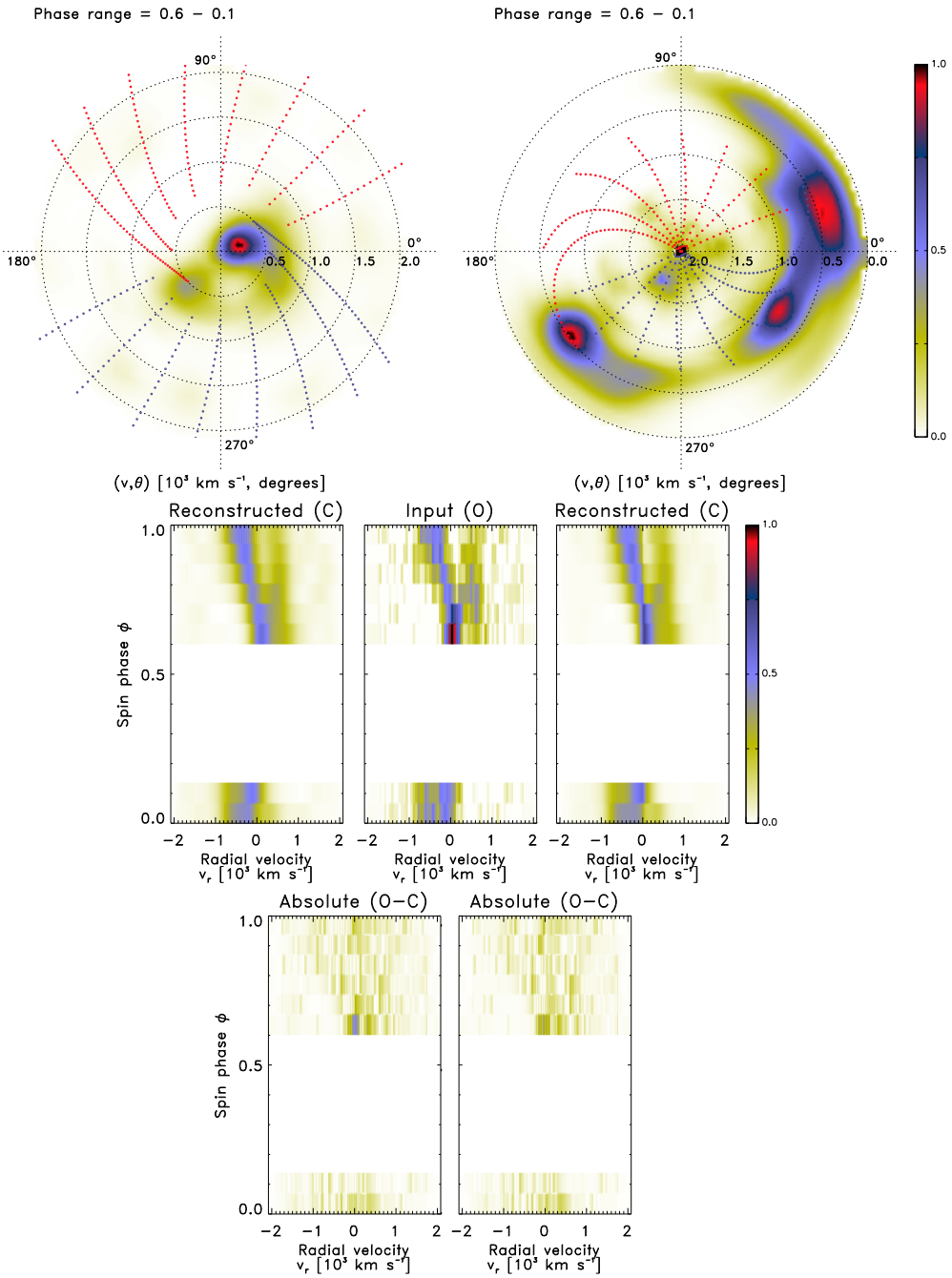

Figure A.27. Half-phase Doppler tomography of PQ Gem: orbital phase range $0.6 - 0.1$.

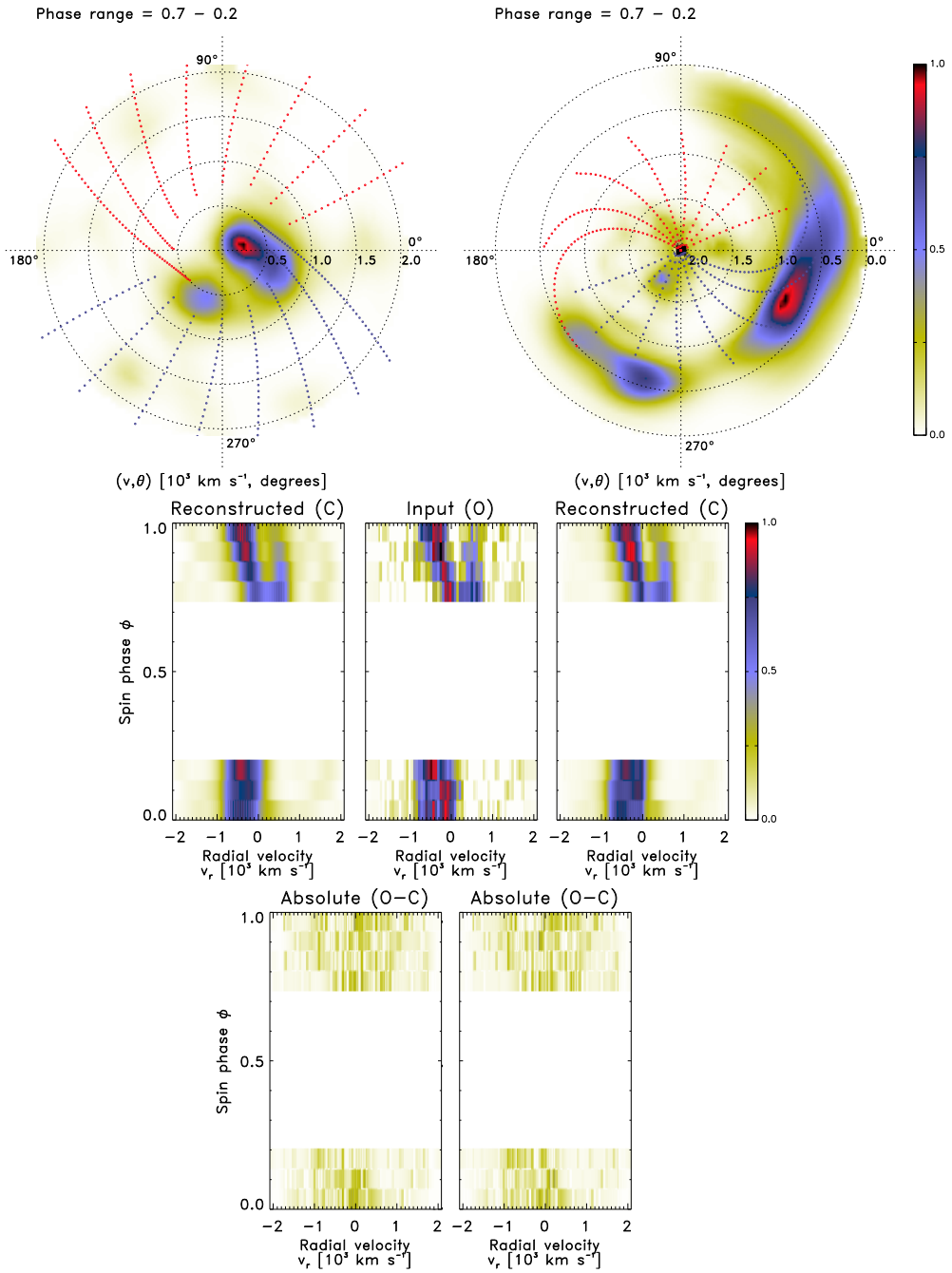

Figure A.28. Half-phase Doppler tomography of PQ Gem: orbital phase range 0.7 – 0.2.

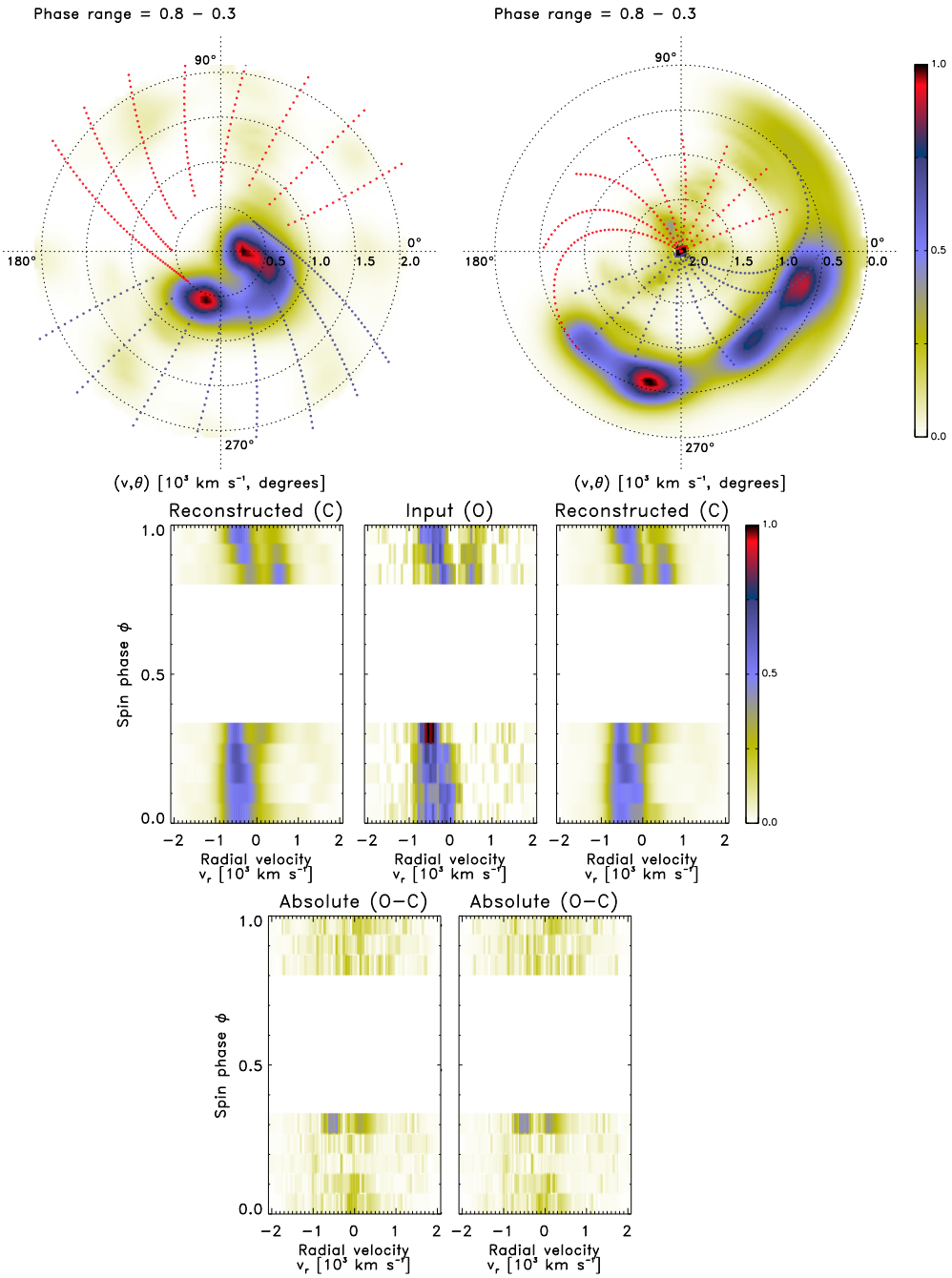

Figure A.29. Half-phase Doppler tomography of PQ Gem: orbital phase range $0.8 - 0.3$.

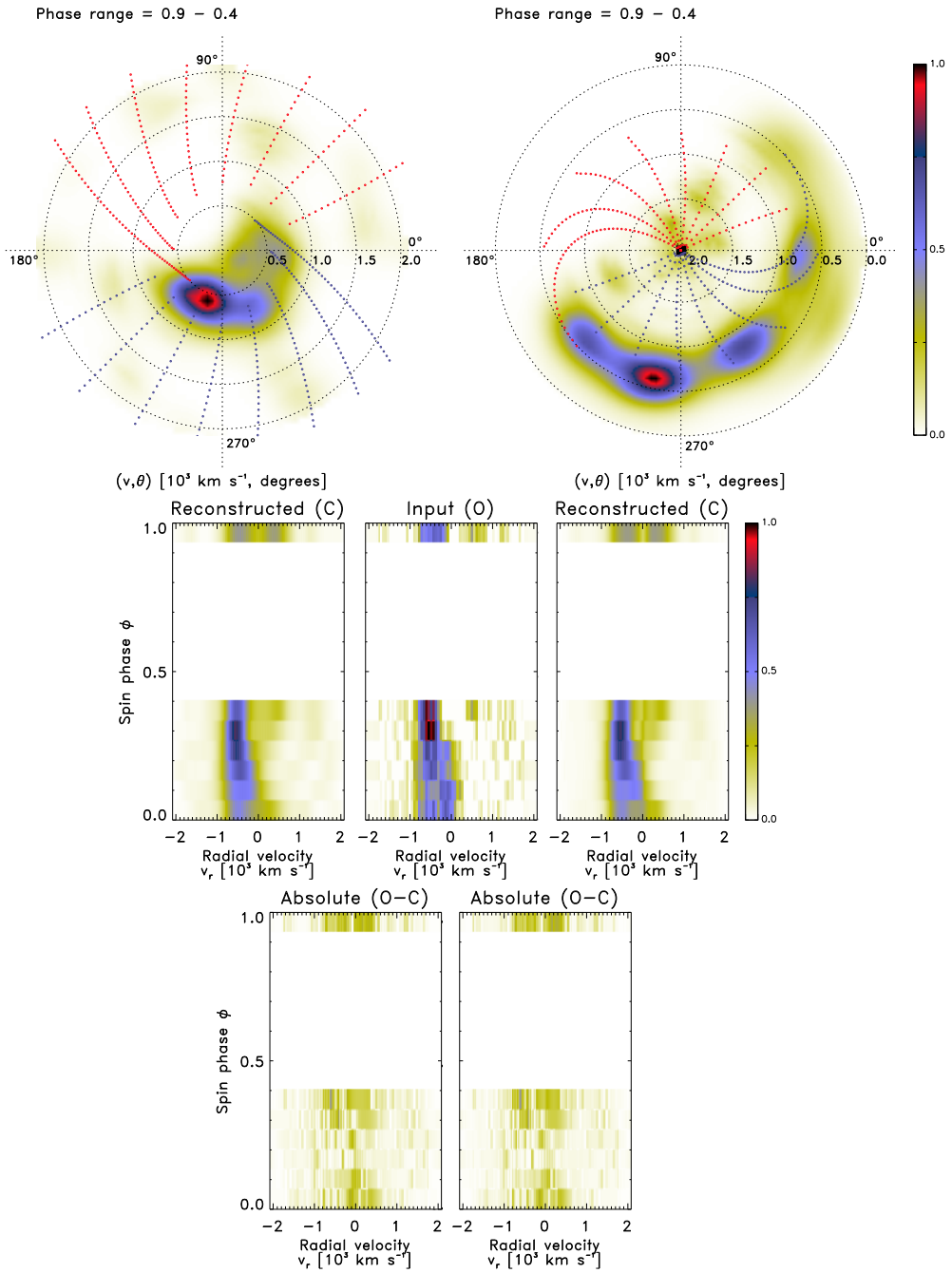

Figure A.30. Half-phase Doppler tomography of PQ Gem: orbital phase range 0.9 – 0.4.

A.4 CTCV J1928–5001: an eclipsing polar

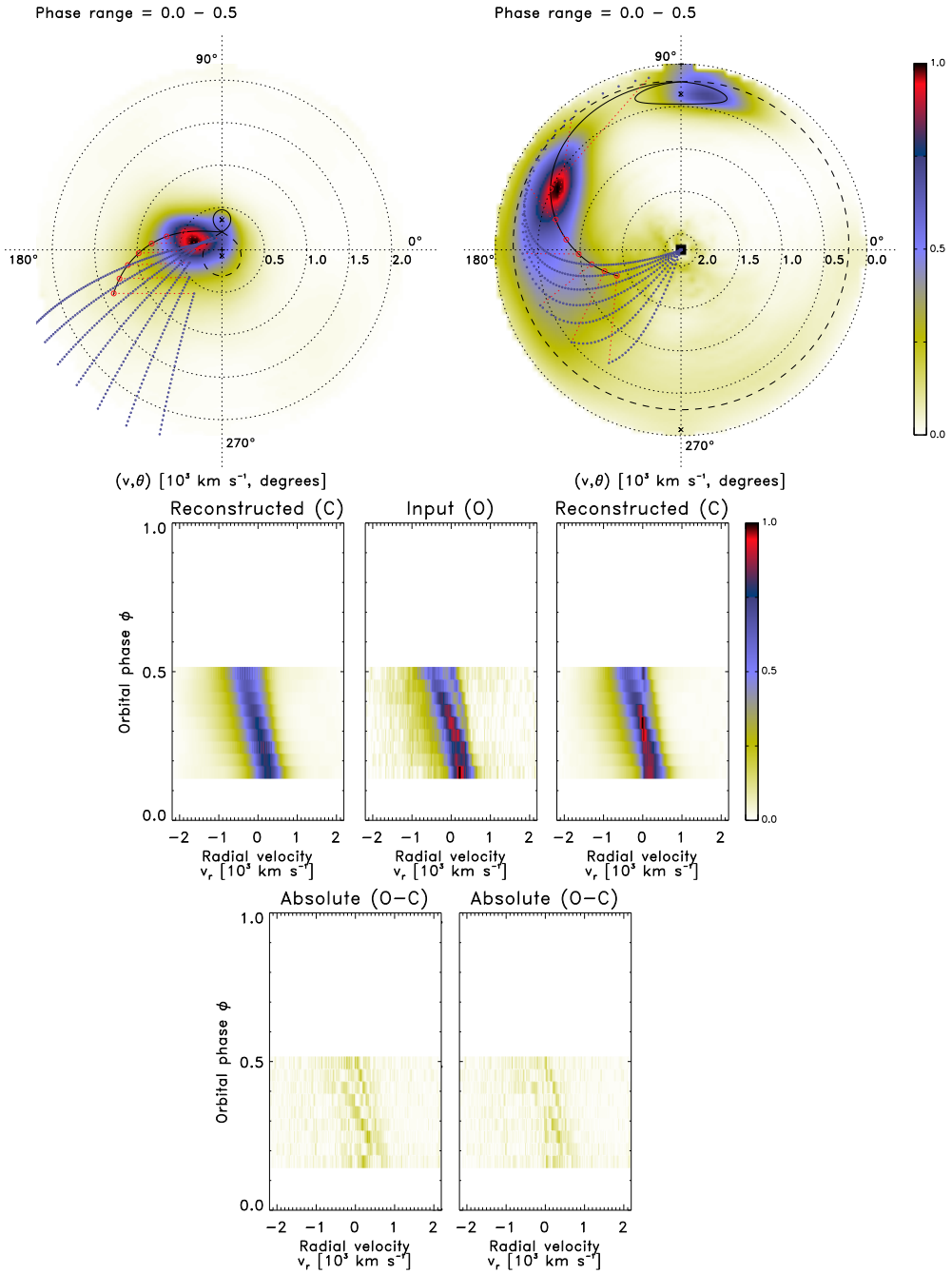

Figure A.31. Half-phase Doppler tomography of CTCV J1928−5001: orbital phase range $0.0 - 0.5$.

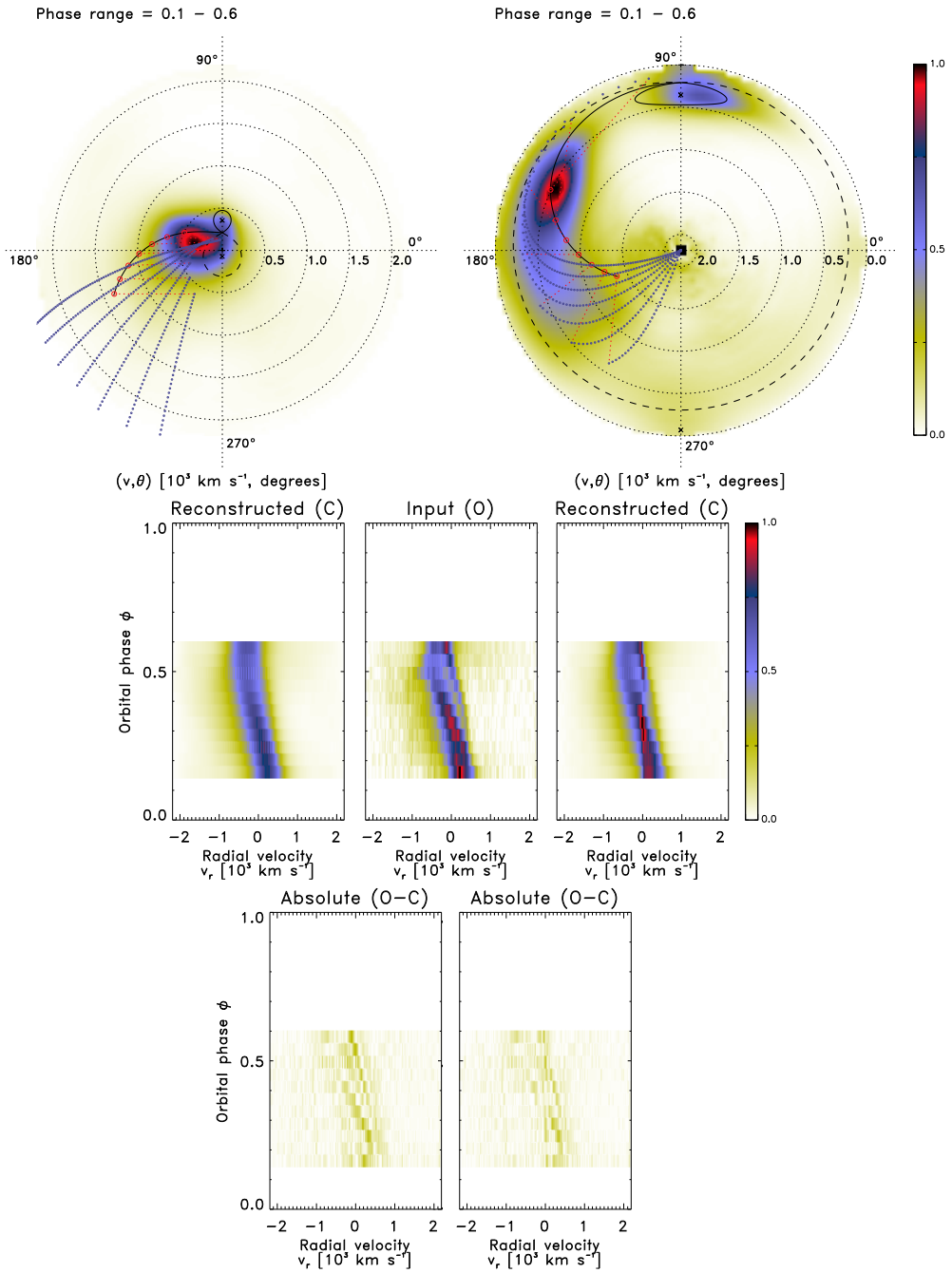

Figure A.32. Half-phase Doppler tomography of CTCV J1928−5001: orbital phase range $0.1 - 0.6$.

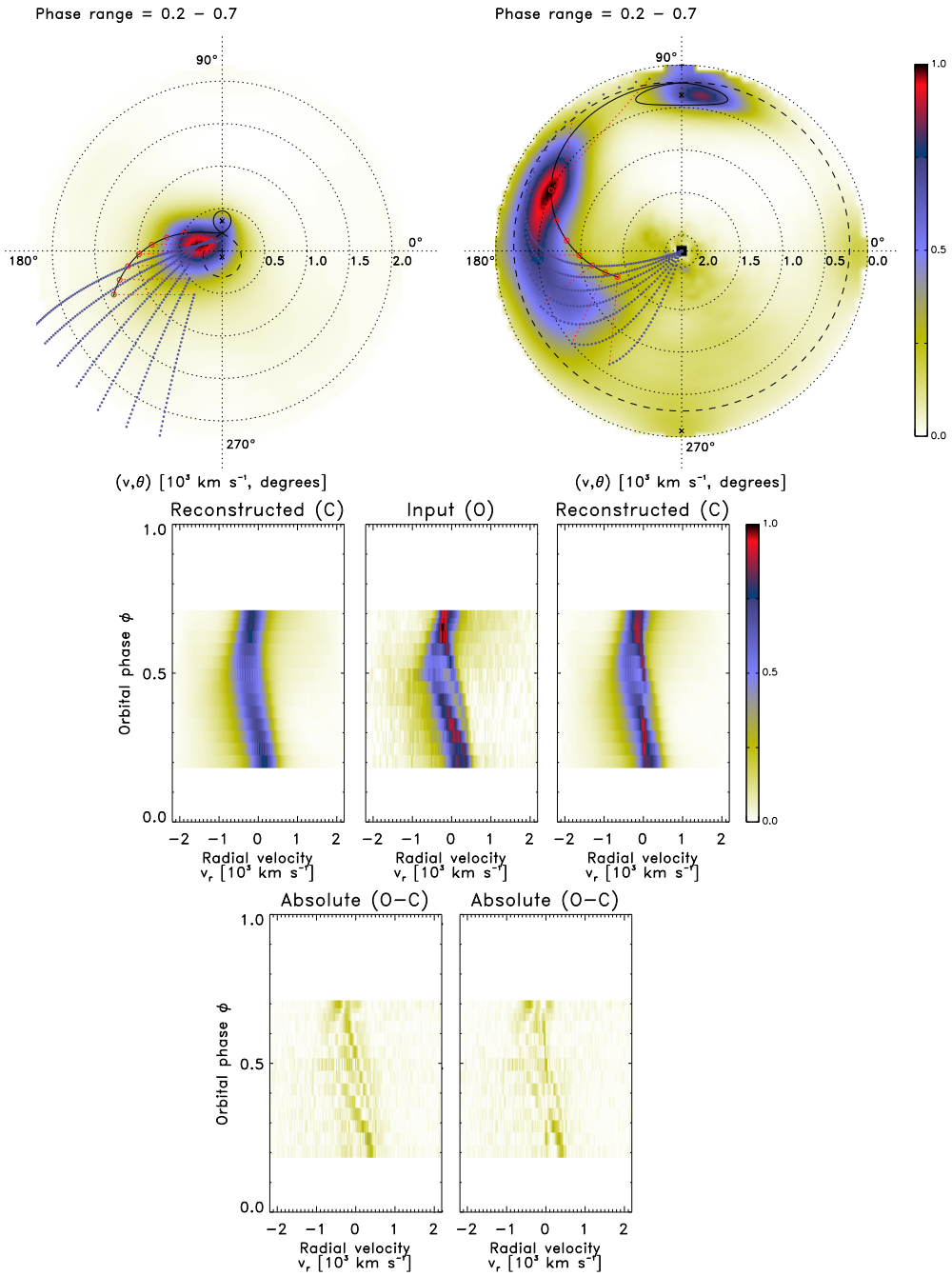

Figure A.33. Half-phase Doppler tomography of CTCV J1928−5001: orbital phase range $0.2 - 0.7$.

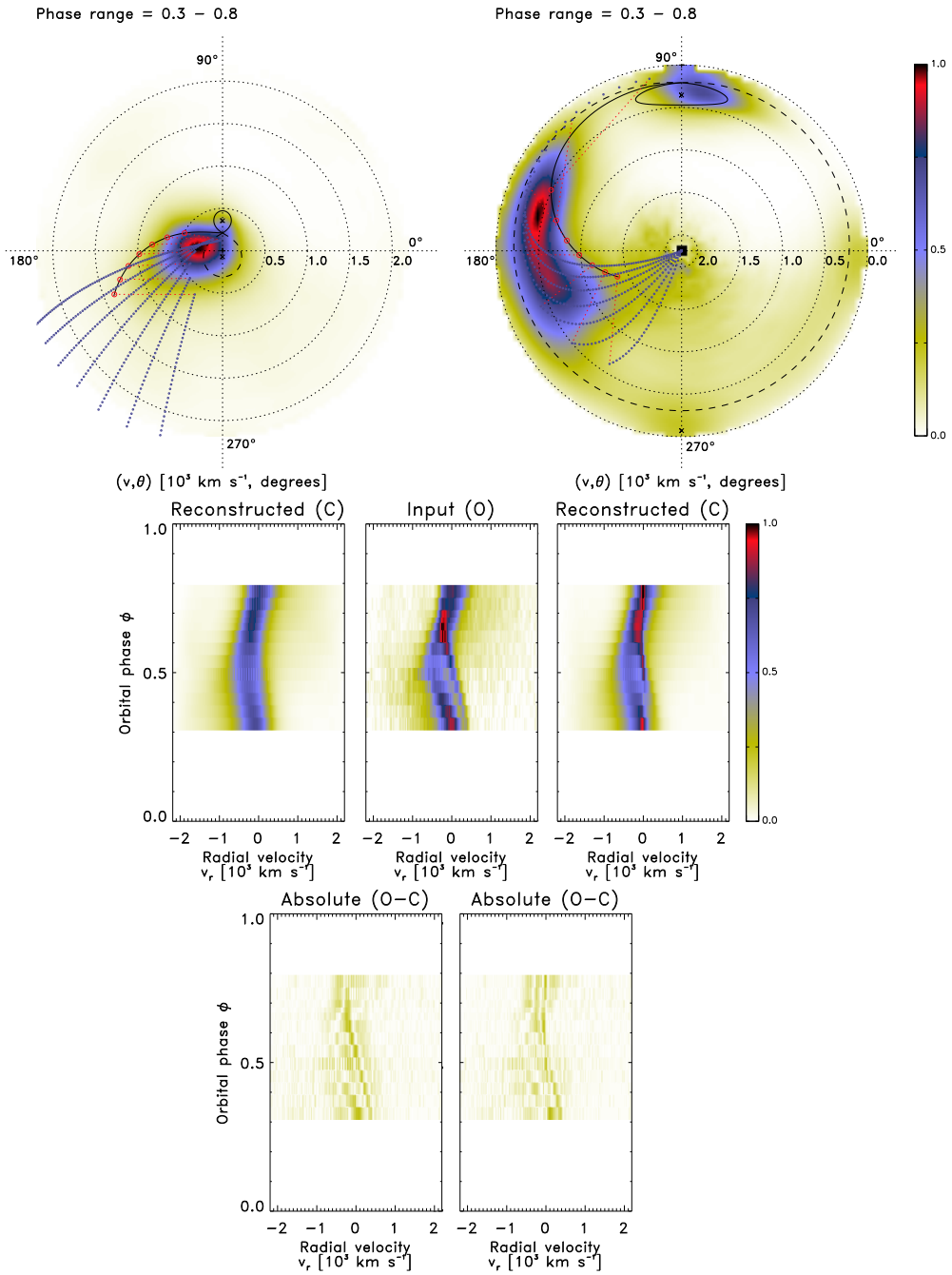

Figure A.34. Half-phase Doppler tomography of CTCV J1928−5001: orbital phase range 0.3 – 0.8.

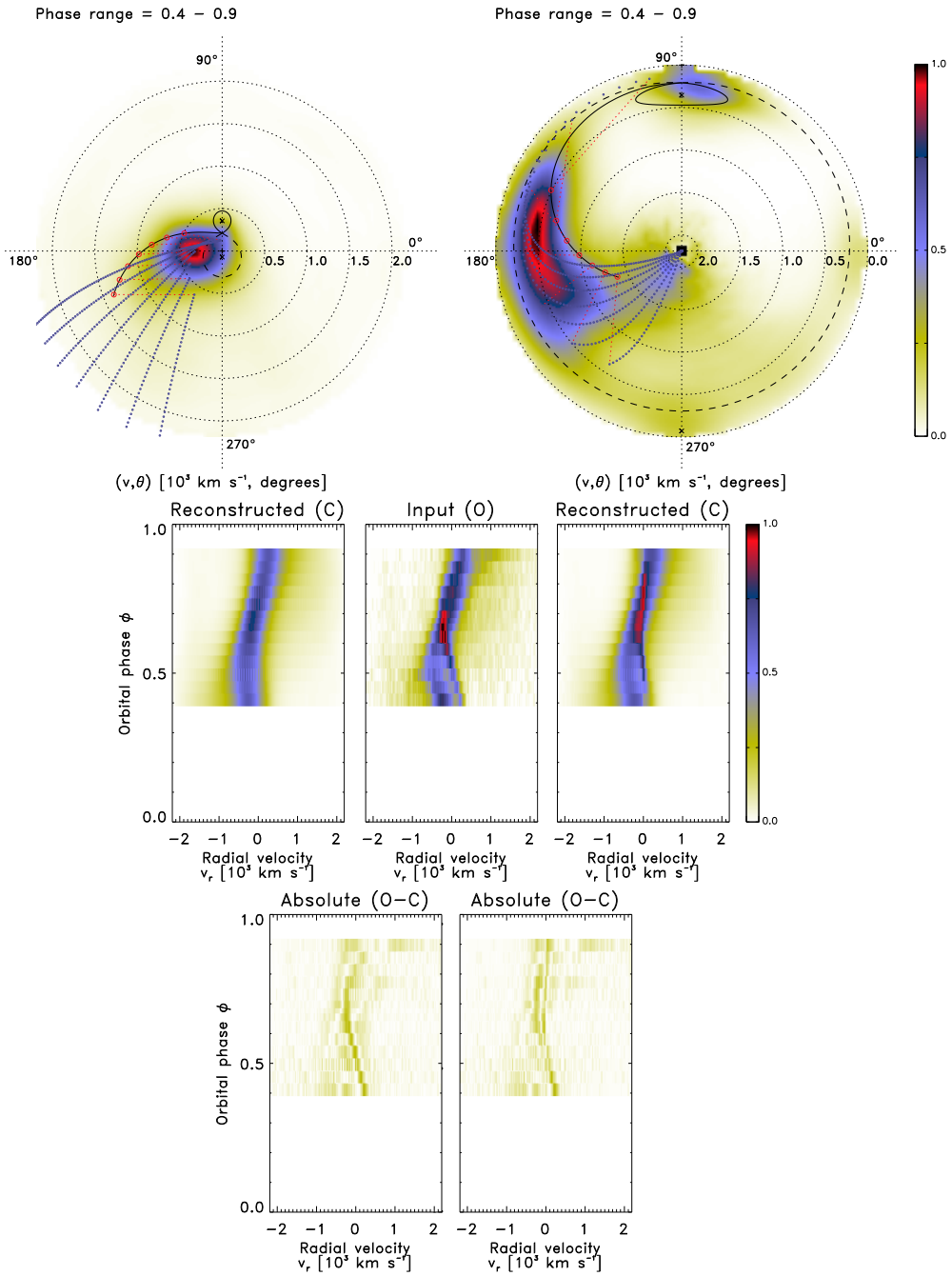

Figure A.35. Half-phase Doppler tomography of CTCV J1928−5001: orbital phase range $0.4 - 0.9$.

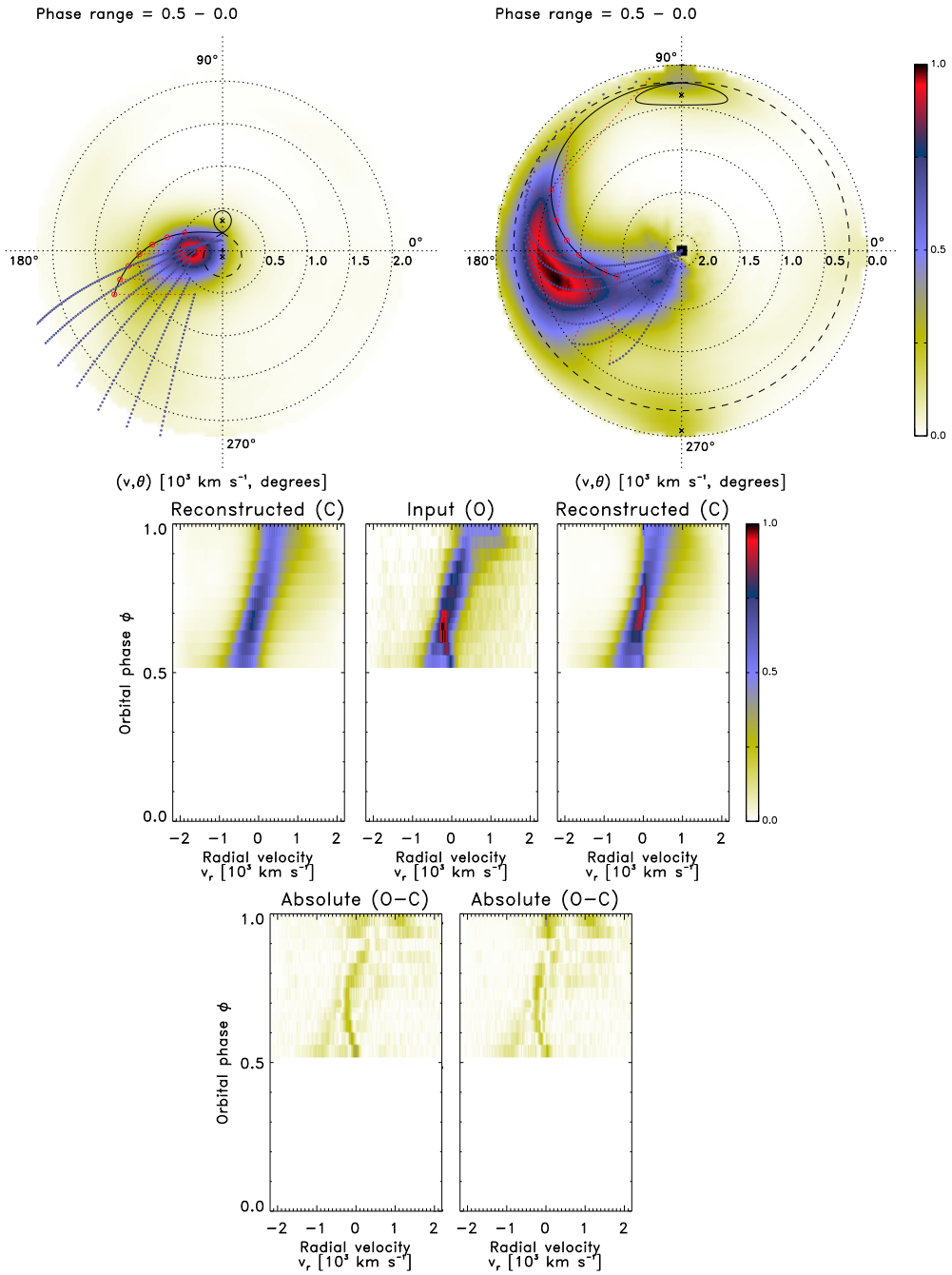

Figure A.36. Half-phase Doppler tomography of CTCV J1928−5001: orbital phase range 0.5 − 0.0.

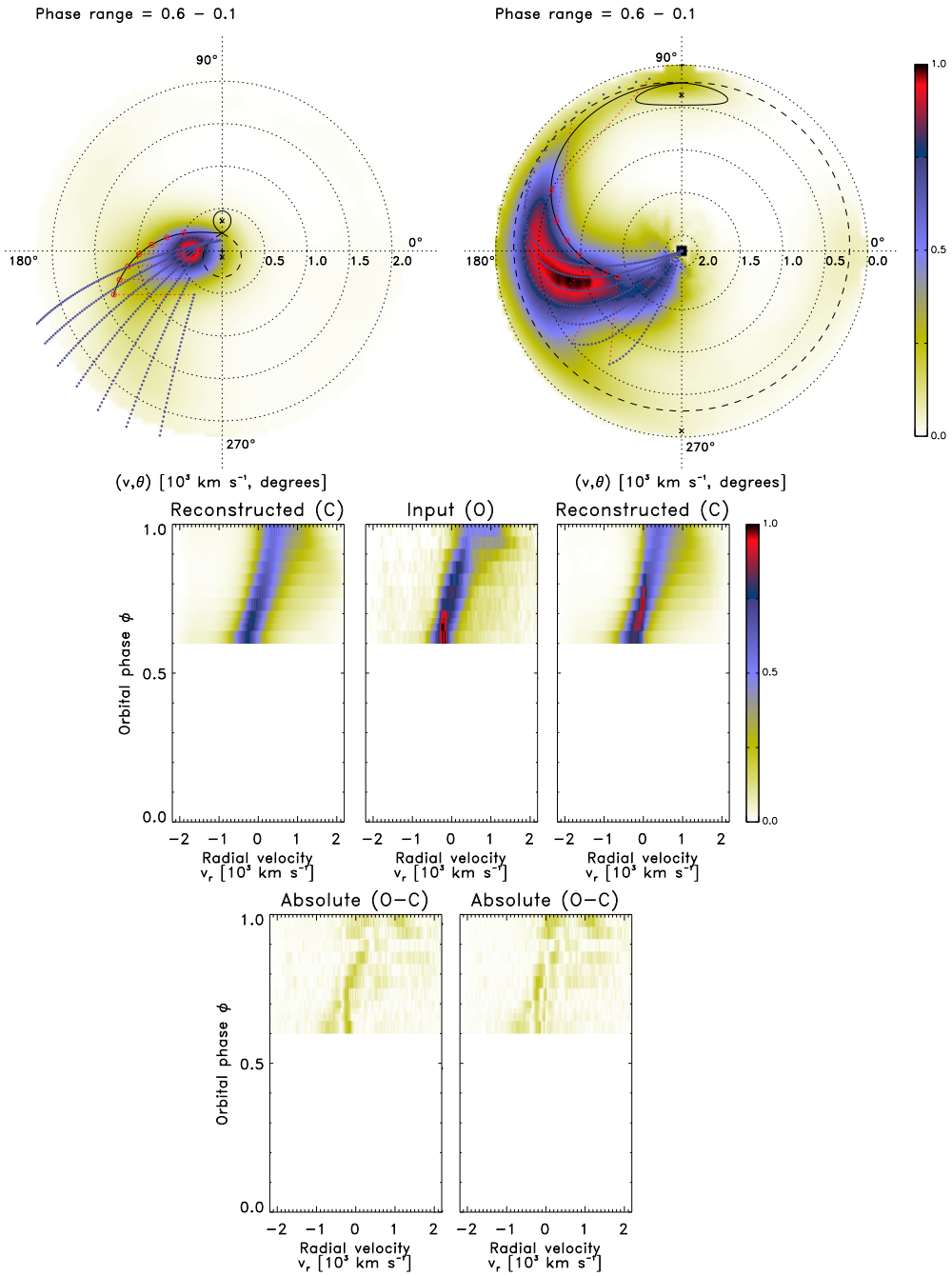

Figure A.37. Half-phase Doppler tomography of CTCV J1928−5001: orbital phase range $0.6 - 0.1$.

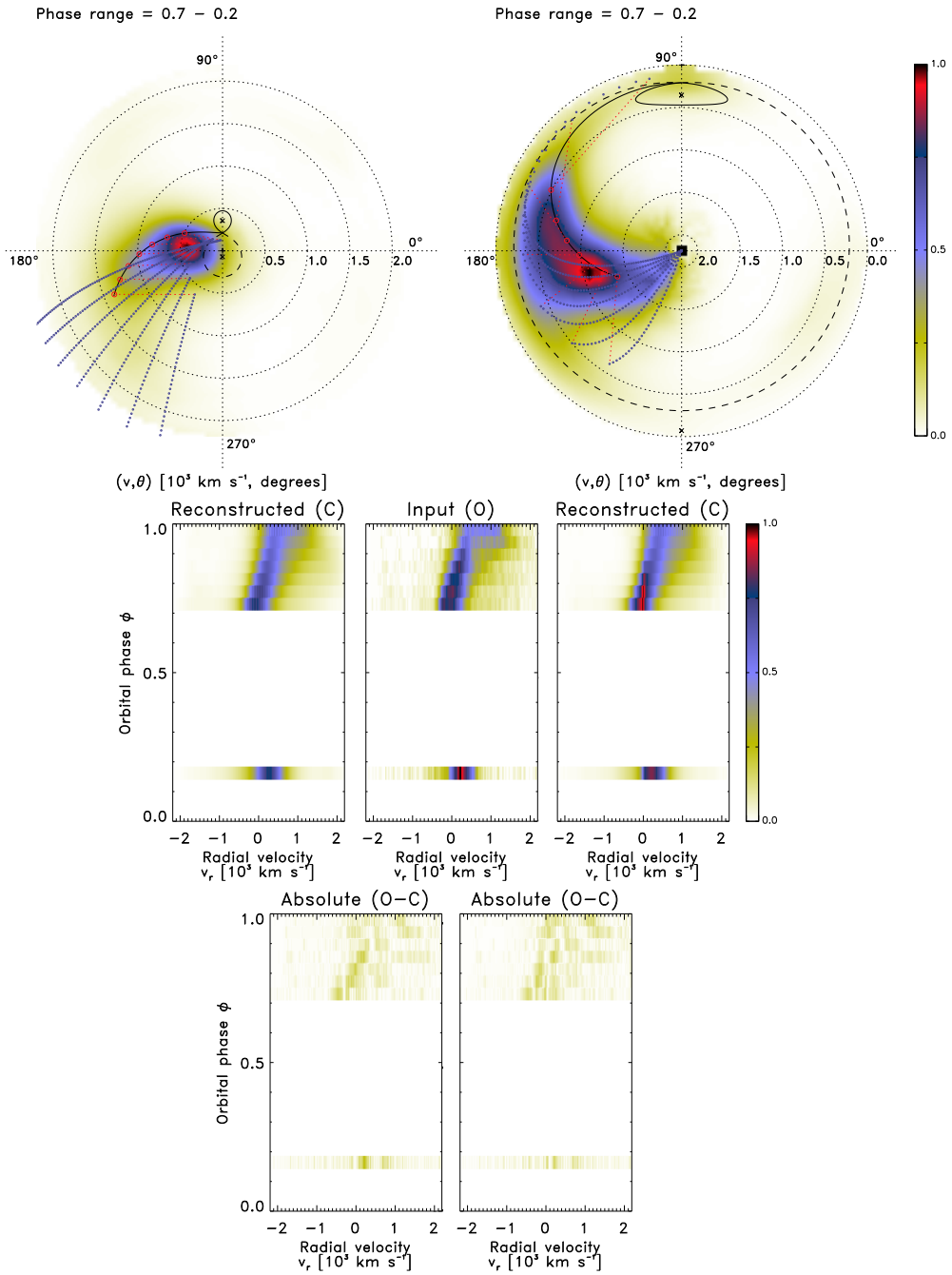

Figure A.38. Half-phase Doppler tomography of CTCV J1928−5001: orbital phase range 0.7 − 0.2.

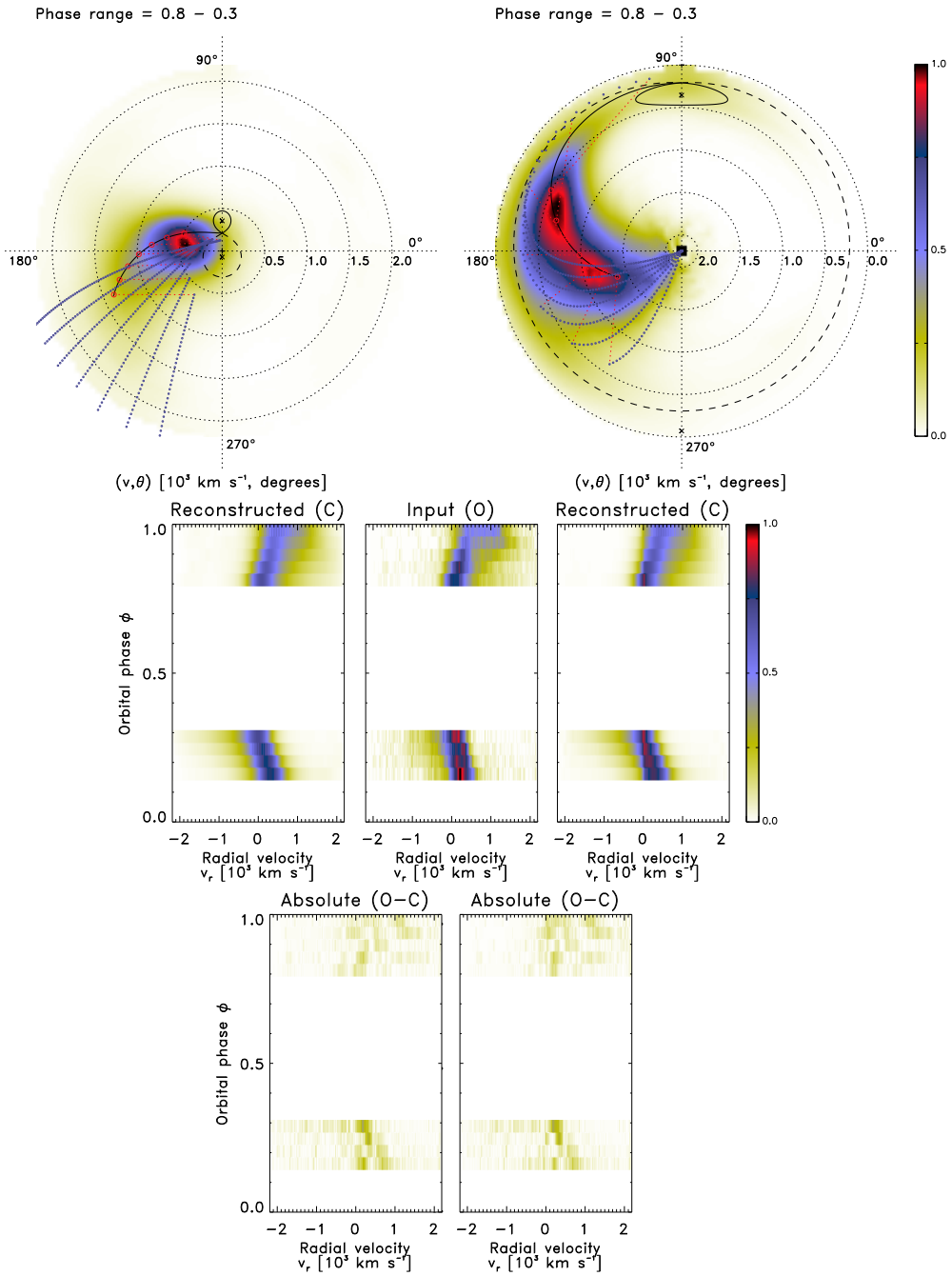

Figure A.39. Half-phase Doppler tomography of CTCV J1928−5001: orbital phase range $0.8 - 0.3$.

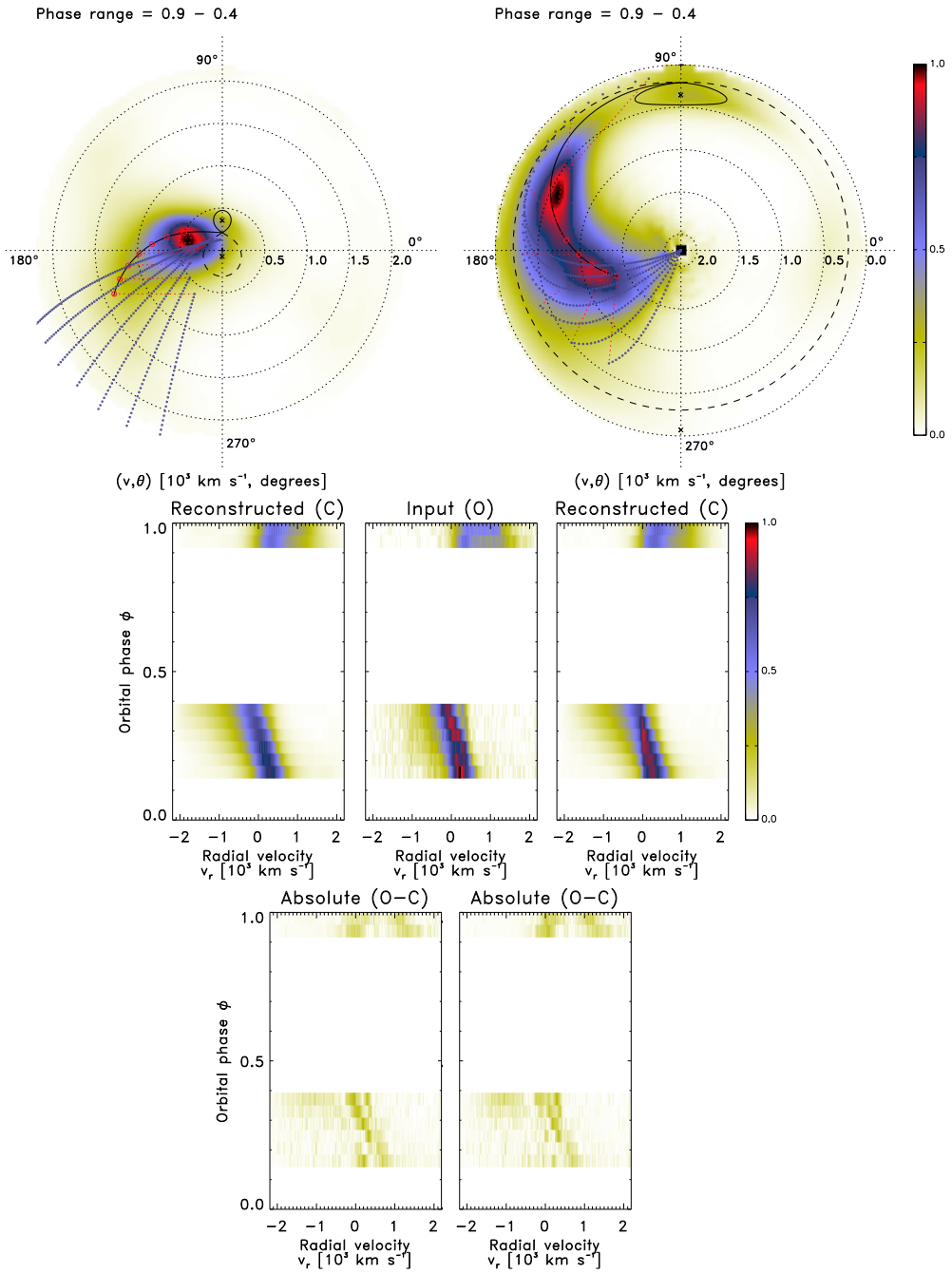

Figure A.40. Half-phase Doppler tomography of CTCV J1928−5001: orbital phase range $0.9 - 0.4$.

Bibliography

Bailey, J. 1979, MNRAS, 189, 41P

Bailey, J., Watts, D. J., Sherrington, M. R., Axon, D. J., Giles, A. B., Hanes, D. A., Heathcote, S. R., Hough, J. H., Hughes, S., Jameson, R. F., & McLean, I. 1985, MNRAS, 215, 179

Baptista, R. 2001, in Lecture Notes in Physics, Berlin Springer Verlag, Vol. 573, Astrotomography, Indirect Imaging Methods in Observational Astronomy, ed. H. M. J. Boffin, D. Steeghs, & J. Cuypers, 307

Baptista, R. 2016, in Astrophysics and Space Science Library, Vol. 439, Astrophysics and Space Science Library, ed. H. M. J. Boffin, G. Hussain, J.-P. Berger, & L. Schmidtobreick, 155

Baptista, R. & Catalán, M. S. 2000, ApJ, 539, L55

Beuermann, K., Baraffe, I., Kolb, U., & Weichhold, M. 1998, A&A, 339, 518

Beuermann, K., Buhlmann, J., Diese, J., Dreizler, S., Hessman, F. V., Husser, T.-O., Miller, G. F., Nickol, N., Pons, R., Ruhr, D., Schmülling, H., Schwope, A. D., Sorge, T., Ulrichs, L., Winget, D. E., & Winget, K. I. 2011, A&A, 526, A53

Bisikalo, D. V., Kononov, D. A., Kaigorodov, P. V., Zhilkin, A. G., & Boyarchuk, A. A. 2008, Astronomy Reports, 52, 318

Bisikalo, D. V., Zhilkin, A. G., Kaygorodov, P. V., Ustyugov, V. A., & Montgomery, M. M. 2013, Astronomy Reports, 57, 327

Blinova, A. A., Romanova, M. M., & Lovelace, R. V. E. 2016, MNRAS, 459, 2354

Boneva, D., Kaigorodov, P. V., Bisikalo, D. V., & Kononov, D. A. 2009, Astronomy Reports, 53, 1004

Brocklehurst, M. 1971, MNRAS, 153, 471

Buckley, D. A. H., Swart, G. P., & Meiring, J. G. 2006, in Proc. SPIE, Vol. 6267, Society of Photo-Optical Instrumentation Engineers (SPIE) Conference Series, 62670Z

Burgh, E. B., Nordsieck, K. H., Kobulnicky, H. A., Williams, T. B., O'Donoghue, D., Smith, M. P., & Percival, J. W. 2003, in Proc. SPIE, Vol. 4841, Instrument Design and Performance for Optical/Infrared Ground-based Telescopes, ed. M. Iye & A. F. M. Moorwood, 1463–1471

Carroll, B. W. & Ostlie, D. A. 2007, An Introduction to Modern Astrophysics (San Francisco: Pearson Addison Wesley)

Čechura, J., Vrtilek, S. D., & Hadrava, P. 2015, MNRAS, 450, 2410

Charbonneau, P. 1995, ApJS, 101, 309

Clarke, J. T., Bowyer, S., & Capel, D. 1984, ApJ, 287, 845

Copperwheat, C. M., Marsh, T. R., Dhillon, V. S., Littlefair, S. P., Hickman, R., Gänsicke, B. T., & Southworth, J. 2010, MNRAS, 402, 1824

Crawford, J. A. & Kraft, R. P. 1956, ApJ, 123, 44

Crawford, S. M., Still, M., Schellart, P., Balona, L., Buckley, D. A. H., Dugmore, G., Gulbis, A. A. S., Kniazev, A., Kotze, M., Loaring, N., Nordsieck, K. H., Pickering, T. E., Potter, S., Romero Colmenero, E., Vaisanen, P., Williams, T., & Zietsman, E. 2010, in Proc. SPIE, Vol. 7737, Observatory Operations: Strategies, Processes, and Systems III, 773725

Cropper, M. 1990, Space Sci. Rev., 54, 195

Dai, Z.-B., Qian, S.-B., Fernández Lajús, E., & Baume, G. L. 2010, MNRAS, 409, 1195

Dhillon, V. S. & Watson, C. A. 2001, in Lecture Notes in Physics, Berlin Springer Verlag, Vol. 573, Astrotomography, Indirect Imaging Methods in Observational Astronomy, ed. H. M. J. Boffin, D. Steeghs, & J. Cuypers, 94

Dunford, A., Watson, C. A., & Smith, R. C. 2012, MNRAS, 422, 3444

Eastman, J., Siverd, R., & Gaudi, B. S. 2010, PASP, 122, 935

Eggleton, P. P. 1976, in IAU Symposium, Vol. 73, Structure and Evolution of Close Binary Systems, ed. P. Eggleton, S. Mitton, & J. Whelan, 209

Einstein, A. 1905, Annalen der Physik, 322, 891

Faulkner, J. 1971, ApJ, 170, L99

Faulkner, J. 1976, in IAU Symposium, Vol. 73, Structure and Evolution of Close Binary Systems, ed. P. Eggleton, S. Mitton, & J. Whelan, 193

Ferrario, L., de Martino, D., & Gänsicke, B. T. 2015, Space Sci. Rev., 191, 111

Frank, J., King, A., & Raine, D. J. 2002, Accretion Power in Astrophysics: Third Edition (Cambridge: Cambridge Univ. Press), 398

Gänsicke, B. T., Dillon, M., Southworth, J., Thorstensen, J. R., Rodríguez-Gil, P., Aungwerojwit, A., Marsh, T. R., Szkody, P., Barros, S. C. C., Casares, J., de Martino, D., Groot, P. J., Hakala, P., Kolb, U., Littlefair, S. P., Martínez-Pais, I. G., Nelemans, G., & Schreiber, M. R. 2009, MNRAS, 397, 2170

Gerke, J. R., Howell, S. B., & Walter, F. M. 2006, PASP, 118, 678

Hakala, P., Cropper, M., & Ramsay, G. 2002, MNRAS, 334, 990

Hakala, P. J. 1995, A&A, 296, 164

Hamuy, M., Suntzeff, N. B., Heathcote, S. R., Walker, A. R., Gigoux, P., & Phillips, M. M. 1994, PASP, 106, 566

Harlaftis, E. T., Baptista, R., Morales-Rueda, L., Marsh, T. R., & Steeghs, D. 2004, A&A, 417, 1063

Harlaftis, E. T., Steeghs, D., Horne, K., Martín, E., & Magazzú, A. 1999, MNRAS, 306, 348

Harrop-Allin, M. K., Cropper, M., Hakala, P. J., Hellier, C., & Ramseyer, T. 1999a, MNRAS, 308, 807

Harrop-Allin, M. K., Hakala, P. J., & Cropper, M. 1999b, MNRAS, 302, 362

Heerlein, C., Horne, K., & Schwope, A. D. 1999, MNRAS, 304, 145

Hellier, C. 1997, MNRAS, 288, 817

—. 1999, ApJ, 519, 324

—. 2001, Cataclysmic Variable Stars (Chichester, UK: Springer-Praxis Publishing)

Hill, C. A., Watson, C. A., Shahbaz, T., Steeghs, D., & Dhillon, V. S. 2014, MNRAS, 444, 192

Horne, K. 1985, MNRAS, 213, 129

Horne, K. 1991, in Fundamental Properties of Cataclysmic Variable Stars, ed. A. W. Shafter, Proceedings 12th North American Workshop on CVs and Low Mass X-Ray Binaries (San Diego: San Diego Univ. Press)

Horne, K. & Marsh, T. R. 1986, MNRAS, 218, 761

Howell, S. B., Nelson, L. A., & Rappaport, S. 2001, ApJ, 550, 897

Huang, S.-S. 1966, Annales d'Astrophysique, 29, 331

—. 1972, ApJ, 171, 549

Hulse, R. A. & Taylor, J. H. 1975, ApJ, 195, L51

Hut, P. 1981, A&A, 99, 126

Iben, Jr., I. & Livio, M. 1993, PASP, 105, 1373

Jaynes, E. T. 1957, Physical Review, 106, 620

Ju, W., Stone, J. M., & Zhu, Z. 2016, ApJ, 823, 81

Kiplinger, A. L. 1979, ApJ, 234, 997

Knigge, C. 2006, MNRAS, 373, 484

Knigge, C. 2011, in Astronomical Society of the Pacific Conference Series, Vol. 447, Evolution of Compact Binaries, ed. L. Schmidtobreick, M. R. Schreiber, & C. Tappert, 3

Knigge, C., Baraffe, I., & Patterson, J. 2011, ApJS, 194, 28

Kobulnicky, H. A., Nordsieck, K. H., Burgh, E. B., Smith, M. P., Percival, J. W., Williams, T. B., & O'Donoghue, D. 2003, in Proc. SPIE, Vol. 4841, Instrument Design and Performance for Optical/Infrared Ground-based Telescopes, ed. M. Iye & A. F. M. Moorwood, 1634–1644

Kolb, U. & Baraffe, I. 1999, MNRAS, 309, 1034

Kononov, D. A., Giovannelli, F., Bruni, I., & Bisikalo, D. V. 2012, A&A, 538, A94

Kopal, Z. 1959, Close Binary Systems (London: Chapman & Hall)

Kotze, E. J., Potter, S. B., & McBride, V. A. 2015, A&A, 579, A77

—. 2016, A&A, 580, A99

Kraft, R. P. 1962, ApJ, 135, 408

Krzemiński, W. & Serkowski, K. 1977, ApJ, 216, L45

Kuiper, G. P. 1941, ApJ, 93, 133

Li, J. & Wickramasinghe, D. T. 1998, MNRAS, 300, 718

Lucy, L. B. 1974, AJ, 79, 745

—. 1994, A&A, 289, 983

Marsh, T. R. 2001, in Lecture Notes in Physics, Berlin Springer Verlag, Vol. 573, Astrotomography, Indirect Imaging Methods in Observational Astronomy, ed. H. M. J. Boffin, D. Steeghs, & J. Cuypers, 1

Marsh, T. R. 2005, Ap&SS, 296, 403

Marsh, T. R. & Horne, K. 1988, MNRAS, 235, 269

Marsh, T. R., Horne, K., Schlegel, E. M., Honeycutt, R. K., & Kaitchuck, R. H. 1990, ApJ, 364, 637

Marsh, T. R. & Schwope, A. D. 2016, in Astrophysics and Space Science Library, Vol. 439, Astrophysics and Space Science Library, ed. H. M. J. Boffin, G. Hussain, J.-P. Berger, & L. Schmidtobreick, 195

Meggitt, S. M. A. & Wickramasinghe, D. T. 1982, MNRAS, 198, 71

Morin, J., Hill, C. A., & Watson, C. A. 2016, in Astrophysics and Space Science Library, Vol. 439, Astrophysics and Space Science Library, ed. H. M. J. Boffin, G. Hussain, J.-P. Berger, & L. Schmidtobreick, 223

Mukai, K. 1988, MNRAS, 232, 175

Narayan, R. & Nityananda, R. 1986, ARA&A, 24, 127

O'Donoghue, D., Buckley, D. A. H., Balona, L. A., Bester, D., Botha, L., Brink, J., Carter, D. B., Charles, P. A., Christians, A., Ebrahim, F., Emmerich, R., Esterhuyse, W., Evans, G. P., Fourie, C., Fourie, P., Gajjar, H., Gordon, M., Gumede, C., de Kock, M., Koeslag, A., Koorts, W. P., Kriel, H., Marang, F., Meiring, J. G., Menzies, J. W., Menzies, P., Metcalfe, D., Meyer, B., Nel, L., O'Connor, J., Osman, F., Du Plessis, C., Rall, H., Riddick, A., Romero-Colmenero, E., Potter, S. B., Sass, C., Schalekamp, H., Sessions, N., Siyengo, S., Sopela, V., Steyn, H., Stoffels, J., Scholtz, J., Swart, G., Swat, A., Swiegers, J., Tiheli, T., Vaisanen, P., Whittaker, W., & van Wyk, F. 2006, MNRAS, 372, 151

Osaki, Y. 1974, PASJ, 26, 429

Paczyński, B. 1967, AcA, 17, 287

Paczynski, B. 1981, AcA, 31, 1

Paczyński, B. & Sienkiewicz, R. 1981, ApJ, 248, L27

Papadaki, C., Boffin, H. M. J., & Steeghs, D. 2008, Journal of Astronomical Data, 14, 2

Patterson, J. 1984, ApJS, 54, 443

—. 1994, PASP, 106, 209

—. 2011, MNRAS, 411, 2695

Patterson, J. & Raymond, J. C. 1985, ApJ, 292, 535

Patterson, J., Richman, H., Kemp, J., & Mukai, K. 1998, PASP, 110, 403

Patterson, J., Skillman, D. R., Thorstensen, J., & Hellier, C. 1995, PASP, 107, 307

Peris, C. S., Vrtilek, S. D., Steiner, J. F., Vrtilek, J. M., Wu, J., McClintock, J. E., Longa-Peña, P., Steeghs, D., Callanan, P., Ho, L. C., Orosz, J. A., & Reynolds, M. T. 2015, MNRAS, 449, 1584

Potter, S., Ramsay, G., Wu, K., & Cropper, M. 2002, in Astronomical Society of the Pacific Conference Series, Vol. 261, The Physics of Cataclysmic Variables and Related Objects, ed. B. T. Gänsicke, K. Beuermann, & K. Reinsch, 165

Potter, S., Romero-Colmenero, E., Buckley, D. A. H., Cropper, M., & Hakala, P. 2001, in Lecture Notes in Physics, Berlin Springer Verlag, Vol. 573, Astrotomography, Indirect Imaging Methods in Observational Astronomy, ed. H. M. J. Boffin, D. Steeghs, & J. Cuypers, 244

Potter, S. B. 2016, in Astrophysics and Space Science Library, Vol. 439, Astrophysics and Space Science Library, ed. H. M. J. Boffin, G. Hussain, J.-P. Berger, & L. Schmidtobreick, 179

Potter, S. B., Augusteijn, T., & Tappert, C. 2005, MNRAS, 364, 565

Potter, S. B., Buckley, D. A. H., O'Donoghue, D., Romero-Colmenero, E., O'Connor, J., Fourie, P., Evans, G., Sass, C., Crause, L., Still, M., Butters, O. W., Norton, A. J., & Mukai, K. 2010, MNRAS, 402, 1161

Potter, S. B., Cropper, M., Mason, K. O., Hough, J. H., & Bailey, J. A. 1997, MNRAS, 285, 82

Potter, S. B., Hakala, P. J., & Cropper, M. 1998, MNRAS, 297, 1261

Potter, S. B., Romero-Colmenero, E., Ramsay, G., Crawford, S., Gulbis, A., Barway, S., Zietsman, E., Kotze, M., Buckley, D. A. H., O'Donoghue, D., Siegmund, O. H. W., McPhate, J., Welsh, B. Y., & Vallerga, J. 2011, MNRAS, 416, 2202

Potter, S. B., Romero-Colmenero, E., Watson, C. A., Buckley, D. A. H., & Phillips, A. 2004, MNRAS, 348, 316

Pretorius, M. L., Knigge, C., & Schwope, A. D. 2013, MNRAS, 432, 570

Qian, S.-B., Liao, W.-P., Zhu, L.-Y., & Dai, Z.-B. 2010, ApJ, 708, L66

Qian, S.-B., Liu, L., Liao, W.-P., Li, L.-J., Zhu, L.-Y., Dai, Z.-B., He, J.-J., Zhao, E.-G., Zhang, J., & Li, K. 2011, MNRAS, 414, L16

Ramsay, G. 1994, Information Bulletin on Variable Stars, 4075

Ramsay, G., Cropper, M., Wu, K., & Potter, S. 1996, MNRAS, 282, 726

Ramsay, G., Potter, S. B., Buckley, D. A. H., & Wheatley, P. J. 1999, MNRAS, 306, 809

Rappaport, S., Joss, P. C., & Webbink, R. F. 1982, ApJ, 254, 616

Rappaport, S., Verbunt, F., & Joss, P. C. 1983, ApJ, 275, 713

Regős, E. & Tout, C. A. 1995, MNRAS, 273, 146

Richardson, W. H. 1972, J. Opt. Soc. Am., 62, 55

Ritter, H. 2012, Mem. Soc. Astron. Italiana, 83, 505

Ritter, H. & Kolb, U. 2003, A&A, 404, 301

Romanova, M. M. & Owocki, S. P. 2015, Space Sci. Rev., 191, 339

Rutten, R. G. M. 1998, A&AS, 127, 581

Rutten, R. G. M. & Dhillon, V. S. 1994, A&A, 288, 773

Rutten, R. G. M., Dhillon, V. S., Horne, K., & Kuulkers, E. 1994, A&A, 283, 441

Schachter, J., Filippenko, A. V., Kahn, S. M., & Paerels, F. B. S. 1991, ApJ, 373, 633

Schwarzenberg-Czerny, A. 1981, AcA, 31, 241

Schwope, A. 2001, in Lecture Notes in Physics, Berlin Springer Verlag, Vol. 573, Astrotomography, Indirect Imaging Methods in Observational Astronomy, ed. H. M. J. Boffin, D. Steeghs, & J. Cuypers, 127

Schwope, A. D., Buckley, D. A. H., O'Donoghue, D., Hasinger, G., Truemper, J., & Voges, W. 1997a, A&A, 326, 195

Schwope, A. D., Catalán, M. S., Beuermann, K., Metzner, A., Smith, R. C., & Steeghs, D. 2000, MNRAS, 313, 533

Schwope, A. D., Hambaryan, V., Schwarz, R., Kanbach, G., & Gänsicke, B. T. 2002, A&A, 392, 541

Schwope, A. D., Mantel, K.-H., & Horne, K. 1997b, A&A, 319, 894

Schwope, A. D., Schwarz, R., Sirk, M., & Howell, S. B. 2001, A&A, 375, 419

Schwope, A. D., Thomas, H.-C., Beuermann, K., & Reinsch, K. 1993, A&A, 267, 103

Seward, F. D. & Charles, P. A. 2010, Exploring the X-ray Universe (Cambridge: Cambridge Univ. Press)

Silber, A., Bradt, H. V., Ishida, M., Ohashi, T., & Remillard, R. A. 1992, ApJ, 389, 704

Sion, E. M. 1991, AJ, 102, 295

Skilling, J. & Bryan, R. K. 1984, MNRAS, 211, 111

Smak, J. 1969, AcA, 19, 155

—. 1981, AcA, 31, 395

Spruit, H. C. 1994, A&A, 289, 441

—. 1998, arXiv:astro-ph/9806141

Spruit, H. C. & Ritter, H. 1983, A&A, 124, 267

Spruit, H. C. & Rutten, R. G. M. 1998, MNRAS, 299, 768

Spruit, H. C. & Taam, R. E. 2001, ApJ, 548, 900

Steeghs, D. 2003, MNRAS, 344, 448

Steeghs, D., Harlaftis, E. T., & Horne, K. 1997, MNRAS, 290, L28

Steeghs, D., Horne, K., Marsh, T. R., & Donati, J. F. 1996, MNRAS, 281, 626

Steeghs, D., Howell, S. B., Knigge, C., Gänsicke, B. T., Sion, E. M., & Welsh, W. F. 2007, ApJ, 667, 442

Stockman, H. S., Schmidt, G. D., & Lamb, D. Q. 1988, ApJ, 332, 282

Tappert, C., Augusteijn, T., & Maza, J. 2004, MNRAS, 354, 321

Tout, C. A. & Pringle, J. E. 1992, MNRAS, 256, 269

Townsley, D. M. & Gänsicke, B. T. 2009, ApJ, 693, 1007

Tylenda, R. 1981, AcA, 31, 127

Ustyugov, V. A., Zhilkin, A. G., & Bisikalo, D. V. 2013, Astronomy Reports, 57, 811

Van Dokkum, P. G. 2001, PASP, 113, 1420

Verbunt, F. & Zwaan, C. 1981, A&A, 100, L7

Vrielmann, S., Horne, K., & Hessman, F. V. 1999, MNRAS, 306, 766

Vrielmann, S. & Schwope, A. D. 2001, MNRAS, 322, 269

Warner, B. 1976, in IAU Symposium, Vol. 73, Structure and Evolution of Close Binary Systems, ed. P. Eggleton, S. Mitton, & J. Whelan, 85

Warner, B. 1995, Ap&SS, 232, 89

—. 2003, Cataclysmic Variable Stars (Cambridge: Cambridge Univ. Press), 592

Watson, C. A. & Dhillon, V. S. 2001, MNRAS, 326, 67

Watson, C. A., Dhillon, V. S., Rutten, R. G. M., & Schwope, A. D. 2003, MNRAS, 341, 129

Watson, C. A., Dhillon, V. S., & Shahbaz, T. 2006, MNRAS, 368, 637

Watson, C. A., Steeghs, D., Shahbaz, T., & Dhillon, V. S. 2007, MNRAS, 382, 1105

Wickramasinghe, D. T. & Meggitt, S. M. A. 1985, MNRAS, 214, 605

Wickramasinghe, D. T. & Wu, K. 1994, MNRAS, 266, L1

Williams, G. 1983, ApJS, 53, 523

Williams, G. A. 1991, AJ, 101, 1929

Williams, R. E. 1980, ApJ, 235, 939

Zhang, C. M., Wickramasinghe, D. T., & Ferrario, L. 2009, MNRAS, 397, 2208

Zhilkin, A. G. 2007, Computational Mathematics and Mathematical Physics, 47, 1819

—. 2010, Matematicheskoe Modelirovanie, 22, 110

Zhilkin, A. G. & Bisikalo, D. V. 2009, Astronomy Reports, 53, 436

—. 2010a, Astronomy Reports, 54, 840

—. 2010b, Advances in Space Research, 45, 437

Zhilkin, A. G. & Bisikalo, D. V. 2011, in Astronomical Society of the Pacific Conference Series, Vol. 444, 5th International Conference of Numerical Modeling of Space Plasma Flows (ASTRONUM 2010), ed. N. V. Pogorelov, E. Audit, & G. P. Zank, 91

Zhilkin, A. G., Bisikalo, D. V., & Mason, P. A. 2012, Astronomy Reports, 56, 257

The devil can cite Scripture for his purpose.

– William Shakespeare, *The Merchant of Venice*, Act I, Scene 3